

Axonal projections from mouse whisker-related sensory cortex

Présentée le 6 octobre 2023

Faculté des sciences de la vie
Laboratoire de traitement sensoriel
Programme doctoral en neurosciences

pour l'obtention du grade de Docteur ès Sciences

par

Yanqi LIU

Acceptée sur proposition du jury

Prof. R. Schneggenburger, président du jury
Prof. C. Petersen, directeur de thèse
Prof. A. Holtmaat, rapporteur
Prof. L. Luo, rapporteur
Prof. M. Mathis, rapporteuse

Acknowledgement

Five years ago, I came across Carl's lab by pure serendipity. Every time I scrutinize the series of events that led me to myself today, I feel awe in front of the mysterious forces in life. This work would not have been possible without the supports from my supervisors, colleagues, fellow scientists, family and friends.

Luck has visited me often and having Carl and Sylvain as my supervisors is definitely one example. My supervisors trusted me on the project, handed me as much as resources as I needed and encouraged me to actively discuss with others. I am deeply inspired by their meticulousness towards science, their emphasis on data quality, and their commitments to convey simple and clear messages. Carl and Sylvain were also always attentive and supportive to my personal career development which I am also very grateful of.

Sciences is rarely approached in solitary and this project was no exception. Solidarity from colleagues and fellow scientist within and outside of the EPFL are also essential for my mental well being. I would like to express my gratitude toward all my colleagues in LSENS especially to Georgios, Jun, Vahid, Keita, Candice, and Lucas for their constant patience and their support. Helpful discussions with various scientists throughout my project are glowing examples for open science. I would like to especially thank Ms. Ivanna Gantar, Dr. Stéphane Pagès, Dr. Rob Campbell, Prof. Hanchuan Peng, Prof. Nicolas Renier, Prof. Liqun Luo, Dr. Drew Friedmann among many others. I would also like to thank my PhD Candidacy examiners and PhD thesis examiners Prof. Anthony Holtmaat, Prof. Graham Knott, Prof. Liqun Luo, Prof. Mackenzie Mathis, and Prof. Ralf Schneggenburger.

Although I've only been back home for two times in five years, home was always a safe sanctuary for both my mind and body. My parents would constantly say 'don't worry, in the worst case just come back and live in the basement' in response to my devastations. They always encouraged me to pursue whatever I have chosen and I've always looked up to my parents for their diligence, determination and curiosity.

I was also fortunate for being surrounded by a warm group of friends. I would like to express my gratitude towards all my friends that I met during my time in Lausanne. A special mention goes to my dota2 friends who carried me not only '*in silico*' but also during numerous hikes, ski trips, board games nights, and other outings. Finally, to my partner Kemi who was a great source of inspiration and was always there to sooth my nerves, especially during the last stages of my PhD.

Abstract

The nervous system involves complex networks and circuits that underly behaviour and cognition. These networks are formed by excitatory and inhibitory neurons working in finely orchestrated manners. Excitatory neurons are the main players to receive information with their dendrites and convey information to the next neurons via their axons, especially over long distances. Mapping of axonal projection then becomes a critical task which provides anatomical basis for functional studies and circuitry information for computational modeling of the brain. In addition, mapping projections, or establishing connectomes in different species allow appreciation not only to the common organizing principles of the nervous system but also to evolutionary pressure reflected in discrepancies. Rodents rely their whiskers to sense objects in their environment. They have developed a highly specialized neural circuitry to process whisker information, making the whisker system a valuable model for neuroscience.

In this PhD thesis, I take advantage of this well studied system and aim to 1) describe important anatomical pathways involved in whisker-related learning, 2) reconstruct detailed morphology at the single neuron level in the whisker related primary sensory area (SSp-bfd), and finally 3) map neural projections in a cell-type specific and layer specific manners in the SSp-bfd and secondary sensory area (SSs). To address these aims, I adopted multiple forms of sample labeling, pre-treatment, microscopy and image processing method suitable for the specific question.

First, I helped to describe a parallel pathway from the SSp-bfd to primary motor area (MOp) and the SSs to secondary motor area (MOs). In a sensorimotor learning task, mice must learn to transform whisker information into a motor plan in order to lick and obtain a reward. Previous studies have shown that lick plan is maintained in the MOs when the animal has learned and become expert at this task. We now provide a possible pathway for whisker information to be conveyed from the SSp-bfd, SSs and finally to MOs.

Then I attempted to obtain full morphological reconstructions of single neurons in the layer 2/3 of the SSp-bfd. We managed to successfully reconstruct 10 neurons and their processes through volumetric imaging. The dataset showed an incredible diversity of projection patterns even with just 10 neurons. Each neuron sends axon only to a subset of the innervation regions and there was no pair of neurons with identical projections. Our result highlights the enormous diversity of neuron morphology and the need for future characterisations at the fine scale level.

In the last chapter, I aim to establish a projection map for the SSp-bfd and SSs in a layer and cell class specific manner using transgenic mouse lines. We found that superficial neurons in the layer 2/3 and layer 4 innervated the ipsilateral hemisphere heavily but showed fewer targets on the contralateral hemisphere. In comparison, superficial layer 5 neurons showed great coverages of bilateral regions in the isocortex. Deep layer 5 had fewer cortical targets but projected heavily to subcortical and brainstem regions. These findings suggest the different roles of neurons in various layers in the microcircuitry with superficial layers responsible for cortical computation and global broadcasting while deep neurons are responsible for disseminating top-down information to subcortical and brain stem effectors.

Key words: sensory perception, mouse, whisker, sensorimotor transformation, barrel cortex, neuron reconstructions, morphology, axons, connectome, cortical layers, cortical microcircuitry.

Résumé

Le système nerveux implique des réseaux complexes et des circuits qui sous-tendent le comportement et la cognition. Ces réseaux sont formés par des neurones excitateurs qui reçoivent des informations via leurs dendrites et transmettent ces informations aux neurones suivants par le biais de leurs axones. La cartographie de la projection axonale devient alors une tâche cruciale qui fournit une base anatomique pour les études fonctionnelles et des informations sur la connectivité pour la modélisation computationnelle du cerveau. De plus, la cartographie des projections ou l'établissement de connectomes chez différentes espèces permettent d'apprécier non seulement les principes d'organisation communs du système nerveux, mais aussi les pressions évolutives reflétées dans les divergences. En tant qu'animaux nocturnes, les rongeurs comptent sur leurs vibrisses pour détecter les objets dans leur environnement. Ils ont développé un circuit neural hautement spécialisé pour traiter les informations des vibrisses, faisant du système des vibrisses un modèle précieux pour les neurosciences.

Dans cette thèse de doctorat, je profite de ce système bien étudié et vise à : 1) décrire les voies anatomiques importantes impliquées dans l'apprentissage lié aux vibrisses, 2) reconstruire la morphologie détaillée au niveau des neurones individuels dans la région sensorielle primaire liée aux vibrisses (SSp-bfd), et enfin 3) cartographier les projections neuronales de manière spécifique aux types cellulaires et aux couches dans le SSp-bfd et la région sensorielle secondaire (SSs). Pour atteindre ces objectifs, j'ai adopté plusieurs formes d'étiquetage des échantillons, de prétraitement, de microscopie et de méthodes de traitement d'images adaptées à la question spécifique.

Tout d'abord, j'ai contribué à décrire une voie parallèle du SSp-bfd vers la région motrice primaire (MOp) et du SSs vers la région motrice secondaire (MOs). Dans une tâche d'apprentissage sensorimoteur, les souris doivent apprendre à transformer les informations des vibrisses en un plan moteur pour lécher et obtenir une récompense. Des études antérieures ont montré que le plan de léchage est maintenu dans le MOs lorsque l'animal a appris et est devenu expert dans cette tâche. Nous fournissons maintenant une possible voie pour que les informations des vibrisses soient transmises du SSp-bfd, du SSs et enfin du MOs.

Ensuite, j'ai tenté d'obtenir des reconstructions morphologiques complètes de neurones individuels dans la couche 2/3 du SSp-bfd. Nous avons réussi à reconstruire avec succès 10 neurones et leurs processus grâce à l'imagerie volumétrique. Le jeu de données a montré une incroyable diversité de schémas de projection même avec seulement 10 neurones. Chaque neurone envoie son axone uniquement à un sous-ensemble des régions innervées, et il n'y avait pas de paire de neurones avec des projections identiques. Nos résultats mettent en évidence l'énorme diversité de la morphologie neuronale et la nécessité de futures caractérisations à l'échelle fine.

Dans le dernier chapitre, j'ambitionne d'établir une carte de projection pour le SSp-bfd et le SSs de manière spécifique aux couches et aux classes de cellules en utilisant des lignées de souris transgéniques. Nous avons constaté que les neurones superficiels dans la couche 2/3 et la couche 4 innervaient fortement l'hémisphère ipsilatéral, mais montraient moins de cibles dans l'hémisphère contralatéral. En comparaison, les neurones de la couche

superficielle 5 couvraient largement les régions bilatérales dans l'isocortex. Les neurones profonds de la couche 5 avaient moins de cibles corticales mais projetaient fortement vers les régions sous-corticales et du tronc cérébral. Ces découvertes suggèrent les différentes fonctions des neurones dans différentes couches de la microcircuitry, les couches superficielles étant responsables de la computation corticale et de la diffusion globale, tandis que les neurones profonds sont responsables de la diffusion d'informations descendantes vers les effecteurs sous-corticaux et du tronc cérébral.

Mots-clés : perception sensorielle, souris, vibrisses, transformation sensorimotrice, cortex des barils, reconstructions neuronales, morphologie, axones, connectome, couches corticales, microcircuit cortical.

List of Figures

Figure 1-1 Cajal's illustration indicating information flow arriving to the cerebral cortex.	15
Figure 1-2 Laminar organisations of the cerebral cortex at the transition of the calcarine sulcus.	18
Figure 1-3 Proposed excitatory neuron subclasses based on projection patters in layers 2 - 5 and the direction of information flow.	19
Figure 1-4 Work flow of the 3D mouse common coordinate framework from the Allen Brain Institute.	21
Figure 1-5 Schematics of fluorescent micro-optical sectioning tomography (fMOST), serial two-photon tomographic microscope (STPT) and the light sheet fluorescent microscopy (LSFM).	24
Figure 1-6 Specialized pathway for whisker related information in mice.	29
Figure 1-7 Microcircuits within the barrel cortex.	31
Figure 2-1 Multi-area recordings during delayed whisker detection task and assignment of RS and FS units to cortical sub-divisions.	37
Figure 2-2 FS neurons had similar but larger task-modulation compared to RS neurons in the same region.	41
Figure 2-3 Fast propagation of sensory responses across cell classes and cortical regions.	43
Figure 2-4 Fast whisker responses in FS neurons of sensory areas.	46
Figure 2-5 Distinct frontal projections of wS1 and wS2.	48
Figure 2-6 Learning differently modulated sensory responses of RS and FS neurons in wM1 and wM2 areas.	51
Figure 2-7 FS neuronal responses in tjM1 and ALM changed similarly to RS neurons.	54
Figure 2-8 Diverse changes of putative excitation-inhibition balance in different cortical regions across learning.	55
Figure 2-9 S1 Fig. Anatomical localisation of neurons.	63
Figure 2-10 S2 Fig. Distribution of spike width in different cortical areas.	64
Figure 2-11 S3 Fig. Baseline firing rates of RS and FS neurons.	66
Figure 2-12 S4 Fig. Opto-tagging GABAergic neurons in VGAT-ChR2 mice.	67
Figure 2-13 S5 Fig. FS neurons remain at baseline level during correct rejection trials.	68
Figure 2-14 S6 Fig. Sequential activation of cortical regions upon whisker stimulation.	69
Figure 2-15 S7 Fig. Early sensory response map across different probes.	70
Figure 2-16 S8 Fig. Faster and larger sensory response in FS neurons across all layers of wS1 and wS2.	71
Figure 2-17 S9 Fig. Layer-specific quantification of RS and FS neuronal responses during the secondary late response in wS1 and wS2 across learning.	73
Figure 2-18 S10 Fig. Layer-specific quantification of RS and FS neurons in wM1 across learning.	75
Figure 2-19 S11 Fig. Layer-specific quantification of RS and FS neuronal activity in wM2 across learning.	77
Figure 2-20 S12 Fig. Inter-areal functional connectivity.	79
Figure 2-21 S13 Fig. Layer-specific quantification of RS and FS neurons in tjM1 across learning.	81
Figure 2-22 S14 Fig. Suppression of activity in tjM1 during response window in no-lick trials of Expert mice.	82
Figure 2-23 S15 Fig. Layer-specific quantification of RS and FS neuronal activity in ALM.	84
Figure 2-24 S16 Fig. Preparatory neuronal activity in ALM is decreased, but remains significant in quiet trials devoid of movements.	85
Figure 3-1 Acquisition and analysis pipeline for single cell reconstruction.	91
Figure 3-2 Reconstruction and quantification of example neuron AL110 with projections to the supplementary somatosensory cortex.	95

Figure 3-3 Reconstruction and quantification of example neuron AL126 with projections to the primary and secondary motor cortex.	97
Figure 3-4 Reconstruction and quantification of example neuron AL157 with projections to the primary somatosensory cortex upper limb area.	99
Figure 3-5 Reconstruction and quantification of example neuron GF243 with projections to an unassigned region of primary somatosensory cortex and an anterior visual area.	101
Figure 3-6 Reconstruction and quantification of example neuron AL131 with projections to the caudoputamen and multiple visual areas.	103
Figure 3-7 Reconstruction and quantification of example neuron AL142 with projections to the lateral caudoputamen and towards the amygdala.	105
Figure 3-8 Summary of the ten reconstructed neurons.	106
Figure 3-9 Supplementary Figure 1. Anatomical locations of different cortical areas in a horizontal view of the mouse dorsal cortex.	114
Figure 3-10 Supplementary Figure 2. Example section demonstrating that antibody staining reveals axonal structures not found in the two-photon tomography.	115
Figure 3-11 Supplementary Figure 3. Reconstruction and quantification of example neuron AL066 with projections to visual areas.	117
Figure 3-12 Supplementary Figure 4. Reconstruction and quantification of example neuron AL080 with projections to visual areas and the secondary somatosensory cortex.	118
Figure 3-13 Supplementary Figure 5. Reconstruction and quantification of example neuron AL092 with projections to the primary somatosensory area upper limb area.	120
Figure 3-14 Supplementary Figure 6. Reconstruction and quantification of example neuron AL140 with projections to the primary somatosensory upper limb area, the secondary somatosensory area and visual areas.	121
Figure 3-15 Supplementary Figure 7. Dendritic morphologies.	122
Figure 4-1. Sample preparation and injection site identification.	127
Figure 4-2 Identification of injection site size and location for SSp-bfd and SSs injections in the current study.	128
Figure 4-3 Image substack and labels for training Trailmap network and training curves	129
Figure 4-4 TrailMap segmentation and selections of connected components.	130
Figure 4-5 Cre-independent expression of reporter viruses and the subsequent TrailMap segmentations.	131
Figure 4-6 Hierarchy and Nomenclature of broad brain region categories based on the Allen brain institute mouse CCF.	133
Figure 4-4-7 Overview of all SSp-bfd and SSs projections.	134
Figure 4-8 Averaged sum axonal projections for each of the six mouse lines for SSp-bfd and SSs injections.	135
Figure 4-9 Quantification of axonal projections in cerebrum, brainstem and cerebellum.	137
Figure 4-10 Quantification of axonal projections in brain subregions.	138
Figure 4-11 Axonal projections for samples with SSp-bfd injections in detailed subregions of cerebrum and brain stem, presented in linear color scale.	141
Figure 4-12 Axonal projections for samples with SSp-bfd injections in detailed subregions of cerebrum and brain stem, presented in logarithmic color scale.	143
Figure 4-13 Axonal projections for samples with SSs injections in subregions of cerebrum and brain stem, presented in linear color scale.	145
Figure 4-14 Axonal projections for samples with SSs injections in subregions of cerebrum and brain stem, presented in logarithmic color scale.	147
Figure 4-15 Correlation matrix comparing axonal projections in SSp-bfd and SSs samples.	148

Figure 4-16 Averaged sum axonal projections in the isocortex for each mouse line for SSp-bfd and SSs injections.	149
Figure 4-17 Averaged sum axonal projections in the isocortex for each mouse line for SSp-bfd and SSs injections in horizontal view.	151
Figure 4-18 Axonal projections of samples with SSp-bfd injections in subregions the isocortex, presented in linear color scale.	152
Figure 4-19 Axonal projections of samples with SSp-bfd injections in subregions the isocortex, presented in logarithmic color scale.	153
Figure 4-20 Axonal projections of samples with SSs injections in subregions the isocortex, presented in linear color scale.	154
Figure 4-21 Axonal projections of samples with SSs injections in subregions the isocortex, presented in logarithmic color scale.	155
Figure 4-22 Amounts of axons in isocortex subregions for Rasgrf2-dCre brains injected in the SSp-bfd or SSs.	156
Figure 4-23 Amounts of axons in isocortex subregions for Scnn1a-Cre brains injected in the SSp-bfd or SSs.	157
Figure 4-24 Amounts of axons in isocortex subregions for Tlx3-Cre brains injected in the SSp-bfd or SSs.	157
Figure 4-25 Amounts of axons in isocortex subregions for Rbp4-Cre brains injected in the SSp-bfd or SSs.	158
Figure 4-26. Amounts of axons in isocortex subregions for Sim1-Cre brains injected in the SSp-bfd or SSs.	158
Figure 4-27 Amounts of axons in isocortex subregions for Ntsr1-Cre brains injected in the SSp-bfd or SSs.	159
Figure 4-28 Averaged sum axonal projections in layers of the somatomotor regions in each mouse lines for SSp-bfd and SSs injections in horizontal views.	160
Figure 4-29 Contours and centers of axons hot spots in layer 2/3 of the MO region	161
Figure 4-30 Amounts of axons in layers of the somatomotor regions for neurons of all six genotypes injected in the SSp-bfd or SSs.	162

List of tables

Table 1 List of anatomical regions and their acronyms.....	191
--	-----

Table of Contents

Acknowledgement.....	1
Abstract	2
Résumé	4
Chapter 1 Introduction	13
1.1 General cortical architecture.....	16
1.2 Digital mouse atlases.....	19
1.3 Volumetric brain imaging and analysis.....	22
1.5 Current major single neuron reconstruction projects.....	25
1.6 Current major projection mapping projects	26
1.7 The whisker system	27
1.7 Microcircuits in the rodent barrel cortex	30
1.8 Projections from whisker related somatosensory cortices	31
1.9 Conclusion and aim of PhD.....	32
Chapter 2 Learning-related congruent and incongruent changes of excitation and inhibition in distinct cortical areas.	33
2.1 Abstract	33
2.2 Introduction.....	33
2.3 Results	35
2.3.1 Localisation and classification of cortical neurons.....	35
2.3.2 Strong task-modulation of fast-spiking neurons	38
2.3.3 Rapid excitation of FS neurons.....	41
2.3.4 Fast sensory processing in wS1 and wS2.....	44
2.3.5 Parallel anatomical pathways from wS1 and wS2 to wM1 and wM2	46
2.3.6 Changes in fast sensory processing in wM1 and wM2.....	48
2.3.7 Neuronal activity in tongue and jaw-related motor cortices	51
2.3.8 Changes in excitation and inhibition across learning.	54
2.4 Discussion	56
2.5 Methods	58
2.5.1 Behavioral paradigm and electrophysiological recordings	58
2.5.2 Optogenetic tagging of GABAergic neurons.....	59
2.5.3 Anatomical analysis of axonal projections from wS1 and wS2 to frontal	59
cortex.....	59
3.5.4 Data analysis and statistics.....	60
2.5.5 Inter-areal functional connectivity measures	61

2.5.6 Quantifying learning modulation index.....	62
2.5.7 Statistics.....	62
2.6 Additional information	63
Chapter 3 Axonal and dendritic morphology of excitatory neurons in layer 2/3 mouse barrel cortex imaged through whole-brain tomography and registered to digital brain atlas	86
3.1 Abstract	86
3.2 Introduction.....	86
3.3 Results	88
3.3.1 Reconstruction of dendrites and axons of single neurons in layer 2/3 barrel cortex.....	88
3.3.2 Diverse axonal projections of single neurons in layer 2/3 of wS1	92
3.3.3 Summary of all SSp-bfd layer 2/3 neurons reconstructed	93
3.4 Discussion	107
3.4.1 Diverse projection areas of individual neurons in layer 2/3 barrel cortex.....	107
3.4.2 Axons in the fiber bundles.....	108
3.4.3 Limitations and future perspectives.....	109
3.5 Methods	110
3.5.1 Head-post Implantation	110
3.5.2 Single-cell Electroporation	111
3.5.3 Sample Preparation and Two-photon Tomography.....	112
3.5.4 Tracing of Axons and Dendrites	112
3.5.5 Extracting barrel column masks from the Digital Atlas	113
3.5.6 Registration to a Digital Atlas	113
3.5.7 Quantification of neurite length.....	113
3.5.8 Immunohistochemistry	113
3.5.9 Data availability	114
3.6 Additional information	114
Chapter 4 Cell class dependent, layer specific projections from primary and secondary whisker-related somatosensory cortices.	123
4.1 Introduction.....	123
4.2 Results	125
4.2.1 Sample preparation and analysis workflow	125
4.2.2 Axonal projections from primary and secondary whisker related somatosensory cortex	132
4.2.3 Projection targets within the isocortex.....	148
4.2.4 Projection patterns in the somatomotor regions	159
4.3 Discussion	163
4.4 Methods	168

4.4.1 Animals	168
4.4.2 Headpost implantation and intrinsic optical imaging	168
4.4.3 Virus injection and perfusion	169
4.4.4 Whole brain immunostaining and clearing	169
4.4.5 Imaging	170
4.4.6 Axon segmentations and post processing.....	170
4.4.7 Registration to Allen CCF v3 and injection site identification	171
4.4.8 Analysis and visualizations	171
Chapter 5 Conclusions and future directions	172
5.1 Conclusions.....	172
5.1.1 Pathways involved in learning of whisker related sensorimotor task	172
5.1.2 Single neuron morphologies in layer 2/3 of the barrel cortex	172
5.1.3 Cell-type specific projections of neurons in the whisker related primary and secondary somatosensory cortex	173
5.2 Outlook.....	174
Chapter 6 References	175
Chapter 7 List of anatomical regions.....	189
Chapter 8 Curriculum vitae	192

Chapter 1 Introduction

The nervous system supports an incredibly wide range of tasks that enables the organism's survival. Ranging from simple functions such as sensory perceptions and motor reflexes to sophisticated behaviors such as learning and planning, how the brain supports behavior and cognition remains enigmatic. Spanish neuroscientist and Nobel prize winner Ramón y Cajal established the neuron doctrine that marks the beginning of modern neuroscience (Cajal, 1894). Through pure anatomical observations, Cajal suggested that neurons are the basic functional units of the brain such that they receive information through their dendrites and output information to the next neurons through their axons (Figure 1.1). The following decades of work confirmed that neurons communicate through electrochemical synapses between their axons and dendrites and also showed that neurons display a vast variety of morphologies in terms of cell body, dendrite, and axon shapes.

Although functional connectivity between brain regions could be established via measurements such as the functional magnetic resonance imaging, electrophysiological recordings and calcium imaging, the existence of axonal connections provides a physical conduit of signal propagation. Hence, maps of neural connections, or connectomes, give a comprehensive view of possible routes of communication between different areas of the brain and potential sites of signal integration. Typically, these anatomical maps can be revealed by electron microscopy (EM) or specific tracers in combination with light microscopy.

Establishing connectomes has become one of the fundamental resources for studying the nervous systems of popular model organisms such as the *Caenorhabditis elegans* (White, Southgate, Thomson, and Brenner. 1986; Varshney et al. 2011; Cook et al. 2019), *Drosophila melanogaster* (Chiang et al. 2011; Zheng et al. 2018; Scheffer et al. 2020), *Mus musculus* (Oh et al. 2014; Zingg et al. 2014b), *Callithrix jacchus* (marmosets, www.marmosetbrain.org), Macaques (cocomac.g-node.org, Stephan et al. 2001; Kötter 2004; Bakker, Wachtler, and Diesmann 2012) and human. Thanks to their smaller sized nervous system with fewer neurons, full connectomes by EM of *C. elegans* and *Drosophila* have been established (Zheng et al. 2018; Cook et al. 2019). Connection maps for more evolved nervous systems remain an ongoing effort that require diligent collaborations. The human connectome project was launched by the National Institution of Health of the United States and envisions to provide structural and functional connections of the human brain. While the five-year project was launched in 2009, it is still ongoing today which reflects the challenging nature of such an endeavor.

Connectomes not only provide an anatomical basis of functional connections for experimental neuroscientists but also spark interests in the field of computational neuroscience. The richness of these datasets allows the classifications of neuron types as well as the identification of connection hubs and motifs formed by brain regions (Varshney et al. 2011; Towlson et al. 2013; Scheffer et al. 2020 and many others). Anatomical and functional connections also provide valuable starting points for brain simulation and modeling (Fan and Markram 2019). Finally, establishing connectomes for multiple species allows for comparative connectomics. Examining connection topography of simpler and more complex species allows identifications of common themes that might be conserved through evolution and variations that arise from adaptive needs (Van Den Heuvel, Bullmore, and Sporns 2016).

Overall, comprehensive maps of neural connections provide indispensable resources to experimental, theoretical, and comparative neuroscience. These fields then contribute collectively toward the ultimate goal of understanding brain physiology and functions. The main proportion of the current PhD work focuses on establishing projections from two whisker related somatosensory regions of the *Mus musculus* cortex. This first chapter begins with a summary of cortical architecture, followed by the introduction of several technical aspects and efforts in circuit mapping, and finally focuses on known connections involved in the mouse whisker sensory system.

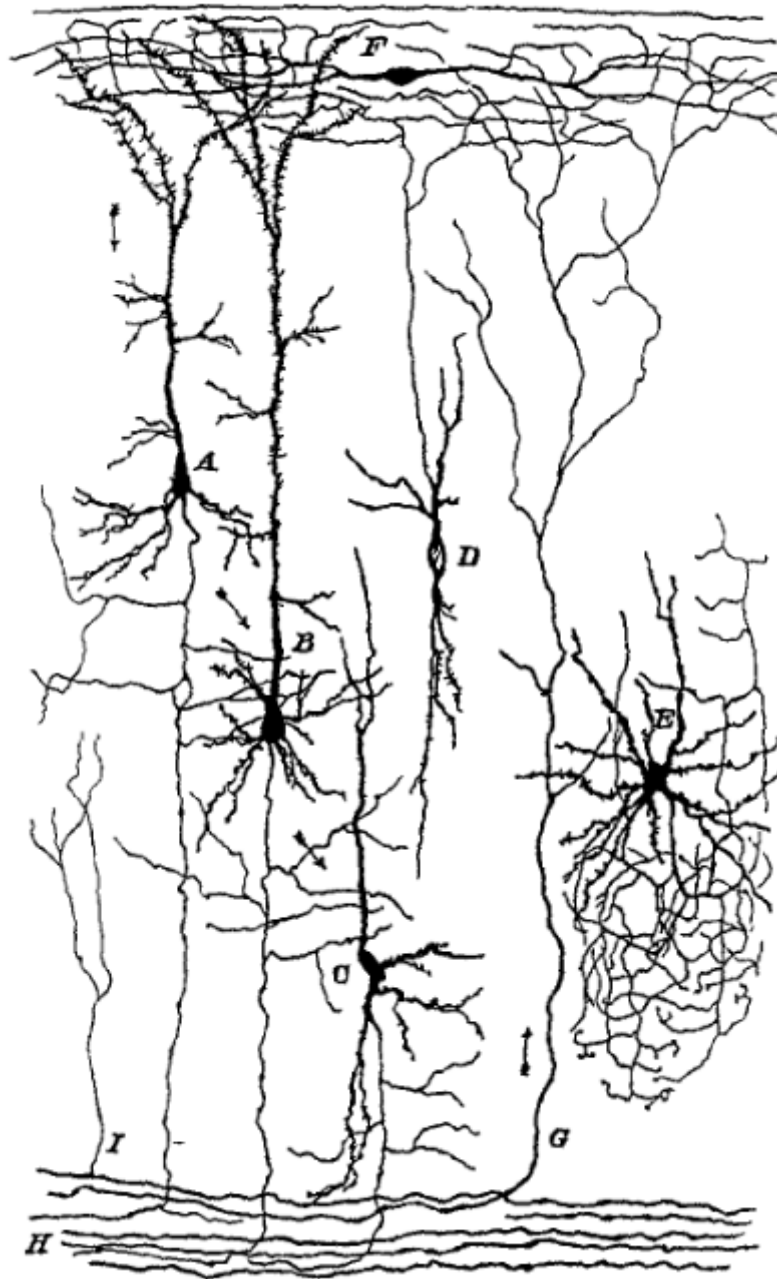


Figure 1-1 Cajal's illustration indicating information flow arriving to the cerebral cortex.

Arrows show the direction of flow from white matter and their collaterals (I, H and G) to various cell class in the cerebral cortex (A - E). Adapted from (Jones 1994).

1.1 General cortical architecture

The cortex is organized on a laminar architecture that runs parallel to the surface of the cerebral cortex. These laminarizations are formed by differential distributions and densities of cells bodies and their processes. Neurons, the principal cells in the cortex, convey and integrate information while glial cells act to support neuronal function. Among neocortical neurons, excitatory (mostly glutamatergic) cells send their axons to their local surrounding and also remotely to other brain regions. In contrast, inhibitory (mostly GABAergic) neurons typically have shorter processes and are mainly responsible for modulating local circuitry with rare exceptions in hippocampal related regions (Freund and Antal 1988; Tamamaki and Tomioka 2010; Urrutia-Piñones et al. 2022) .

Starting from the late 1800s, pioneers in neuroanatomy investigated laminations in the mammalian neocortex by observing stained sliced samples. Identification of cortical functional elements based on anatomical observations was first proposed by Meynert (Meynert 1868) and further investigated by Betz (Betz 1881), Brodmann (Brodmann 1909, Brodmann and Gary 2006) and many others. Expert neuroanatomists adopted both ontogenic and comparative approaches to pinpoint the basic cortical cytoarchitectural organization. It is now generally agreed upon that the mammalian neocortex follows a six layer scheme (Figure 1.2) with variations across brain areas and across species (Brodmann 1909, Brodmann and Gary 2006). Layer 1, the *Lamina zonalis* (molecular layer) consists mostly of fibers and sparse population of GABAergic interneurons, and forms the most superficial layer in the cortex. Layer 2, the *Lamina granularis externa* (outer granular layer) contains small pyramidal cells and stellate cells located just beneath layer 1. In layer 3, the *Lamina pyramidalis* (pyramidal layer), medium sized pyramidal cells are of the major type. In layer 4, the *Lamina granularis interna*, stellate cells are the major cell class. Layer 5, *Lamina ganglionaris* (ganglion cell layer) are the home to large pyramidal neurons. The deepest layer of the cortex, layer 6, *the Lamina multiformis* (spindle cell layer) contains a variety of cells such as small pyramidal cells and spindle cells (Brodmann 1909, Brodmann and Gary 2006; Thomson 2010).

Based on the microscopic structures of the cortex, Brodmann segregated of the cerebral cortex into 52 patches known as the Brodmann areas (Brodmann 1909, Brodmann and Gary 2006). He argued for elemental localization where patches of tissue with the same structure must have the same physiological function. Features such as the patterns of lamination, cell shape, size and density were taken into consideration. Hence, sudden change of cytoarchitecture indicate a transition between patches of cortex with different functions. For instance, Brodmann area 4 ("*giant pyramidal area*", later identified as the primary motor area by others) lacks a clear presence of layer 4 but show prominent pyramidal cell bodies, also known as Betz cells (Betz, 1874), in layer 5. In contrast, layer 4 is expanded in to three sub-layers in Brodmann area 17 ("*striate area*", later identified as the primary visual area) as shown in Figure 1.2. In higher order sensory areas or multimodal areas such as Brodmann area 7, 18 and 39, the size of cell bodies in layer 3 is larger relative to those in layer 5. Through observations with reference to anatomical landmarks (such as lobes and gyrus), homologues of Brodmann areas were identified across various mammals such as human, marmosets, rabbits, and hedgehog (Brodmann 1909, Brodmann and Gary 2006).

Later development in neuroanatomical techniques have provided insights of cortical micro-circuitry not only highlighting cell bodies and fiber patterns but also revealing their connections. Procedures such as single neuron biocytin filling, or anterograde and retrograde viral vectors could label specific group of neurons and labelled their processes. Based on the connections of neurons, it was proposed that excitatory neurons could be further classified into 3 subclasses based on their general projection patterns (Reiner et al 2003; Gerfen, Paletzki, and Heintz 2013; K. D. Harris and Shepherd 2015). Intra-telencephalic (IT) neurons can be found in layers 2 to 6 (L2 -L6) and projects heavily within the telencephalon but not beyond. Among the IT class, layer 4 IT neurons are considered a special case due to their input primarily from the first order thalamic nucleus and their limited output to other cortical regions (Figure 1.3). Other IT neurons receive inputs from thalamic centers, layer 4 IT and other cortical areas. Pyramidal tract (PT) neurons projects to sub-cerebral structures such as the brainstem and spinal cord and reside mostly in L5b. Cortical thalamic (CT) neurons that projects primarily to the thalamus are located mostly in L6. Note that the projections of both PT and CT neurons are mostly ipsilateral while the axons of IT neurons can be found in the contralateral hemisphere. In the framework of cortical circuit hierarchy, the IT class neurons likely serve as the initial steps of receiving thalamic input and integrate inter-area information. PT neurons may then act as the final player to convey integrated information to subcortical areas (Figure 1.3). The functions of CT neurons, on the other hand, remain less obvious and may be involved throughout the stages since they are in a good position to modulate the thalamic-cortical circuit activity. It has been suggested that this scheme of neuron classification is well conserved across multiple areas and inter-area differences are quantitative but not qualitative (K. D. Harris and Shepherd 2015a). In reality, it is very probable to have further subdivisions within each of the 3 main subclasses based on gene expression, projection profiles and functional properties.

Modern techniques allow more precise morphological and functional characterization of cortical laminarities. Systemic screening of genetic markers identified markers that show specificity toward given layer(s) in given brain region(s) in mouse (Gerfen, Paletzki, and Heintz 2013; J. A. Harris et al. 2014). For instance, in the cortex, *Ntsr1* and *Ctgf* genes expression is highly restricted in L6. *Sim1*, *Fezf2*, *Tlx3*, *Efr3a* and *Rbp4* are strong indicator of L5 neurons (Gerfen, Paletzki, and Heintz 2013; E. J. Kim et al. 2015; J. A. Harris et al. 2014; Matho et al. 2021). In addition, *Scnn1a* and *Rorb* expression show layer specificity in L4. And finally, *Rasgrf2*, *Cux1* and *Sepw1* are generally considered markers for L2/3 (Madisen et al. 2010; J. A. Harris et al. 2014; Matho et al. 2021). Such valuable resource provides an additional level of precision in establishing a brain atlas for one of the most common model organisms for neuroscience.

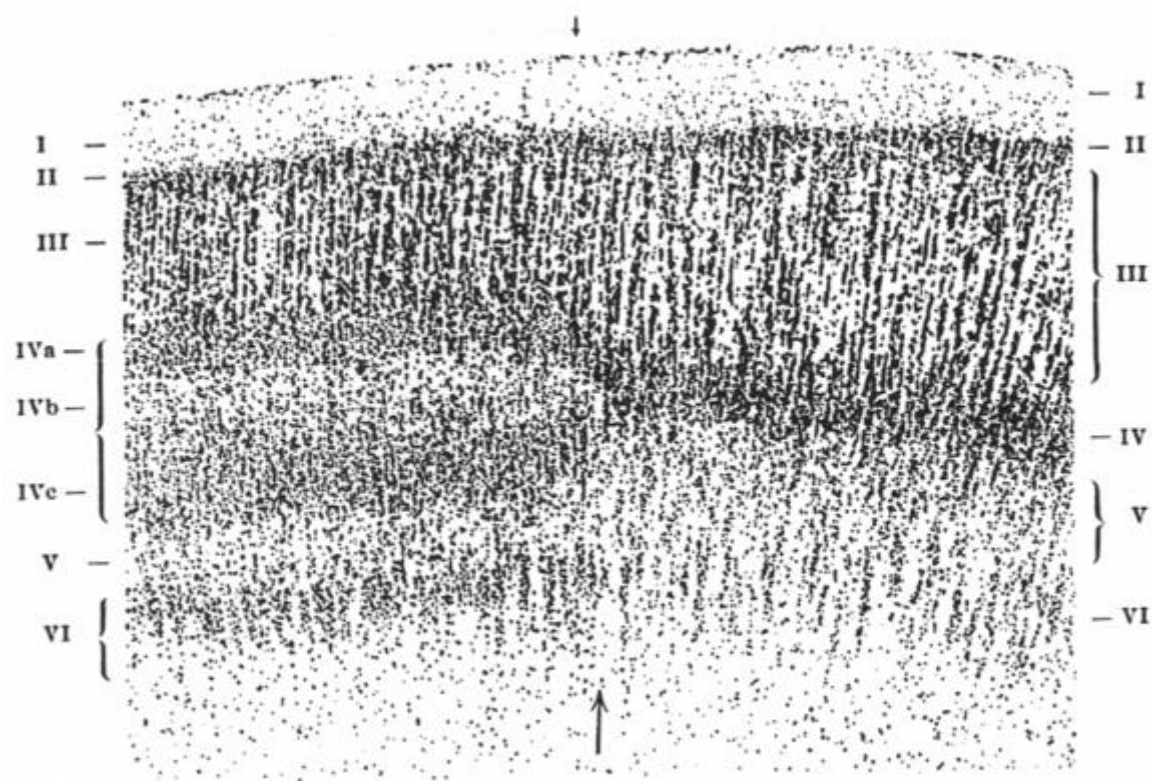


Figure 1-2 Laminar organisations of the cerebral cortex at the transition of the calcarine sulcus.

Brain sample from a human fetus at 8 months. A typical six layered cortex (I to VI) is shown on the right of transition (arrow). In comparison, the calcarine cortex (left of arrow), where the primary visual cortex is located, show a thickening of layer IV that further separates into three sublayers IVa, IVb and IVc. Adapted from (Brodmann and Gary 2006).

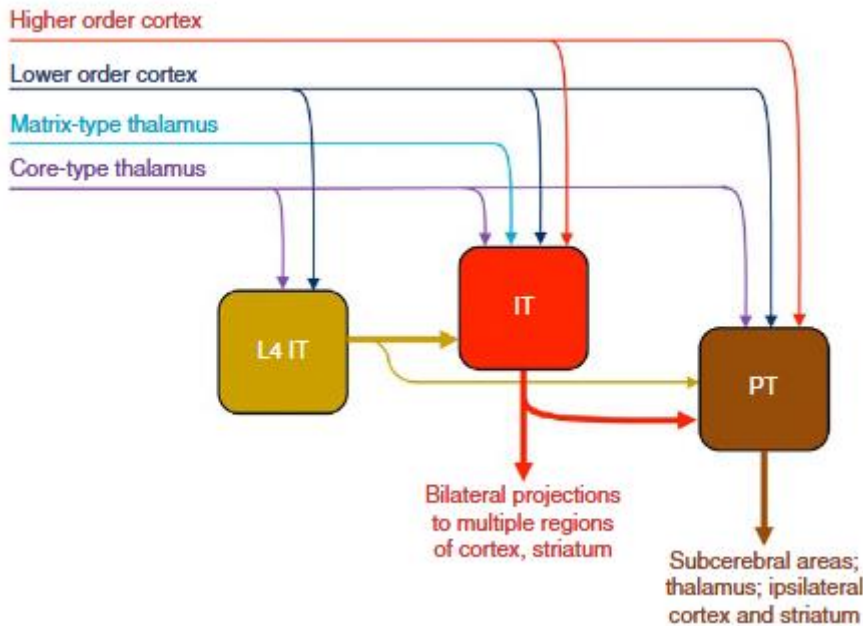


Figure 1-3 Proposed excitatory neuron subclasses based on projection patterns in layers 2 - 5 and the direction of information flow.

Layer 4 intratelencephalic projecting neurons (L4 IT) projects mostly to intratelencephalic neurons in other layers (IT) and to pyramidal tract neurons (PT) to a lesser extent. The IT group then projects to PT class neurons as well as other brain regions. Asymmetry in projections dictates the unidirectional flow of information across L4IT, IT and PT subclasses. Note that each subclass likely receives different types of information from the cortex and the thalamus. Extensive interconnection within each class and layer 6 related class (IT and cortical thalamic) are not shown. Adapted from K. D. Harris and Shepherd 2015.

1.2 Digital mouse atlases

Neuroanatomical studies require a standardized brain atlas to map neural structures to anatomical regions in a unified way. Aligning regions in the sample to a common atlas allows cross validation of results across experiments, experimenters and laboratories. For many decades, many relied on serial section atlases such as the Paxinos and Franklin mouse brain atlas first published in 1997 with many further editions (Franklin and Paxinos, 1997) or the Swanson's Brain Maps (Swanson, 2004). Typically, the atlas is composed of serial images of graphics outlining brain structures in coronal sections with hundreds of micrometers spacing. Brain samples were first sectioned with a microtome, then stained for neural structures (typically with acetylcholinesterase staining or Nissl staining), mounted on glass slides and finally imaged with a bright field microscope. Finally, experts hand draw outlines of brain region boundaries on papers placed over the photograph. Locating brain structures from one's own sample images typically involves simple visual inspection and comparison with the atlas. This approach can introduce inaccuracies at multiple steps. For instance, slicing and mounting can produce tissue distortions that makes comparison difficult. Results of simple visual comparison can also vary from experimenter to experimenter. In the decades passed since 1996, the advancement of technology allowed for more modernized digital atlas. This could then address some of the problems mentioned above and improve the reliability of identifying brain structures in neuroanatomical studies.

The Allen Institute of Brain Science made major efforts toward the creation of a digitized mouse brain atlas (Wang et al. 2020). There are three major components to this atlas, background fluorescent of brain images (template), image of parcellated brain structures (atlas), and a dictionary to translate indexes of the parcellation to sensible neuroanatomical terms. The brain image template was produced by signal intensity averaging over thousands of samples. Each sample is imaged through a serial two-photon tomographic microscope (STPT) that couples a microtome with a two-photon microscope. The sample is embedded in a gel, the microscope images the surface of the brain, then the microtome removes the already imaged plane and the microscope follows to image the newly exposed surface. This iterative process is repeated until the whole brain has been imaged and produces a volumetric stack of images with minimal handling and less distortion. Expert annotators then manually delineate anatomical structures and borders utilizing previous literature in combination with datasets such as brain images of neuron projections, transgenic mice, and *in situ* hybridization data (Figure 1.4). The resulting digital atlas has a voxel size of 10, 25 or 50 μm^3 and can be freely re-orientated in coronal, sagittal, horizontal views as well as other intermediate rotations. The template then acts as a starting material for image registration with one's own volumetric images such as those collected also with STPT or light-sheet microscopy. Registration of sample image to the atlas also allows cross-validations of results across experiments.

The Allen Institute mouse common coordinate framework (CCF) is a beautiful example of interdisciplinary work that requires expertise in fields of biochemistry, neuroanatomy, image processing, informatics among many others. To date, the latest version of the Allen mouse brain CCF has been referenced over 400 times. More details can be found in Wang et al., 2020 and the Allen Mouse Common Coordinate Framework technical white paper (<https://atlas.brain-map.org/>, under adult mouse- documentation). Numerous others also devoted efforts in developing tools for exploration, visualization, processing and analysis tools based on CCF (such as those in Han et al. 2018; Chon et al. 2019; Tyson et al. 2022).

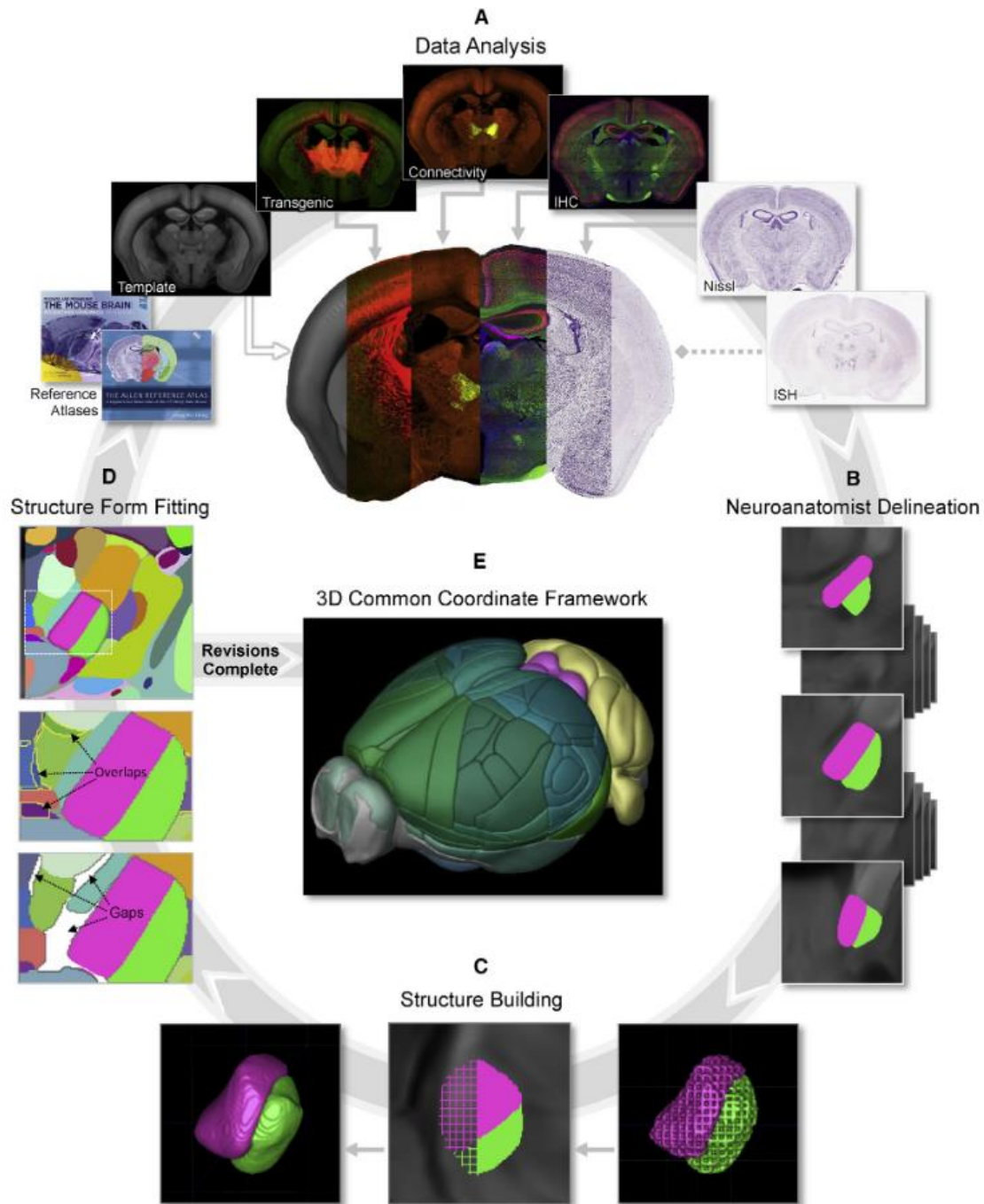


Figure 1-4 Work flow of the 3D mouse common coordinate framework from the Allen Brain Institute.

A) Expert neuroanatomists utilize previous atlases and datasets such as images of targeted injections, transgenic mouse line, immunohistochemistry as starting materials for atlas annotation. B) Neuroanatomists then label voxels on the template for each anatomical structure. The figure shows two neighboring structures side by side as magenta and green. C) 3D rendering of individual structures from 2D planes. D) anatomical structures are then fitted together and manually curated to fix gaps and overlaps between structures. E) Final product of the 3D common coordinate frame work. Figure adapted from Wang et al. 2020.

1.3 Volumetric brain imaging and analysis

Modern optical methods and microscopy are increasingly replacing the traditional slice staining and mounting procedures. Whole-brain clearing and staining enhances signal intensity while lowering background fluorescence. Automated volumetric imaging of the brain increases reliability and throughput compare to the laborious slice mounting procedures. This approach largely resolves the tissue distortion and alignment issue that may arise during slice handling. While volumetric brain imaging maintains greater sample integrity and can provide higher axial resolution, the resulting data size grows rapidly and the subsequent analysis requires more consideration. Data size can range from tens of gigabytes to few terabytes depending on the resolution and the number of channels. Infrastructures to handle big data as well as algorithms to analyse these enormous amounts of data are becoming more accessible.

Biological tissues are composed of various molecules and structures that have different refractive indexes. Inhomogeneity of these 'scatterers' contributes to the milky appearance samples, this led to the lack of clarity required for a sharp image (Richardson and Lichtman 2015). Various clearing methods enhance clarity by increasing uniformity of these scatterers via different principles. Passive immersion-based clearing uses immersion solutions with high refractive index, usually at least 1.45. The tissue is placed in an aqueous solution with gradually increasing gradient of high refractive index molecule such as sucrose, fructose, or glycerol (Richardson and Lichtman 2015; Ueda et al. 2020). While such method is simple and uses accessible reagents, these solutions are typically high in viscosity and can precipitate at room temperature. Solutions with high refractive index and low viscosity such as Histodenz™ and Hypaque™ have been developed but also come with a high price. The sample refractive index can also be decreased to around 1.38 by hyperhydration and lipid removal-based methods such as Scale (Hama et al. 2011) and CUBIC (Susaki et al. 2014). Samples are immersed in aqueous solutions that contain detergents for long periods of time. The end product has an expanded size, and the clearing effect increases with greater degree of hydration, potentially mediated by spreading of dense scatterers. However, lipid removal may result in protein loss (Chung et al. 2013) and sample expansion comes with increased imaging time and data size. Hydrogel based methods such as CLARITY (Chung et al. 2013) and PACT/PARS (Tomer et al. 2014) embeds the tissue in hydrogel polymers first in order to prevent protein loss, then followed by lipid removal and refractive index matching. This forms the basis of expansion microscopy where samples are expanded up to 4.5 times in each dimension following hydrogel embedding and hydration (Wassie, Zhao, and Boyden 2019). This methodology 'magnifies' small structures in the tissue, compensating for the limited resolutions in current optical microscopy. Non-aqueous based clearing involves sample dehydration, lipid removal and refractive index matching, incubated in organic solvents. BABB (Dent, Polson, and Klymkowsky 1989), 3DISCO (Becker et al. 2012; Ertürk et al. 2012), and iDISCO (Renier et al. 2014) belong to this non-aqueous category. For example, during iDISCO, samples go through series of methanol gradients to remove water followed by lipid removal with dichloromethane. The resulting sample shrinks due to dehydration and has a refractive index of > 1.5 , contributed mainly by proteins. Finally, the sample is immersed in a refractive index matching solution. Although solvent based clearing quenches native fluorescence `protein, it remains a robust

technique that is relatively fast and works in multiple organs when combined with immunohistochemistry.

Developments of modern fluorescent microscopy enable the volumetric imaging of cleared and non-cleared whole brain (Figure 1.5). The fluorescent micro-optical sectioning tomography (fMOST, figure 1.5a) has a similar design but with a laser scanning microscope and a diamond blade (A. Li et al. 2010; Gong et al. 2013). The sample was dehydrated with ethanol gradients, and then embedded with glycol methacrylate and resin. This pre-treatment preserves fluorescence and achieves sample hardness for the subsequent ultra-thin sectioning. High axial resolution (1 μm) is achieved by ultra-thin sectioning with the diamond knife and the microscope is designed to directly image the section on the blade. The serial two-photon tomographic microscope (SPTP, figure 1.5b) coordinates a vibratome and a two-photon microscope (Ragan et al. 2012; Economo et al. 2016a). Non-cleared brain is embedded in an agarose block and glued to a glass slide that is secured in the imaging chamber filled with phosphate buffer. The two-photon microscope images the available surface, then the vibratome shaves off the imaged block and reveals the next surface to be imaged. Optical sectioning with the two-photon excitation enables higher axial resolution compared with slice-mounting procedure with confocal microscope which is limited by the thickness of the section. Working distances of most objectives is a major obstacle in two-photon imaging in cleared sample since an adult mouse brain is around 8 mm in the dorsal ventral axis and even more in the other dimensions. The ideal objective would possess a long working distance without sacrificing the numerical aperture. However, cleared samples are either too soft (such as samples processed with hydrogel and hydration-based clearing) to be sectioned uniformly or too hard (samples treated with solvent based clearing) to be cut at all. Perhaps, the best option for imaging cleared sample is the light sheet fluorescent microscopy (LSFM, or selective plane illumination microscopy, SPIM, figure 1.5c). LSFMs decouples excitation and imaging path such that they are perpendicular to each other (Ahrens et al. 2013; Keller and Ahrens 2015; Voigt et al. 2019). A sheet of laser illuminates a given plane of the sample while the imaging objective lies perpendicular to this plane and captures the illuminated image. Axial resolution is determined by the thickness of the light sheet, commonly around 5 μm , and hence may or many not be sufficient depending on the specific research question. It is also critical that the clearing of the sample must be as homogenous as possible to interfere as little as possible with the light path. A major advantage of this approach is that the sample can be re-imaged several times, thanks to the absence of mechanical sectioning. Depending on the research question, multiple options for volumetric brain imaging are available by different combinations of sample preparation methods and the subsequent microscopy.

Comprehensive acquisition of images of a full mouse brain generates an enormous amount of image data. The amount of data can range from tens of gigabytes to several terabytes, making it unrealistic to be analysed purely by humans. Automated image analysis is already a substantial component of medical image diagnostics. Artificial intelligence has been implicated in the diagnosing pathologies such as embolism and tumours from computed tomographic image and magnetic resonance images (Erickson et al. 2017). Recently, machine-learning based tools are implemented to identify and segment structures such as cell bodies, vasculature, and axons from mouse brain images (Quan et al. 2016; Falk et al. 2019; Friedmann

et al. 2020; Gongwer et al. 2022; Tyson et al. 2021). Axon identification is especially challenging due to its narrow diameter in the nanometer range that limits brightness. In comparison, neuron cell bodies are around 10 microns in diameter and even greater for vasculatures. The wide repertoire of axon appearance adds another layer of complexity, it can be thin when in isolation but also forms meshes at dense innervation regions. Deep convolutional neural networks are especially successful in dealing with this intricate problem due to its complex yet flexible architectural design (Çiçek et al. 2016; Ronneberger, Fischer and Brox 2015; Friedmann et al. 2020). The relationship between neuroscience and computer vision is yet another encouraging case of interdisciplinary research. Fundamental structures of neural networks are largely inspired by the neurobiology of vision and now return the favor back.

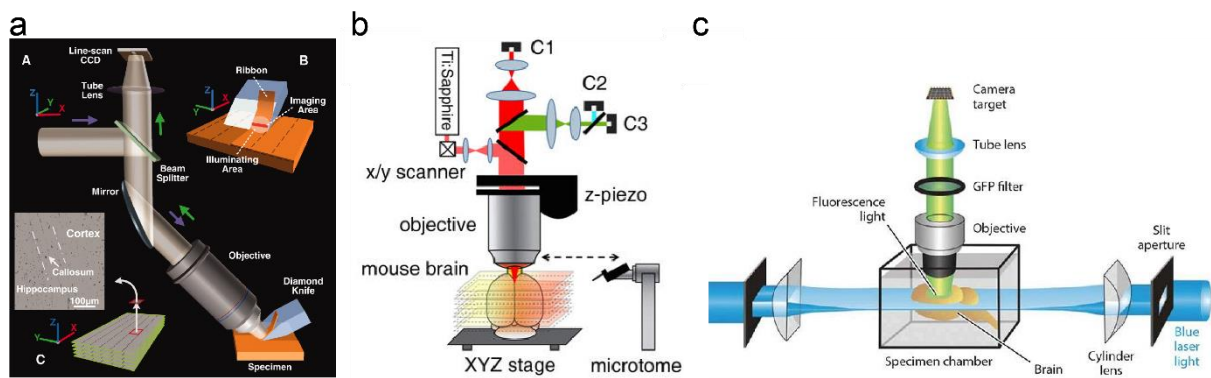


Figure 1-5 Schematics of fluorescent micro-optical sectioning tomography (fMOST), serial two-photon tomographic microscope (STPT) and the light sheet fluorescent microscopy (LSFM).

a) In the fMOST system, a thin ribbon of the specimen is shaved off by a diamond knife, illuminated and imaged by the microscope. This process generates a subregion of the sample and is repeated to reconstitute the entire surface and stack. b) In the STPT system, a computerized stage moves the sample between the two-photon microscope that images the exposed surface and the microtome to remove the imaged surface. This process is repeated in the z direction to image the full axial range of the brain. c) Unlike the fMOST and STPT systems, the illumination and detection path are perpendicular in the LSFM system. The sample is excited by a thin sheet of light allowing optical sectioning. This illuminated plane is captured by a camera before the sample moves to the next plane. Figures modified from Li et al. 2010; Ragan et al. 2012; Hillman et al. 2019.

1.5 Current major single neuron reconstruction projects

In the late 1800s, Ramon y Cajal proposed important principals such as the neuron doctrine and the law of dynamic polarization, based on pure observations of single cell morphology achieved by Golgi staining (Cajal 1888, Cajal 1899). Decades have passed and knowledge on full morphologies of neurons are still limited despite there being ongoing efforts from major institutions all around the world. Morphology of neurons is undoubtedly a critical property to disentangle the mysteries of brain function. Neuronal morphology reconstructions are difficult due to the complex nature of axonal networks. Unlike dendritic arborizations, axonal projections can span across multiple brain regions over millimetres (Mao et al. 2011b; Economo et al. 2016a). The amount of imaging data acquired has dramatically increased, making the annotation process more laborious. Furthermore, axonal terminations can be very thin and require extra considerations for visualization.

Currently, two major platforms have developed reconstruction pipelines to study single neuron morphology. The *Big Neuron* project (<https://alleninstitute.org/bigneuron/>) led by the *Allen Institute for Brain Science* published thousands of fully reconstructed neurons in the cerebral cortex, striatum and thalamus (Wang et al. 2019). In the *Big Neuron* project, cells were labelled by crossing of Cre-reporter mouse lines with various Cre-lines to achieve sparse but strong labelling in multiple classes of projection neurons. The brain samples then went under dehydration and resin impregnation (and later alkaline treatment during imaging) to amplify fluorescent signals. Images were acquired by fluorescent microscopic optical sectioning tomography (fMOST, Li et al. 2010) which is an epifluorescent microscope coupled with a sectioning system. Images were then viewed in 3D and annotated in semi-automatic procedures. The group showed that although the general anatomy of neurons that share similar transcriptomics profiles is similar, there are flourishing diversities at finer morphological details. This work highlighted the importance of systemic characterization of neuron morphology with meticulous details. The *Janelia* research campus also has developed pipelines to achieve similar goal, the *Mouse Light* project (<http://mouselight.janelia.org/>), and has published reconstructions of 1000 neurons that are mostly located in the thalamus and cortical motor areas (Winnubst et al. 2019a). Brain areas were injected with Cre-reporter GFP virus mixed with highly diluted Cre-virus. A series of treatment consisting of lipid removal, refractive index matching, and immunochemical signal enhancement was applied to the fixed brain for better signal visualizations. Brain images were collected using serial two photon tomography (Economo et al. 2016a). Following visualization and tracing, a network was trained to perform automatic segmentation. These algorithms then generated automatic segmentations that were proof read by multiple human annotators.

The *Big Neuron* and the *Mouse Light* projects are contributing great insights on neuronal morphology and categorization. The sparseness of viral expressions enhanced the throughput of the pipelines by having multiple cells labelled per brain. However, the exact locations and numbers of cells are not fully controlled. In addition, the probability of viral transfection and expression in all cell class might not be equal. Thus, the resulting catalogues

of morphology may not be as fully reflective of all cell class. Finally, it is very difficult to incorporate functional characterization into these pipelines.

Individual laboratories also reconstructed single neurons in a more focused way related to their own research interest. Reconstructions of neurons in various areas such the visual cortex (Han et al. 2018), somatosensory cortex (Yamashita et al. 2018), auditory cortex (M. Wang et al. 2022), somatomotor cortex (Economo et al. 2016), ventral pallidum (Feng et al. 2021), and prefrontal cortex (L. Gao et al. 2022) has been reported.

1.6 Current major projection mapping projects

Due to current technical limitations in single neuron reconstructions, mapping projections of groups of neurons might be an intermediate solution. Typically, these meso-scale approach labels hundreds of neurons by bulk injection of tracers or viral vectors.

In addition to the Big Neuron project, the Allen institute also spent major effort on mouse brain connectivity mapping systematically using viral approaches. Reporter viruses were injected in target regions of wild type mice that allows labelling of populations of neurons in a given region. Samples were harvested and imaged through STPT and axons were segmented by edge/line detection in combination of morphological filtering. The resulting segmentations were registered to the Allen mouse CCF and quantified based on brain regions. Overall, this comprehensive data set contains 469 experiments that covers 213 different injection sites (Oh et al. 2014) and provided valuable resource for researchers to further explore neural circuitries and mechanisms. In the second phase of the study, Cre- dependent reporter viruses were injected in target regions of Cre-recombinase expressing mouse lines, allowing specific labelling of genetically identified populations of neurons in a given region. Pre-processed datasets are available online (<https://connectivity.brain-map.org/>) while more comprehensive analyses remain yet to be published. Results from phase two of the study would further enhance the field's understanding on cell-type specific projection patterns. While these observations act as a great starting point, the datasets are often not specific enough to address a particular question. For instance, most injections spreads to surrounding areas of the intended brain region and this is especially troublesome when the region of specific interest only had 1 or 2 datasets available.

The Mouse connectome project based in the University of Southern California also provides a repository of anterograde and retrograde projection patterns using non-viral based tracers (Zingg et al. 2014, <https://cic.ini.usc.edu/>) Two non-overlapping co-injection of an anterograde (Phaseolus vulgaris leucoagglutinin, PHAL or biotinylated dextran amine, BDA) and a retrograde tracer (cholera toxin subunit b, CTb or Fluorogold, FG) allow visualization of innervations upstream and downstream of the injection site. Hence, there are 4 different channels in each image stack that reveals four pathways simultaneously inside the same sample. Brains were harvested, sliced, immunostained (for PHAL), and mounted on coverslips and imaged via a confocal microscope. Following manual annotation of signals and semi-automated registration, the density of labelling in anatomical location was obtained. The results highlights that the cortex is organized as four major cortical subnetworks that each

processes different information. The somatic-sensorimotor subnetwork allows rapid integration of sensory information and produces appropriate motor responses. The medial subnetworks involve the visual, auditory higher order association areas, and orbital frontal cortex might be implicated in head and body coordination and orientation involved in search and navigation behaviours. A separate medial subnetwork that involves structures such as hippocampus, the retrosplenial cortex, cingulate cortex and frontal regions may play a role in memory. Finally, the lateral subnetwork, where sensory information of different modalities converges in the anterior insular, temporal association area, perirhinal and entorhinal areas may mediate perception, emotion and internal states. Datasets and experimental details are available at www.mouseconnectome.org.

On a smaller scale, numerous groups had also investigated neuron projections in a more focused manner. For instance, attempts to map connectivity have been reported for the insular cortex (Gehrlach et al. 2020), primary somatosensory forelimb and posterior insular cortex (Bokinić et al. 2022), medial prefrontal cortex (Gongwer et al. 2022), and many others.

Collectively, both the platform-based efforts and the more focused investigation in individual laboratories make important contribute to the repertoire of neural morphologies and projections at multiple levels.

1.7 The whisker system

Organisms rely on incoming sensory signals to respond to their immediate surroundings and make appropriate actions. Rodents rely heavily on their whiskers to sense the environment. Therefore, they have developed highly specialized pathways and brain regions to process whisker-related signals (Figure 1.6). Arrangements of highly stereotypical cytoarchitectural structures are organized in the whisker related somatosensory cortex (barrels) in a somatotopic way such that each cortical barrel correspond to an individual whisker (Woolsey and Van der Loos 1970). Scientists have extensively characterized whisker-related pathways from the whisker follicle to the brain and used this system to their advantage to study sensory-related processing.

The trigeminal nerve fibers wrap the base of the whisker follicles and have their cell bodies located in the trigeminal ganglion. These neurons then project to the principal trigeminal nucleus (PrV) and the spinal trigeminal nuclei (SpV). Each whisker is represented by a barrelette arranged in somatotopic maps in the PrV and some parts of SpV. From PrV and SpV, two main trigeminal-thalamic-cortical pathways arise to code various aspects of whisker sensation. The lemniscal pathway faithfully convey single whisker information from PrV to ventral posterior medial thalamic nucleus (VPM) and then to the whisker related primary somatosensory cortex (SSp-bfd, or wS1) with precise timing and low latency. Somatotopic representation of whiskers in the VPM (barreloids) receive inputs from the corresponding barrelette in the PrV and pass down to the corresponding barrels in the SSp-bfd layer 4. In comparison, whisker information is less precise in pathways involving the medial posterior nucleus of the thalamus (POm) which lacks clear somatotopic organisation. Neurons in the POm show longer latency, more variability and response to multiple whiskers. Two separate

pathways involving the POm have been described. Neurons in the first-order POm receive inputs from the SPV and projects to layer 4 of the supplementary somatosensory area (El-Boustani et al. 2020). POm Neurons in the higher-order Pom receive inputs from cortical layer 5 and layer 6 and project to layer 5a and layer 1 of SSp-bfd (El-Boustani et al. 2020). POm neurons also innervate the whisker related secondary somatosensory cortex (SSs, or wS2), the whisker related primary motor cortex (MOp, or wM1), striatum, perirhinal cortex, and the insular cortex. In addition, there are other pathways that convey multi-whisker sensation to the septa (region in between barrels) of SSp-bfd and higher order areas such as the cingulate cortex, retrosplenial cortex, perirhinal cortex, and the amygdala. Modulations can occur at multiple levels between reciprocal connections within the trigeminal-thalamic-cortical pathways and feedback loops via other structures such as the reticular nucleus and the zona incerta (Petersen 2007; Bosman et al. 2011; Feldmeyer 2012; Petersen 2019; Staiger and Petersen 2021).

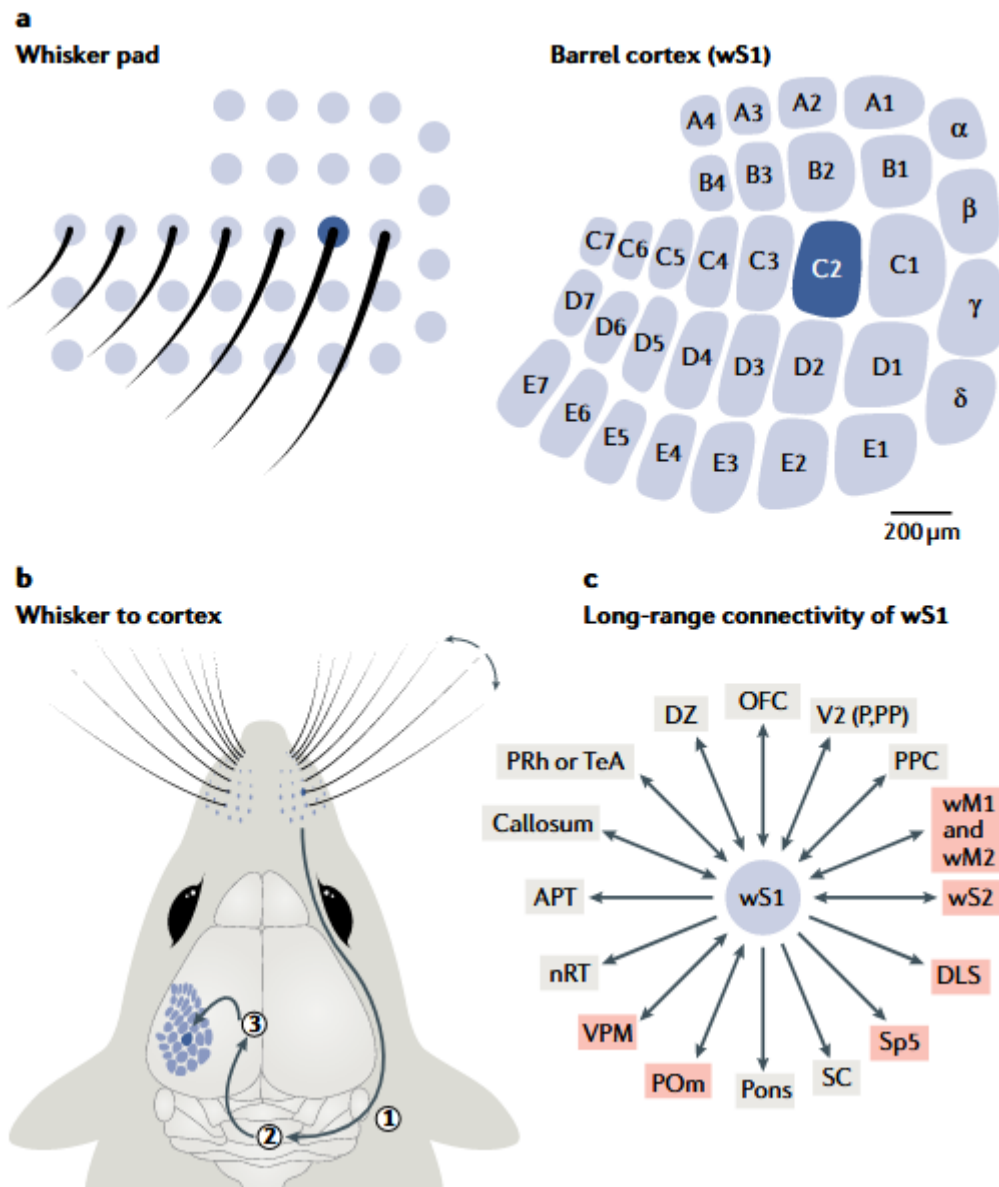


Figure 1-6 Specialized pathway for whisker related information in mice.

Specialized structures, 'barrels', are somatotopically organized in the whisker related primary somatosensory cortex (wS1 or SSp-bfd) such that each barrel represents a whisker on the mouse snout (a). Whisker related information travels (b) through the trigeminal ganglion (1), then the brain stem centers (2), then the thalamic centers (3) and finally reaching to the wS1. Long range connections of the wS1, arrows indicating unidirectional or bi-directional connection. Regions highlighted in red are strong target regions. APT, anterior pretectal nucleus; DLS, dorsolateral striatum; DZ, dysgranular zone surrounding wS1; nRT, nucleus reticularis of the thalamus; OFC, orbitofrontal cortex; PONS, posterior medial nucleus of the thalamus; PPC, posterior parietal cortex; PRh, perirhinal cortex; SC, superior colliculus; Sp5, spinal trigeminal nuclei; TeA, temporal association cortex; wM1, whisker primary motor cortex; wM2, whisker secondary motor cortex; wS2, whisker related secondary somatosensory cortex; VPM, ventral posterior medial nucleus of the thalamus; V2 (pons,PP), secondary visual area. Adapted from Petersen 2007.

1.7 Microcircuits in the rodent barrel cortex

The rodent barrel cortex is located in the dorsal lateral regions of the cortex. It is identifiable by its characteristic somatotopic arrangement of 'barrels' in layer 4. The thickness of the barrel cortex around ~1.2 mm and it covers around ~200 μm x ~300 μm of the cortex (Petersen 2019). The barrel column specific for the C2 whisker contains about 6500 neurons, of which 85% are excitatory glutamatergic neurons and 15% are GABAergic inhibitory neurons (Lefort et al. 2009).

The cortical microcircuits of the barrel field have been extensively studied. The barrel field layer 1 contains mostly cell bodies of interneurons and neuronal processes. Typically, the L1 receives long-range inputs from other regions. Layer 4 contain small spiny stellate cells that receive concise sensory information from the VPM and sends its output to layer 2/3 within the same column (Petersen 2007; Bosman et al. 2011; Feldmeyer 2012; Staiger and Petersen 2021). In comparison, layer 2/3 and layer 5 contain larger pyramidal neurons that form connections not only locally within the barrel field but also connects to other brain regions. Layer 2/3 pyramidal neurons are of the IT class and projects to other cortical regions such as the secondary somatosensory cortex and the whisker related motor cortex. These IT neurons in the layer 2/3 also their axons branches in local and nearby layer 2/3 layer 5 (Aronoff et al. 2010; Yamashita et al. 2018). Excitatory neurons in layer 5 send their dendrites vertically to layer 1 and receive input from all cortical layers as well as the POm thalamus. Two class of layer 5 can be identified based on their projection targets. Layer 5 IT neurons are primarily located in upper layer 5 (L5A) and projects to other cortical regions. Layer 5 PT neurons are located in deeper layer 5 (L5B) and show fewer cortical targets but project strongly to subcortical and brainstem regions (Guo et al. 2017; Kim et al. 2015). Finally, Layer 6 neurons sends the majority of their processes to the thalamus but also to other cortical areas (Thomson 2010).

To summarize, layer 4 is considered as the initial entry of sensory information, layer 2/3 and layer 5 are considered the major output layer with layer 1 and layer 6 serving modulatory roles in the local circuitry (Feldmeyer 2012; Staiger and Petersen 2021).

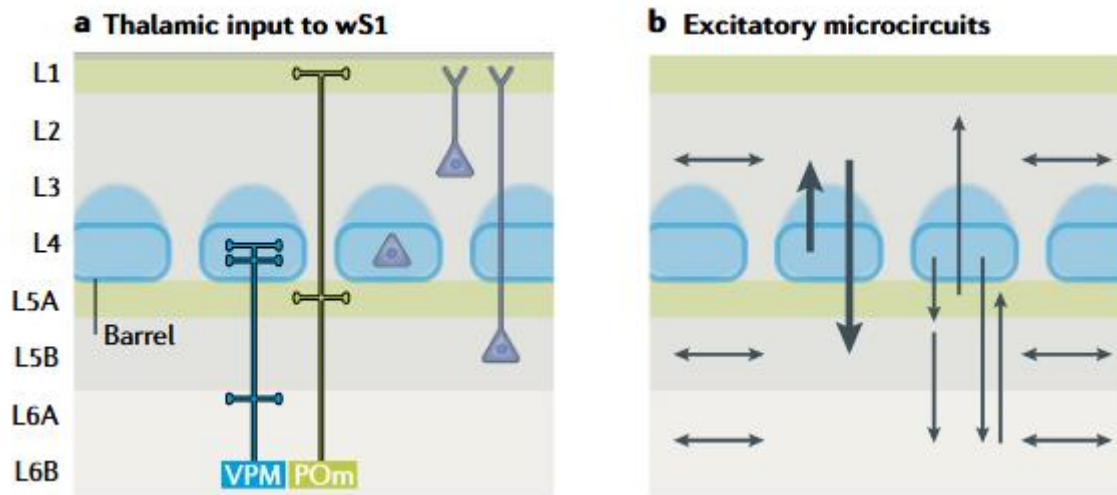


Figure 1-7 Microcircuits within the barrel cortex.

a) Precise whisker sensation arrives from the ventral posterior medial nucleus of the thalamus (VPM) primarily to layer 4 (L4). L1 and L5A receives higher order thalamus input from the posterior medial nucleus of the thalamus (POM). b) the canonical route of information flow from L4 to L2/3, the L2/3 to L5 (thick arrows). Other columnar pathways and horizontal connections of L2/3 and L5 are also depicted (thin arrows). Figure adapted from Petersen 2019.

1.8 Projections from whisker related somatosensory cortices

The barrel field is a group of somatotopically organized structures, barrels, in layer 4 of the SSp-bfd (Woolsey and Van der Loos 1970). As the recipient of the lemniscal pathway, each barrel receives rapid information from a corresponding whisker. In mice, each barrel is around 280 μm in diameter with the septa separating the barrels (Woolsey and Van der Loos 1970). Somatotopy is also observed in the wS2 which account for around 14% of total Sss (Bosman et al. 2011). Whisker related information arrives wS2 through the paralemniscal pathway through SpV and Pom. Hence, neurons in wS2 have larger receptive field and respond to several whiskers that are adjacent on the whisker pad. The SSp-bfd and the SSs forms strong reciprocal networks (Aronoff et al., 2010; Mao et al. 2011; Yamashita et al. 2018) and both regions are activated almost simultaneously upon whisker deflection (Aronoff et al., 2010; Esmaeili et al. 2021; Matteucci et al. 2022). Recent studies also highlighted two parallel projections from SSs-bfd and SSs to MOp and MOs, respectively (Esmaeili et al. 2022; Matteucci et al. 2022). Differential input and outputs patterns of the SSp-bfd and SSs likely highlight their roles and hierarchy in the whisker sensory processing circuitry.

As a critical component in the whisker sensory processing, connections of the SSp-bfd has been extensively studied. Among others, the SSp-bfd forms strong and reciprocal connections with the primary motor cortex (MOp) and the SSs. Interestingly, L2/3 neurons of the SSp-bfd forms dense arborizations in L2/3 and L5 of MOp while L5/6 neurons preferentially show innervation in L1 of the MOp (Aronoff 2008). Other projection targets of the SSp-bfd includes the dorsal lateral striatum, ipsilateral and contralateral perirhinal cortex, contralateral SSp-bfd and SSs, contralateral MOp, dysgranular zone, posterior parietal cortex (PPC), temporal association area (TEa), secondary visual areas, VPM and POM, superior

colliculus, zona incerta, anterior pretectal nucleus, pontine nucleus and spinal trigeminal nucleus (Figure 1.6c) (Petreanu et al. 2007; Aronoff 2008; Yamashita et al. 2018b; Mao et al. 2011b; Oh et al. 2014; Zingg et al. 2014b; C. Guo et al. 2017a; Petersen 2019a; Liu et al. 2022). It is important to note that many of these target regions, such as the perirhinal cortex and the thalamic nuclei VPM and POM also form reciprocal connections with SSp-bfd (Aronoff 2008).

The SSs, on the other hand, received less attention from the barrel field. There are less anatomical studies with specific focus on SSs while large scale connectomic studies also had fewer data sets with injection sites centered around the SSs. As mentioned in the previous section, SSs form extensive bidirectional connections with the SSp-bfd. The SSs to SSp-bfd projections are topographically arranged with L4 and L6 neurons of the SSs acting as the main contributors in SSs (Minamisawa et al. 2018). Anterograde labeling in the agouti brain (*Dasyprocta aguti*, a medium sized Amazonian rodent) showed that the SSs send two separate axon patches in a frontal motor region and a multisensory region caudal-lateral to SSs in addition to the main SSp projection (Santiago et al. 2019). The Allen Institute mouse connectivity (Oh et al. 2014) and the University of Southern California Mouse connectome project (Zingg et al. 2014b) do provide data with injection sites centered at SSs to a certain extent. In these data sets, the SSs receive strong inputs from the MOp, Secondary motor cortex (MOs), SSp-lower limb and trunk (SSp-l and SSp-tr) and SSp-mouth and nose (SSp-m and SSp-n). The SSs also receive moderate amounts of inputs from the auditory cortices (AUDd and AUDp), claustrum (CLA), entorhinal cortex (ECT), perirhinal cortex (PERI), SSp-bfd, TEa, and visceral areas (VISC). Anterograde tracing studies showed that the SSs project extensively to the MOp, MOs, dorsal agranular insular (Ald), gustatory areas (GU), SSp-l and SSp-tr, as well as SSp-m and SSp-n. The SSs project moderately to AUDd and AUDp, ECT, PERI, SSp-bfd, TEa, and VISC. Many of these target regions connect with the SSs bidirectionally and many of the regions are also observed to form connections with the SSp-bfd. Unfortunately, none of the two large scale projects discussed the striatum, thalamus, or any other subcortical regions in detail in their studies.

1.9 Conclusion and aim of PhD

Basic units of the brain, neurons, convey information by sending electrical signals down their long and elaborate networks of axons. To understand brain functions, it is essential to establish a detailed connectome complementary with other information such as genetic and electrophysiological properties. The aim of the current PhD project is to provide neuroanatomical knowledge of neurons in the mouse whisker-related somatosensory cortices at the single neuron level and at the population level in a cell-type layer-specific manner. Among other substantial efforts on connectomics, this project contributes in a precise and quantitative way that provides an anatomical basis for future studies that take advantage of the mouse-whisker system.

Chapter 2 Learning-related congruent and incongruent changes of excitation and inhibition in distinct cortical areas.

Text and figures under this chapter are obtained from the following manuscript.

Learning-related congruent and incongruent changes of excitation and inhibition in distinct cortical areas.

Vahid Esmaeili, Anastasiia Oryshchuk, Reza Asri, Keita Tamura, Georgios Foustoukos, Yanqi Liu, Romain Guet, Sylvain Crochet, Carl C H Petersen (2022)

PLoS Biol 2022 ;20: e3001667. doi: 10.1371/journal.pbio.3001667

I contributed to this manuscript by providing assistance for sample preparation and imaging with the two-photon tomographic microscope in order for identifying anatomical locations of axonal projections. The results are presented in Figure 2.5 and described in Section 2.3.5.

2.1 Abstract

Excitatory and inhibitory neurons in diverse cortical regions are likely to contribute differentially to the transformation of sensory information into goal-directed motor plans. Here, we investigate the relative changes across mouse sensorimotor cortex in the activity of putative excitatory and inhibitory neurons - categorized as regular or fast spiking according to their action potential waveform - comparing before and after learning of a whisker detection task with delayed licking as perceptual report. Surprisingly, we found that the whisker-evoked activity of regular versus fast spiking neurons changed in opposite directions after learning in primary and secondary whisker motor cortices, while it changed similarly in primary and secondary orofacial motor cortices. Our results suggest that changes in the balance of excitation and inhibition in local circuits concurrent with changes in the long-range synaptic inputs in distinct cortical regions might contribute to performance of delayed sensory-to-motor transformation.

2.2 Introduction

Many brain regions are thought to contribute to the performance of goal-directed sensory-to-motor transformations. An increasingly well-defined sensorimotor transformation studied in rodents is the learned association between a whisker sensory input and licking for reward (Petersen 2019b; Staiger and Petersen 2021b; Feldmeyer et al. 2013; Diamond et al. 2008; Brecht 2007; Sachidhanandam et al. 2013; O'Connor et al. 2010; Yang et al. 2016; Takahashi et al. 2016; Esmaeili et al. 2020; J. L. Chen et al. 2013; Esmaeili and Diamond 2019; Mehta et al. 2007; Knutsen, Pietr, and Ahissar 2006; Hong et al. 2018; Isett et al. 2018; Svoboda and Li 2018; Miyashita and Feldman 2013; Kwon et al. 2016). From a cortical perspective considering whisker-dependent tasks requiring licking for perceptual report, sensory processing is prominent in the somatosensory cortices, whereas neuronal activity linked to motor planning during delay periods is primarily found in premotor cortices, and motor commands are more prominent in primary motor cortex (Z. V. Guo et al. 2014; 2017;

Esmaeili et al. 2021b; Gilad et al. 2018). We recently showed that in a whisker detection task with delayed licking, the correct execution of the task involves a stereotypical spatiotemporal sequence of whisker deflection-evoked neuronal firing by which sensory cortex appeared to contribute to exciting frontal cortical regions to initiate neuronal delay period activity (Esmaeili et al. 2021). Comparing novice and expert mice, we also found that the learning of the task is accompanied by region- and temporal-specific changes in cortical activity (Esmaeili et al. 2021). (Esmaeili et al. 2021) These experience-dependent changes in evoked-activity likely result from changes in long-range synaptic inputs and changes within local synaptically-connected neocortical microcircuits.

Neocortex has regional specializations and a columnar organization divided into layers each containing many classes of neurons varying across diverse features (K. D. Harris and Mrsic-Flogel 2013; Z. J. Huang 2014; L. Luo, Callaway, and Svoboda 2018; Tremblay, Lee, and Rudy 2016; Tasic et al. 2018). At the most basic level, neocortical neurons can be classified as excitatory (releasing glutamate) or inhibitory (releasing GABA). Many neocortical excitatory neurons send long-range axons projecting to diverse brain regions, whereas most neocortical inhibitory neurons only have local axonal arborisations, thus contributing primarily to the regulation of local microcircuit activity. The balance between excitation and inhibition is likely to have a major impact on neocortical microcircuit computations and previous work has suggested important changes in this balance across development, brain states, sensorimotor processing and models of brain diseases (Sohal and Rubenstein 2019; Yizhar et al. 2011; Haider, Häusser, and Carandini 2013; Froemke 2015; Antoine et al. 2019; Mateo et al. 2011; Sun et al. 2010; Woloszyn and Sheinberg 2012). Inhibitory GABAergic neurons can be further divided into many subclasses, with one of the most prominent being the parvalbumin-expressing (PV) neurons. PV cells provide potent inhibition onto excitatory cells by prominently innervating either the soma and proximal dendrites or the axonal initial segment, thus playing a critical role in controlling the discharge of excitatory neurons. At the millisecond timescale, the PV neurons appear specialized for high-speed synaptic computations with fast membrane time-constants and large fast synaptic conductances, receiving substantial excitatory input from many nearby excitatory neurons as well as long-range inputs (Hu, Gan, and Jonas 2014; Isaacson and Scanziani 2011; Freund and Katona 2007; Avermann et al. 2012; Sermet et al. 2019; Cardin 2018). Within a neocortical microcircuit, PV neurons are likely to play a critical role in controlling the balance between excitation and inhibition. PV cells typically fire at high rates and have short action potential (AP) durations that can be identified from extracellular recordings. In fact, neurons recorded from extracellular recordings are typically classified based of their AP duration, as regular spiking (RS) units, which have broad AP waveforms and correspond mostly to excitatory neurons; and fast spiking (FS) units, which have narrow AP waveforms and largely correspond to inhibitory PV neurons. Previous whisker-related studies have reported experience-dependent plasticity of both excitatory and inhibitory synaptic transmission, with prominent changes reported in PV GABAergic neurons, for example following whisker deprivation (Gainey, Aman, and Feldman 2018; Chittajallu and Isaac 2010). However, it remains unknown how reward-based learning in whisker-dependent tasks might affect the activity of PV neurons, although previous work has revealed prominent changes in PV neuronal activity in mouse motor cortex during learning of a lever-press task (S.

X. Chen et al. 2015) and in visual cortex during learning of a visual discrimination task (Poort et al. 2022).

In the present study, we investigate whether the changes observed during the learning of the whisker detection task with delayed licking are associated with a change in the balance between excitation and inhibition. We used our recently published dataset of high-density silicon probe recordings from six cortical regions previously identified to be important during this behavior (Esmaeili et al. 2021) and compared the changes in evoked activity of RS and FS units. Interestingly, we found that upon task learning, RS and FS showed opposite changes in some cortical areas, suggesting important changes in local computation, whereas in other regions, RS and FS changed in parallel suggesting rather an overall shift in the synaptic drive to these areas.

2.3 Results

2.3.1 Localisation and classification of cortical neurons

In this study, we further analysed a data set of extracellular silicon probe recordings of neuronal spiking activity we published recently (Esmaeili et al. 2021). We focused our analyses on six key neocortical regions: whisker primary somatosensory cortex (wS1), whisker secondary somatosensory cortex (wS2), whisker primary motor cortex (wM1), whisker secondary motor cortex (wM2), anterior lateral motor cortex (ALM) and tongue-jaw primary motor cortex (tjM1) (Figure 2-1A). These regions participate in a whisker detection task with delayed licking to report perceived stimuli (Esmaeili et al. 2021). Mice first went through pretraining to the task structure, which included a brief light flash to indicate trial onset followed 2 s later by a brief auditory tone to indicate the beginning of the 1-s reporting period, during which the thirsty mice could lick to receive a water reward (Figure 2-1B). We recorded from two separate groups of mice referred to as “Novice” and “Expert” hereafter, while a brief whisker stimulus was introduced 1 s after the visual cue in a randomized half of the trials, and licking in the reporting window was only rewarded in whisker stimulus trials (Figure 2-1B and C). Expert mice were given additional whisker training through which they learned to lick preferentially in trials with a whisker stimulus (Figure 2-1B and C). However, Novice mice had not learned the stimulus-reward contingency and licked equally in trials with and without whisker stimulus (Esmaeili et al. 2021). Through anatomical reconstruction of fluorescently-labelled electrode tracks and registration to a digital mouse brain atlas, here we precisely localize units to specific layers and cortical regions annotated in the Allen Mouse Brain Common Coordinate Framework (Wang et al. 2020) (Figure 2-1D and Figure 2-9). The neuronal location was assigned to the recording site with the largest amplitude spike waveform along the shank of the silicon probe (Figure 2-1E). Neurons in different cortical regions and layers had diverse firing patterns during task performance (Figure 2-1F and Figure 2-9). We further distinguished neurons according to the duration of the action potential waveform. In both Novice and Expert mice, we found a bimodal distribution of spike duration, which we labelled as FS units (spike duration below 0.26 ms) and RS units (spike duration above 0.34 ms), according to standard nomenclature (Simons 1978; McCormick et al. 1985) (Figure 2-1G and Figure 2-10). Unexpectedly, we found a larger fraction of FS units in sensory areas compared

to frontal areas (Figure 2-10), which could in part reflect differential distribution of PV neurons (Y. Kim et al. 2017) and in part might indicate the known sampling bias of extracellular recordings limited to high-firing neurons, whereas sensory cortex typically has rather sparse activity. During task performance, both FS and RS units had a broad range of baseline firing rates (Figure 2-1H), which appeared to have a near log-normal distribution in both Novice and Expert mice (Figure 2-11). In agreement with previous literature, FS units fired at significantly higher rates than RS units in both Expert and Novice mice (Figure 2-1I and Figure 2-11).

To investigate the classification of FS and RS units, we conducted a new set of recordings in which we measured the impact of stimulating genetically-defined GABAergic neurons in mice expressing channelrhodopsin-2 (ChR2) under the control of the vesicular GABA transporter (VGAT) (Zhao et al. 2011). Blue light modulated the firing rate of RS and FS neurons in opposite directions, quantified both at the level of population (Figure 2-1J) and at the level of individual neurons (Figure 2-1K). Overall, light stimulation increased the firing rate of FS units (blue light off: 4.3 ± 4.9 Hz; blue light on: 33.9 ± 32.7 Hz; 51 units recorded in 4 mice; non-parametric permutation test, $p < 10^{-4}$), whereas it decreased the spike rate of RS units (blue light off: 3.2 ± 3.4 Hz; blue light on: 1.3 ± 7.2 Hz; 130 units recorded in 4 mice; non-parametric permutation test, $p = 0.009$) (Figure 2-1L). As a second approach, and to avoid network effects of light stimulation (Sanzeni et al. 2020), we focused only on the first 10-ms window after the onset of light stimulation and identified the opto-tagged neurons based on their fidelity of responses, response onset latency and jitter (Fig 1M-O and S4). A larger fraction of neurons was opto-tagged among FS neurons compared to RS neurons. These data are therefore consistent with the hypothesis that the majority of FS units are likely to be inhibitory neurons, whereas the majority of RS units are likely to be excitatory neurons.

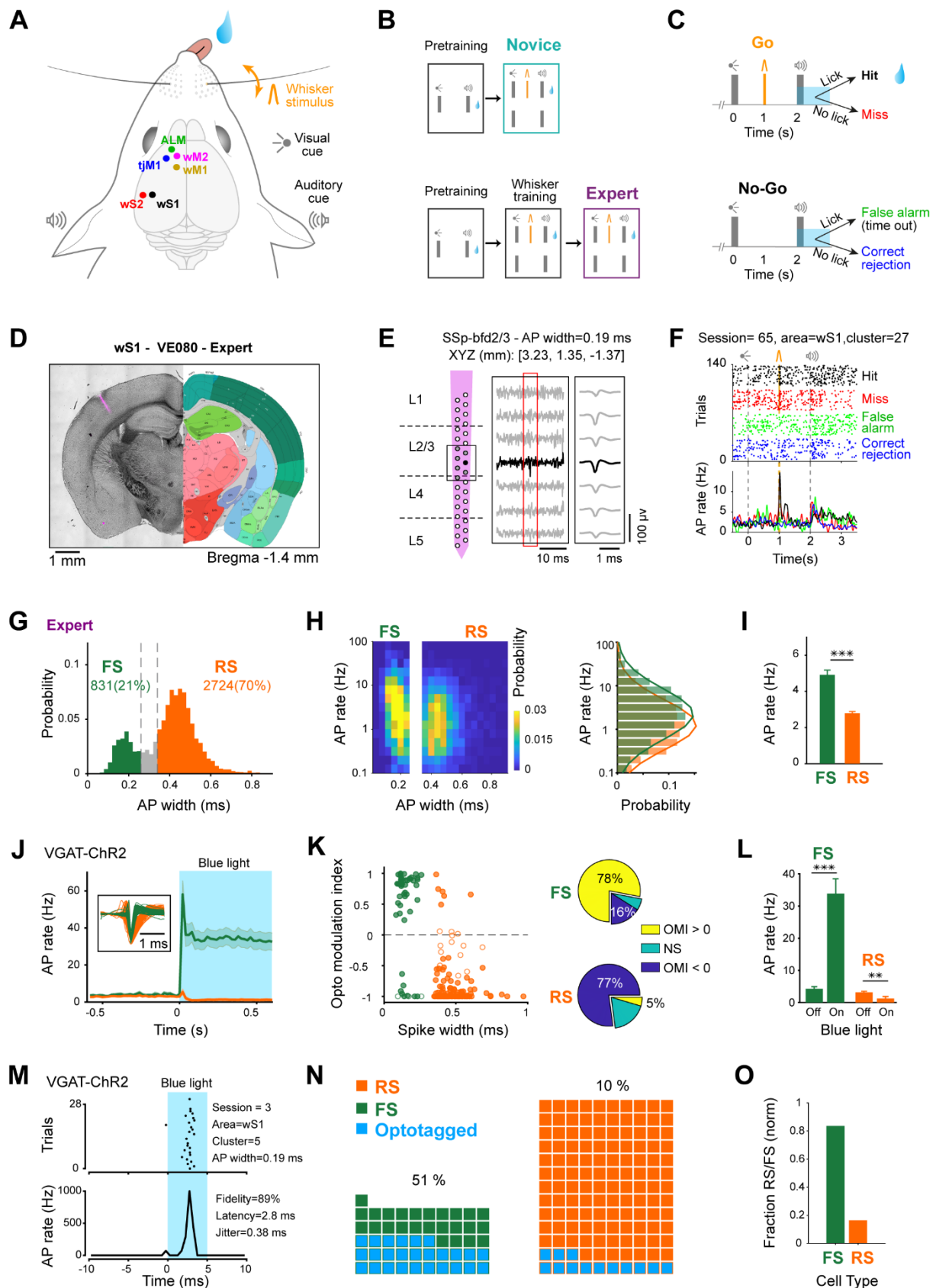


Figure 2-1 Multi-area recordings during delayed whisker detection task and assignment of RS and FS units to cortical sub-divisions.

(A) Schematic of the whisker detection task with delayed response and the targets of silicon probe recordings. (B) Training paradigm. Novice and Expert mice were first pretrained in a task, where licking after the auditory cue

was rewarded. Expert mice were further trained to only lick in whisker trials. (C) Final task structure used during recording sessions (for both groups of mice) and behavioral outcomes. (D) Example coronal section of an Expert mouse brain with fluorescent track of a probe in wS1, registered to the Allen Mouse Brain Atlas, <https://mouse.brain-map.org> (Q. Wang et al. 2020b). (E) Reconstructed laminar location of recording sites of the silicon probe shown in (D) according to the Allen Atlas (left); filtered recorded raw data of 7 sites around one detected spike; and average extracted spike waveform for this example neuron (right). After spike sorting, the position of each cluster (i.e. neuron) was assigned to the location of recording site with the largest spike amplitude (filled circle), and spike width was calculated on the average spike waveform from this site. (F) Raster plot and peri-stimulus time histogram for the example neuron shown in (E). Trials are grouped based on outcome. (G) Spike width distribution for neurons recorded in Expert mice. Neurons were categorized as fast-spiking (FS, spike width < 0.26 ms) or regular-spiking (RS, spike width > 0.34 ms). Neurons with intermediate spike width (gray bins) were excluded from further analyses. (H) Baseline AP rate in Expert mice. Spike width distribution vs baseline AP rate (left) and overlay of spike rate distribution for RS and FS units. Note the log-normal distribution of baseline firing rates for both RS and FS units. Normal distributions were fitted to the RS and FS histograms (solid lines). (I) Comparison of mean spike rate in RS vs FS neurons of Expert mice. Error bars: SEM. ***: $p < 0.001$, non-parametric permutation test. (J-O) Opto-tagging GABAergic neurons in VGAT-ChR2 mice. (J) Grand average firing rate of RS (orange, spike width > 0.34 ms, 130 neurons from 4 mice) and FS (green, spike width < 0.26 ms, 51 neurons from 4 mice) units upon 100-Hz blue light stimulation (shading shows SEM). Note the suppression of activity in RS and the strong increase of activity in FS population. Inset shows the overlay of average spike waveforms for all RS and FS neurons. (K) Opto modulation index (OMI) vs spike width (left) and percentage of modulated neurons (right). Each circle represents one neuron, filled circles indicate neurons with significant OMI ($p < 0.05$, non-parametric permutation tests). Pie charts show the percentage of neurons in each group with non-significant modulation (NS), and significant positive (OMI > 0) or negative (OMI < 0) modulation upon blue light stimulation. (L) Blue light stimulation in VGAT-ChR2 mice increased the activity of narrow-spike neurons labeled as FS; while it suppressed the activity of broad-spike neurons labeled as RS. 100-500 ms after light onset. Error bars: SEM; **: $p < 0.01$; ***: $p < 0.001$. (M) Raster plot and peri-stimulus time histogram during the first 10-ms of the 100-Hz trains of blue light stimulation for an example opto-tagged neuron. (N) Waffle plots showing broad-spike (orange) and narrow-spike (green) neurons, and the opto-tagged neurons (blue) in each group. Numbers indicate the percentage of opto-tagged neurons in each group. (O) Weighted proportion of neurons with narrow (FS) or broad (RS) spike among opto-tagged neurons in (N). The underlying data for Figure 2-1 can be found in S1 Data.

2.3.2 Strong task-modulation of fast-spiking neurons

Many RS units across all six cortical regions change their action potential firing rates in response to the whisker deflection (Esmaeili et al. 2021). Here, we analyzed the responses of FS units during task performance in Novice and Expert mice (Figure 2-2). Averaged across cortical areas and quantified over the first 100 ms after whisker deflection, FS neurons in Novice mice increased their firing rate by 4.6 ± 7.9 Hz (392 units recorded in 8 mice) which was significantly higher (Wilcoxon rank-sum test, $p = 1 \times 10^{-34}$) than the increase in firing rate of RS neurons of 1.0 ± 2.4 Hz (1089 units recorded in 8 mice) (Figure 2-2A). Task-modulated RS and FS neurons were mainly excited, with only a small fraction showing significant reduction in firing rate (Figure 2-2B). Similarly, for Expert mice, whisker deflection evoked an increase of FS firing rate of 4.7 ± 9.1 Hz (831 units recorded in 18 mice) which was significantly higher (Wilcoxon rank-sum test, $p = 4 \times 10^{-71}$) than the increase in firing rate of RS neurons of 1.1 ± 3.9 Hz (2724 units recorded in 18 mice) (Figure 2-2C). In addition, for Expert mice, FS neurons were more strongly excited during the delay period compared to RS units (change in firing rate of FS neurons: 1.9 ± 4.8 Hz, 831 units recorded in 18 mice; change in firing rate of RS neurons: 0.7 ± 3.2 Hz, 2724 units recorded in 18 mice; Wilcoxon rank-sum test, $p = 1 \times 10^{-30}$). In Novice mice there was little delay period activity in either RS or FS units. The largest fraction of modulated neurons during the delay period were FS units in ALM of Expert mice, which

were strongly excited (Figure 2-2D). Analysis of correct rejection trials in Novice and Expert mice, revealed that in the absence of the whisker stimulation neuronal activity remained at baseline levels during the delay period in both RS and FS neurons (Figure 2-13). Thus, the overall task selectivity of FS unit activity changed in a similar manner across learning compared to our previous quantification of RS units (Esmaeili et al. 2021), with FS units having overall larger responses.

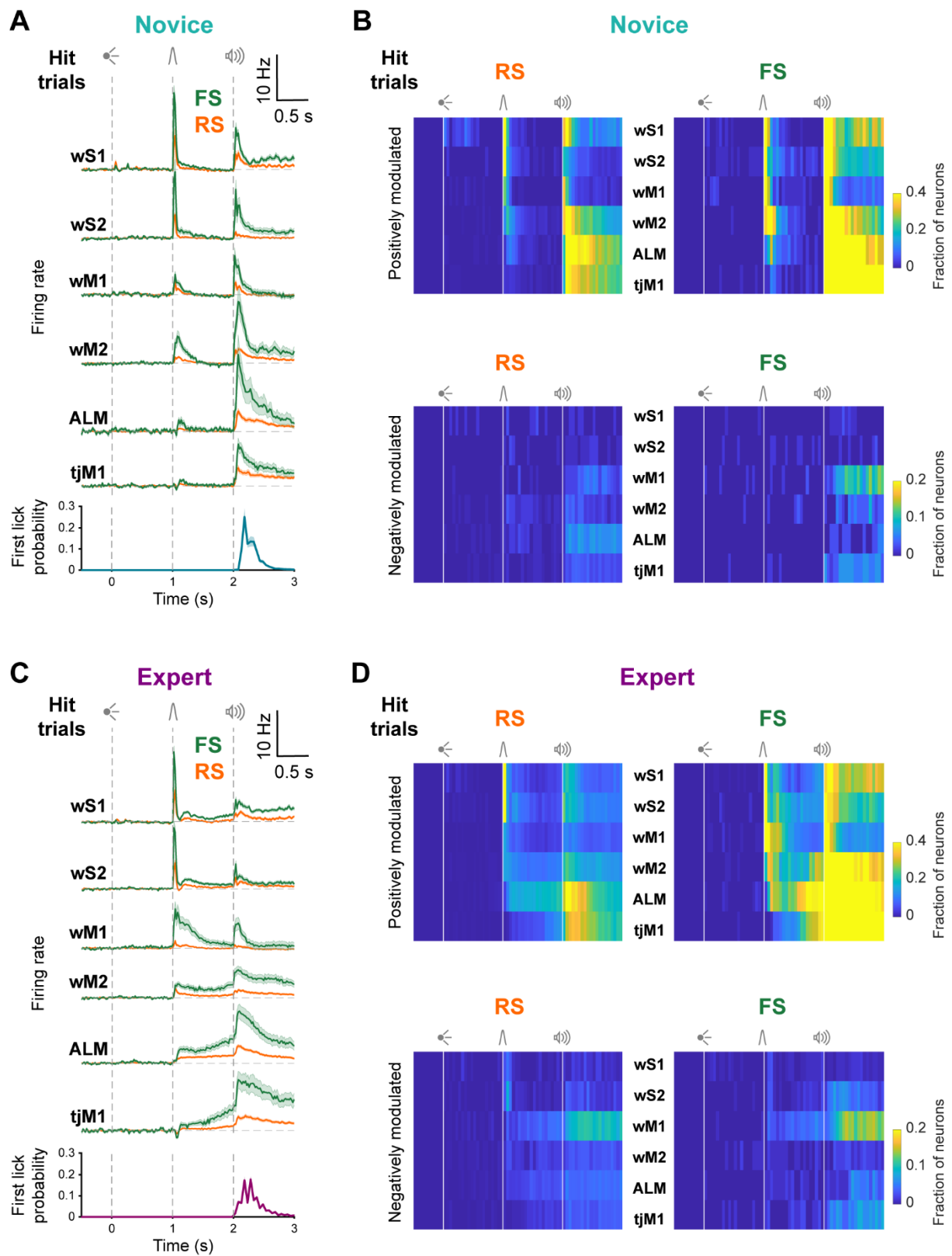


Figure 2-2 FS neurons had similar but larger task-modulation compared to RS neurons in the same region.

(A) Baseline-subtracted (2 s prior to visual onset) population firing rates (mean \pm SEM) of RS and FS neurons from different regions of Novice mice are superimposed for hit trials. wS1: 73 RS units in 7 mice, 103 FS units in 7 mice; wS2: 120 RS units in 8 mice, 68 FS units in 8 mice; wM1: 147 RS units in 7 mice, 66 FS units in 7 mice; wM2: 244 RS units in 7 mice, 57 FS units in 7 mice; ALM: 234 RS units in 6 mice, 37 FS units in 5 mice; tjM1: 271 RS units in 8 mice, 61 FS units in 8 mice. Average first lick histogram for all Novice mice is shown in the bottom. (B) Percentage of RS (left) and FS (right) neurons in different regions of Novice mice which are positively (top) or negatively (bottom) modulated compared to baseline (non-parametric permutation test, $p < 0.025$). (C) Similar to (A), but for Expert mice. wS1: 258 RS units in 15 mice, 237 FS units in 15 mice; wS2: 342 RS units in 12 mice, 161 FS units in 12 mice; wM1: 452 RS units in 11 mice, 134 FS units in 11 mice; wM2: 401 RS units in 10 mice, 107 FS units in 10 mice; ALM: 766 RS units in 12 mice, 109 FS units in 12 mice; tjM1: 505 RS units in 11 mice, 83 FS units in 11 mice. Average first lick histogram for all Expert mice is shown in the bottom. (D) Similar to (B), but for Expert mice. Note the difference in color scales for fraction of positively or negatively modulated neurons in b and d. The underlying data for Figure 2-2 can be found in S2 Data.

2.3.3 Rapid excitation of FS neurons

Investigating fast sensory processing evoked by the whisker deflection, we found an overall similar sequential recruitment of RS and FS units across cortical areas in both Novice and Expert mice (Figure 2-3, Figure 2-14 and Figure 2-15). The earliest excitation occurred in wS1 and wS2, followed by wM1 and wM2 (Fig 3A, 3B, S6 and S7). In wS1 and wS2, FS neurons responded at significantly shorter latency than RS units in both Novice and Expert mice (Figure 2-3C), as described later in more detail. Among the other areas, in Novice mice FS neurons responded with shorter latency than RS units in wM2 (FS: 47.7 ± 38.7 ms, 44/57 units in 8 mice; RS: 61.7 ± 40.7 ms, 126/244 units in 18 mice; Wilcoxon rank-sum test, $p = 0.047$, false discovery rate (FDR) corrected for multiple comparison), whereas in Expert mice FS neurons responded with shorter latency than RS units in wM1 (FS: 33.1 ± 35.1 ms, 101/134 units in 8 mice; RS: 54.2 ± 48.7 ms, 243/452 units in 18 mice; Wilcoxon rank-sum test, $p = 3 \times 10^{-5}$, FDR-corrected for multiple comparison) (Figure 2-3C). Comparing Novice and Expert mice, the latency of RS units increased in wM1, but decreased in wM2, upon whisker learning (Figure 2-3D and Figure 2-14B) (Esmaeili et al. 2021). In contrast FS units did not significantly change their latency across learning in any of the six cortical regions (Figure 2-3D and Figure 2-14B). These latency differences reveal that task learning is accompanied by fast dynamic changes in the relative timing of the recruitment of FS and RS units across wM1 and wM2.

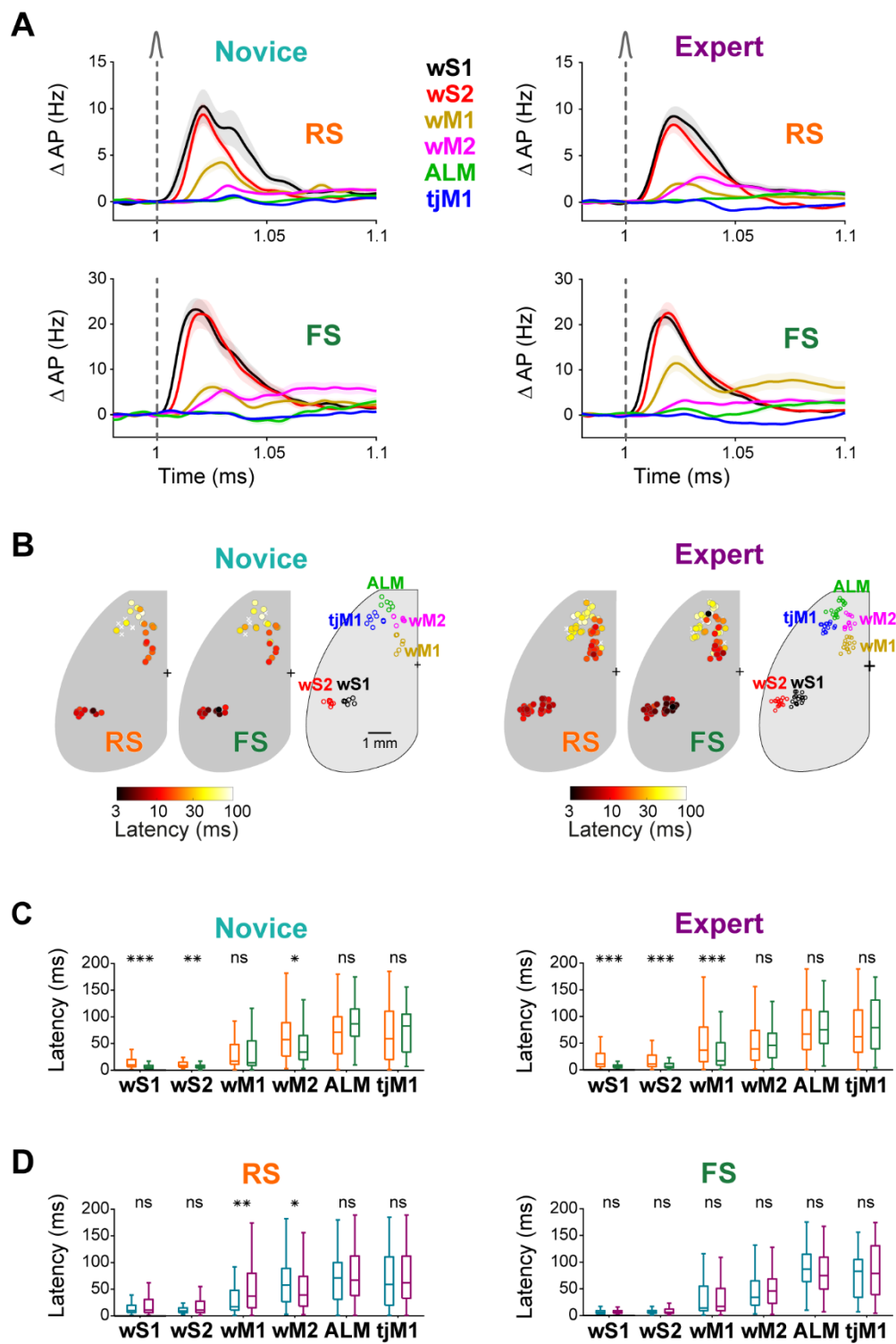


Figure 2-3 Fast propagation of sensory responses across cell classes and cortical regions.

(A) Change in firing rate ($\text{mean} \pm \text{SEM}$) of different cortical regions in the first 100-ms window after whisker deflection for RS (top) and FS (bottom) neurons in Novice (left) and Expert (right) mice (numbers of units and mice are the same as in Fig 2). **(B)** Whisker-evoked response latency maps. For each silicon probe in Novice (left) and Expert (right) mice, average latency of whisker-evoked response is shown separately for RS and FS units. Circles represent silicon probes and are colored according to the average latency across all responsive neurons recorded on the probe. **(C)** Comparison of latency of RS vs FS neurons in Novice (left) and Expert (right) mice. **(D)** Comparison of latency of neurons from Novice vs Expert mice for RS (left) and FS (right) neurons. In (C) and (D), only neurons with a significant whisker response in the first 200 ms (compared to 200 ms before whisker onset, non-parametric permutation test, $p < 0.05$) were included. Midline represents the median, bottom and top edges show the interquartile range, and whiskers extend to 1.5 times the interquartile range. ***: $p < 0.001$, **: $p < 0.01$, *: $p < 0.05$, ns: $p \geq 0.05$. The underlying data for Fig 2-3 can be found in S4 and S5 Data.

2.3.4 Fast sensory processing in wS1 and wS2

Having observed the fastest whisker-evoked responses in wS1 and wS2 (Fig 3), we further compared RS and FS units in these areas, by focusing on their response in the first 50-ms window (Figure 2-4). The whisker-evoked change in firing rates of RS and FS units in wS1 and wS2 remained unchanged across Novice and Expert mice (Figure 2-4A to Figure 2-4C). However, in both regions and both groups of mice, FS units had larger evoked responses compared to RS units (Novice wS1: 6.0 ± 9.6 Hz for 73 RS units vs 13.9 ± 16.1 Hz for 103 FS units in 8 mice, $p < 10^{-4}$; Novice wS2: 4.0 ± 4.6 Hz, for 120 RS units vs 12.2 ± 15.8 Hz for 68 FS units in 8 mice, $p < 10^{-4}$; Expert wS1: 5.3 ± 9.1 Hz for 258 RS units vs 11.9 ± 13.9 Hz for 237 FS units in 18 mice, $p < 10^{-4}$; Expert wS2: 4.3 ± 8.7 Hz for 342 RS units vs 11.5 ± 13.6 Hz for 161 FS units in 18 mice, $p < 10^{-4}$; non-parametric permutation tests, FDR-corrected for multiple comparison) (Figure 2-4C). Neuronal responses in wS1 and wS2 often showed a biphasic response; a fast and sharp evoked response followed by a later secondary wave of spiking activity. While, the fast early response remained unchanged (Figure 2-2A and Figure 2-2C), the late response increased across learning in RS and FS units of both wS1 and wS2 areas (Figure 2-17), consistent with previous work in wS1 in a whisker detection task without a delay period (Sachidhanandam et al. 2013).

The latencies of evoked activity in wS1 and wS2 were shorter for FS units compared to RS units for both Novice and Expert mice (Wilcoxon rank-sum tests FDR-corrected for multiple comparison: Novice wS1 $p = 1 \times 10^{-7}$; Novice wS2 $p = 1 \times 10^{-3}$; Expert wS1 $p = 1 \times 10^{-10}$; Expert wS2 $p = 9 \times 10^{-6}$) (Figure 2-4D). Comparing wS1 and wS2 areas, we found no significant difference in RS units response latencies, whereas FS units in wS1 fired at shorter latencies than FS units in wS2 (Wilcoxon rank-sum test FDR-corrected for multiple comparison, Novice: $p = 1 \times 10^{-4}$, Expert: $p = 3 \times 10^{-4}$). Both wS1 and wS2 therefore responded strongly and similarly to whisker stimulation in both Novice and Expert mice and no significant change was found in the response of RS or FS units across learning (Figure 2-4C and Figure 2-4D).

Optogenetic inactivation by applying blue light in VGAT-ChR2 mice to either wS1 and wS2 during the delivery of the whisker stimulus induced a significant decrease in hit rate (Esmaeili et al. 2021). Here, we reanalyzed this inactivation data in a direct comparison across these two areas, and found a significantly stronger deficit induced by inactivation of wS2 compared to wS1 (wS1: $\Delta \text{hit} = -0.30 \pm 0.13$; wS2: $\Delta \text{hit} = -0.49 \pm 0.12$; Wilcoxon signed-rank test, $p = 0.0039$; 9 mice) (Figure 2-4E). However, potential differences in the spatial extent of the whisker deflection-evoked responses and the efficacy of optogenetic inactivation in wS1 versus wS2 make it difficult to conclude the relative importance of sensory processing in these two areas. Nonetheless, the data suggest that neuronal activity in both wS1 and wS2 is involved in execution of this whisker detection task.

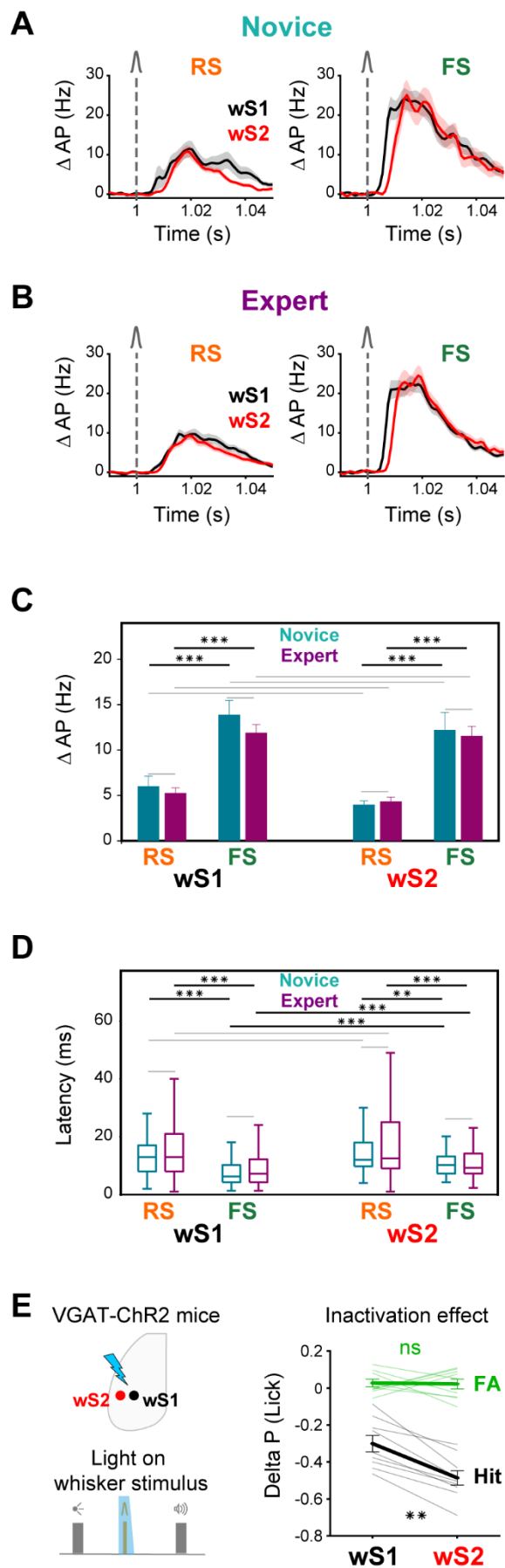


Figure 2-4 Fast whisker responses in FS neurons of sensory areas.

(A) Baseline-subtracted (50 ms prior to whisker onset) population firing rate (mean \pm SEM) of RS (left) and FS (right) neurons in wS1 and wS2 of Novice mice. wS1: 73 RS units in 7 mice, 103 FS units in 7 mice; wS2: 120 RS units in 8 mice, 68 FS units in 8 mice. (B) Same as (A) but for Expert mice. wS1: 258 RS units in 15 mice, 237 FS units in 15 mice; wS2: 342 RS units in 12 mice, 161 FS units in 12 mice. (C) Whisker-evoked change in spike rate in the first 50 ms (mean \pm SEM) in wS1 and wS2 for RS and FS units and in Novice and Expert mice. ***: $p < 0.001$. Gray lines show non-significant comparisons. (D) Latency of the whisker-evoked response in wS1 and wS2. Only neurons with a significant whisker response in the first 100 ms (compared to 100 ms before whisker onset, non-parametric permutation test, $p < 0.05$) were included (Novice wS1: 56/73 RS units, 96/103 FS units, 8 mice; Novice wS2: 97/120 RS units, 57/68 FS units, 8 mice; Expert wS1: 190/258 RS units, 210/237 FS units, 18 mice; Expert wS2: 262/342 RS units, 148/161 FS units, 18 mice). Boxplots represent the distribution of the latency defined as the time to reach to half-maximum response. Midline represents the median, bottom and top edges show the interquartile range, and whiskers extend to 1.5 times the interquartile range. ***: $p < 0.001$, **: $p < 0.01$. Gray lines show non-significant comparisons. (E) Inactivation of wS1 and wS2. Left: Schematic showing the inactivation of wS1 and wS2 areas during whisker stimulus presentation, in VGAT-ChR2 mice (Esmaili et al. 2021b; Zhao et al. 2011). Light trials were interleaved with no-light control trials and comprised 1/3 of total trials. Right: Change in hit and false-alarm (FA) rate - comparing light and no-light trials - upon optogenetic inactivation of wS1 and wS2. Light colors show individual mice (9 mice), thick lines represent averages, and error bars show SEM. **: $p < 0.01$, ns: $p > 0.05$. The underlying data for Fig 2-4 can be found in S6 Data.

2.3.5 Parallel anatomical pathways from wS1 and wS2 to wM1 and wM2

Neuronal activity in wS1 and wS2 can only contribute to task execution by communicating with other brain regions. Along with various subcortical projections (Sippy et al. 2015; Takahashi et al. 2020), innervation of frontal cortical areas might be of particular importance in connecting sensation and movement (Esmaili et al. 2021; 2020). Neurons in wS1 have previously been shown to innervate wM1 (Aronoff et al. 2010; Yamashita et al. 2018a; Ferezou et al. 2007; Mao et al. 2011), but much less is known about the long-range output of wS2. We therefore carried out a set of experiments in which we expressed fluorescent proteins in neurons of wS1 and wS2 to examine their relative innervation targets in frontal cortex (Figure 2-5A). In the example experiment we injected virus expressing a red fluorescent protein in wS1 and a green fluorescent protein in wS2. The fixed brains were imaged through serial section two photon tomography and registered to the Allen Mouse Brain Common Coordinate Framework (Q. Wang et al. 2020) (Figure 2-5B). As previously shown, wS1 innervates frontal cortex with a column of axons in a cortical region we label as wM1 (Figure 2-5C). Similarly, wS2 axons project to frontal cortex in a columnar manner in a region we label as wM2 (Figure 2-5D). The location of wM2 appeared to be more anterior compared to the location of wM1 (Figure 2-5E and Figure 2-5F), which is further confirmed by overlaying the projections (Figure 2-5G). Quantification of the location of the peak on average fluorescence across mice (Figure 2-5G and Figure 2-5H, contours) revealed that wM1 was located at 1.0 mm anterior and 1.0 mm lateral to bregma, while wM2 was located at 1.9 mm anterior and 1.2 mm lateral to bregma. We further quantified wM1 and wM2 locations by averaging among frontal projection centers from individual mice (Figure 2-5H, markers) finding similar results (wM1: 1.0 ± 0.1 mm anterior and 1.0 ± 0.1 mm lateral to bregma across 4 mice; wM2: 1.7 ± 0.1 mm anterior and 1.0 ± 0.3 mm lateral to bregma across 4 mice). Primary and secondary somatosensory cortex therefore map onto frontal cortex in a pattern consistent with mirror-symmetric somatotopy (Mao et al. 2011a) and the frontal projections from visual cortex (Sreenivasan et al. 2017).

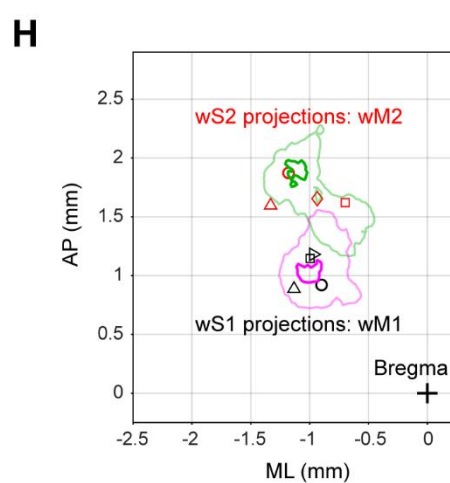
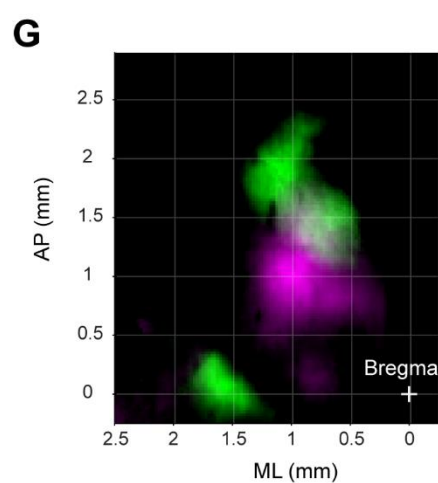
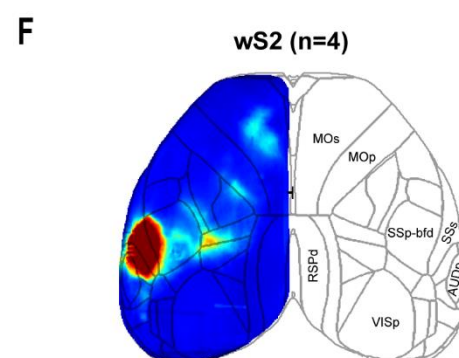
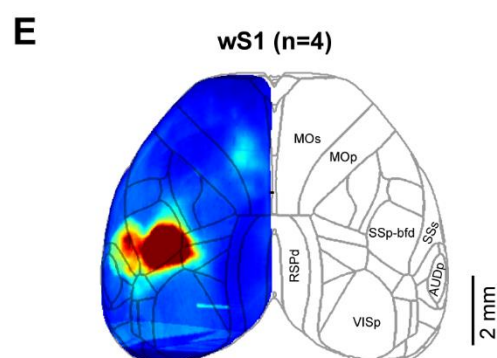
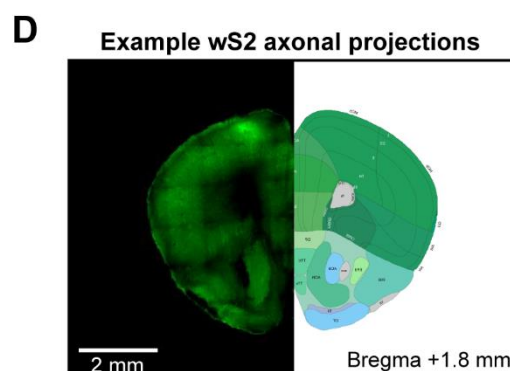
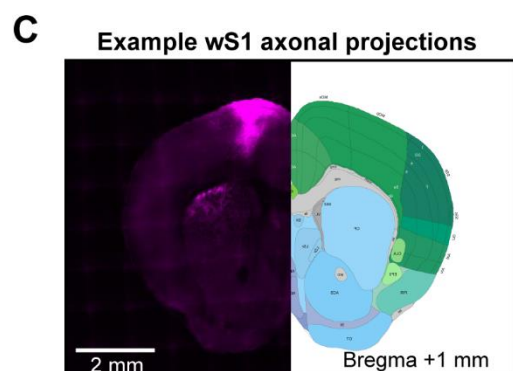
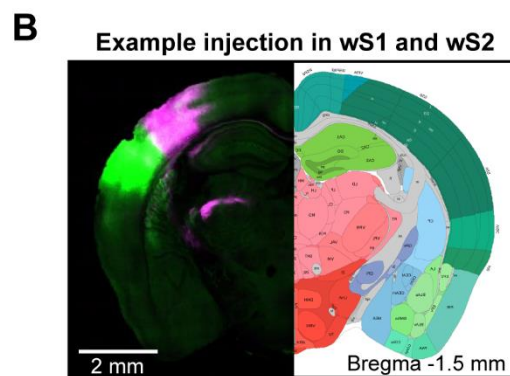
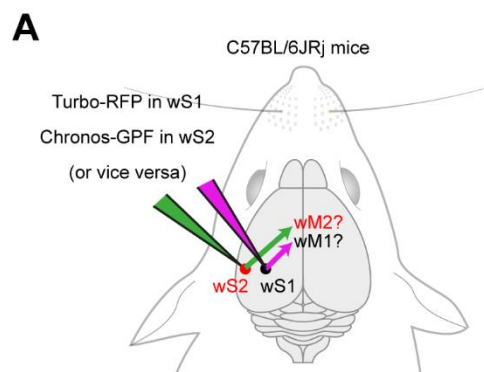


Figure 2-5 Distinct frontal projections of wS1 and wS2.

(A) Schematic of anterograde axonal tracing of wS1 and wS2 projections in frontal cortex. Fluorescent proteins of different colors were expressed in wS1 and wS2 regions and frontal projection patterns were identified using anatomical reconstructions and registration to Allen Brain Atlas. (B, C, D) Coronal sections showing example two-color injections in wS1 (magenta) and wS2 (green) and their frontal projection centers. Viral expression in wS1 and wS2 (B) and frontal sections showing the center of frontal projections in wM1 (C) and wM2 (D). All brains were registered to the Allen Mouse Brain Atlas, <https://mouse.brain-map.org>. (E) Grand average cortical fluorescent map of wS1 projections (4 mice). (F) Same as (E) but for wS2 projections (4 mice). (G) Overlay of grand average fluorescent map of wS1 (magenta) and wS2 (green) projections in frontal cortex. (H) Center of projections from wS1 and wS2 in frontal cortex. Contour plots at 95% and 75% maximum of the grand average fluorescent intensity from wS1 (magenta) and wS2 (green) projections, showing the location of wM1 and wM2 respectively. Markers show the center of projections for different mice. Projections in the same mice are indicated with similar markers. The underlying data for Fig 2-5 can be found in S7 Data.

2.3.6 Changes in fast sensory processing in wM1 and wM2

We next investigated the changes in whisker deflection-evoked neuronal activity in wM1 and wM2 across task learning. RS and FS neurons in both wM1 and wM2 and in both Novice and Expert mice showed obvious fast sensory-evoked modulation, dominated by units with increased action potential firing (Figure 2-2, 2-3 and 2-6). However, RS and FS neurons changed their activity patterns differentially across learning in these two neighbouring cortical areas. In wM1, RS units had a smaller whisker-evoked response in Expert compared to Novice mice (Novice: 1.8 ± 3.0 Hz, 147 units recorded in 7 mice, Expert: 0.9 ± 3.9 Hz, 452 units recorded in 11 mice; non-parametric permutation test, $p = 0.002$) (Figure 2-6A and Figure 2-18, whereas FS units had a larger response in Expert mice (Novice: 3.1 ± 3.6 Hz, 66 units recorded in 7 mice, Expert: 7.3 ± 16.9 Hz, 134 units recorded in 11 mice; non-parametric permutation test, $p = 0.0008$) (Figure 2-6b and Figure 2-18). The ratio of RS to FS firing in wM1 is therefore strongly changed in Expert mice in favor of FS units.

In contrast, we found that neuronal activity in wM2 changed in a very different way across learning compared to wM1. In wM2, whisker deflection evoked an increased action potential firing in RS units of Expert mice compared to Novice mice (Novice: 1.0 ± 2.2 Hz, 244 units recorded in 7 mice, Expert: 1.5 ± 4.5 Hz, 401 units recorded in 10 mice; non-parametric permutation test, $p = 0.016$) (Figure 2-6C and S11), but a decreased firing of FS units (Novice: 4.5 ± 6.8 Hz, 57 units recorded in 7 mice, Expert: 2.7 ± 3.9 Hz, 107 units recorded in 10 mice; non-parametric permutation test, $p = 0.021$) (Figure 2-6D and Figure 2-19). The balance of RS to FS unit activity in wM2 is therefore enhanced in favor of RS units across task learning.

To test how the coordination between sensory and motor cortices changed across learning, we quantified inter-areal interactions between wS1->wM1 and wS2->wM2 in the subset of sessions during which we obtained simultaneous paired recordings from these areas (Figure 2-6E and Figure 2-6F). Averaged over individual pairs of neurons, trial-by-trial correlation between evoked activity of wS2-RS units with wM2-RS units increased across learning (Novice: 876 neuron pairs recorded in 6 mice, Expert: 583 neuron pairs recorded in 3 mice; Wilcoxon rank-sum test, $p = 0.039$) while it decreased between wS2-RS units and wM2-FS units (Novice: 343 neuron pairs recorded in 6 mouse, Expert: 209 neuron pairs recorded in

3 mice; Wilcoxon rank-sum test, $p = 2.9 \times 10^{-4}$). Learning-related changes in firing rates might contribute to these apparent changes in correlations. However, while the activity of wM1-FS units increased across learning, the correlation between wS1-RS units and wM1-FS units did not change significantly, nor did the correlation between wS1-RS units and wM1-RS units. As an additional control, we measured inter-areal pairwise correlations using the spike time tiling coefficient (STTC) method (Cutts and Eglen 2014), which is suggested to be insensitive to firing rate (Fig Figure 2-20B). Quantified using STTC analysis, the only significant increase in correlation across learning was observed between wS2-RS to wM2-RS units (Novice: 3482 neuron pairs recorded in 6 mice, Expert: 2461 neuron pairs recorded in 3 mice; Wilcoxon rank-sum test, $p = 4.7 \times 10^{-11}$).

Trial-by-trial correlation of the population response showed similar patterns of change across learning in both area pairs as those observed in pair-wise correlation changes (Fig S12A). To further evaluate functional connectivity changes, we identified the number of directional connections (putative direct mono-synaptic connections) based on short-latency sharp peaks in the cross-correlograms between pairs of neurons from whisker sensory and whisker motor cortices (Figure 2-6F and Figure 2-20C). The percentage of connections between wS2-RS units to wM2-RS units increased significantly across learning (Novice: 3 out of 1077 pairs in 6 mice, Expert: 17 out of 1066 pairs in 3 mice; Chi-squared proportion test, $p = 0.0032$).

All together, these data suggest that learning might increase the excitation to inhibition ratio of the sensory-evoked response in wM2, but decreases the ratio in wM1 in favor of inhibition. Increased activity of excitatory neurons in wM2 across learning could arise from the increase in functional connectivity between wS2 to wM2, and could in turn contribute to driving excitation in other frontal areas including ALM, which is known to be important for the motor planning of licking (Z. V. Guo et al. 2014; Esmaeili et al. 2021).

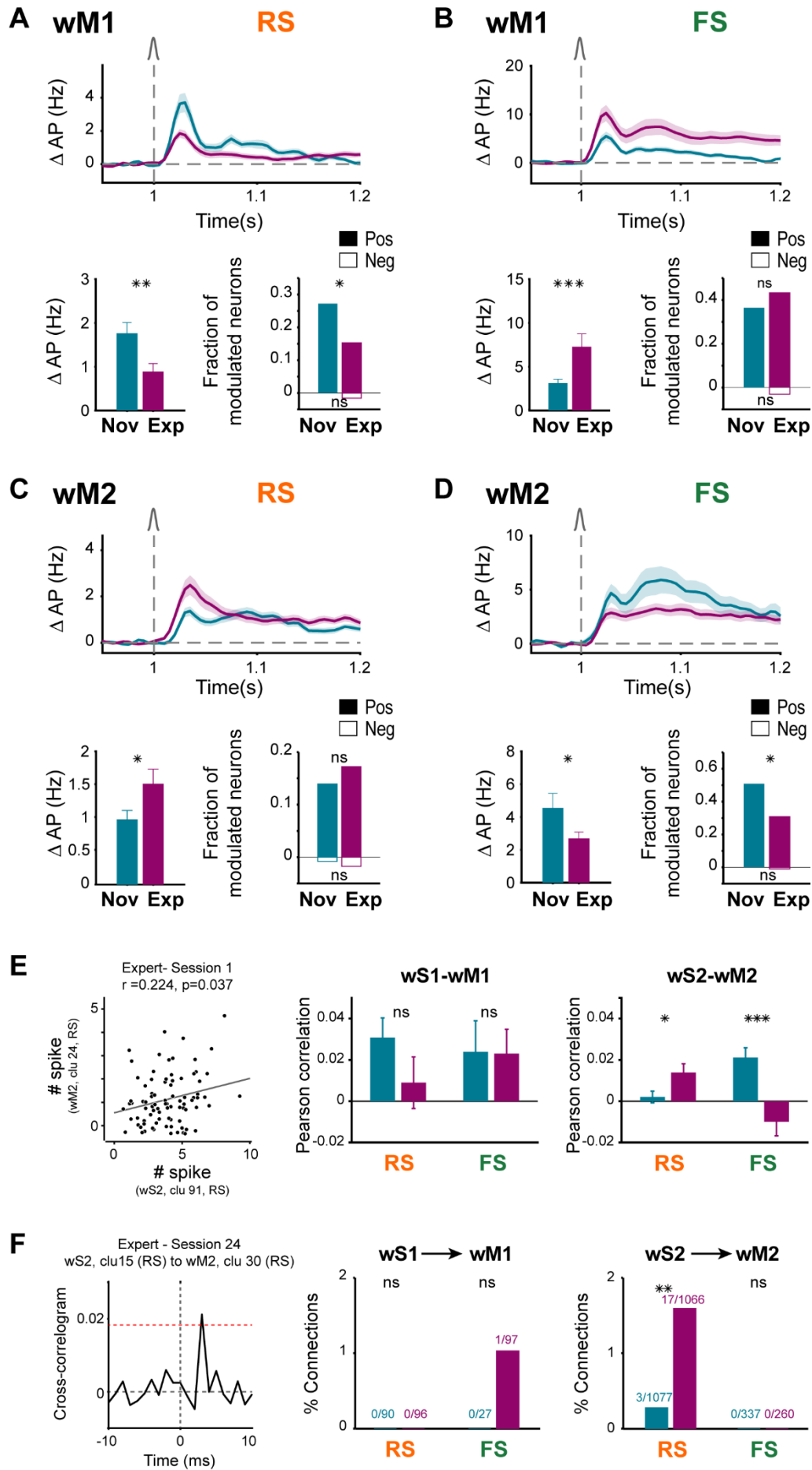


Figure 2-6 Learning differently modulated sensory responses of RS and FS neurons in wM1 and wM2 areas.

(A) Decrease of whisker response in wM1 RS neurons across learning. Top: baseline-subtracted (50 ms prior to whisker onset) population firing rate (mean \pm SEM) overlaid for Novice mice (147 neurons in 7 mice) and Expert mice (452 neurons in 11 mice). Bottom: Comparison of whisker-evoked response in Novice and Expert mice. Bar plots showing average population rate in 10-90 ms window (mean \pm SEM) after whisker onset and statistical comparison using non-parametric permutation test (left) (**: $p < 0.01$; *: $p < 0.05$). The fraction of positively (filled bars) or negatively (empty bars) modulated neurons in the same window (right). Modulation of individual neurons compared to a similar window size prior to whisker onset, was identified using non-parametric permutation test ($p < 0.005$). The fractions of modulated neurons in Novice and Expert were compared using a Chi-squared proportion test (*: $p < 0.05$; ns: $p \geq 0.05$). (B) Increase of whisker response in wM1 FS neurons across learning. Panels are similar to (A) but for wM1 FS neurons in Novice (66 neurons in 7 mice) and Expert mice (134 neurons in 11 mice) (***: $p < 0.001$). (C) Increase of whisker response in wM2 RS neurons across learning. Panels are similar to (A) but for wM2 RS neurons in Novice (244 neurons in 7 mice) and Expert mice (401 neurons in 10 mice). (D) Decrease of whisker response in wM2 FS neurons across learning. Panels are similar to (A) but for wM2 FS neurons in Novice (57 neurons in 7 mice) and Expert mice (107 neurons in 10 mice). (E) Pair-wise correlation between sensory and motor cortices in Novice and Expert mice. Left: Scatter plot showing the trial-by-trial correlation between the whisker-evoked response of an example pair of neurons in wS2 and wM2. Each circle represents the response of the neuronal pair in one trial. Circles were jittered slightly for the purpose of visualization. Gray line: least-squares regression. Middle: Average pair-wise Pearson correlation of wS1-RS units with wM1-RS (110 neuron pairs in 1 Novice mouse, and 68 neuron pairs in 2 Expert mice) and wS1-RS units with wM1-FS units (44 neuron pairs in 1 Novice mouse, and 89 neuron pairs in 2 Expert mice) separately. Right: Average pair-wise Pearson correlation of wS2-RS units with wM2-RS (876 neuron pairs in 6 Novice mouse, and 583 neuron pairs in 3 Expert mice) and wS2-RS units with wM2-FS units (343 neuron pairs in 6 Novice mouse, and 209 neuron pairs in 3 Expert mice). Error bars: SEM. Statistical comparison between Novice and Expert was performed using Wilcoxon rank-sum test (ns: $p \geq 0.05$; *: $p < 0.05$; ***: $p < 0.001$). (F) Inter-areal functional connectivity identified based on cross-correlograms. Left: Example cross-correlogram between a pair of simultaneously recorded neurons from wS2 and wM2. Red dotted line shows the threshold for detecting sharp peaks. A directional connection from wS2 to wM2 was detected as there is a threshold crossing within the time lags between 0-10 ms. Middle: Percentage of detected directional connections from wS1-RS units to wM1-RS and wM1-FS units in 1 Novice and 2 Expert mice. Right: Percentage of detected directional connections from wS2-RS units to wM2-RS and wM2-FS units in 6 Novice and 3 Expert mice. The numbers on each bar represent the number of identified connections and the total number of recorded pairs. The fractions of connections in Novice and Expert were compared using a Chi-squared proportion test (ns: $p \geq 0.05$; *: $p < 0.01$). The underlying data for Fig 2-6 can be found in S8 Data.

2.3.7 Neuronal activity in tongue and jaw-related motor cortices

Previous studies have identified motor (tjM1) and premotor (ALM) areas of neocortex associated with licking (Z. V. Guo et al. 2014; Mayrhofer et al. 2019). Whisker deflection evoked a rapid decrease in both RS (Figure 2-7A) and FS (Figure 2-7B) neuronal activity in tjM1 of Expert mice (RS Novice: 0.0 ± 1.2 Hz, 271 units recorded in 8 mice, RS Expert: -0.6 ± 1.7 Hz, 505 units recorded in 11 mice; non-parametric permutation test, $p < 0.0001$; FS Novice: -0.2 ± 2.1 Hz, 61 units recorded in 8 mice, FS Expert: -1.5 ± 2.6 Hz, 83 units recorded in 11 mice; non-parametric permutation test, $p = 0.0003$). The observed suppression of neuronal activity in tjM1 evoked by the whisker stimulus in Expert mice was present across superficial and deep layers (Figure 2-21). The suppression of neuronal activity in tjM1 in Expert mice may help suppress early licking (Esmaeili et al. 2021). An active suppression of licking during the response window after the auditory cue is also required in correct rejection trials compared to miss trials, and we previously reported stronger suppression of RS units in correct rejection trials (Esmaeili et al. 2021). Here, we similarly observed a larger reduction of activity of FS

neurons during the response window in correct rejection trials compared to miss trials (Figure 2-22). Thus, in periods when licking should be suppressed, there appears to be a decrease in firing of both RS and FS neurons in tJM1 across learning.

Delay period activity emerges in RS units of ALM after task learning, and is causally involved in motor planning (Esmaeili et al. 2021). Analysis of FS units revealed a similar activity pattern, indicating that in ALM of Expert mice both RS and FS units increased their firing rate after whisker stimulus and remain elevated throughout the delay period (RS Novice: 0.1 ± 0.7 Hz, 234 units recorded in 6 mice, RS Expert: 1.4 ± 4.1 Hz, 766 units recorded in 12 mice; non-parametric permutation test, $p = 0.0001$; FS Novice: 0.2 ± 1.5 Hz, 37 units recorded in 5 mice, FS Expert: 3.7 ± 6.8 Hz, 109 units recorded in 12 mice; non-parametric permutation test, $p = 0.0001$). Furthermore, in Expert compared to Novice mice, a larger fraction of RS and FS units were significantly modulated during the delay, primarily with an increase in firing rate (Figure 2-7C and Figure 2-7D). The delay period activity was more prominent in deeper layers of ALM for both RS and FS neurons (Figure 2-23).

Preparatory movements were prominent during delay periods in Expert mice and accounted for a large part of the neuronal activity during the delay period (Esmaeili et al. 2021). Nonetheless, investigating the subset of quiet trials without delay period movements, we found that significant neuronal delay period activity still remains in both RS and FS units (Figure 2-24). Therefore, both RS and FS units in ALM develop persistent delay period activity across learning which likely contributes to the storage of a licking motor plan.

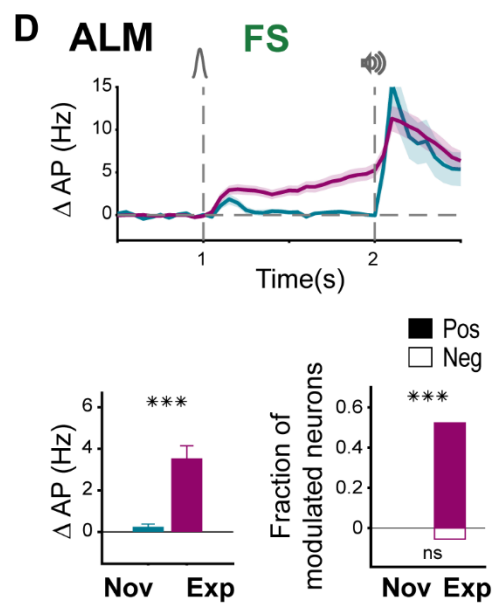
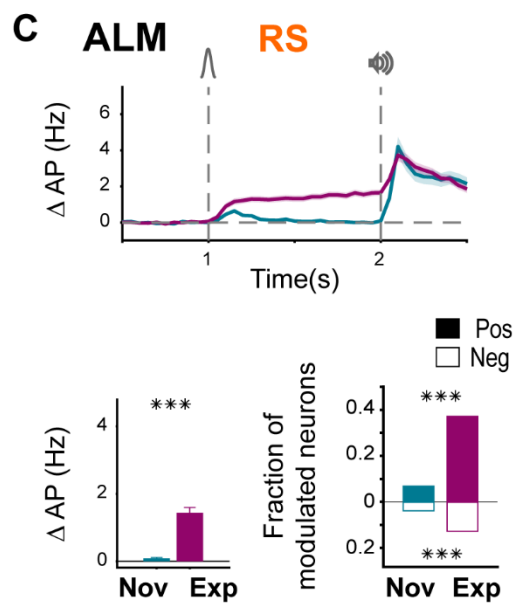
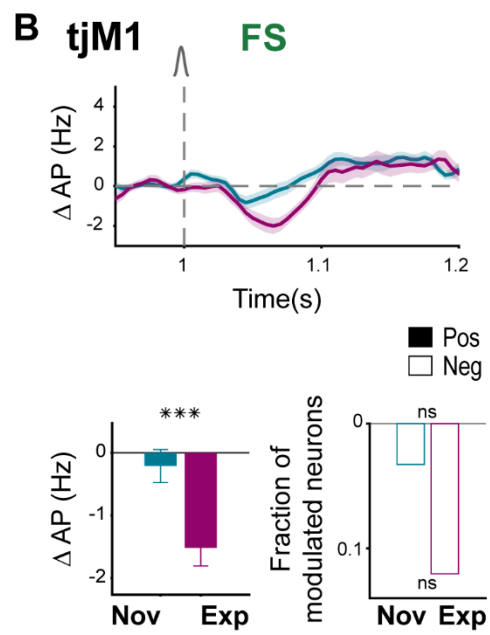
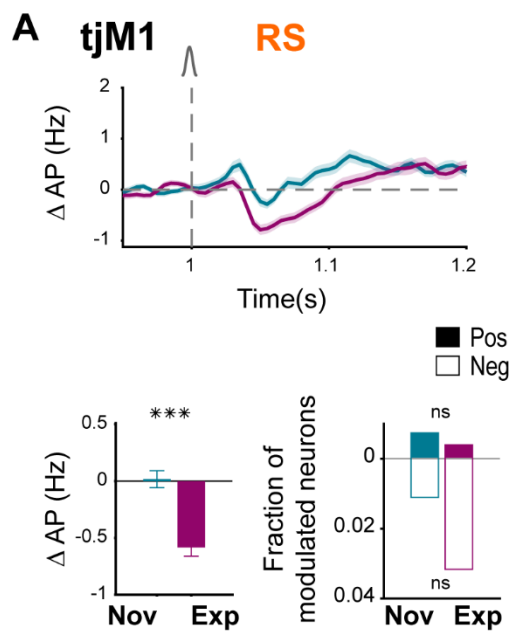


Figure 2-7 FS neuronal responses in tjM1 and ALM changed similarly to RS neurons.

(A) Suppression of tjM1 RS neurons in Expert mice. Top: baseline-subtracted (50 ms before whisker onset) firing rate (mean \pm SEM) overlaid for Novice (271 RS units in 8 mice) and Expert mice (505 RS units in 11 mice). Bottom: Comparison of whisker-evoked response in Novice and Expert mice. Bar plots showing population rate in 40-90 ms window (mean \pm SEM) after whisker onset and statistical comparison using non-parametric permutation test (left, ***: $p < 0.001$); fraction of positively (filled bars) or negatively (empty bars) modulated neurons in the same window (right). Modulation of individual neurons compared to a similar window size prior to whisker onset, was identified using non-parametric permutation test ($p < 0.005$). Fraction of modulated neurons in Novice and Expert were compared using a Chi-squared proportion test (ns: $p \geq 0.05$). (B) Suppression of tjM1 FS neurons in Expert mice. Panels are similar to (A) but for tjM1 FS neurons in Novice (61 neurons in 8 mice) and Expert mice (83 neurons in 11 mice). (C) Delay activity of RS neurons in Expert mice. Top: baseline-subtracted (1 s before whisker onset) firing rate (mean \pm SEM) overlaid for Novice (234 RS units in 6 mice) and Expert mice (766 RS units in 12 mice). Bottom: Comparison of whisker-evoked response in Novice and Expert mice. Bar plots showing population rate in 200-1000 ms window (mean \pm SEM) after whisker onset and statistical comparison using non-parametric permutation test (left, ***: $p < 0.001$); fraction of positively (filled bars) or negatively (empty bars) modulated neurons in the same window (right). Modulation of individual neurons compared to a similar window size prior to whisker onset, was identified using non-parametric permutation test ($p < 0.005$). Chi-squared proportion test: ***: $p < 0.001$, ns: $p \geq 0.05$. (D) Delay activity of ALM FS neurons in Expert mice. Panels are similar to (C) but for ALM FS neurons in Novice (37 FS units in 5 mice) and Expert mice (109 FS units in 12 mice). The underlying data for Fig 2-7 can be found in S9 Data.

2.3.8 Changes in excitation and inhibition across learning.

To the extent that we can equate RS units with excitatory neurons and FS units with inhibitory neurons (Figure 2-8A), we can begin to compute changes in the putative balance of excitation and inhibition as the changes in RS and FS firing rates across learning, providing a simple summary for comparisons (Figure 2-8). To do so, for each area (Figure 2-8B) and cell class (RS or FS), we calculated a learning modulation index (LMI) defined as the normalized difference between mean firing rate in Expert and Novice mice. Positive LMI values indicate an increase in neuronal activity across learning, while negative values represent suppression. The putative excitation and inhibition changed in opposite directions in wM1 (RS LMI = -0.33; FS LMI = 0.38) and wM2 (RS LMI = 0.22; FS LMI = -0.25) (Figure 2-8C and Figure 2-8D). In contrast, putative excitation and inhibition changed in the same direction across learning in ALM (RS LMI = 0.88; FS LMI = 0.87) and tjM1 (RS LMI = -0.92; FS LMI = -0.75) (Figure 2-8C and Figure 2-8D). Subtraction of the LMI of RS from the LMI of FS units as a measure of the change in the putative excitation-inhibition balance across learning, showed a decreased putative excitation-inhibition balance in wM1, but an increased putative excitation-inhibition balance in wM2 (E-I LMI wM1 = -0.72; E-I LMI wM2 = 0.46) (Figure 2-8E and Figure 2-8F). Interestingly, the apparent balance of excitation and inhibition thus appears to change differently across learning in distinct cortical areas.

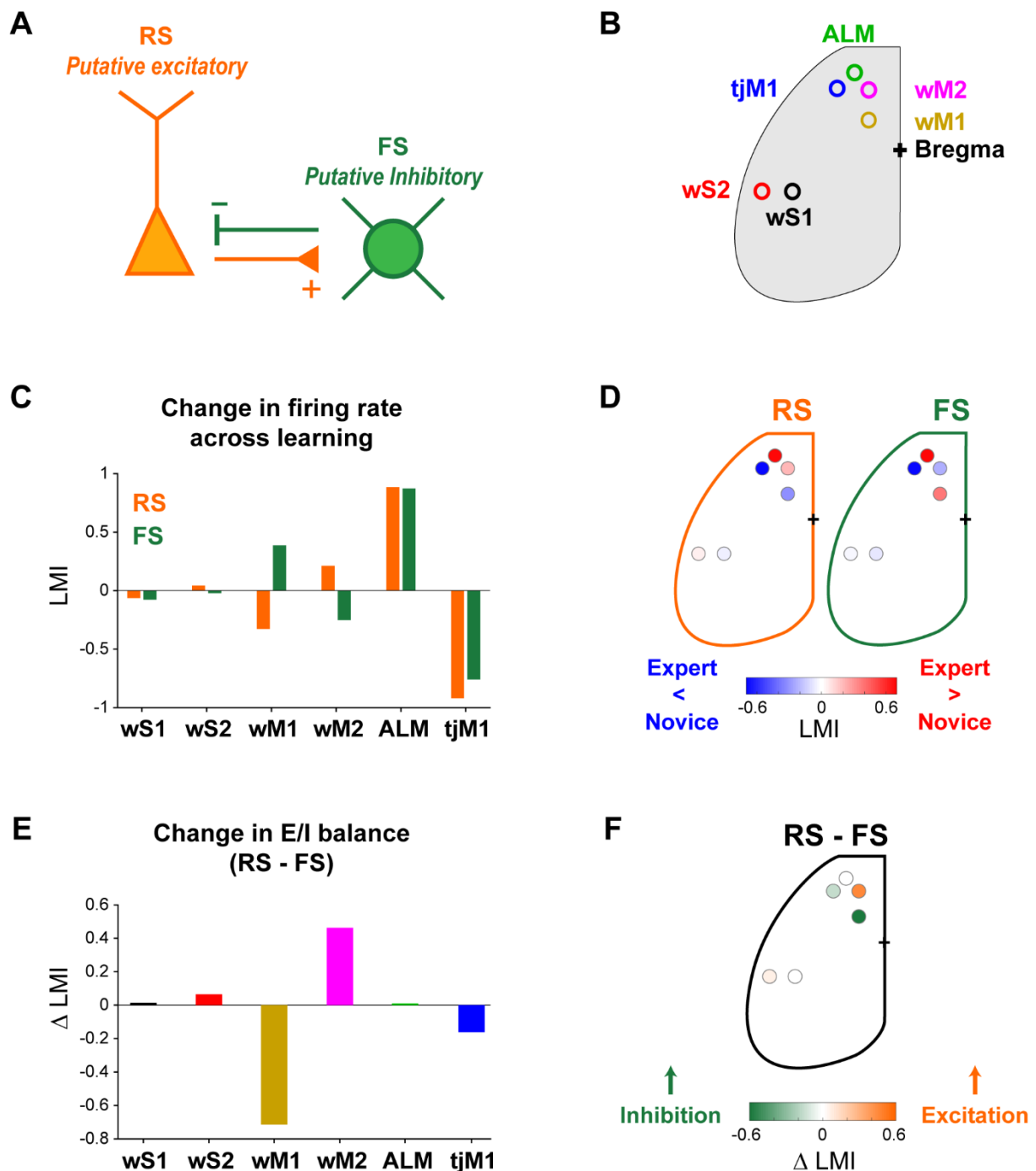


Figure 2-8 Diverse changes of putative excitation-inhibition balance in different cortical regions across learning.

(A) FS (putative PV GABAergic inhibitory) neurons and RS (putative glutamatergic excitatory pyramidal) neurons are typically considered to be strongly and reciprocally connected in local cortical microcircuits providing fast balance of excitation and inhibition. (B) Schematic showing the location of different cortical regions. (C) Learning modulation index (LMI) in different cortical regions for RS and FS units, representing learning-induced change in putative excitation and inhibition, respectively. LMI was quantified as the normalized difference between whisker-evoked firing rate in Novice and Expert mice. (D) Map of the putative excitation-inhibition change across learning, shown as LMI across cortical regions for RS and FS neurons. (E) Change in the putative excitation-inhibition balance across learning, quantified as difference between LMI of RS and FS neurons in different cortical regions. (F) Cortical map of the putative excitation-inhibition balance change across learning, calculated as LMI difference between RS and FS neurons. The underlying data for Fig 2-8 can be found in S10 Data.

2.4 Discussion

Comparing neuronal activity across task learning revealed distinct changes in RS and FS units in various neocortical areas. Strikingly, in tJM1 and ALM, RS and FS neurons changed firing rates congruently across learning, but in wM1 and wM2, RS and FS changed firing rate incongruently, pointing towards learning-related changes in the balance of cortical excitation and inhibition, with an overall change across learning towards excitation of wM2 and inhibition of wM1.

In wS1 and wS2, we found that there was little change in overall neuronal activity across learning, consistent with a robust coding of the sensory stimulus in these areas of somatosensory cortex (Figure 2-4). Our results do not rule out a possible reorganization of neuronal activity across learning with some neurons increasing and others decreasing their response to whisker stimulation. Indeed, in a whisker detection task without a delay period, we previously found in wS1 of expert mice that neurons projecting to wS2 had stronger task-related depolarizations compared to neurons projecting to wM1, whereas we found the converse in naive mice (Yamashita and Petersen 2016). Consistent with an important role for wS2 in whisker detection tasks (Esmaili et al. 2021b; Le Merre et al. 2018a; Kwon et al. 2016), here we found that optogenetic inactivation of wS2, as well as wS1 inactivation, induced a strong impairment in task performance (Figure 2-4E).

Neuronal activity in wS1 and wS2 can directly influence frontal cortex through direct monosynaptic connections with wM1 and wM2, which we characterized anatomically in this study (Figure 2-5). Interestingly, neuronal activity in wM1 and wM2 changed profoundly across learning (Fig 6). RS units in wM1 decreased their sensory-evoked response, whereas RS units in wM2 increased their response across learning (Esmaili et al. 2021b). Trial-by-trial correlations (Figure 2-6E) and spike-triggered connectivity analyses (Figure 2-6F) both pointed to enhanced coupling between wS2-RS units and wM2-RS units, which could, at least in part, result from potentiation of monosynaptic inputs from wS2-RS units to wM2-RS units, although other more complex mechanisms could equally play a role. In contrast FS units in wM1 increased their response across learning, whereas FS units in wM2 decreased their evoked neuronal activity. Our data thus suggest differential change in the balance between excitation and inhibition with learning in wM1 and wM2, with enhanced sensory-evoked inhibition relative to excitation in wM1 but enhanced excitation relative to inhibition in wM2 (Fig 8). Changes in inhibitory neuronal activity could contribute importantly to task learning. Increased recruitment of fast inhibition in wM1 across learning could suppress the response of excitatory neurons in wM1. We speculate that suppression of activity in wM1 could enhance whisker detection performance by reducing whisker movements (Sreenivasan et al. 2016), which otherwise could cause confounding sensory-reafference signals. On the other hand, reduced firing of inhibitory neurons in wM2 across learning could allow the excitatory neurons to respond more strongly. Disinhibition of wM2 might be an important step allowing the propagation of whisker sensory information in higher order motor cortex, perhaps contributing to exciting ALM through local intracortical connections (Esmaili et al. 2021). Interestingly, disinhibition of wS1 has previously been reported to contribute to execution of a whisker detection task without a delay (Sachidhanandam, Sermet, and Petersen 2016), suggesting the general importance of considering changes in inhibitory neuronal activity for

controlling goal-directed sensorimotor transformations (Hofer et al. 2011; Pinto and Dan 2015; Allen et al. 2017). Several mechanisms could contribute to disinhibition, including the activation of GABAergic neurons preferentially innervating other GABAergic neurons, as found in auditory cortex during fear learning (Letzkus et al. 2011). Neuromodulation could also play an important role, for example through cholinergic reward signals (Hangya et al. 2015), which could drive excitation of vasoactive intestinal peptide-expressing GABAergic neurons (Fu et al. 2014; Gasselino et al. 2021), in turn causing disinhibition through their prominent innervation of PV and somatostatin-expressing GABAergic neurons (S. Lee et al. 2013; Pfeffer et al. 2013; Pi et al. 2013).

In contrast to the divergent changes across learning in RS and FS unit activity in wM1 and wM2, RS and FS units changed their activity patterns in the same way in ALM and tJM1 (Figure 2-7). Suppression of tJM1 activity in Expert mice has a causal role in delayed licking behavior (Esmaeili et al. 2021). The rapid suppression of RS units across learning in tJM1 was mirrored by a rapid suppression of FS unit firing (Figure 2-7A and Figure 2-7B). Overall there was thus no apparent change in the balance of excitation and inhibition in tJM1 across learning (Fig 8). The rapid decrease in firing of both RS and FS units evoked by the whisker deflection in Expert mice could result from many different mechanisms, including a possible reduced thalamic or other long-range input to orofacial sensorimotor cortex.

Neuronal delay period activity in ALM is of critical importance for motor planning of licking (Z. V. Guo et al. 2014; 2017; Esmaeili et al. 2021). We found that both RS and FS units increase firing rate during the delay period in Expert mice, but not Novice mice (Figure 2-7). Similar to tJM1, there was therefore no apparent change in the balance of excitation and inhibition in ALM across learning (Figure 2-8). Thalamic activity has been shown to be necessary for maintaining ALM activity during delay periods (Z. V. Guo et al. 2017; Chabrol, Blot, and Mrcic-Flogel 2019; Z. Gao et al. 2018), and increased thalamic input likely excites both RS and FS neurons either directly (Sermet et al. 2019; Cruikshank, Lewis, and Connors 2007; Gabernet et al. 2005; Bagnall et al. 2011; Delevich et al. 2015; Anastasiades, Collins, and Carter 2021; Rodriguez-Moreno et al. 2020; Shepherd and Yamawaki 2021) or indirectly through local cortical microcircuitry. ALM neurons in turn, project to thalamic nuclei (Z. V. Guo et al. 2017). In agreement with this, we observed larger delay activity in layer 6 of ALM where many corticothalamic neurons are located (K. D. Harris and Shepherd 2015) (Figure 2-23).

In future studies, it will be of importance to better define the various classes of neurons beyond our current classification of RS and FS units. For example diverse classes of GABAergic neurons can be defined through expression of Cre and Flp recombinase under different promoters (Taniguchi et al. 2011; He et al. 2016), enabling functional identification of these neurons through opto-tagging (Kvitsiani et al. 2013). Different classes of excitatory neurons might be best classified through their long-range axonal projections, which could be functionally identified through optogenetic stimulation of axonal branches in target regions (Economo et al. 2018). The current study thus takes a first step towards differentiating neuronal activity in various cortical regions across learning, but further experiments will be needed in order to gain a more complete understanding of neocortical cell class-specific

changes, as well as, importantly, investigating subcortical regions which are likely to play profound roles in both learning and execution of goal-directed sensorimotor transformations.

2.5 Methods

The results in this study are largely based on further analysis of our recently published dataset available Open Access via the CERN database Zenodo (<https://doi.org/10.5281/zenodo.4720013>). The methods used to obtain the published dataset were fully described in the accompanying journal publication (Esmaeili et al. 2021b), and are only briefly introduced here. The new analyses are described in detail below. We also carried out two new series of experiments: i) optogenetic tagging of GABAergic neurons and ii) anatomical analysis of axonal projections from wS1 and wS2 to frontal cortex. All experimental procedures were approved by the Swiss Federal Veterinary Office (Licences VD1628.7 and VD1889.4) and were conducted in accordance with the Swiss guidelines for the use of research animals. The methods for obtaining the new data are described in detail below. The full data set and analysis code used to generate the figures and results described in this study are available via the Open Access CERN database Zenodo: <https://doi.org/10.5281/zenodo.6511622>.

2.5.1 Behavioral paradigm and electrophysiological recordings

Both Novice and Expert mice were trained in the first stage of the task, where in all trials a visual (trial onset) and auditory cues were presented, and licks during a 1-second response window following the auditory cue were rewarded (Fig 1A and 1B). To initiate a trial, mice needed to withhold licking (i.e. not touching the water spout) for a quiet period of 2-3 seconds following an inter-trial-interval of 6-8 seconds. Visual cue (200 ms, green LED) and auditory cue (200 ms, 10 kHz tone of 9 dB added on top of the continuous background white noise of 80 dB) were separated with a delay period which gradually was increased to 2 seconds over Pretraining days. Licking before the response period (Early lick) aborted the trial and introduced a 3-5 second timeout. The Expert mice went through a second training phase (Whisker-training), in which only Go trials (i.e. trials with a whisker stimulus) were rewarded. Whisker stimulus (10 ms cosine 100 Hz pulse through a glass tube attached to a piezoelectric driver) was delivered to the right C2 whisker 1 second after the visual cue onset in half of the trials. Electrophysiological data from both groups of mice were acquired during the final task conditions (Fig 1C). Novice mice licked in both Go and No-Go trials; while Expert mice had learned to lick selectively in Go trials (Esmaeili et al. 2021).

Extracellular recordings were performed using single-shank silicon probes (A1x32-Poly2-10mm-50 s-177, NeuroNexus, MI, USA) with 32 recording sites covering 775 μm of the cortical depth. In each session two probes were inserted in two different brain targets acutely. Probes were coated with Dil (1,1'-Diocetyl-3,3',3'-Tetramethylindocarbocyanine Perchlorate, Invitrogen, USA) for post-hoc recovery of the recording location (see below). The neural data were filtered between 0.3 Hz and 7.5 kHz and amplified using a digital headstage (CerePlex™ M32, Blackrock Microsystems, UT, USA). The headstage digitized the data with a sampling frequency of 30 kHz. The digitized signal was transferred to our data acquisition system (CerePlex™ Direct, Blackrock Microsystems, UT, USA) and stored on an internal HDD of the host PC for offline analysis.

2.5.2 Optogenetic tagging of GABAergic neurons

To evaluate to what extent the categorization of units as RS or FS based on spike width is useful for assessing the activity of excitatory versus inhibitory neurons, we performed simultaneous electrophysiological recordings and blue light stimulations in wS1 in 5 sessions from 4 VGAT-ChR2 mice, which express ChR2 in all neocortical GABAergic neuron types. A craniotomy was made over the C2 barrel column, identified by optical intrinsic imaging. For each mouse, a silicon probe (A1x32-Poly2-10mm-50 s-177-A32, NeuroNexus, MI, USA) was slowly lowered to a depth of $\sim 1000\ \mu\text{m}$ in the C2 barrel column, and an optic fiber (400 μm ; NA = 0.39, Thorlabs) coupled to a 470 nm high power LED (M470F3, Thorlabs, USA) was positioned close to the brain surface and the probe. A 100 Hz train of blue light pulses (50% duty cycle, mean power 1-2 mW) with the duration of 600 ms was applied. Light pulse train was followed by an additional 100 ms ramping down to prevent rebound excitation. In total, 51 FS and 130 RS units were identified in 5 sessions from 4 mice.

2.5.3 Anatomical analysis of axonal projections from wS1 and wS2 to frontal cortex

An AAV1.hSyn.TurboRFP.WRPE.rBG (titer: 6.5×10^{13} vg/ml, AV-1-PV2642, UPenn Vector Core, USA) was injected at the center of C2 barrel column in wS1 (or in the C2 whisker representation in wS2), and an AAV5.Syn.Chronos-GFP.WPRE.bGH (titer: 3.82×10^{13} vg/ml, AV-5-PV3446, UPenn Vector Core, USA) or AAV5.hSyn.hChR2(H134R)-eYFP.WRPE.hGH (titer: 7×10^{12} vg/ml, AV-1-26973P, UPenn Vector Core, USA) was injected in the C2 whisker representation in wS2 (or C2 barrel column in wS1). In total 100 nl of virus was delivered in each area at 300-400 μm and 700-800 μm below the dura, through a glass pipette (PCR Micropipets 1 – 10 ml, Drummond Scientific Company, USA) with a 21 – 27 μm inner tip diameter. After 4 weeks of expression, mice were perfused with phosphate buffered saline (PBS) followed by 4% paraformaldehyde (Electron Microscopy Science, USA) in PBS. The brains were post-fixed overnight at room temperature. Next, we embedded the brains in 3-5 % oxidized agarose (Type-I agarose, Merck KGaA, Germany) and covalently cross-linked the brain to the agarose by incubating overnight at 4 °C in 0.5 – 1 % sodium borohydride (NaBH_4 , Merck KGaA, Germany) in 0.05 M sodium borate buffer. We imaged the brains in a custom-made two-photon serial sectioning microscope, which was controlled using Matlab-based software (ScanImage 2017b, Vidrio Technologies, USA) and BakingTray (<https://github.com/BaselLaserMouse/BakingTray>, version master: 2019/05/20, extension for serial sectioning) (Han et al. 2018). The setup consists of a two-photon microscope coupled with a vibratome (VT1000S, Leica, Germany) and a high-precision X/Y/Z stage (X/Y: V-580; Z: L-310, Physik Instrumente, Germany). The thickness of a physical slice was set to be 50 μm for the entire brain and we acquired optical sections at 10 μm using a high-precision piezo objective scanner (PIFOC pons-725, Physik Instrumente, Germany) in two channels (green channel: 500 – 550 nm, ET525/50, Chroma, USA; red channel: 580 – 630 nm, ET605/70, Chroma, USA). Each section was imaged by 7 % overlapping 1025x1025- μm tiles. A 16x water immersion objective lens (LWD 16x/0.80W; MRP07220, Nikon, Japan), with a resolution of 1 μm in X and Y and measured axial point spread function of $\sim 5\ \mu\text{m}$ full width at half maximum. After image acquisition, the raw images were stitched using a Matlab-based software (StitchIt, <https://github.com/BaselLaserMouse/StitchIt>). The stitched images were then down-sampled

by a factor of 25 in X and Y obtaining a voxel size of 25 x 25 x 25 μm , using a Matlab-based software (MaSIV, <https://github.com/alexanderbrown/masiv>) or using the software Fiji (<https://imagej.net/Fiji>). The brains were then registered to Allen Mouse Common Coordinate Framework version 3 (Q. Wang et al. 2020) using a python-based tool (Brainreg, <https://github.com/brainlobe/brainreg>) (Tyson et al. 2022). We then acquired 2-D maps of cortical projection patterns, by only considering layer 2/3 of cortex and calculating 99% intensity levels across cortical depth using custom-developed analysis routine (https://renkulab.io/projects/guier.romain/brainreg/files/blob/notebooks/notebooks_napari_brainreg.ipynb). Grand average 2-D maps of cortical projections (Fig 5E and F) were obtained by first normalizing each mouse's map to its global maximum (i.e. injection site intensity value), and then averaging across mice. The 95% and 75% contours (Fig 5H) for wS1 and wS2 frontal projections sites were calculated on these grand average maps. The center of frontal projection site for individual mice was identified by finding the local maxima in the frontal cortical region (Fig 5H).

3.5.4 Data analysis and statistics

3.5.4.1 Single neuron whisker-evoked response latency

When measuring the latency of the whisker-evoked response in the firing rate of individual neurons in all cortical areas (Fig 3.3C and 3.3D), the analysis was limited to the first 200-ms window following the whisker stimulus. First, we examined whether each neuron was modulated (positively or negatively) in the 200-ms window following the whisker stimulus compared to a 200-ms window prior to the whisker onset. For responsive neurons ($p < 0.05$, non-parametric permutation test), latency - calculated on the temporally smoothed peristimulus time histograms (1 ms non-overlapping bins filtered with a Gaussian kernel with $\sigma = 10$ ms) - was defined as the time where the neural activity reached half maximum (half minimum for suppressed neurons) within the 200-ms window. Only responsive neurons are included in boxplots in Fig 3.3C and 3.3D and Fig. 3.14. For wS1 and wS2 regions, where neurons had shorter latencies, we recalculated the latencies with higher temporal resolution (Fig 3.4D). We limited the analysis to 100-ms window following the whisker onset, and calculated latencies on smoothed peristimulus time histograms (1 ms non-overlapping bins filtered with a Gaussian kernel with $\sigma = 5$ ms).

3.5.4.2 Quantifying opto-tagged neurons

In recordings from VGAT-ChR2 mice (Fig 3.1J-O and 3.12), we quantified the effect of blue light stimulation on firing rates, on both slow and fast time scales. To quantify the effect of light on each individual neuron we first calculated an opto modulation index (OMI, Fig 1K). OMI was defined, in light trials, as the normalized difference between the average firing rate during the light window (100-500 ms after light onset) vs a baseline of similar duration (-400-0 ms prior to light onset):

$$OMI_n = \frac{AP_{light_n} - AP_{baseline_n}}{AP_{light_n} + AP_{baseline_n}}$$

Subsequently, to measure the effect of light stimulation devoid of potential network effects, we focused on the first 10-ms immediately after light onset. We then quantified within this window the following parameters: fidelity, defined as the percentage of trials with at least one spike during this window; latency, as the average delay to first spike in trials with at least one spike during 10-ms window; and jitter as the standard deviation of the latency. We then

labeled neurons as opto-tagged with fidelity > 20%, latency < 4.5 ms, and jitter < 2 ms (Fig 3.1M-O and 3.12).

2.5.5 Inter-areal functional connectivity measures

Taking advantage of the subset of sessions with simultaneous paired recordings from whisker sensory and motor cortices, we used two separate methods to examine the changes across learning in the coordination of inter-areal neural activity (Fig 3.6E and 3.6F, and 3.20). First, we measured Pearson correlation between trial-by-trial whisker-evoked responses in pairs of individual neurons recorded from wS1/wS2 (5-55 ms window after whisker onset) and wM1/wM2 (10-90 ms window after whisker onset) (Fig 6E). For the pair-wise correlation analysis, we only considered neurons with average firing rate > 2.5 Hz within the corresponding analysis windows. Similarly, the Pearson correlation in trial-by-trial average population responses in the same task epochs between pairs of simultaneously recorded areas were quantified (Fig S12A). As a second measure of pair-wise correlation, which is suggested to be insensitive to firing rate, we applied the spike time tiling coefficient (STTC) approach (Cutts and Eglen 2014). The STTC was calculated during a 1-s window centered on the whisker stimulus (Figure S12B), and was defined for spike trains A and B as:

$$STTC = \frac{1}{2} \left(\frac{P_A - T_B}{1 - P_A T_B} + \frac{P_B - T_A}{1 - P_B T_A} \right)$$

where P_A and P_B are the proportion of spikes from A falling within $\pm\Delta t$ (± 10 ms) of a spike in B and vice versa; and T_A and T_B are the proportion of the total recording time which falls within $\pm\Delta t$ of a spike from B or A respectively.

In addition, we identified directional functional connectivity from wS1 to wM1 and from wS2 to wM2 by calculating cross-correlograms (CCG) during a 1-second window centered on whisker stimulus (Fig 6F and S12C). The CCG was defined as:

$$CCG(\tau) = \frac{\frac{1}{M} \sum_{i=1}^M \sum_{t=1}^N \chi_1^i(t) \chi_2^i(t + \tau)}{\theta(\tau) \sqrt{\lambda_1 \lambda_2}}$$

where M is the number of trials, N is the number of bins in the trial, χ_1^i and χ_2^i are the spike trains of the two units on trial i , τ is the time lag relative to reference spikes, and λ_1 and λ_2 are the mean firing rates of the reference and target units respectively. $\theta(\tau)$ is the triangular function which corrects for the overlap time bins caused by the sliding window (Perkel et al. 1967). Neurons with firing rate > 1 Hz within the analysis window were included in this analysis.

To better capture fast timescale changes related to feedforward connections, cross-correlograms were corrected by subtracting a jittered version (Smith and Kohn 2008; Siegle et al. 2021) (Fig S12C):

$$CCG_{corrected} = CCG - CCG_{jittered}$$

The jittered CCG was produced as the average of 100-times resampling the original dataset where spike times within each 25-ms window were randomly permuted across different trials. This method, removes the stimulus-locked and slow timescale correlations larger than the jitter window, while preserving the trial-averaged PSTH and number of spikes for each unit (Harrison and Geman 2009). For each pair of recorded units, the significant directional connection from reference to target neuron was identified if the maximum CCG within time lags between 0 to 10 ms was larger than 6-fold standard deviation of the jitter-corrected CCG flanks (between ± 50 -100 ms).

For both analytical methods, in wS1/wS2 we focused only on the RS units, as they are known to have long-range projections. In wM1/wM2, we quantified correlations and directional connections separately for RS and FS units.

2.5.6 Quantifying learning modulation index

The learning modulation index (LMI) for each cell class ('cc', i.e. RS or FS) and cortical area ('a', i.e. wS1, wS2, wM1, wM2, ALM, or tjM1) was defined as the normalized difference of whisker-evoked response in Novice and Expert mice (Fig 8C and 8D):

$$LMI_{ct,a} = \frac{\Delta AP_{Expert_{cc,a}} - \Delta AP_{Novice_{cc,a}}}{|\Delta AP_{Expert_{cc,a}}| + |\Delta AP_{Novice_{cc,a}}|}$$

where ΔAP is the grand average change in firing rate (compared to pre-whisker baseline) across all neurons from that mouse group, cortical region and cell class.

2.5.7 Statistics

Data are represented as mean \pm SEM unless otherwise noted. The Wilcoxon signed-rank test was used to assess significance in paired comparisons; and the Wilcoxon rank-sum test was used for unpaired comparisons (Matlab implementations). Analysis of spiking activity was performed using non-parametric permutation test. Comparisons of the number of modulated neurons were performed using a Chi-squared proportion test. The statistical tests used and n numbers are reported explicitly in the main text or figure legends. *p*-values are corrected for multiple comparisons when necessary and methods are indicated in main text or figure legends.

2.6 Additional information

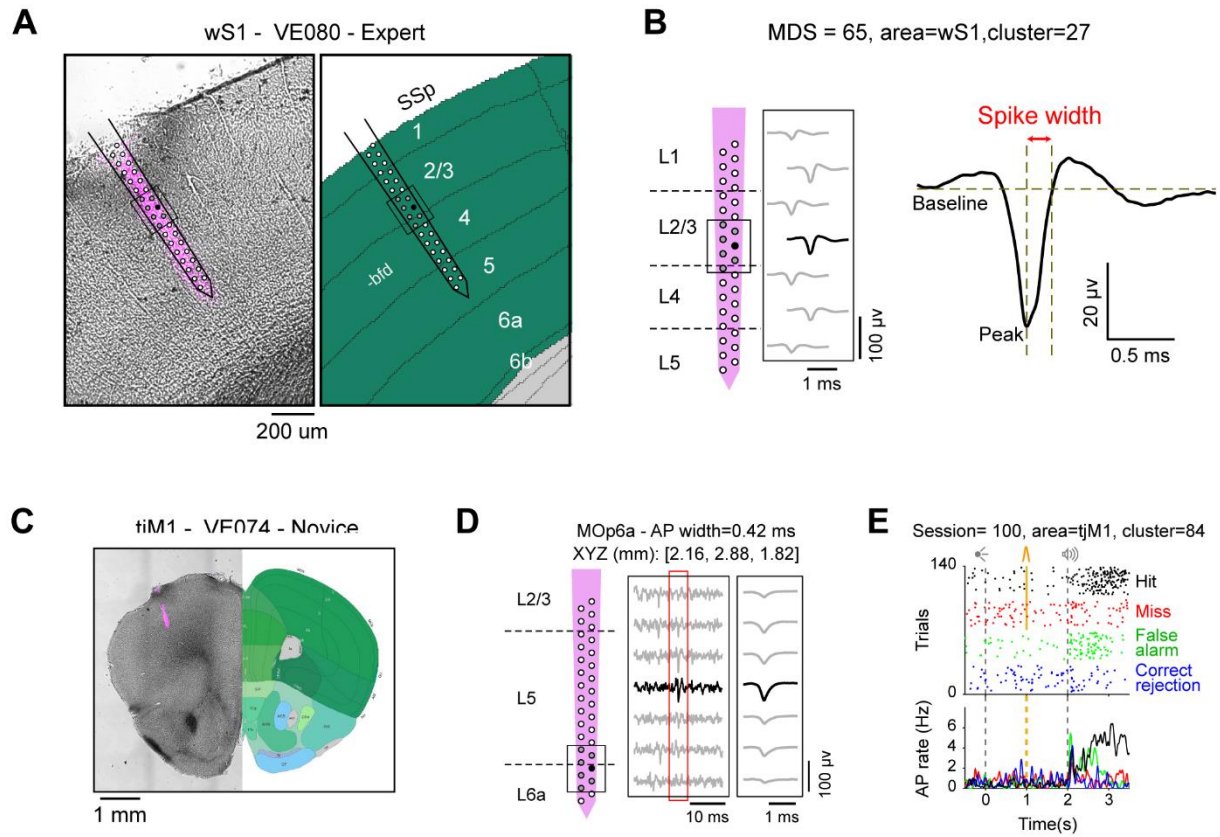
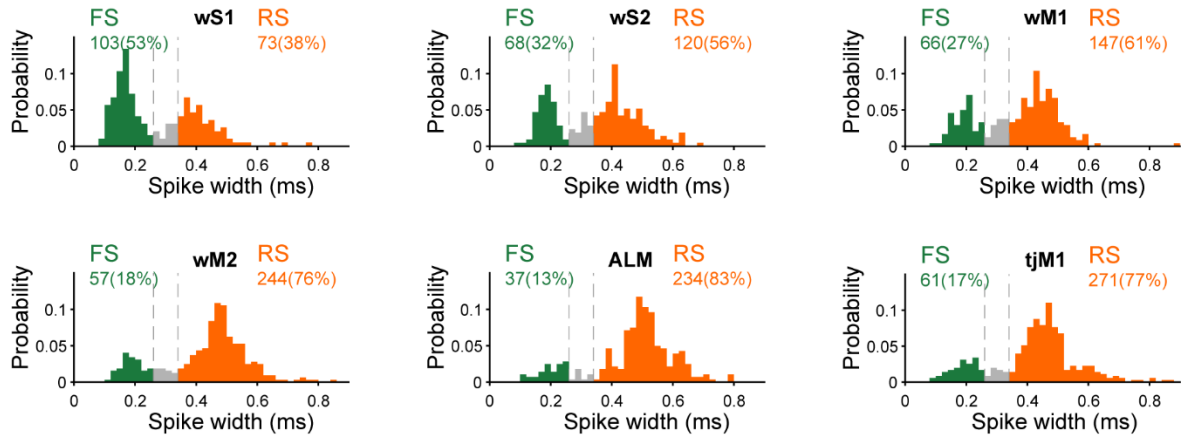


Figure 2-9 S1 Fig. Anatomical localisation of neurons.

(A) Magnified example fluorescent track of the silicon probe in wS1 shown in Fig 1D, and location of different probe sites after registration to the Allen Mouse Brain Atlas, <https://mouse.brain-map.org>. The small rectangular box and black recording site highlight the location of the example neuron shown in (B). (B) Silicon probe, example shown in (A), with site locations across cortical layers and example neuron recorded on the probe. Spikes from each neuron were observed across several sites (shown with circles) of the silicon probe. For calculating the spike width for each neuron, the average spike waveform extracted from the recording site with the largest spike peak amplitude (filled circle) was used. Spike width was defined as the time between the spike peak (minimum) to the time voltage came back to baseline level. Gray horizontal line shows spike baseline, and vertical lines mark where spike width was measured. (C) Example coronal section of a Novice mouse brain with fluorescent track of a single shank silicon probe in tjM1, registered to the Allen Mouse Brain Atlas, <https://mouse.brain-map.org>. (D) Reconstructed location of different recording sites of the example silicon probe shown in (C) according to Allen Atlas (left), filtered recorded raw data of 7 probe sites around one detected spike, and average extracted spike waveform for this example neuron (right). After spike sorting, the position of each neuron was assigned to the location of recording site across the probe with the largest spike amplitude (filled circle). (E) Raster plot and peri-stimulus time histogram (PSTH) for the example neuron shown in (D). Trials are grouped and colored based on trial outcome. The underlying data for Fig S1 can be found in S1 Data.

A Novice



B Expert

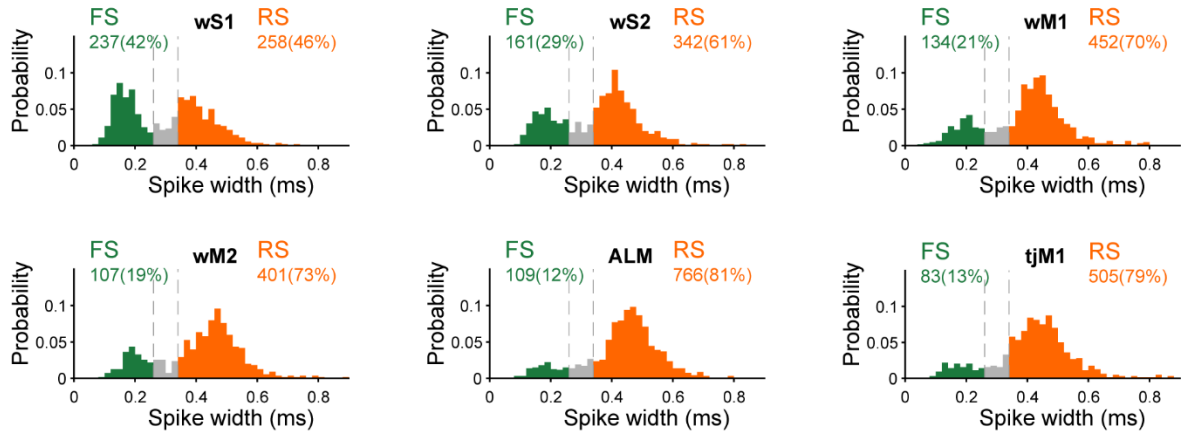


Figure 2-10 S2 Fig. Distribution of spike width in different cortical areas.

(A) Spike width distribution for neurons recorded from Novice mice shown separately for different cortical regions. Neurons were categorized as fast-spiking (FS, spike width < 0.26 ms) or regular-spiking (RS, spike width > 0.34 ms) in all areas. Neurons with intermediate spike width (gray bars) were excluded from the rest of analysis. Percentage of neurons in each area tagged as RS or FS are shown. (B) Same as (A) but for Expert mice. A smaller percentage of FS neurons appears to be found in frontal regions in both Novice (A) and Expert mice (B). The underlying data for Fig S2 can be found in S1 Data.

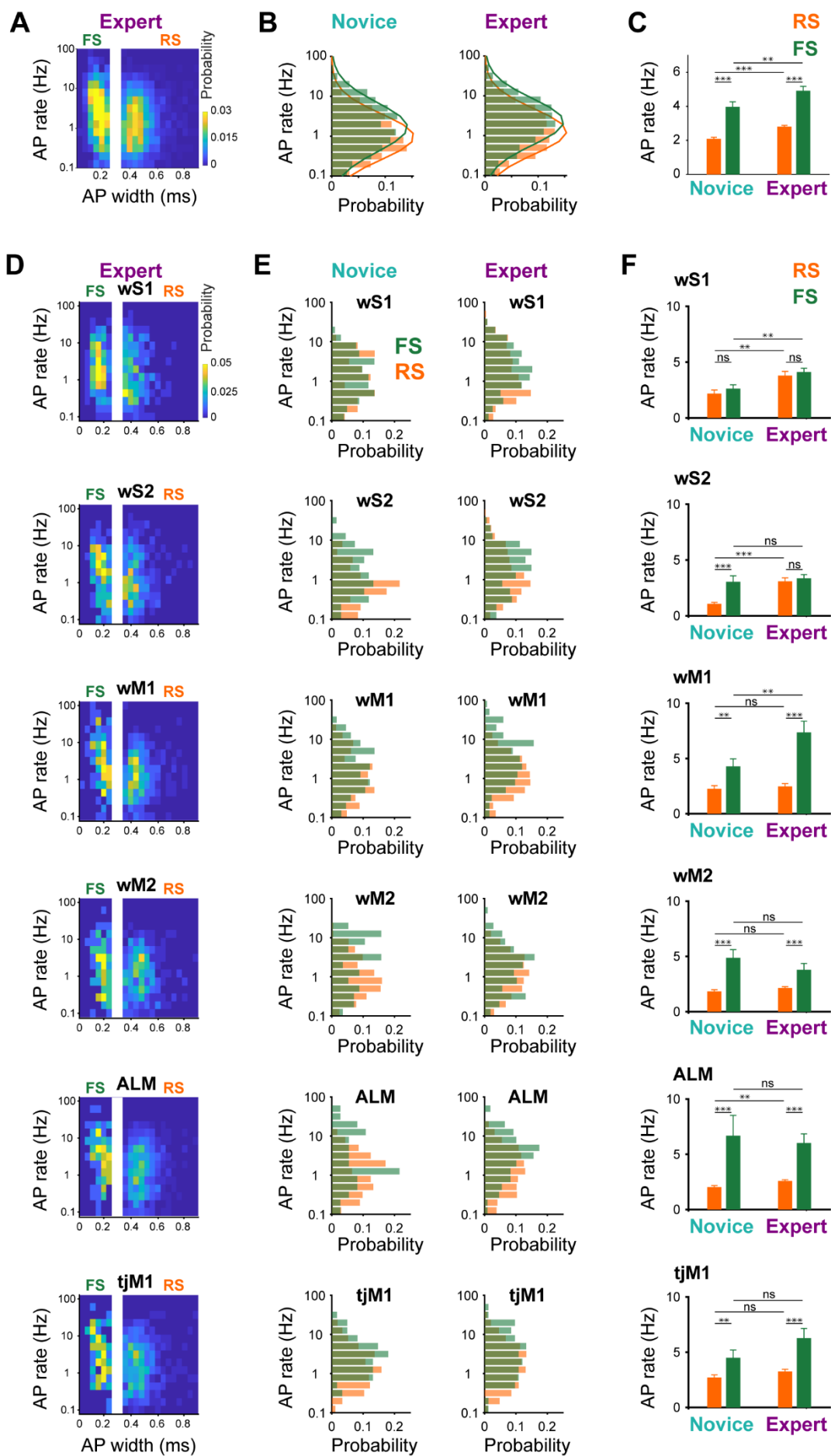


Figure 2-11 S3 Fig. Baseline firing rates of RS and FS neurons.

*(A) Spike width distribution vs spike rate for all neurons recorded from Novice mice. (B) Spike rate distribution for RS and FS units in Novice (left) and Expert (right) mice. Note the log-normal distribution of baseline firing rates for both RS and FS units in Novice and Expert mice. Normal distributions were fit to the RS and FS histograms (solid lines). (C) Comparison of mean spike rate in RS vs FS neurons of Novice and Expert mice. Error bars: SEM. ***: $p < 0.001$, **: $p < 0.01$, *: $p < 0.05$, ns: $p \geq 0.05$, non-parametric permutation test, FDR-corrected for multiple comparison. (D-F) Same as (A-C), but showing data separately for different cortical areas. The underlying data for Fig S3 can be found in S1 Data.*

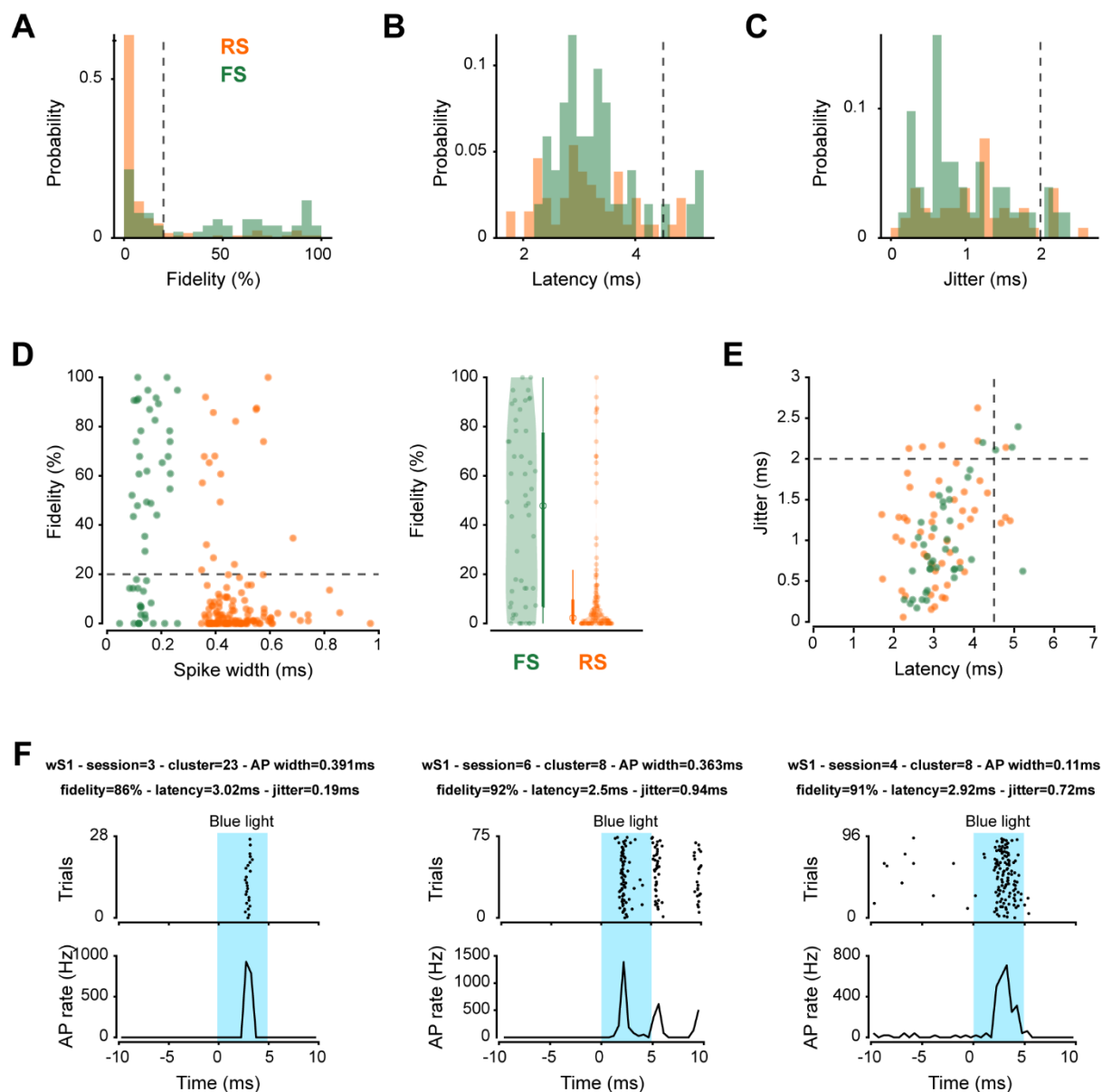


Figure 2-12 S4 Fig. Opto-tagging GABAergic neurons in VGAT-ChR2 mice.

(A-C) Criteria for labeling neurons as opto-tagged upon blue light stimulation in VGAT-ChR2 mice. Probability distribution of fidelity scores (A), first spike latency (B), and jitter (C) for RS units (orange, spike width > 0.34 ms, 130 neurons from 4 mice) and FS units (green, spike width < 0.26 ms, 51 neurons from 4 mice) measured in the first 10-ms window of blue light stimulation. The thresholds for detection of opto-tagged cells (dotted vertical lines) were defined based on previous literature and dips in the observed probability distributions (i.e. fidelity > 20%, latency < 4.5 ms, jitter < 2 ms). (D) Scatter plot of spike width versus fidelity (left) and distribution of fidelity scores shown with violin plots and bar plots (right). (E) Scatter plot of latency versus jitter of light-evoked response for RS and FS units. (F) Raster plot and peri-stimulus time histogram during the first 10-ms of 100-Hz blue light stimulation for three example opto-tagged neurons. The underlying data for Fig S4 can be found in S1 Data.

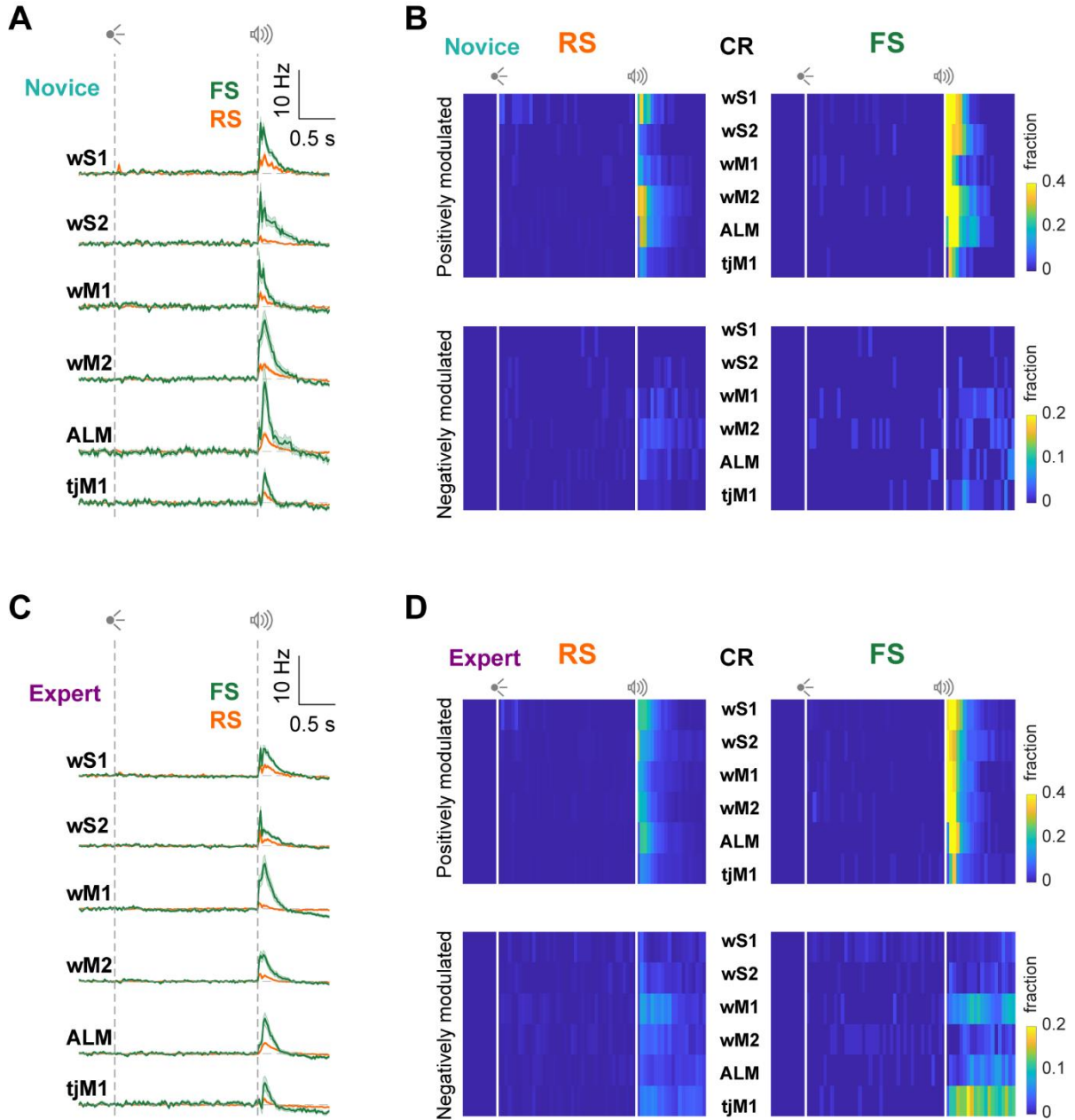


Figure 2-13 S5 Fig. FS neurons remain at baseline level during correct rejection trials.

(A) Baseline-subtracted (2 s prior to visual onset) population firing rates (mean \pm SEM) of RS and FS neurons from different regions of Novice mice are superimposed in correct rejection trials. wS1: 73 RS units in 7 mice, 103 FS units in 7 mice; wS2: 120 RS units in 8 mice, 68 FS units in 8 mice; wM1: 147 RS units in 7 mice, 66 FS units in 7 mice; wM2: 244 RS units in 7 mice, 57 FS units in 7 mice; ALM: 234 RS units in 6 mice, 37 FS units in 5 mice; tjM1: 271 RS units in 8 mice, 61 FS units in 8 mice. (B) Percentage of RS (left) and FS (right) neurons in different regions of Novice mice which are positively (top) or negatively (bottom) modulated compared to baseline (non-parametric permutation test, $p < 0.05$) in correct rejection trials. (C) Similar to (A), but for Expert mice. wS1: 258 RS units in 15 mice, 237 FS units in 15 mice; wS2: 342 RS units in 12 mice, 161 FS units in 12 mice; wM1: 452 RS units in 11 mice, 134 FS units in 11 mice; wM2: 401 RS units in 10 mice, 107 FS units in 10 mice; ALM: 766 RS units in 12 mice, 109 FS units in 12 mice; tjM1: 505 RS units in 11 mice, 83 FS units in 11 mice. (D) Similar to (B), but for Expert mice. There appears to be stronger suppression of both RS and FS neurons of tjM1 during the response window in Expert compared to Novice mice. The underlying data for Fig S5 can be found in S3 Data.

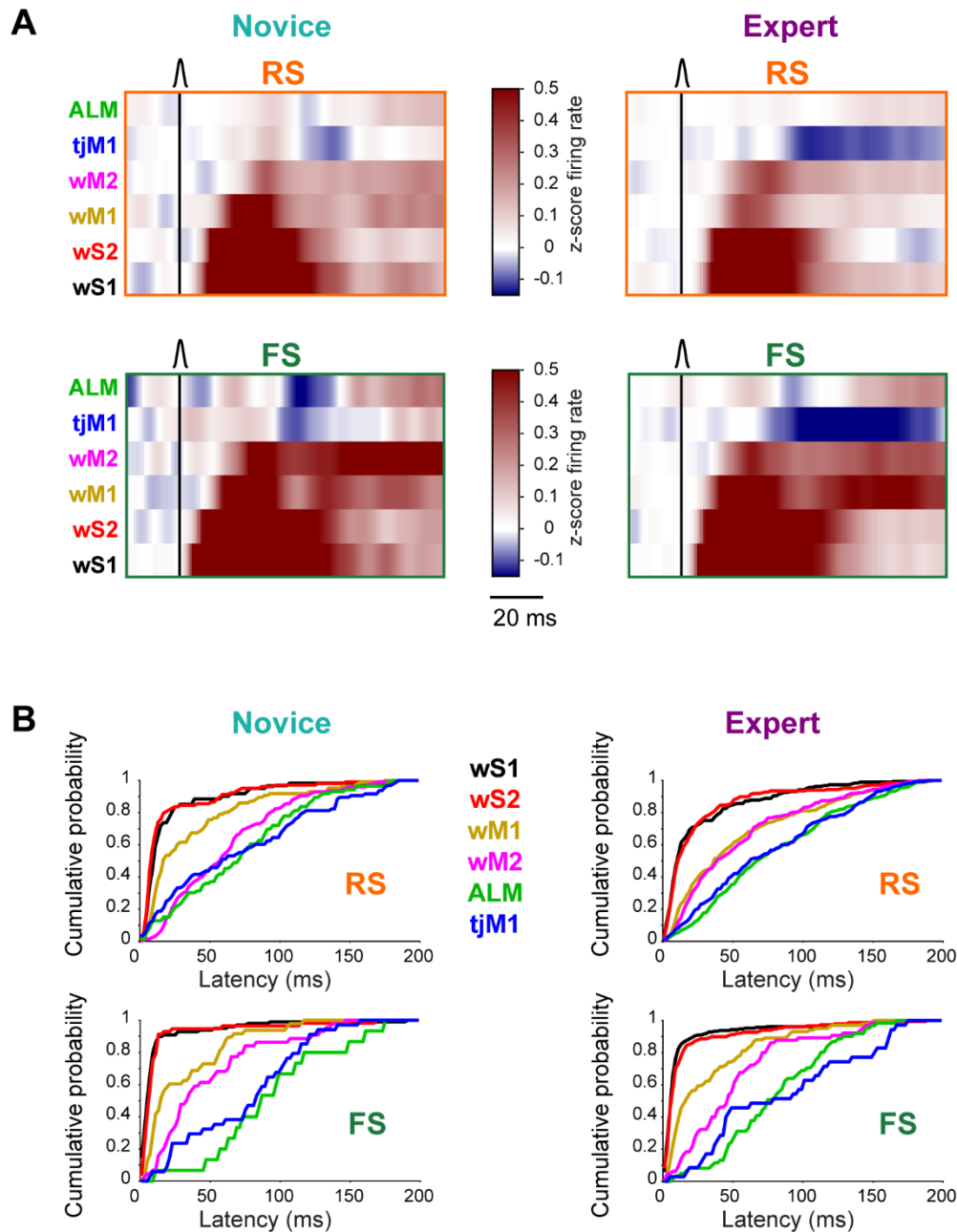


Figure 2-14 S6 Fig. Sequential activation of cortical regions upon whisker stimulation.

(A) Sequential propagation of whisker-evoked spiking responses in hit trials for RS (top) and FS (bottom) neurons from Novice (left) and Expert (right) mice. Mean z-scored firing rate in the first 100 ms window after whisker stimulus is shown. Brain regions are sorted based on their population-average onset latency in RS neurons of Expert mice. (B) Cumulative distribution of latency of individual neurons for different cortical areas in RS (top) and FS (bottom) neurons from Novice (left) and Expert (right) mice. Only neurons with significant modulation in the 200 ms window following whisker stimulus compared to a 200 ms window prior to the whisker stimulus are included ($p < 0.05$, non-parametric permutation test). Latency was defined at the half maximum (minimum for suppressed neurons) response within the 200 ms window. The underlying data for Fig S6 can be found in S4 and S5 Data.

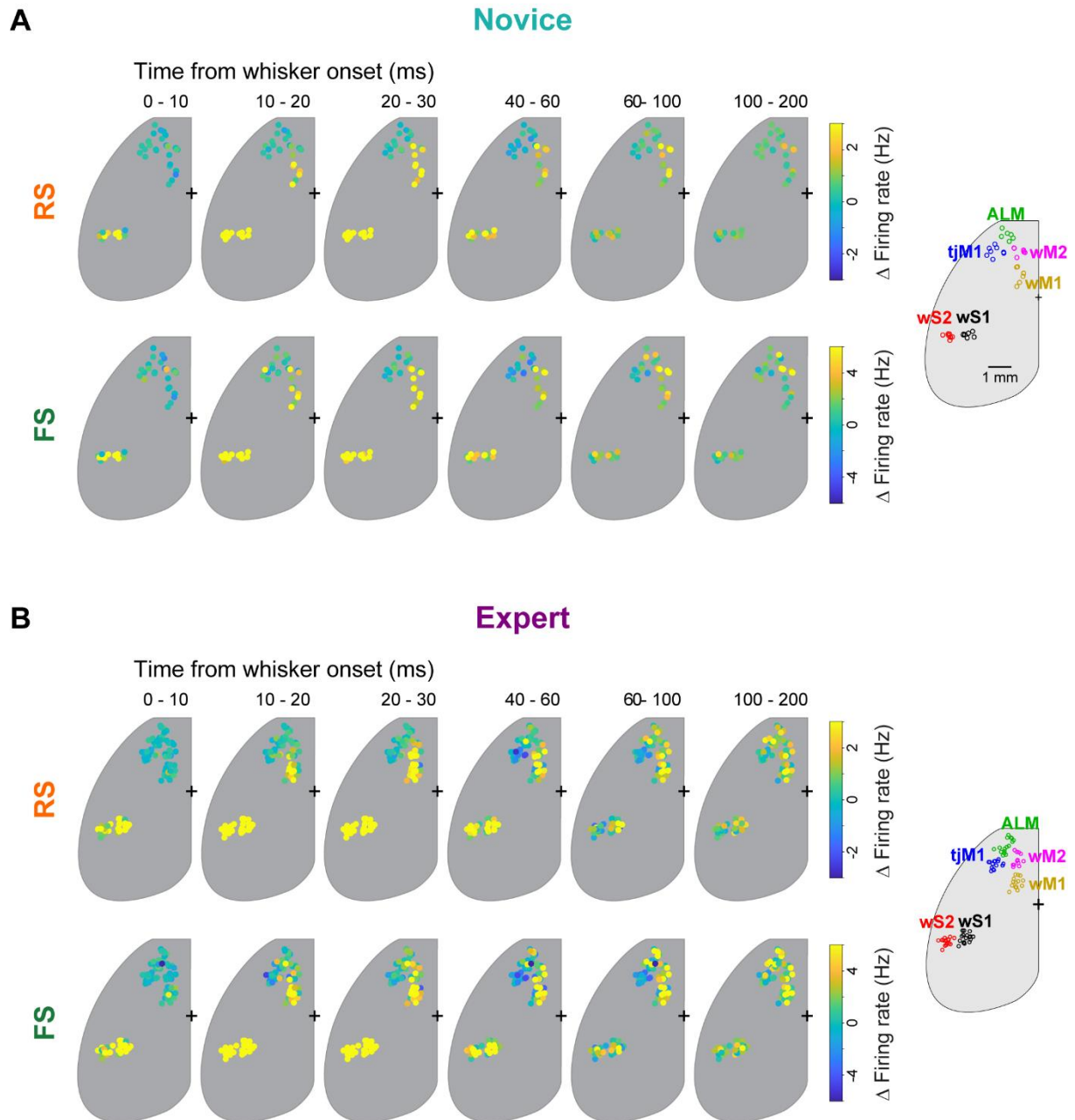


Figure 2-15 S7 Fig. Early sensory response map across different probes.

(A) Time-lapse maps of whisker-evoked firing rate in RS (top) and FS (bottom) neurons of Novice mice in hit trials. Circles represent different probes and colors show mean baseline-subtracted (50 ms before whisker onset) firing rate across each probe at different time windows. Probes from all Novice mice (43 probes in 8 mice) are superimposed. (B) Same as (A) but for Expert mice (90 probes in 18 mice). The underlying data for Fig S7 can be found in S4 and S5 Data.

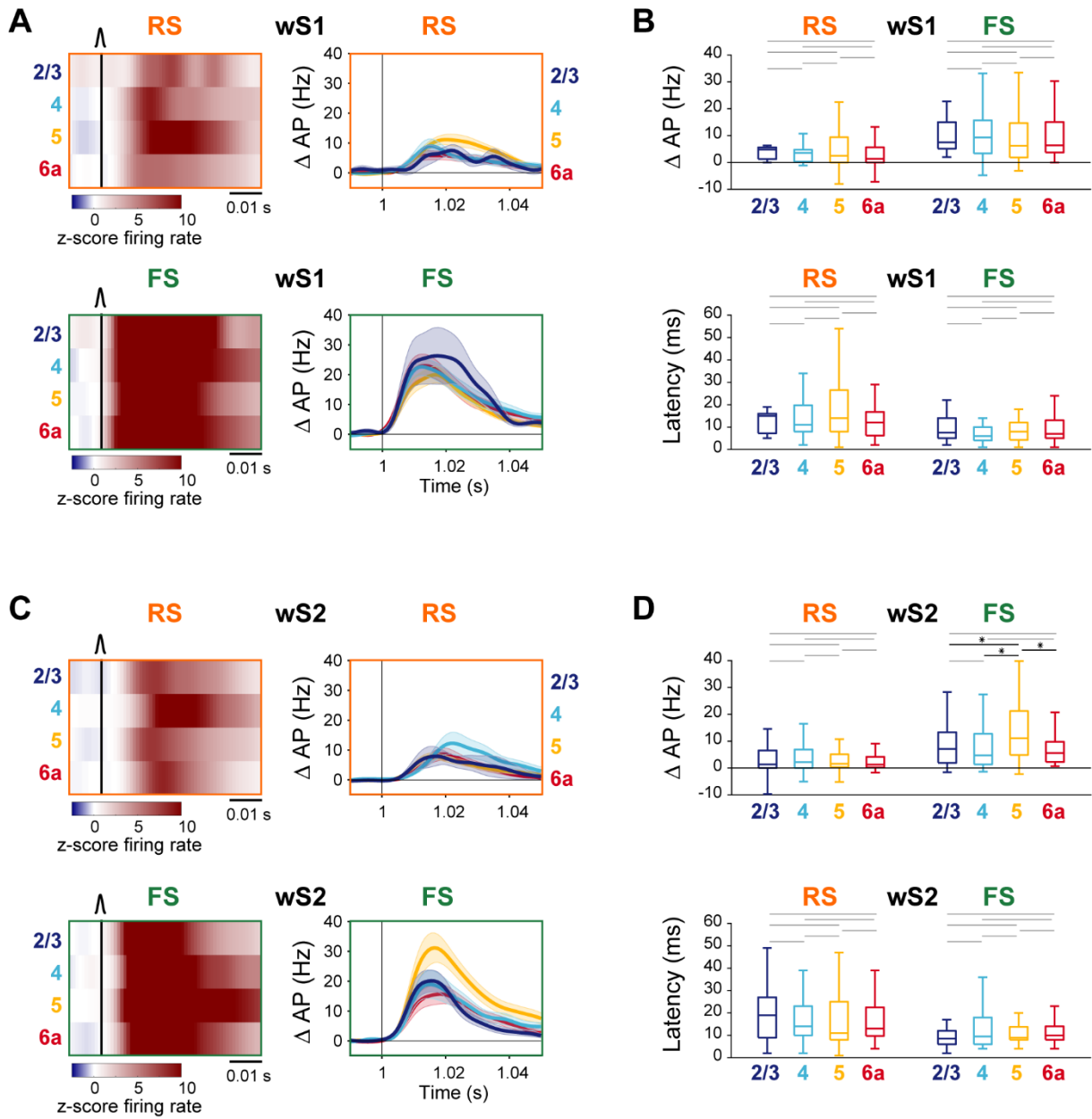


Figure 2-16 S8 Fig. Faster and larger sensory response in FS neurons across all layers of wS1 and wS2.

(A) Mean z-scored firing rate (left) and baseline-subtracted firing rate (right) of RS (top) and FS (bottom) neurons across different cortical layers of wS1. (B) Boxplots representing the distribution of firing rate change (top) and response latency (bottom) of RS and FS units in different layers of wS1. Only neurons with a significant whisker response in the first 100 ms (compared to 100 ms before whisker onset, non-parametric permutation test, $p < 0.05$) were included. Midline represents the median, bottom and top edges show the interquartile range, and whiskers extend to 1.5 times the interquartile range. *: $p < 0.05$. Gray lines show non-significant comparisons. Firing rate change was compared using non-parametric permutation test and latencies were compared using Wilcoxon rank-sum test. (C-D) Same as (A-B), but for wS2 neurons. The underlying data for Fig S8 can be found in S6 Data.

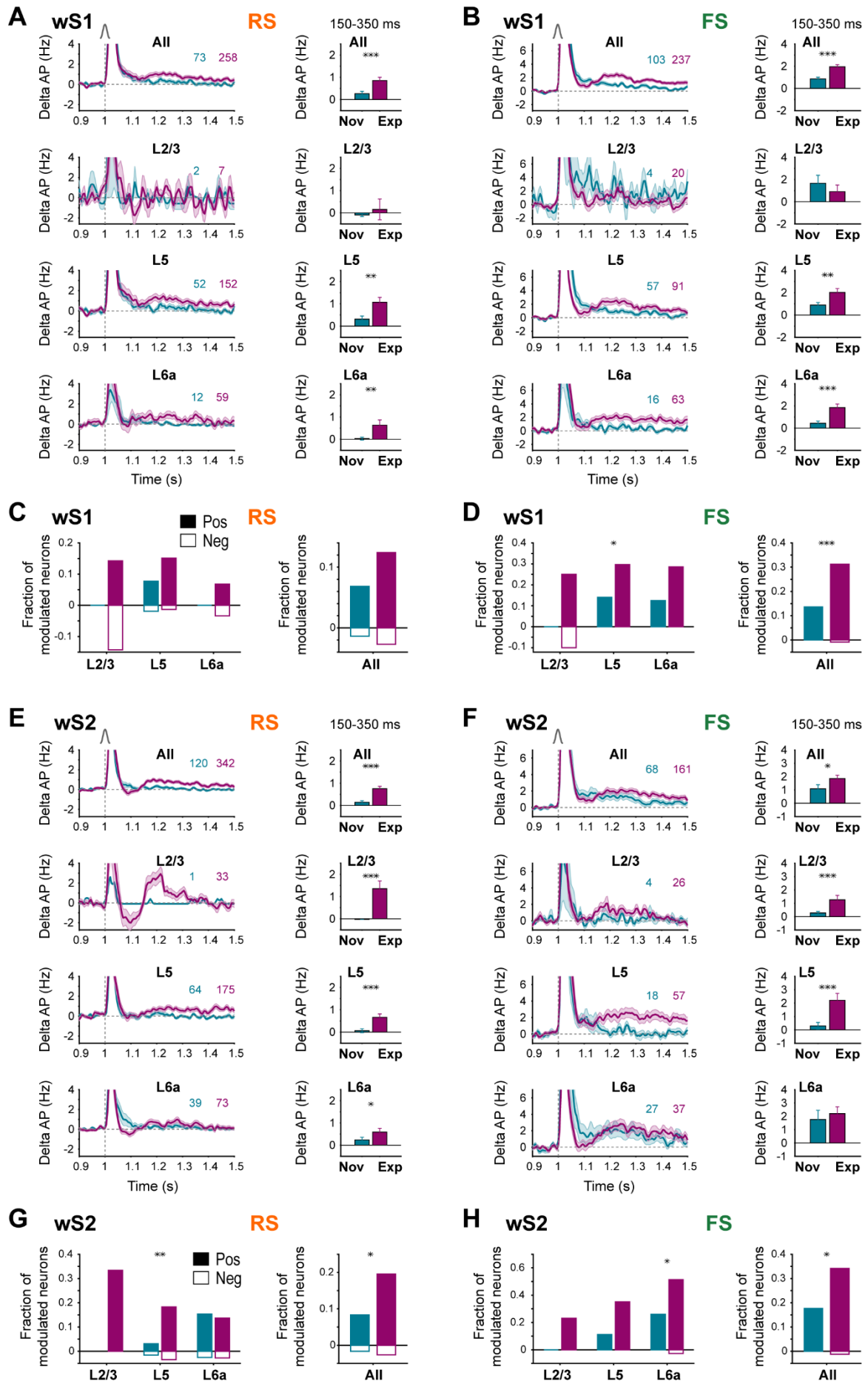


Figure 2-17 S9 Fig. Layer-specific quantification of RS and FS neuronal responses during the secondary late response in wS1 and wS2 across learning.

(A) Increase of late whisker response in wS1 RS neurons across learning. Left: baseline-subtracted (200 ms prior to whisker onset) population firing rate (mean \pm SEM) for all neurons and different cortical layers (L2/3, L5 and L6a) separately overlaid for Novice and Expert mice. The number of neurons is indicated on the figure. Right: change in average spike rate quantified in 150-350 ms window after whisker onset relative to similar window size before whisker onset. ***: $p < 0.001$, **: $p < 0.01$, *: $p < 0.05$, ns: $p \geq 0.05$, non-parametric permutation test, FDR-corrected for multiple comparison. (B) Increase of late whisker response in wS1 FS neurons across learning. Panels are similar to (A) but for wS1 FS neurons in Novice and Expert mice. (C) Fraction of wS1 RS neurons across different layers with significant positive (filled bars) or negative (empty bars) modulation late after whisker stimulus (150-350 ms window after whisker onset relative to similar window size before whisker onset). Positive or negative modulation of neurons was quantified using non-parametric permutation test ($p < 0.005$). ***: $p < 0.001$, **: $p < 0.01$, *: $p < 0.05$, ns: $p \geq 0.05$, Chi-squared proportion test. Fractions are reported for groups with more than five neurons. (D) Similar to (C) but for wS1 FS neurons. (E-H) Similar to (A-D) but for wS2. The underlying data for Fig S9 can be found in S6 Data.

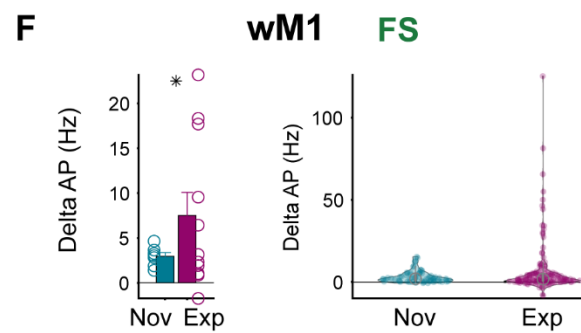
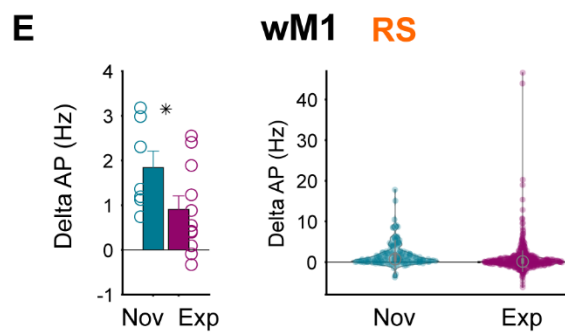
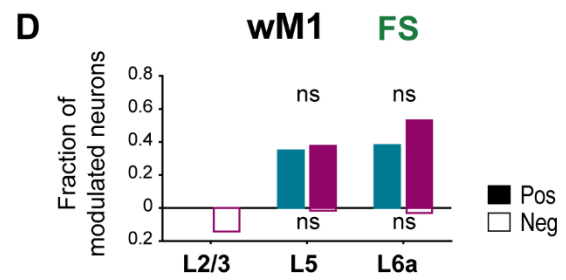
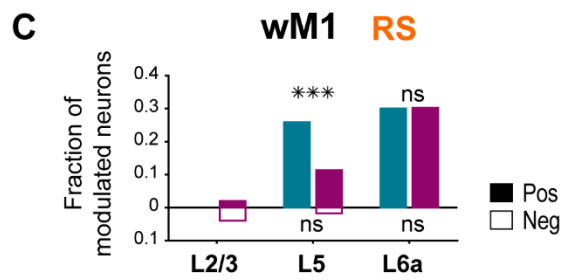
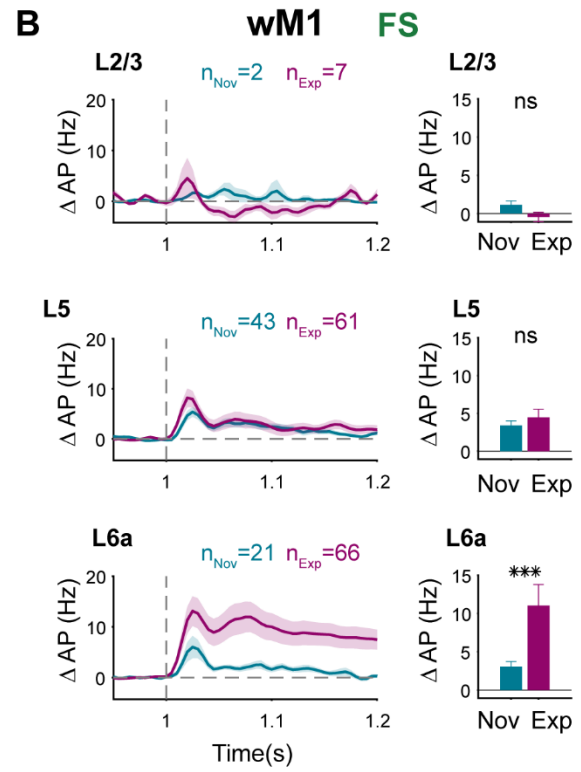
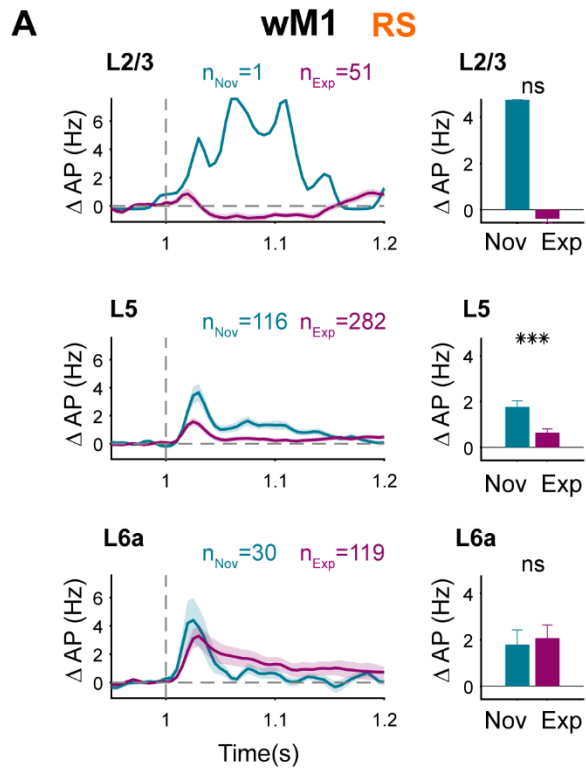


Figure 2-18 S10 Fig. Layer-specific quantification of RS and FS neurons in wM1 across learning.

(A) Decrease of early whisker response in wM1 RS neurons across learning. Left: baseline-subtracted (50 ms prior to whisker onset) population firing rate (mean \pm SEM) for different cortical layers (L2/3, L5 and L6a) overlaid for Novice (147 neurons in 7 mice) and Expert (452 neurons in 11 mice) mice. The number of neurons for each layer is indicated on the figure. Right: change in average spike rate quantified in 10-90 ms window after whisker onset relative to similar window size before whisker onset. ***: $p < 0.001$, ns: $p \geq 0.05$, non-parametric permutation test, FDR-corrected for multiple comparison. (B) Increase of whisker response in wM1 FS neurons across learning. Panels are similar to (A) but for wM1 FS neurons in Novice (66 neurons in 7 mice) and Expert (134 neurons in 11 mice) mice. (C) Fraction of wM1 RS neurons across different layers with significant positive (filled bars) or negative (empty bars) modulation early after whisker stimulus (10-90 ms window after whisker onset relative to similar window size before whisker onset). Positive or negative modulation of neurons was quantified using non-parametric permutation test ($p < 0.005$). ***: $p < 0.001$, ns: $p \geq 0.05$, Chi-squared proportion test. Fractions are reported for groups with more than five neurons. (D) Similar to (C) but wM1 FS neurons. (E) Mouse-by-mouse variability and distribution of whisker-evoked response in RS units in wM1 of Novice and Expert mice. (Left) Bar plots showing average firing rate across mice in 10-90 ms window (mean \pm SEM, 7 Novice and 11 Expert mice) after whisker onset and statistical comparison using non-parametric permutation test (*: $p < 0.05$). Circles show individual mice. (Right) Violin plots showing the distribution of whisker-evoked response in 10-90 ms window for all neurons recorded in Novice (147 neurons in 7 mice) and Expert mice (452 neurons in 11 mice). (F) Same as (E) but for wM1 FS units in Novice (66 neurons in 7 mice) and Expert mice (134 neurons in 11 mice). The underlying data for Fig S10 can be found in S8 Data.

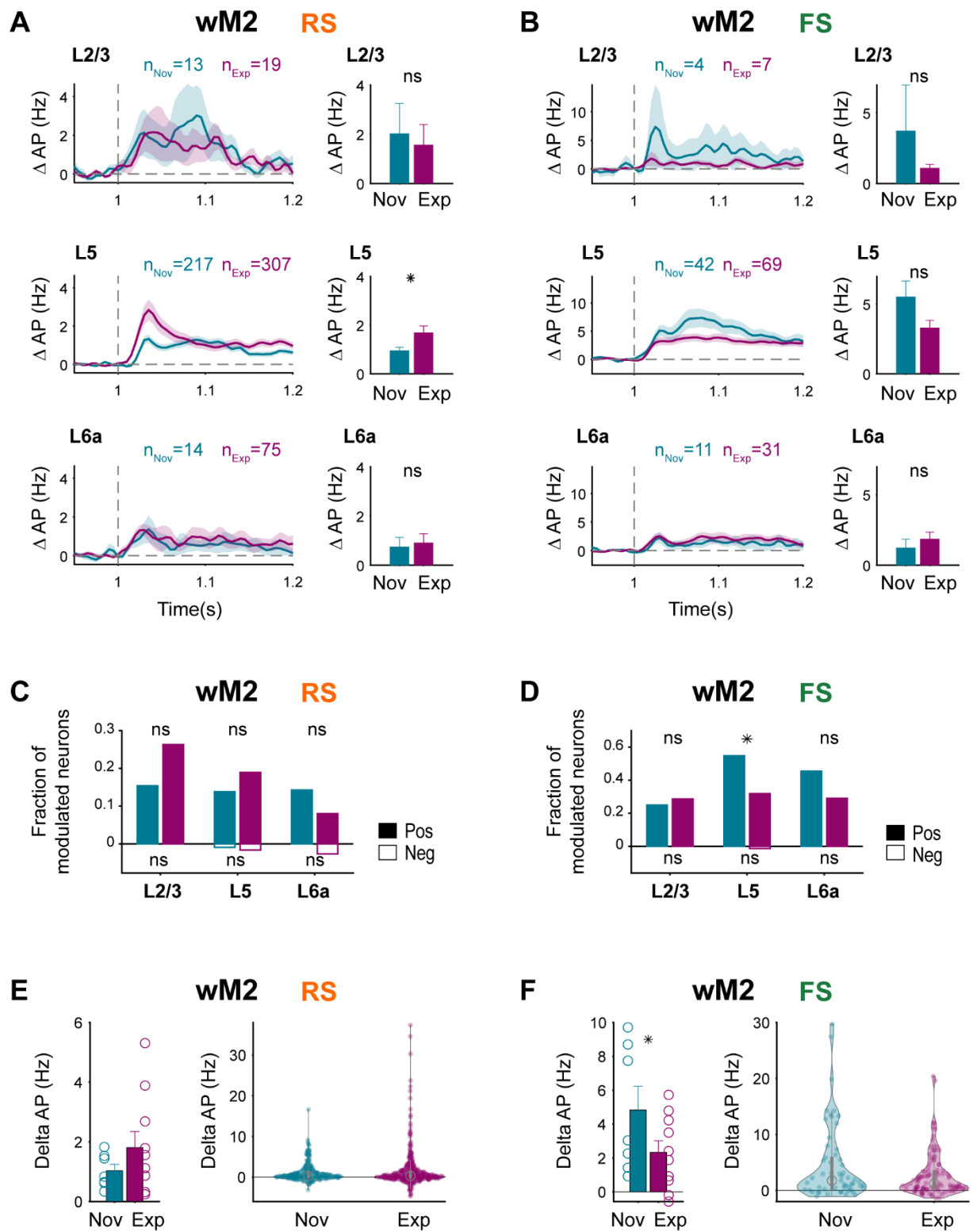


Figure 2-19 S11 Fig. Layer-specific quantification of RS and FS neuronal activity in wM2 across learning.

(A) Increase of early whisker response in wM2 RS neurons across learning. Left: baseline-subtracted (50 ms prior to whisker onset) population firing rate (mean \pm SEM) for different cortical layers (L2/3, L5 and L6a) overlaid for Novice mice (244 neurons in 7 mice) and Expert mice (401 neurons in 11 mice). The number of neurons for each layer is indicated on the figure. Right: change in average spike rate quantified in 10-90 ms window after whisker onset relative to similar window size before whisker onset. *: $p < 0.05$, ns: $p \geq 0.05$, non-parametric permutation test, FDR-corrected for multiple comparison. (B) Decrease of whisker response in wM2 FS neurons across learning. Panels are similar to (A) but for wM2 FS neurons in Novice mice (57 neurons in 7 mice) and Expert mice (107 neurons in 10 mice). (C) Fraction of wM2 RS neurons across different layers with significant positive (filled bars) or negative (empty bars) modulation early after whisker stimulus (10-90 ms window after whisker onset relative to similar window size before whisker onset). Positive or negative modulation of neurons was quantified using non-parametric permutation test ($p < 0.005$). *: $p < 0.05$, ns: $p \geq 0.05$, Chi-squared proportion test. Fractions are reported for groups with more than five neurons. (D) Similar to (C) but wM2 FS neurons. (E) Mouse-by-mouse variability and distribution of whisker-evoked response in RS units in wM2 of Novice and Expert mice. (Left) Bar plot showing average firing rate across mice in 10-90 ms window (mean \pm SEM, 7 Novice and 10 Expert mice) after whisker onset and statistical comparison using non-parametric permutation test (*: $p < 0.05$). Circles show individual mice. (Right) Violin plots showing the distribution of whisker-evoked response in 10-90 ms window for all neurons recorded in Novice (244 neurons in 7 mice) and Expert mice (401 neurons in 10 mice). (F) Same as (E) but for wM2 FS units in Novice (57 neurons in 7 mice) and Expert mice (107 neurons in 10 mice). The underlying data for Fig S11 can be found in S8 Data.

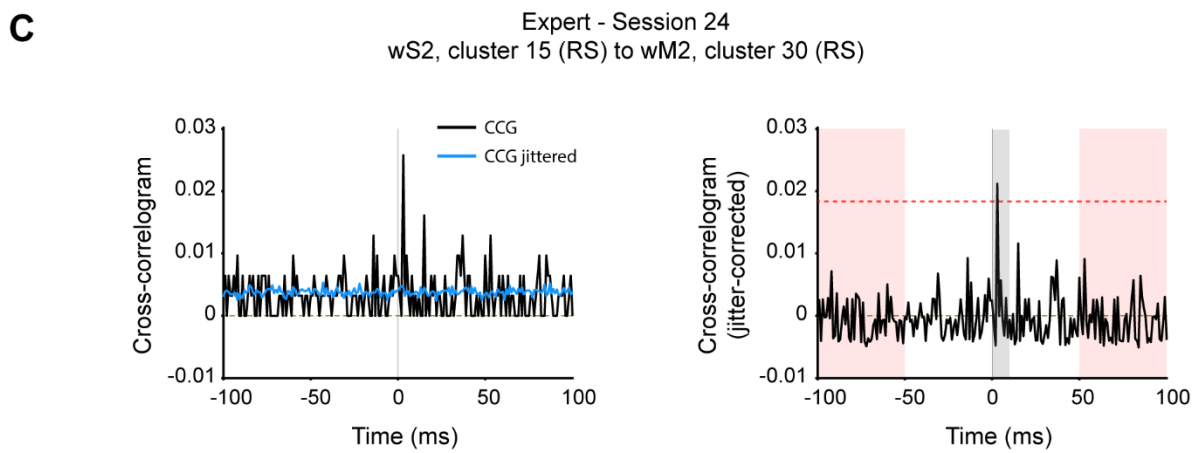
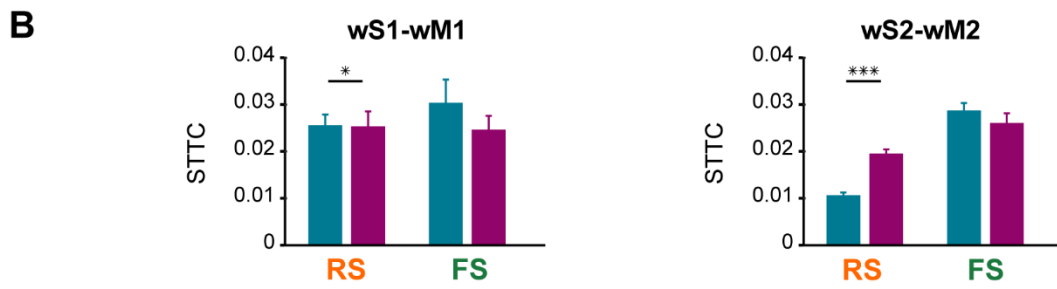
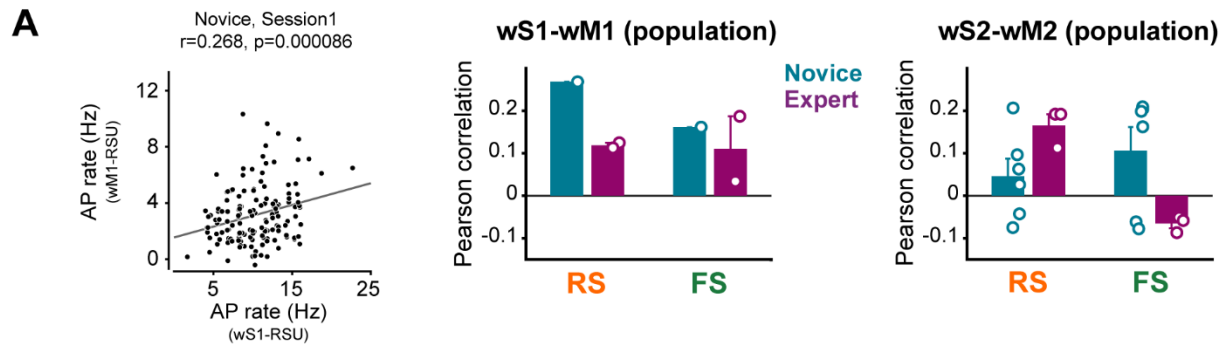


Figure 2-20 S12 Fig. Inter-areal functional connectivity.

(A) Inter-areal correlation of population response in Novice and Expert mice. (Left) Scatter plot of trial-by-trial average population response between wS1-RS units and wM1-RS units for an example Novice session. Circles were jittered slightly for the purpose of visualization. Gray line: least-squares regression. (Middle) Pearson correlation of trial-by-trial average population response of wS1-RS units vs wM1-RS, and wS1-RS units vs wM1-FS units (1 Novice and 2 Expert mice). (Right) Pearson correlation of trial-by-trial population average response of wS2-RS units vs wM2-RS, and wS2-RS units vs wM2-FS units (6 Novice and 3 Expert mice). Circles show individual sessions. Error bars: SEM. (B) Pair-wise correlation between sensory and motor cortices in Novice and Expert mice using the spike time tiling coefficient (STTC) method. Left: Average pair-wise STTC correlation of wS1-RS units with wM1-RS (308 neuron pairs in 1 Novice mouse, and 398 neuron pairs in 2 Expert mice) and wS1-RS units with wM1-FS units (112 neuron pairs in 1 Novice mouse, and 139 neuron pairs in 2 Expert mice) separately. Right: Average pair-wise Pearson correlation of wS2-RS units with wM2-RS (3482 neuron pairs in 6 Novice mouse, and 2461 neuron pairs in 3 Expert mice) and wS2-RS units with wM2-FS units (821 neuron pairs in 6 Novice mouse, and 532 neuron pairs in 3 Expert mice). Error bars: SEM. Statistical comparison between Novice and Expert was performed using Wilcoxon rank-sum test (ns: $p \geq 0.05$; *: $p < 0.05$; ***: $p < 0.001$). (C) Example cross-correlogram (CCG) from pair of neurons recorded simultaneously in wS2 and wM2 of an Expert mouse with a significant connection; same example pair as shown in Figure 6F, but with CCG from -100 to 100 ms time lags. Jitter correction method (left), and detection of significant functional connections (right). Significant connections were detected if any threshold crossing happened within 0 to 10 ms time lags (gray bar) of the jitter-corrected CCG. Threshold (red dotted line) was defined as 6-fold standard deviation of the jitter-corrected CCG flanks (red bars). The underlying data for Fig S12 can be found in S8 Data.

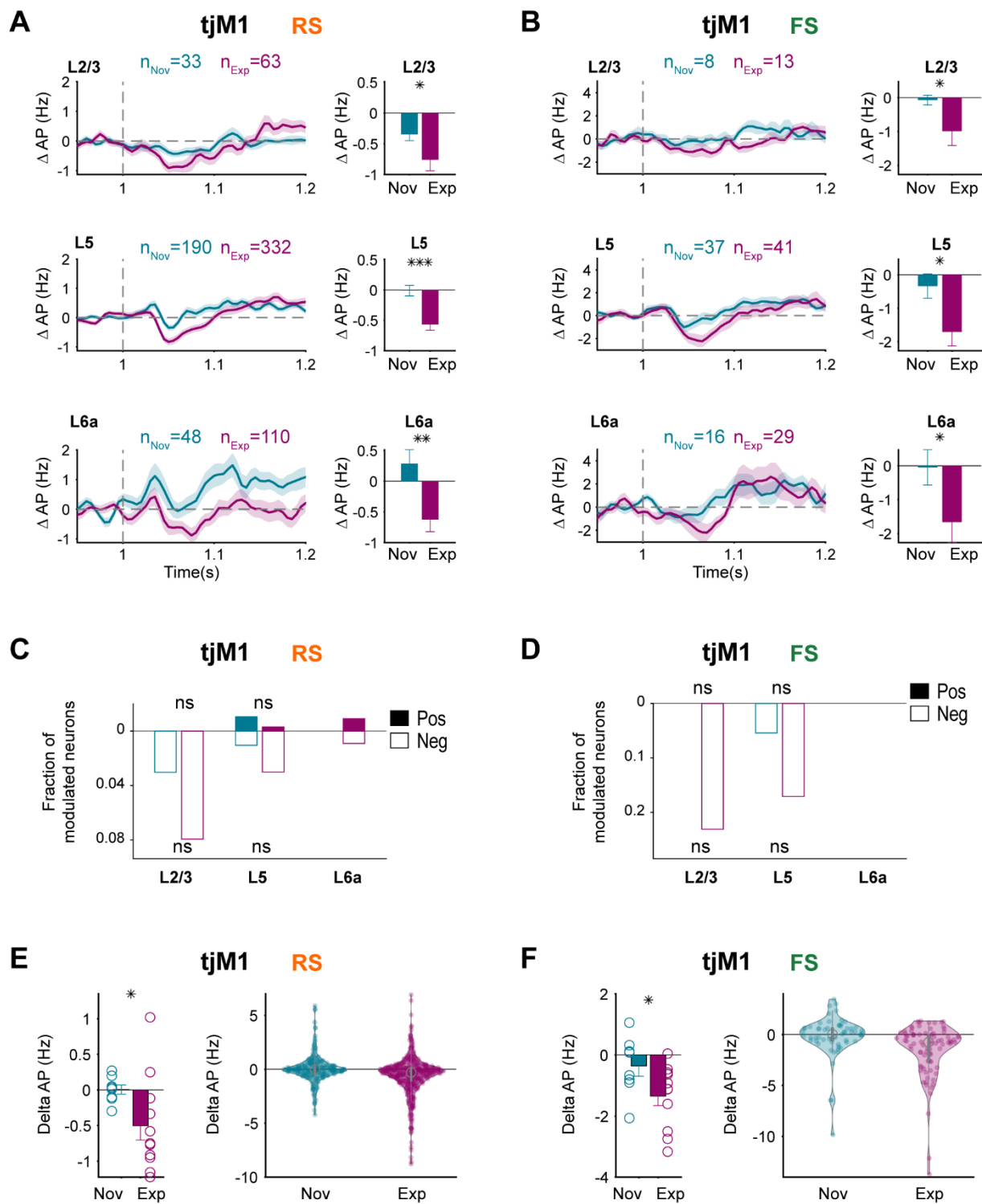


Figure 2-21 S13 Fig. Layer-specific quantification of RS and FS neurons in tjM1 across learning.

(A) Suppression of activity in tjM1 RS neurons across learning. Left: baseline-subtracted (50 ms prior to whisker onset) population firing rate (mean \pm SEM) for different cortical layers (L2/3, L5 and L6a) overlaid for Novice mice (271 neurons in 8 mice) and Expert mice (505 neurons in 11 mice). The number of neurons for each layer is indicated on the figure. Right: change in average spike rate quantified in 40-90 ms window after whisker onset relative to similar window size before whisker onset. ***: $p < 0.001$, **: $p < 0.01$, *: $p < 0.05$, non-parametric permutation test, FDR-corrected for multiple comparison. (B) Suppression of activity in tjM1 FS neurons across learning. Panels are similar to (A) but for tjM1 FS neurons in Novice mice (61 neurons in 8 mice) and Expert mice (83 neurons in 11 mice). (C) Fraction of tjM1 RS neurons across different layers with significant positive (filled bars) or negative (empty bars) modulation early after whisker stimulus (40-90 ms window after whisker onset relative to similar window size before whisker onset). Positive or negative modulation of neurons was quantified using non-parametric permutation test ($p < 0.005$). ns: $p \geq 0.05$, Chi-squared proportion test. Fractions are reported for groups with more than five neurons. (D) Similar to (C) but tjM1 FS neurons. (E) Mouse-by-mouse variability and distribution of whisker-evoked response in RS units in tjM1 of Novice and Expert mice. (Left) Bar plots showing average firing rate across mice in 40-90 ms window (mean \pm SEM, 8 Novice and 11 Expert mice) after whisker onset and statistical comparison using non-parametric permutation test (*: $p < 0.05$). Circles show individual mice. (Right) Violin plots showing the distribution of whisker-evoked response in 40-90 ms window for all neurons recorded in Novice (271 neurons in 8 mice) and Expert mice (505 neurons in 11 mice). (F) Same as (E) but for tjM1 FS units in Novice (61 neurons in 7 mice) and Expert mice (83 neurons in 11 mice). The underlying data for Fig S13 can be found in S9 Data.

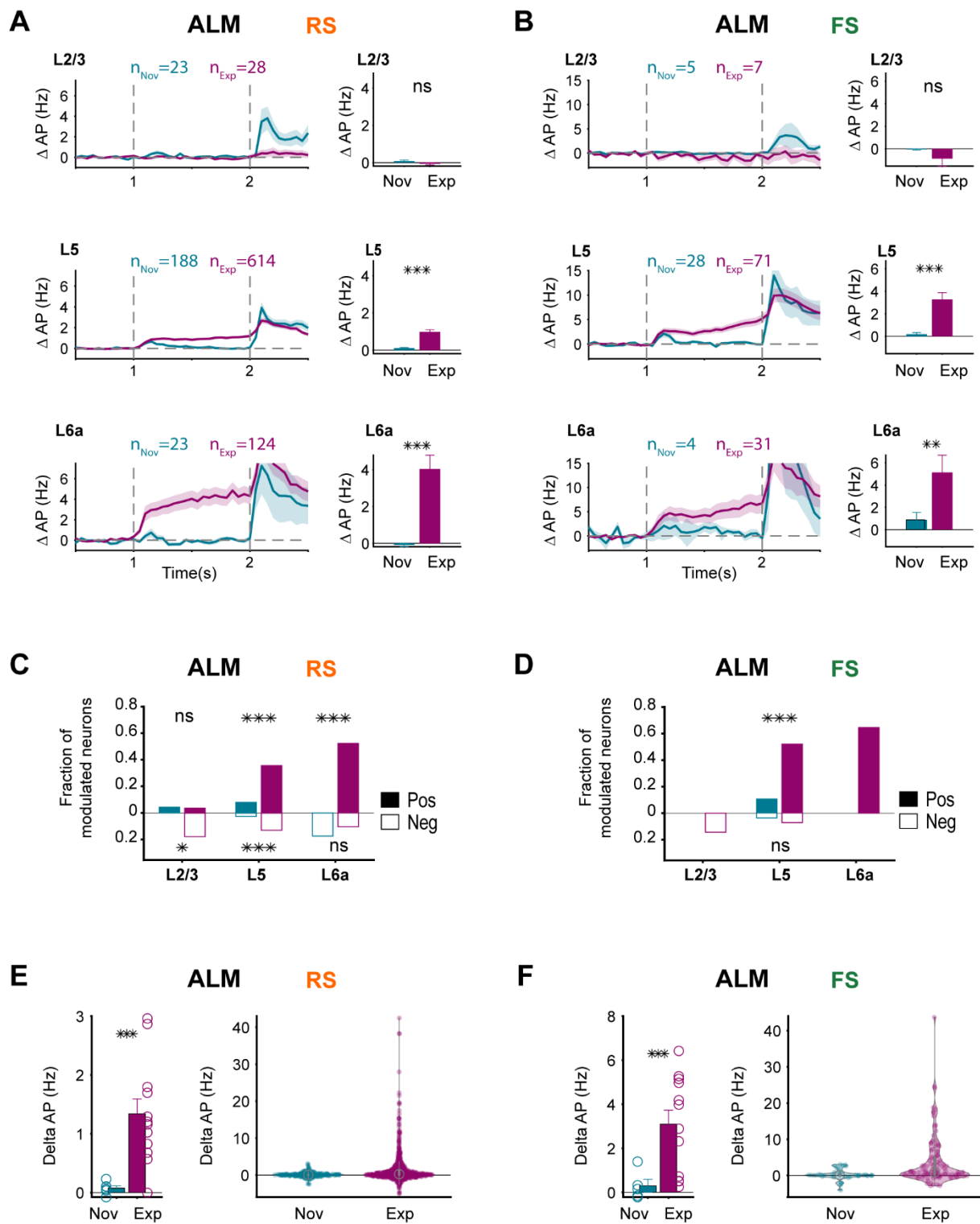


Figure 2-23 S15 Fig. Layer-specific quantification of RS and FS neuronal activity in ALM.

(A) Delay activity in ALM RS neurons upon learning. Left: baseline-subtracted (1 s prior to whisker onset) population firing rate (mean \pm SEM) for different cortical layers (L2/3, L5 and L6a) overlaid for Novice mice (234 neurons in 6 mice) and Expert mice (766 neurons in 12 mice). The number of neurons for each layer is indicated on the figure. Right: change in average spike rate quantified in 200-1000 ms window after whisker onset relative to similar window size before whisker onset. ***: $p < 0.001$, **: $p < 0.01$, ns: $p \geq 0.05$, non-parametric permutation test, FDR-corrected for multiple comparison. (B) Delay activity in ALM FS neurons upon learning. Panels are similar to (A) but for ALM FS neurons in Novice mice (37 neurons in 5 mice) and Expert mice (109 neurons in 12 mice). (C) Fraction of ALM RS neurons across different layers with significant positive (filled bars) or negative (empty bars) modulation during delay period (200-1000 ms window after whisker onset relative to similar window size before whisker onset). Positive or negative modulation of neurons was quantified using non-parametric permutation test ($p < 0.005$). ***: $p < 0.001$, *: $p < 0.05$, ns: $p \geq 0.05$, Chi-squared proportion test. Fractions are reported for groups with more than five neurons. (D) Similar to (C) but for ALM FS neurons. (E) Mouse-by-mouse variability and distribution of delay activity of RS units in ALM of Novice and Expert mice. (Left) Bar plots showing average firing rate across mice in 200-1000 ms window (mean \pm SEM, 6 Novice and 12 Expert mice) after whisker onset and statistical comparison using non-parametric permutation test (*: $p < 0.05$). Circles show individual mice. (Right) Violin plots showing the distribution of delay activity in 200-1000 ms window for all neurons recorded in Novice (234 neurons in 6 mice) and Expert mice (766 neurons in 12 mice). (F) Same as (E) but for ALM FS units in Novice (37 neurons in 5 mice) and Expert mice (109 neurons in 12 mice). The underlying data for Fig S15 can be found in S9 Data.

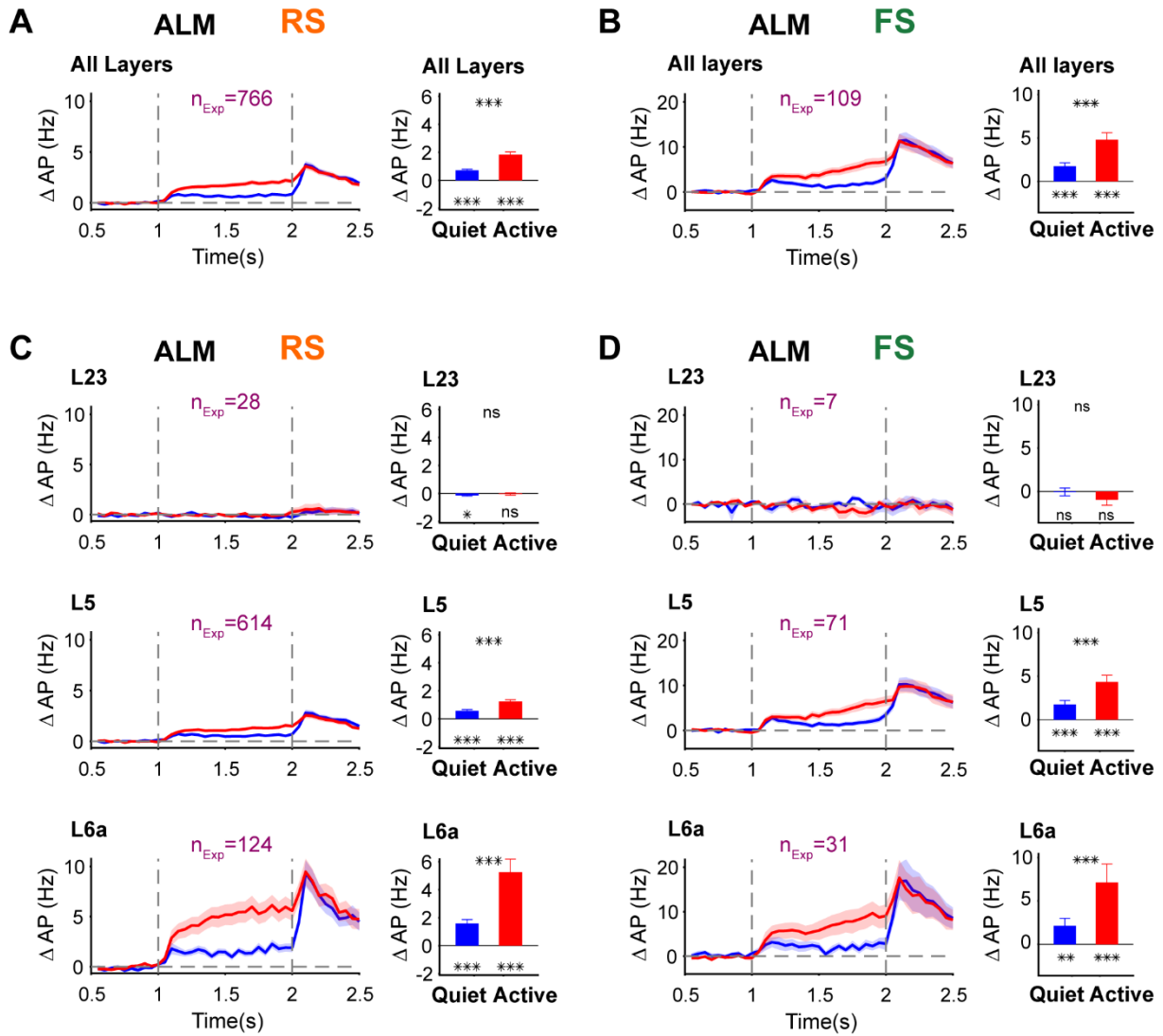


Figure 2-24 S16 Fig. Preparatory neuronal activity in ALM is decreased, but remains significant in quiet trials devoid of movements.

(A) Larger delay period activity of ALM RS neurons in Active vs Quiet hit trials. Left: baseline-subtracted (1 s prior to whisker onset) population firing rate (mean \pm SEM) overlaid for Quiet (blue) and Active (red) hit trials in Expert mice (766 RS units in 12 mice). Right: change in average spike rate quantified in 200-1000 ms window after whisker onset relative to a 1-s window prior to whisker onset. ***: $p < 0.001$, non-parametric permutation test. Asterisks below the bars represent the p value for comparing delay activity in each trial type compared to baseline, while asterisks above the bars represent the p value of the comparison between delay activity in Quiet and Active hit trials. (B) Similar to (A) but for FS neurons (109 FS units in 12 mice). (C) Similar to (A) but separately for RS neurons of different cortical layers. The number of neurons for each layer is indicated on the figure. ***: $p < 0.001$, ns: $p \geq 0.05$, non-parametric permutation test, FDR-corrected for multiple comparison. (D) Similar to (C) but for FS neurons. The underlying data for Fig S16 can be found in S9 Data.

Chapter 3 Axonal and dendritic morphology of excitatory neurons in layer 2/3 mouse barrel cortex imaged through whole-brain tomography and registered to digital brain atlas

Text and figures under this chapter is obtained from the following manuscript.

Axonal and dendritic morphology of excitatory neurons in layer 2/3 mouse barrel cortex imaged through whole-brain tomography and registered to digital brain atlas.

Yanqi Liu⁼¹, Georgios Foustoukos⁼¹, Sylvain Crochet, Carl C H Petersen.

⁼¹, these authors contributed equally to the manuscript.

Frontiers in Neuroanatomy. 2022 Jan 25; 15:791015. doi: 10.3389/fnana.2021.791015.

As the first co-author I contributed to the manuscript significantly throughout all steps involved. I completed most of the experiments in sample preparation, obtained images using the custom microscope built by the joint co-author. Together with the joint co-author, we developed pipelines to process acquired image tiles. I was responsible for axonal tracing for all the sample involved. I also established data analysis pipeline for image registration and axon quantification with helpful discussions from the joint co-author. Finally, I contributed preparations of text and figures for this manuscript.

3.1 Abstract

Communication between cortical areas contributes importantly to sensory perception and cognition. On the millisecond time-scale, information is signaled from one brain area to another by action potentials propagating across long-range axonal arborizations. Here, we develop and test methodology for imaging and annotating the brain-wide axonal arborizations of individual excitatory layer 2/3 neurons in mouse barrel cortex through single-cell electroporation and two-photon serial section tomography followed by registration to a digital brain atlas. Each neuron had extensive local axon within the barrel cortex. In addition, individual neurons innervated subsets of: secondary somatosensory cortex; primary somatosensory cortex for upper limb, trunk and lower limb; primary and secondary motor cortex; visual and auditory cortical regions; dorsolateral striatum; and various fiber bundles. In the future, it will be important to assess if the diversity of axonal projections across individual layer 2/3 mouse barrel cortex neurons is accompanied by functional differences in their activity patterns.

3.2 Introduction

On the millisecond timescale, neurons communicate primarily by releasing neurotransmitter from presynaptic specializations along their axons in response to action

potential firing, with the increased concentration of neurotransmitter acting to open ligand-gated ion channels largely concentrated in postsynaptic specializations on dendrites. In order for any two neurons to be synaptically connected it is essential that the axon of the presynaptic neuron is in close apposition to the dendrite of the postsynaptic neuron. Reconstructing the axon and dendrites of individual neurons therefore provides important information about where they might send and receive signals (Cajal 1995). Whereas dendrites have relatively large diameters and are typically confined to a small region near the cell body of the neuron, axons have smaller diameters and can project long distances across the brain, spinal cord and other parts of the body posing important challenges for their accurate characterization. Here, building on technical advances in single-cell anatomy developed in previous studies (Yamashita et al. 2013; 2018a; Economo et al. 2016; Han et al. 2018b; Winnubst et al. 2019; Peng et al. 2021), we further test procedures for whole-brain imaging, reconstruction, registration and quantification of the axonal and dendritic structure of single labelled neurons in layer 2/3 of mouse barrel cortex.

The barrel cortex is a highly-specialized brain area serving as the primary whisker somatosensory cortex (wS1, also labeled SSp-bfd) for processing sensory information from the array of mystacial vibrissae (Brecht 2007; Diamond et al. 2008; Petersen 2019b; Staiger and Petersen 2021). Each whisker on the snout is mapped onto an anatomically-identifiable structure in layer 4 of wS1, known as a barrel, arranged somatotopically across the horizontal extent of wS1 (Woolsey and Van der Loos 1970), helping with precise structure-function analyses. Bulk anterograde labelling of long-range axonal projections of neurons with cell bodies located in barrel cortex has revealed that they project to a large number of cortical and subcortical brain areas including: secondary whisker somatosensory cortex (wS2, a part of SSs), whisker motor cortex (wM1/2, a part of MOp and MOs), perirhinal cortex, orbitofrontal cortex, secondary visual cortex, posterior parietal cortex, satellite cortical regions around wS1 including the dysgranular zone, contralateral cortex, different thalamic nuclei (VPM, higher-order posterior medial nucleus, and thalamic reticular nucleus), zona incerta, dorsolateral striatum, superior colliculus, anterior pretectal nucleus, pons, hypothalamus and trigeminal nuclei (White and DeAmicis 1977; Welker, Hoogland, and Van der Loos 1988; Aronoff et al. 2010; Matyas et al. 2010; Mao et al. 2011; Sreenivasan et al. 2015; C. Guo et al. 2017; Sumser et al. 2017; Yamashita et al. 2018). Individual neurons appear to largely innervate only subsets of these targets, but the full extent of the anatomical diversity of long-range projection neurons in mouse wS1 is currently unknown. The local axonal arborizations within the barrel field of excitatory neurons with somata in wS1 has been characterized extensively (Schubert et al. 2001; 2006; Feldmeyer, Lübke, and Sakmann 2006; Frick et al. 2008; Oberlaender et al. 2011; Feldmeyer 2012b; Narayanan et al. 2015; Staiger et al. 2015; Rojas-Piloni et al. 2017; Egger et al. 2020). A previous study reported the long-range axonal projections of infragranular pyramidal neurons, finding diverse corticofugal innervation patterns (C. Guo et al. 2017). Furthermore, sparse brain-wide labelling and imaging of genetically-defined neuronal populations revealed the morphology of various neurons in primary somatosensory cortex, including some in the barrel field (Peng et al. 2021). Previous single-cell reconstruction studies targeted specifically to excitatory projection neurons in layer 2/3 of mouse wS1 have differentiated between two selected subsets depending upon retrograde labelling from wS2 and wM1 (Yamashita et al. 2013; 2018), allowing correlation with functional studies, which indicated interesting projection-specific differences in sensorimotor processing (J. L. Chen et al. 2013; 2015; Yamashita et al. 2013; Kwon et al. 2016; Yamashita and Petersen 2016;

Vavladeli et al. 2020). Here, in this study, we sampled layer 2/3 mouse barrel cortex neurons without pre-labelling of their long-range projections, and we made three important methodological advances over our previous work towards quantitatively studying their anatomy: i) we imaged entire mouse brains using two-photon serial section tomography; ii) we registered our data to a standardized digital atlas of the mouse brain; and iii) we quantified axonal length in the context of brain areas annotated in the digital atlas. Through these technical advances, we have begun to further characterize the diversity of the axonal projections of individual layer 2/3 neurons in mouse barrel cortex, adding to the important body of previous knowledge about the single-cell anatomy of excitatory projection neurons in the superficial layers of rodent primary whisker somatosensory cortex (Feldmeyer, Lübke, and Sakmann 2006; Lübke and Feldmeyer 2007; Yamashita et al. 2018a; Egger et al. 2020; Peng et al. 2021a; Staiger and Petersen 2021). However, immunohistochemical labeling of processed tissue also pointed to important technical limitations indicating that our methodology revealed incomplete axonal arborizations.

3.3 Results

3.3.1 Reconstruction of dendrites and axons of single neurons in layer 2/3 barrel cortex

In order to reconstruct neuronal arborizations of single neurons in layer 2/3 of the primary somatosensory cortex barrel field (SSp-bfd), we performed “shadow” single-cell electroporation *in vivo* under the guidance of a two-photon microscope (Judkewitz et al. 2009) (Figure 3-1 Acquisition and analysis pipeline for single cell reconstruction. Figure 3-1A and B). A glass pipette filled with intracellular solution, fluorescent dye and GFP DNA plasmids was inserted through a craniotomy into layer 2/3 of the SSp-bfd and positioned in close contact to the cell membrane of a randomly chosen cell in our field-of-view (Figure 3-1B). Afterwards, a train of negative electrical pulses was delivered in order to transiently rupture the cell’s membrane, permitting the entrance of the pipette solution into the cell’s cytoplasm. If the electroporation procedure was successful, the cell was immediately filled with the fluorescent dye and remained intact after pipette retraction. After 3-5 days, a quality check of the cell’s health and the expression levels of GFP was performed under the two-photon microscope through a cranial window (Figure 3-1C). If only a single neuron per mouse expressed GFP and it did not show any signs of dendritic ‘blebbing’ or cell death (Batista Napotnik, Polajžer, and Miklavčič 2021), the animal was transcardially perfused with PFA in order to fix the brain. Subsequently the extracted brain was partially cleared using mCUBIC (Susaki et al. 2015) and prepared for two-photon serial section tomographic 3D imaging (Han et al. 2018) (Figure 3-1D). After imaging the whole brain, individual tiles were computationally stitched to reassemble full brain slices which were then imported into Vaa3D software for semi-automatic annotation of the neuronal structures, based on the GFP fluorescence signal (Figure 3-1 D and E). Following annotation, the tomographic structural images were used for registration to the Allen Mouse Brain Common Coordinate Framework (CCF). Once this step was completed, the location of the different neuronal arborizations in various brain areas was assessed for each of the 10 reconstructed neurons in this study, using the Allen Mouse Brain standardized parcellations (Figure 3-1F, Figure 3-9 and Supplementary Table 1).

Importantly, we do not think that our anatomical reconstructions are complete because anti-GFP immunolabelling to enhance the signal-to-noise ratio of axonal fluorescence

revealed additional axon not found through two-photon tomography (Supplementary Figure 2). The anatomical reconstructions presented in this study therefore only reveal a portion of the full extent of the axons, but nonetheless provide important information characterizing their apparent diversity.

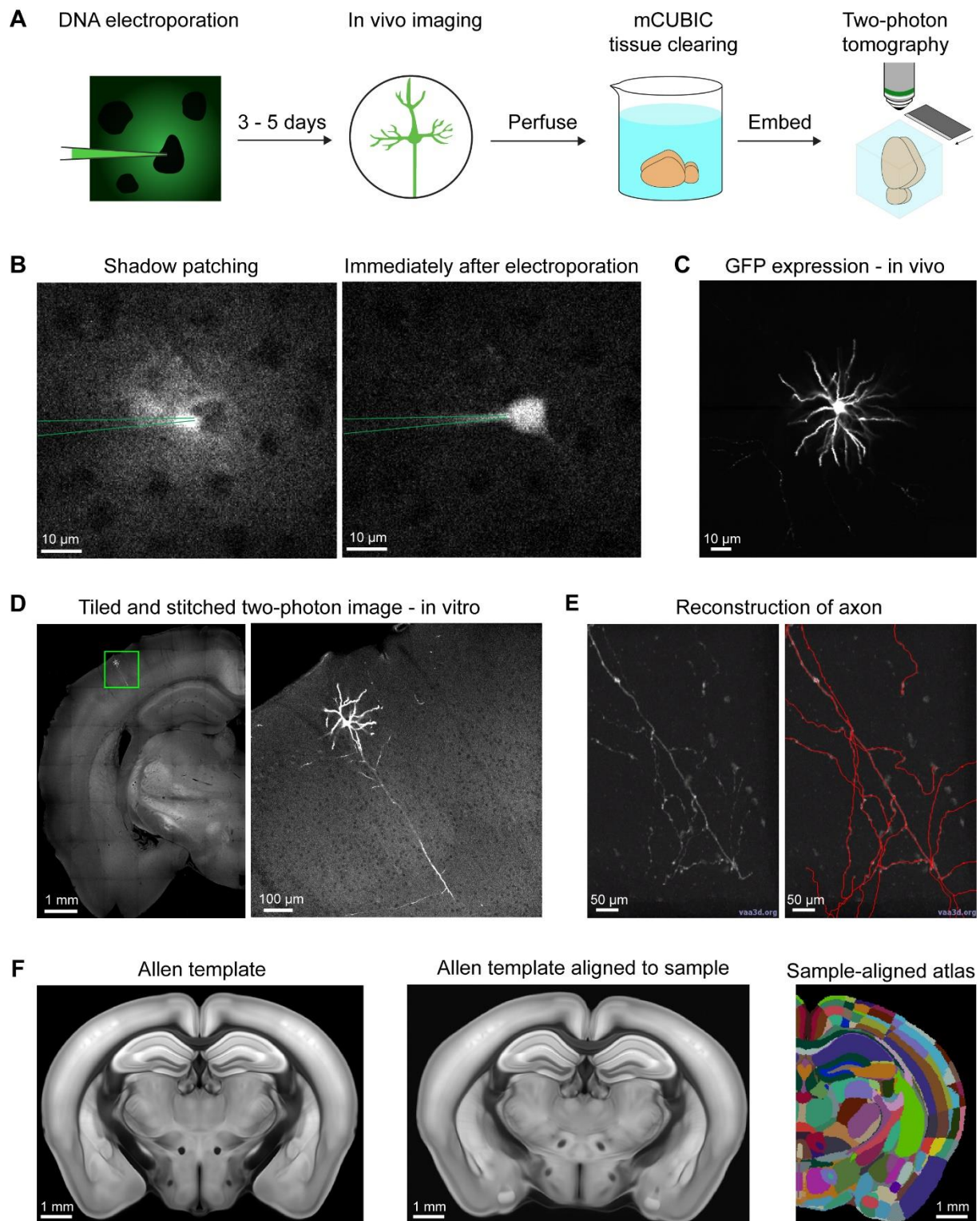


Figure 1
Liu, Foustoukos et al.

Figure 3-1 Acquisition and analysis pipeline for single cell reconstruction.

(A) Shadow electroporation labels a single neuron by introducing GFP plasmids. After 3 to 5 days of expression time, the cell was viewed through a cranial window under a two-photon microscope to control for GFP expression and the absence of any sign of apoptosis. Animals were then perfused and the brain was cleared in modified CUBIC solution. Finally, the sample was embedded in agarose and imaged under a two-photon tomographic microscope. (B) Example snapshots of an electroporation session. Left, fluorescent dye from the electroporation pipette fills the extracellular space revealing cell bodies as shadows in the image. The pipette approaches and contacts a randomly selected neuron. Right, following electroporation, the fluorescent dye rapidly fills the cell indicating successful pipette content delivery into the cell. (C) Quality check of the labelled neuron through the cranial window before perfusion. (D) Example image acquired from two-photon tomography. Left, a coronal section with a region of interest near the cell body. Right, the region of interest at higher resolution, showing the cell body, its dendrites and its main descending axon. (E) Semi-automatic neuron reconstruction using Vaa3d. Left, an example region with axon in Vaa3d. Right, same region with annotations (red) highlighting the axon. (F) Alignment with the Allen Mouse CCFv3. Left, a coronal section of the CCFv3 template. Middle, the template deformed to align with the sample space. Right, the CCFv3 atlas deformed in the same way as the template to match the sample space.

3.3.2 Diverse axonal projections of single neurons in layer 2/3 of wS1

Previous bulk anterograde labelling of long-range axons of neurons with somata in SSp-bfd showed a prominent projection target in the secondary somatosensory cortex (SSs) (White and DeAmicis 1977; Welker, Hoogland, and Van der Loos 1988; Aronoff et al. 2010; Yamashita et al. 2018). In this study, we also found a layer 2/3 neuron (AL110) with a prominent axonal arborization in SSs (Figure 3-2). The soma of this neuron was located in the D3 barrel column. The neuron had a total length of 70.7 mm of axon and 8.1 mm of dendrites. The majority of the axon extended within the granular and supragranular layers of SSp-bfd, although the layer assignments should be interpreted with caution due to potential registration errors and limitations in the digital atlas. A part of the axon extended to SSs, in particular in layer 1 and layer 2/3. In agreement with previous studies (Frostig et al. 2008; Stehberg, Dang, and Frostig 2014; Yamashita et al. 2018), the long-range axonal branch connecting SSp-bfd and SSs travelled within the cortical grey matter without entering white matter fiber tracts. In addition to innervating SSs, a small portion of its axon also projected to an unassigned region in the primary somatosensory cortex (SSp-un) and the supra-callosal white matter (scwm).

Another important projection target of layer 2/3 neurons is the primary motor cortex (MOp) (Aronoff et al. 2010; Yamashita et al. 2013; 2018; J. L. Chen et al. 2015; Yamashita and Petersen 2016; Vavladeli et al. 2020). In this study we also found a neuron (AL126) with axon in MOp and secondary motor cortex (MOs) (Figure 3-3). Similar to neuron AL110, and in agreement with previous studies (Frostig et al. 2008; Stehberg, Dang, and Frostig 2014; Yamashita et al. 2018a), the long-range axonal branch connecting SSp-bfd and MOp/MOs travelled within the cortical grey matter without entering white matter fiber tracts. This neuron, with 8.2 mm of dendrites was situated in the D1 barrel column. With a total axonal length of 69.8 mm, this neuron extended its axon primarily within SSp-bfd, but also to other primary sensory areas such as the upper limb (SSp-ul), trunk (SSp-tr), lower limb (SSp-l) and SSp-un. One axonal branch of this neuron traveled within the white matter fiber bundle system (cingulum bundle, cing, and the corpus callosum body, ccb).

Among our reconstructed neurons, we found neuron AL157 with a long-range axonal projection largely targeting the SSp-ul, consistent with previously-reported innervation patterns from bulk labelling of rat and mouse barrel cortex showing innervation of forelimb cortex (Zakiewicz et al., 2014, Zingg et al., 2014) (Figure 3-4). The axons of this neuron also extend to the SSp-un in the anterior-medial proximity of the barrel field. Another major branch of axon travels in the callosal fiber bundle system (ccb and scwm), entering the contralateral hemisphere. However, we were unable to identify any further extensions of this callosal axonal branch with our current protocol. In total, we found 6.6 mm of dendrite and 63.5 mm of axon for this neuron located in the E2 barrel column.

Axonal arborizations located in SSp-un were common across several neurons in our current study, including neuron GF243 with a highly localized columnar innervation pattern in SSp-un, as well as innervating VISa (Figure 3-5). We identified 60.1 mm of axons and 6.7 mm of dendrite for this neuron situated in the septa between the C1 and D1 barrel columns. Other target areas for this neuron includes SSp-tr, VISrl, fiber bundle systems (cingulum bundle, cing, scwm, and ccb) and SSp-ul.

Among the subcortical projections of wS1 layer 2/3 excitatory neurons, is the dorsolateral striatum (Sippy et al. 2015; Yamashita et al. 2018). Consistent with those findings, neuron AL131 had prominent axonal targets in dorsolateral part of the caudoputamen (CP) (Figure 3-6). A total length of 69.2 mm of axon was annotated for this neuron as well as 7.3 mm of dendrites located in the C2 barrel column. In addition to the CP, axons were identified in multiple visual areas such as the rostrolateral areas (VISrl), anterolateral areas (VISal) and anterior areas (VISa), as well as several regions in the primary somatosensory area (nose, SSp-n, SSp-tr, SSp-un and SSp-ul). This neuron also has a prominent branch traveling in the callosal fiber bundle system (scwm for this specific case).

Lastly, we show an example neuron (AL142) extending a long axonal branch laterally to the CP, apparently heading towards the most dorsal aspect of the amygdala (Figure 3-7). In comparison to neuron AL131 innervating the dorsolateral striatum (Figure 3-6), the axons of neuron AL142 traversed deeper layers of SSp-bfd, SSs, Visceral area (VISC), external capsule (ec), with our tracing ending in the lateral parts of the CP near the most dorsal aspect of the amygdala (Figure 7). Other target areas for this neuron include the VISa, SSp-un, VISrl and SSp-tr. For this neuron we did not identify any signs of axon within the callosal fiber bundle system. This neuron had a total of 48.8 mm of axon and 6.5 mm of dendrites and its cell body was located in the septa between the D2 and D3 barrel columns.

3.3.3 Summary of all SSp-bfd layer 2/3 neurons reconstructed

Finally, we summarize the ten neurons reconstructed in this study (Figures 3-2 to 3-7 and Figures 3-11 to 3-14) and overlay them in order to get an idea of the overall projection profile (Figure 3-8). We quantified axonal length in each brain region identified summing across layers and subregions (Figure 3-8D). Most of the axonal length resided within the SSp-bfd. It is interesting to note that SSp-ul and VISa ranked second and third, then followed by the SSs and SSp-un as fourth and fifth. Although ranked lower in average amount of axons, nine out of the ten neurons projected to SSp-tr. Other target regions include MOp and MOs, dorsal region of the striatum (STRd), several other SSp regions (SSp-tr, SSp-ll), various visual areas (for instance, VISam, VISp, and VISpm), multiple fiber bundles (stria terminalis, st, fiber tracts, cerebrum related, mfbc, hippocampal commissures, hc, corpus callosum anterior forceps, fa, and fornix system, fxs), retrosplenial areas (lateral agranular part, RSPagl and ventral part, RSPv), auditory areas (such as the dorsal auditory area AUDd and posterior auditory areas, AUDpo), and VISC. Seven of the ten reconstructed neurons had axonal branches in the corpus callosum (cc) with none of these extending outside of the fiber tracts on the opposite hemisphere (Han et al. 2018; Yamashita et al. 2018).

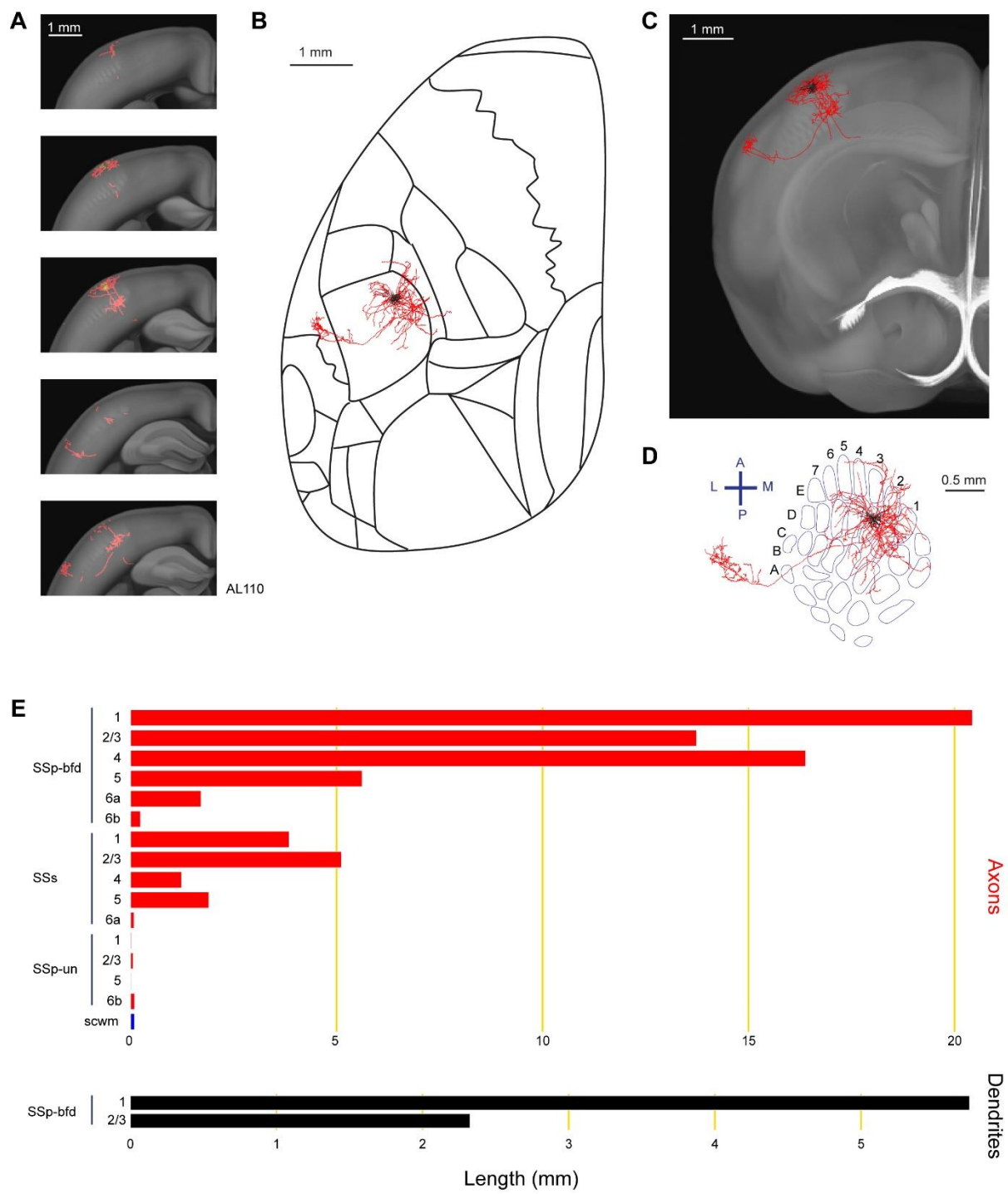


Figure 2
Liu, Foustoukos et al.

Figure 3-2 Reconstruction and quantification of example neuron AL110 with projections to the supplementary somatosensory cortex.

(A) Serial overlays of GFP-labelled axon (red) and dendrites (green) in coronal views encompassing the anterior-posterior span of the axons of 1.5 mm. Each section represents a maximum projection of 300 μ m. (B) Maximum projection of the reconstructed axon and dendrites in horizontal view, aligned to the Allen Mouse CCFv3 to indicate the boundaries between cortical regions. (C) Maximum projection of reconstructed axon and dendrites in coronal view overlaid with an anatomical section from the Allen Mouse CCFv3. (D) Maximum projection of reconstructed axon and dendrites in a tangential view (rotated 30 degrees) over the barrel field (blue). The cell is located in the D3 barrel column. (E) Quantification of axonal (top) and dendritic (bottom) length in respective brain regions identified by the Allen Mouse CCFv3. For (B) to (E): dendrites are shown in black; axon in grey matter is shown in red; and axon in white matter is shown in blue.

Figure 3-3 Reconstruction and quantification of example neuron AL126 with projections to the primary and secondary motor cortex.

(A) Serial overlays of GFP-labelled axon (red) and dendrites (green) in coronal views encompassing the anterior-posterior span of the axons of 3.5 mm. Each section represents a maximum projection of 700 μ m. (B) Maximum projection of the reconstructed axon and dendrites in horizontal view. (C) Maximum projection of the axon and dendrites in coronal view. (D) Maximum projection of the axon and dendrites in tangential view (rotated 30 degrees) over the barrel field. The neuron is located in the D1 barrel column. (E) Quantification of axonal (top) and dendritic (bottom) length in respective brain regions identified by the Allen Mouse CCFv3. For (B) to (E): dendrites are shown in black; axon in neocortical grey matter is shown in red; and axon in white matter is shown in blue.

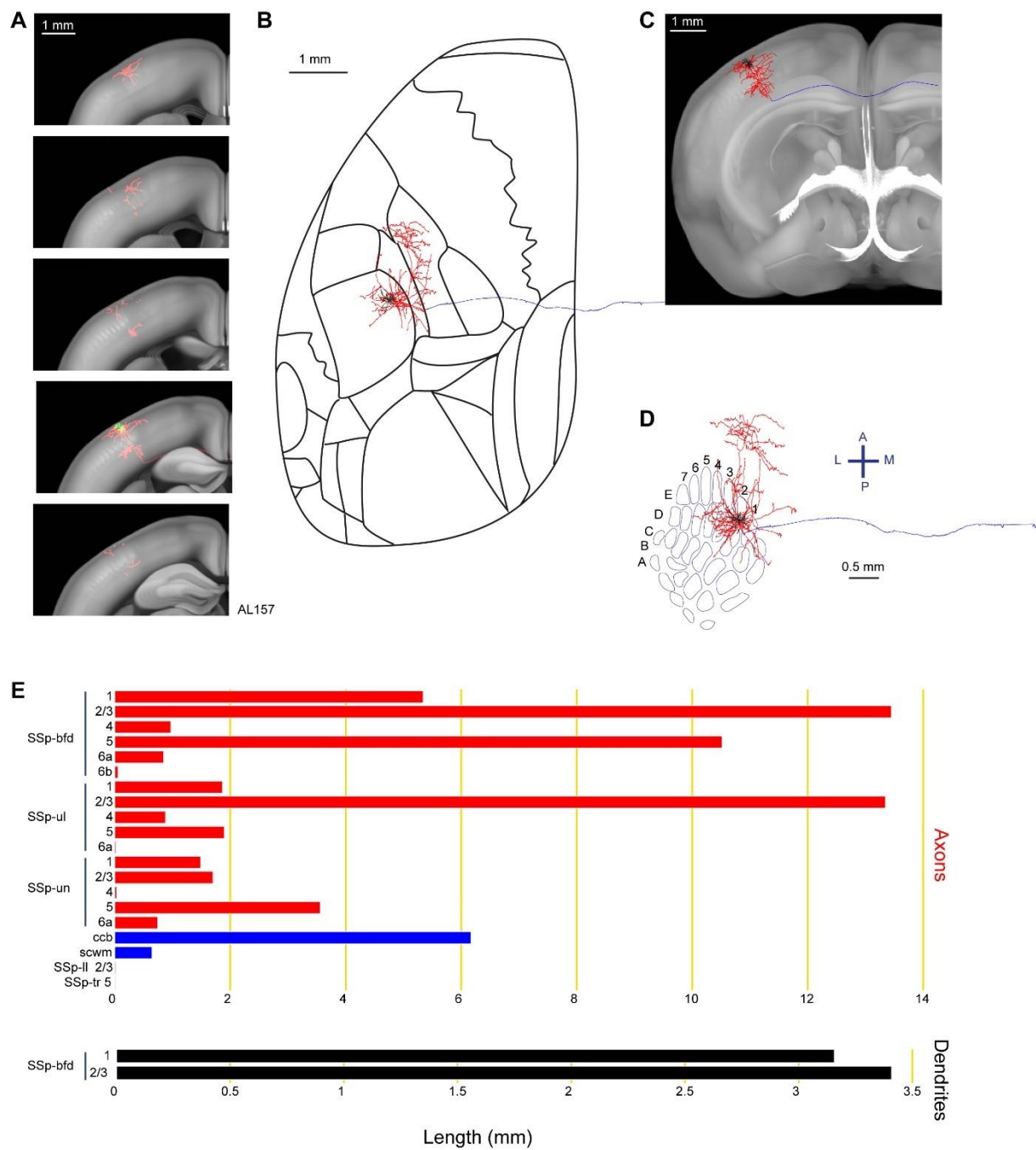


Figure 4
Liu, Foustoukos et al.

Figure 3-4 Reconstruction and quantification of example neuron AL157 with projections to the primary somatosensory cortex upper limb area.

(A) Serial overlays of axon (red) and dendrites (green) in coronal views encompassing the anterior-posterior span of the axons of 2.125 mm. Each section represents a maximum projection of 425 μ m. (B) Maximum projection of the reconstructed axon and dendrites in horizontal view. (C) Maximum projection of the axon and dendrites in coronal view. (D) Maximum projection of the axon and dendrites in tangential view (rotated 30 degrees) over the barrel field. The cell is located in the E2 barrel column. (E) Quantification of axonal (top) and dendritic (bottom) length in respective brain regions identified by the Allen Mouse CCFv3. For (B) to (E): dendrites are shown in black; axon in neocortical grey matter is shown in red; and axon in white matter is shown in blue

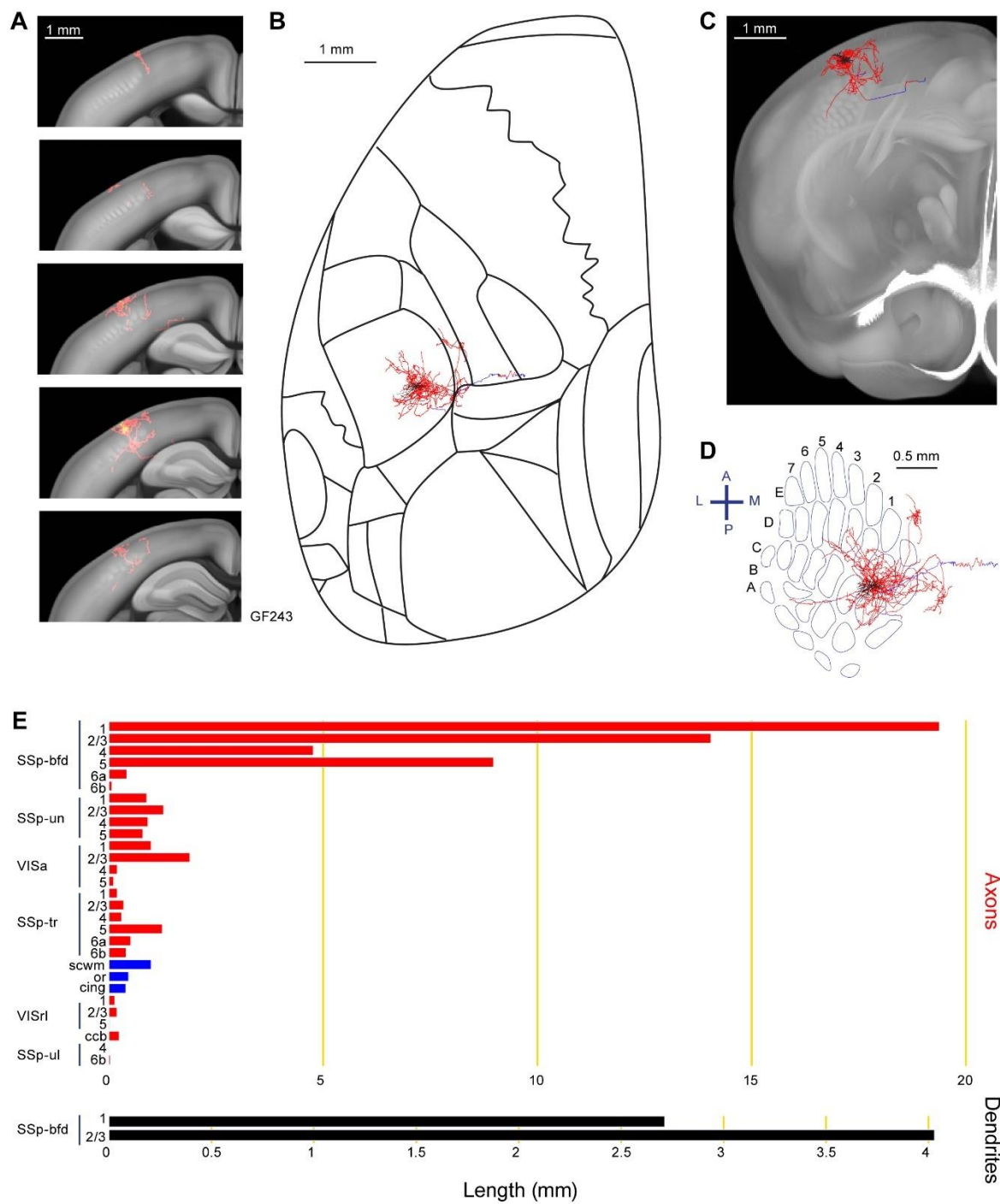


Figure 5
Liu, Foustoukos et al.

Figure 3-5 Reconstruction and quantification of example neuron GF243 with projections to an unassigned region of primary somatosensory cortex and an anterior visual area.

(A) Serial overlays of axon (red) and dendrites (green) in coronal views encompassing the anterior-posterior span of the axons of 1.25 mm. Each section represents a maximum projection of 250 μ m. (B) Maximum projection of the reconstructed axon and dendrites in horizontal view. (C) Maximum projection of the axon and dendrites in coronal view. (D) Maximum projection of the axon and dendrites in tangential view (rotated 30 degrees) over the barrel field. The cell body is in the septa between the C1 and D1 barrel columns. (E) Quantification of axonal (top) and dendritic (bottom) length in respective brain regions identified by the Allen Mouse CCFv3. For (B) to (E): dendrites are shown in black; axon in neocortical grey matter is shown in red; and axon in white matter is shown in blue.

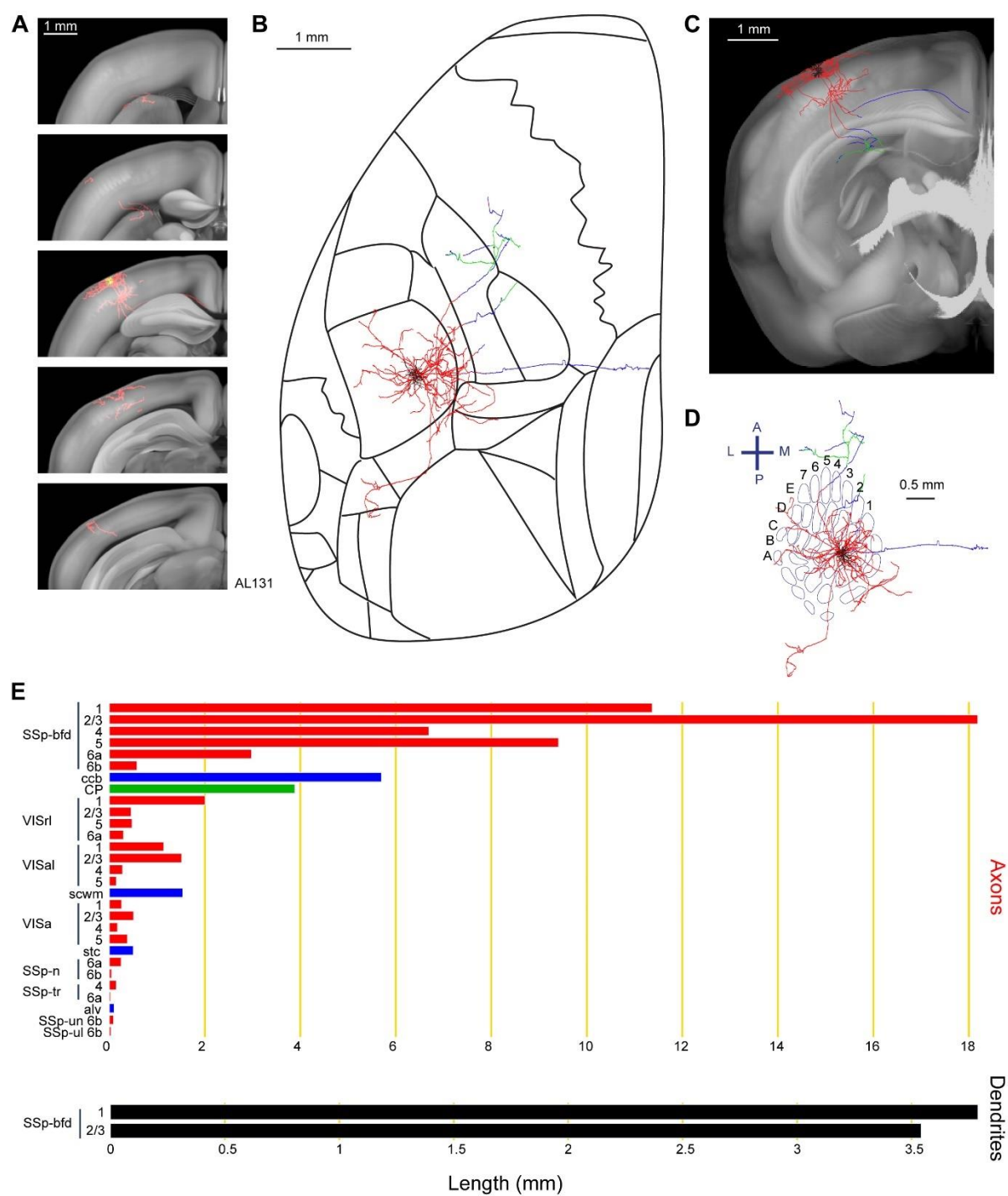


Figure 3-6 Reconstruction and quantification of example neuron AL131 with projections to the caudoputamen and multiple visual areas.

(A) Serial overlays of axon (red) and dendrites (green) in coronal views encompassing the anterior-posterior span of the axons of 4.125 mm. Each section represents a maximum projection of 825 μ m. (B) Maximum projection of the reconstructed axon and dendrites in horizontal view. (C) Maximum projection of the axon and dendrites in coronal view. (D) Maximum projection of the axon and dendrites in tangential view (rotated 30 degrees) over the barrel field. The neuron is in the C2 barrel column. (E) Quantification of axonal (top) and dendritic (bottom) length in respective brain regions identified by the Allen Mouse CCFv3. For (B) to (E): dendrites are shown in black; axon in neocortical grey matter is shown in red; axon in striatum is shown in green; and axon in white matter is shown in blue.

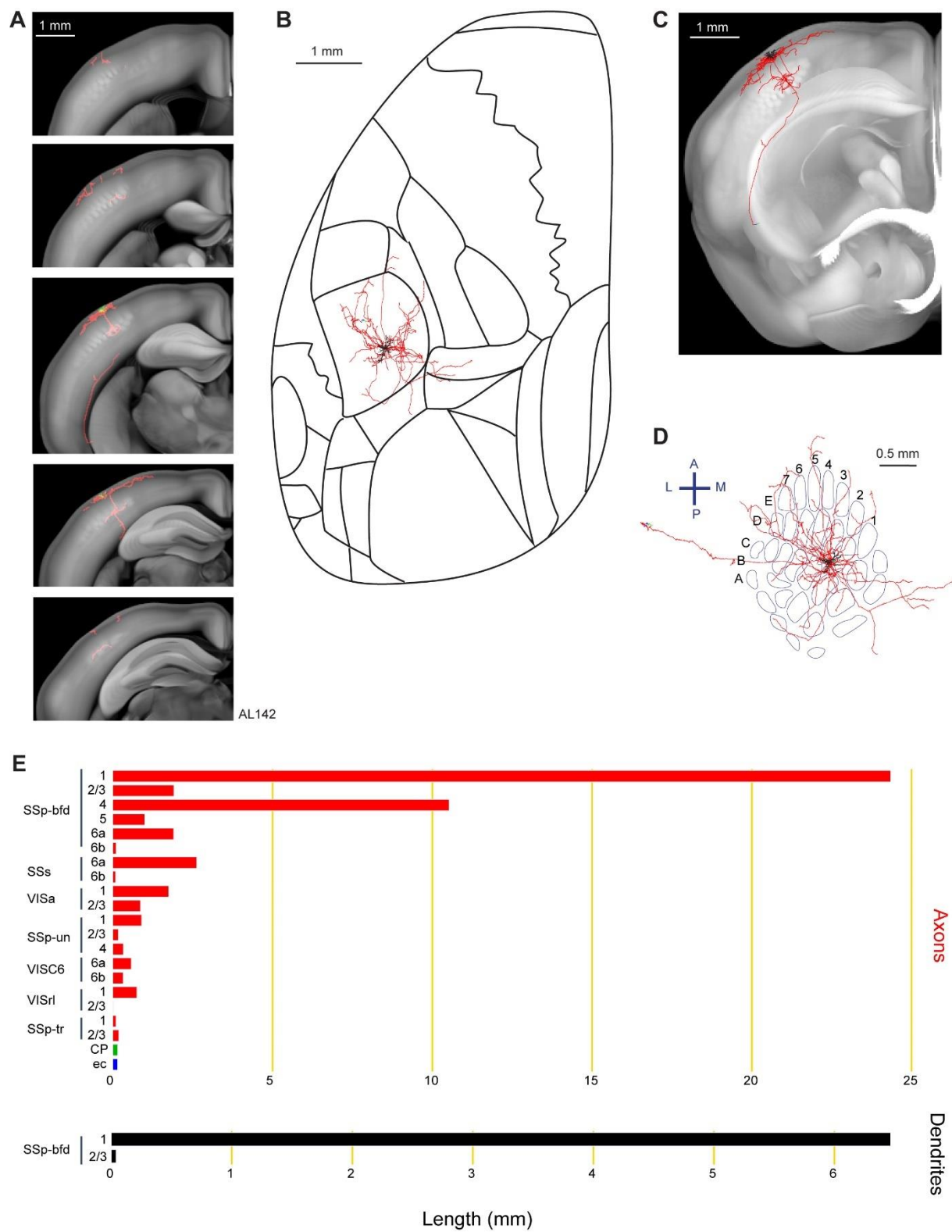


Figure 7
Liu, Foustoukos et al.

Figure 3-7 Reconstruction and quantification of example neuron AL142 with projections to the lateral caudoputamen and towards the amygdala.

(A) Serial overlays of axon (red) and dendrites (green) in coronal views encompassing the anterior-posterior span of the axons of 2.375 mm. Each section represents a maximum projection of 475 μ m. (B) Maximum projection of the reconstructed axon and dendrites in horizontal view. (C) Maximum projection of the axon and dendrites in coronal view. (D) Maximum projection of the axon and dendrites in tangential view (rotated 30 degrees) over the barrel field. The cell is in the septa between the D2 and D3 barrel columns. (E) Quantification of axonal (top) and dendritic (bottom) length in respective brain regions identified by the Allen Mouse CCFv3. For (B) to (E): dendrites are shown in black; axon in neocortical grey matter is shown in red; axon in striatum is shown in green; and axon in white matter is shown in blue.

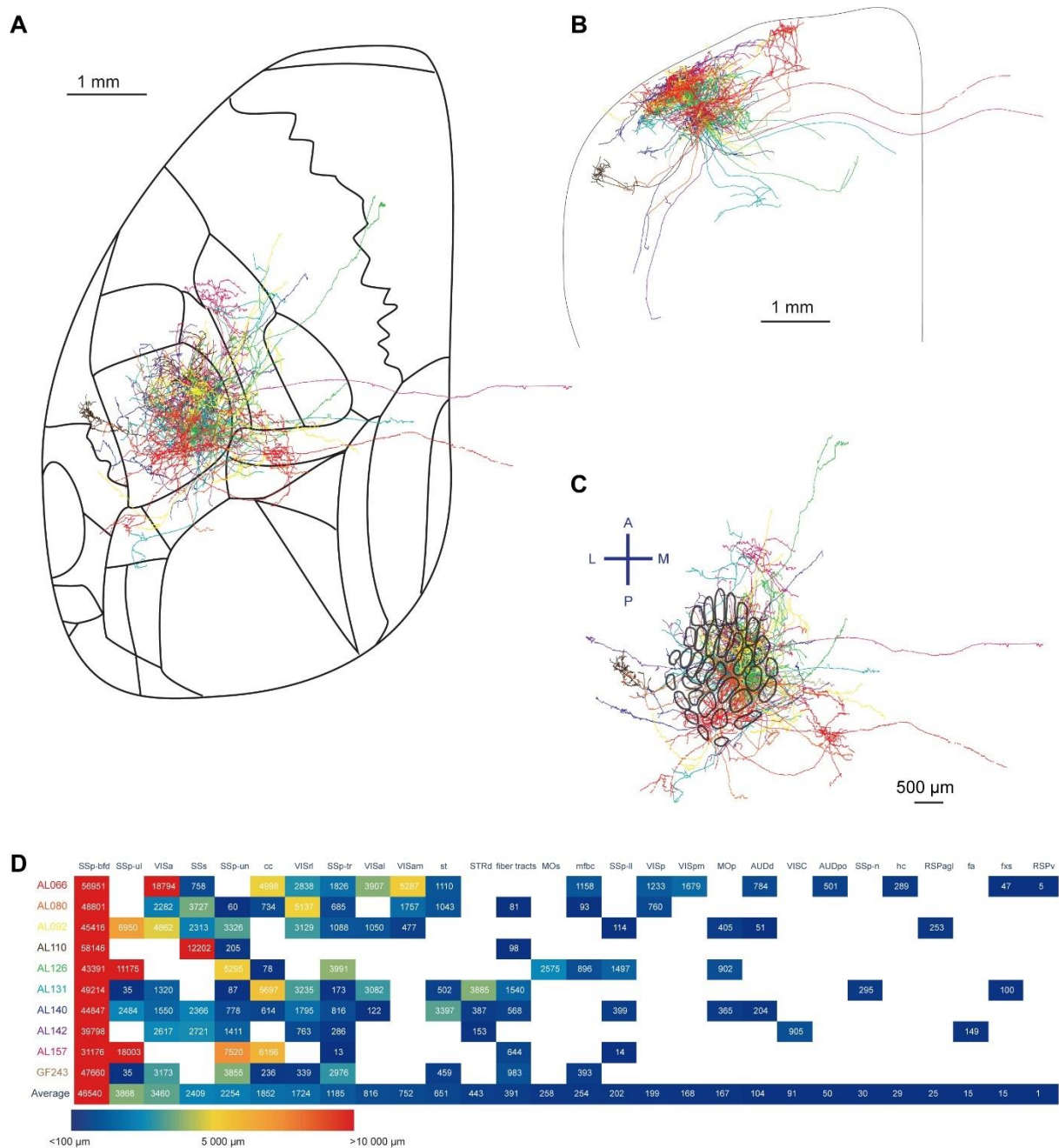


Figure 8
Liu, Foustoukos et al.

Figure 3-8 Summary of the ten reconstructed neurons.

(A) Horizontal overlay of axons aligned to the Allen Mouse CCFv3. The axon of each neuron is shown in a different color. (B) Coronal overlay of axons. (C) Tangential view of axons aligned to the barrel map. (D) Quantification of axonal length in respective brain regions. The length of axon in each layer of a specific region is summed up. The different brain regions receiving projections from the labelled neurons are sorted according to the mean length of reconstructed axon across all neurons in each region of interest, from the longest axonal length on the left to the shortest axonal length on the right.

3.4 Discussion

We performed two-photon guided *in vivo* “shadow” electroporation to label single neurons in layer 2/3 of mouse barrel cortex by expression of GFP (Judkewitz et al. 2009). Through two-photon tomographic imaging and 3-dimensional neuron reconstruction (Han et al. 2018) in relation to a digital mouse brain atlas, we quantified long-range projection regions among the 10 reconstructed cells finding a high degree of diversity.

3.4.1 Diverse projection areas of individual neurons in layer 2/3 barrel cortex

Among the literature, numerous reports have studied the SSp-bfd using broader approaches involving viral injections or other anterograde tracers that label thousands of neurons. Less is known on the finer scale investigation of individual neurons, but it seems likely that each neuron only projects to a subset of the regions that have been identified from bulk labeling approaches (C. Guo et al. 2017; Yamashita et al. 2018).

Projections between the SSp-bfd to the SSs have been shown to be heavily reciprocal, and similar observations between the SSp-bfd and the motor regions (MOp and MOs) have been reported (Aronoff et al. 2010; Mao et al. 2011; Zingg et al. 2014). Here, we further report SSp-bfd axons also project to other parts of the SSp such as the upper limb, lower limb, trunk, and unassigned regions. Projections to these somatosensory regions have been previously reported in the Mouse Connectome project where an anterograde and a retrograde tracer were co-injected into a single area (Zingg et al. 2014), showing reciprocal projections. Such organization likely aids the integration of sensory information across the somatotopic map. The extensive axonal arborization within SSp-bfd is likely important for integrating sensory information across the whisker pad, necessary for determining object shape (Brown et al. 2021; Rodgers et al. 2021). The important projection to SSp-ul might be important during running where the ventral whiskers touch the ground before the forepaw, as if to ensure safe placement of the paw during locomotion (Grant, Breakell, and Prescott 2018). Similar to previous studies (Frostig et al. 2008; Stehberg, Dang, and Frostig 2014; Yamashita et al. 2018a), we found that the long-range axonal projections typically traversed cortical boundaries travelling in the neocortical grey matter rather than entering the white matter fiber tracts. The horizontally extending axons are likely to contribute to the large functional spread of signals evoked by the deflection of even just a single whisker (Ferezou et al. 2007; Frostig et al. 2008; B. A. Johnson and Frostig 2016; Brett A. Johnson and Frostig 2018).

It has also been demonstrated that there is a heterogeneity in the projection pattern within the SSp-bfd (Zingg et al. 2014). The caudal-medial barrel field (cm-bfd) projects to SSp-tr and SSp-ll while the antero-lateral barrel field (al-bfd) showed a preference for SSp nose and mouth regions. With our current study, all labeled neurons are located near the B, C, D or E rows with arc position 1, 2 or 3, which are relatively caudal and medial in the barrel field (Figure 3-8C). In agreement with previous suggestions, our results show all neurons except for AL110 send their axons to the SSp-tr. Furthermore, anterograde tracers injected in the cm-bfd, but not the al-bfd, have also been found to label axonal projections in the AUDd, AUDp and AUDv (Zingg et al. 2014). Projections to the AUDd and AUDp were also observed in the current study (Figure 3-8A and D). In addition, anterograde tracers injected in the cm-bfd, revealed axons in the VISC, but this is not observed in those with al-bfd injections (Zingg et al. 2014). Being the only neuron with axons identified in VISC in this study, AL142 is located near

the D2 barrel which takes a relatively central-medial position in the posterior barrel field (Figure 3-6). Additional reconstructions of single neurons are necessary to make more in-depth comparisons to quantifications obtained from viral labeling.

One of the common projection targets of our reconstructed neurons is the unassigned SSp-un region. In the present study, 9 out of 10 neurons showed axons in SSp-un and it is ranked having the fourth greatest amount of axon among all regions identified (Figure 3-8D). Projections in the same region have also been reported in the Allen Mouse Brain Connectivity atlas (Oh et al. 2014) in a particular experiment (Experiment 298718778) where a Cre-dependent anterograde tracer was injected to SSp-bfd of a *Rasgrf2-dCre* mice that labels mostly layer 2/3 neurons. This region, immediately medial to the SSp-bfd, corresponds to the dysgranular zone that has been reported in both rats and mice (Koralek, Olavarria, and Killackey 1990; Lee and Kim 2012; Yamashita et al. 2018). Neurons within this region send their axons to the striatum, thalamus and midbrain (T. Lee and Kim 2012). In line with previous studies which indicated that there are “hot spots” for axons extending to the dysgranular zone (Yamashita et al. 2018), we also identify a large number of axons in this region. Given the frequency of occurrence in single cell projection profiles and the number of axons it receives, the SSp-un may be an important region to investigate in future experiments.

Additionally, several neurons had axons projecting to higher order visual related areas. These types of projections have been previously reported for both the rat and the mouse barrel cortex and are likely to be reciprocal (Zakiewicz, Bjaalie, and Leergaard 2014; Zingg et al. 2014; Yamashita et al. 2018). One possible hypothesis for the role of this connectivity between SSp and visual areas is multisensory integration (Zakiewicz, Bjaalie, and Leergaard 2014).

Neurons projecting to MOp and to SSs might form two distinct populations both anatomically, functionally and genetically (Chen et al. 2013; 2015; Yamashita et al. 2013; 2018; Sorensen et al. 2015; Yamashita and Petersen 2016). In previous work (Yamashita et al. 2018a), retrograde tracers were injected to SSs or MOp, and neurons in the SSp-bfd labelled with these tracers were selectively targeted for electroporation. Axonal reconstructions suggested that neurons projecting to SSs (S2p) do not project to MOp, while the MOp projecting neurons (M1p) projected only weakly to SSs. Consistent with this, in the small sample of neurons in the current study, the strong projectors to MOp and MOs (AL126) and to SSs (AL110) indeed seem to be non-overlapping in their axonal arborisations (Figure 3-8D). However, there are also neurons that project some axon to both regions (Figure 3-13 and Figure 3-14). Further studies with greater numbers of single neuron reconstructions may provide more accurate depictions of neuron categories based on anatomical information. Given that the M1p and S2p neurons were distinct both functionally and genetically (Yamashita et al. 2013; Sorensen et al. 2015), future studies might reveal more categories of layer 2/3 neurons such as VISam-projecting or STRd-projecting neurons.

3.4.2 Axons in the fiber bundles

Axons in fiber bundles heading toward the contralateral hemisphere were frequently found among our reconstructed neurons. While 7 out of 10 neurons showed axons within the corpus callosum, none continued to exit. Several other studies that aimed to reconstruct single

neurons have also reported a paucity of axons in the contralateral hemisphere (Han et al. 2018; Yamashita et al. 2018). Viral-based anatomical studies show some axons extending within the corpus callosum, winding past the midline and exiting to regions such as the contralateral SSp-bfd (Yamashita et al. 2018; Zingg et al. 2014). A study on developmental refinements of callosal projections in the SSp-bfd showed that although layer 2/3 neurons do show eliminations of contralateral projecting axons, this process stabilizes around postnatal day 15 (De León Reyes et al. 2019). It might be that some of these axons did not fully retract and leaving segments still within the corpus callosum. Our current approach does not detect all axons (Figure 3-10), and it is possible that future studies will reveal more innervation of the contralateral hemisphere by layer 2/3 neurons. As opposed to a detection related issue, this may also arise from incomplete GFP diffusion. The dense fiber bundles may limit the diffusion of fluorescent proteins, resulting in incomplete filling of the axon (Yamashita et al. 2018). To resolve these questions, future viral-based anatomical studies with higher imaging resolution is required to compare the number of axons at different points of the trajectory (such as at the entrance of the corpus callosum versus at the points of exit on the contralateral side). From a single cell labeling approach, further studies could also inject retrograde tracers to the SSp-bfd followed by targeted electroporation in the hemisphere contralateral to the injection and subsequent neuronal reconstruction.

3.4.3 Limitations and future perspectives

A major limitation of the present work is the incompleteness of the reconstructed axonal arborizations. Further signal enhancement appears to be essential (Figure 3-10) and follow up studies will need to incorporate these considerations. Assuming that the labeling method (be it electroporation or viral injections) sufficiently fills up the neuron and its entire extensions, sample pre-processing involving signal amplifications would provide an important step toward the true anatomical representation. Several whole brain volumetric imaging techniques in combination with signal amplification processes have been developed which could be helpful for future experiments (Renier et al. 2014; Gong et al. 2016; X. Wang et al. 2019; Winnubst et al. 2019). Nonetheless, the neurons reconstructed in this study have a total axonal length per neuron of 67.9 ± 13.0 mm (mean \pm SD, $n=10$), which is comparable to that of the only other study that we know of including layer 2/3 mouse barrel cortex neurons registered to the Allen atlas, which found a total axonal length per neuron of 49.9 ± 13.9 mm (mean \pm SD, $n=9$) (Peng et al. 2021).

Anatomical investigations at single neuron resolution provide valuable insights on where each neuron might send information. In addition to quantifying axonal length through GFP, in the future, it would be useful to also use a red fluorescent protein attached to presynaptic proteins in order to identify neurotransmitter release sites. To reveal network level information while maintaining cellular resolution requires large amounts of single neuron data. It is then possible to unravel patterns through clustering-based analysis and categorize projection types (X. Wang et al. 2019; Winnubst et al. 2019). The necessity for large data sets suggests the need to design high throughput methods for sample preparation, image acquisition and axonal annotation. Currently large parts of the published neuronal reconstructions are being done manually by human annotators, which not only require hours

of labor work (Magliaro et al. 2019), but also are susceptible to human errors and/or biases. However, recent advances in machine learning and computer vision may accelerate the later part of the pipeline with minimal human supervision (Zhou et al. 2018; Q. Huang et al. 2020; Q. Li and Shen 2020).

From a scientific perspective, the opportunity of labelling single neurons and recovering their morphology might help, in the future, to better determine the role of projection neurons in complex neural computations, such as reward-based learning. As previously mentioned, studies where projection neurons were retrogradely labeled have shown projection target-dependent neuronal activity, for example during goal-directed sensorimotor transformations (J. L. Chen et al. 2013; 2015; Yamashita and Petersen 2016; Vavladeli et al. 2020). In those cases, an assumption of the projection area(s) to focus on was made before hand in order to bulk inject the retrograde tracer. One can imagine that an unbiased and more refined experimental procedure could be followed during which the activity of different neurons can firstly be measured (for instance, using two-photon calcium or voltage imaging), followed by “activity-targeted” selection of neurons to be electroporated and reconstructed. This way, cells which show interesting activity patterns during learning or execution of different behavioral tasks could be labelled and their morphology and/or projection targets could be revealed. Although technically demanding, this type of experiments could provide unique datasets where morphology and function can be directly linked, shedding light on brain mechanisms that still remain unexplored.

3.5 Methods

All animal procedures were performed in accordance with protocols approved by the Swiss Federal Veterinary Office (license VD1889.4).

3.5.1 Head-post Implantation

The experiments were carried out in 6-9 week-old male and female wild type C57BL/6J mice. Surgeries were performed under isoflurane anesthesia (4 % for induction, then 1.5 %) and the temperature was continuously monitored and held at 37°C using a closed-loop heating system (FHC Inc). All of the right whiskers, except the C2, were trimmed and then mice were positioned in a stereotaxic frame using a nose clamp. In order to protect their eyes from drying, a hydrating eye gel was placed over the eyes during the surgery (VITA-POS, Pharma Medica AG). Pre-operative analgesia included intraperitoneal (i.p.) injections of Carprofen (0.3 ml at 0.5 mg/ml) (Rimadyl, Pfizer) and subcutaneous injections of a mix of lidocaine (2% diluted 1:10) and bupivacaine (0.5% diluted 1:2) at the incision site. For post-operative analgesia, ibuprofen was administered through the water in the home cage drinking bottle for 4 days after surgery (2.5 ml in 250 ml of water bottle) (Algifor Dolo Junior, VERFORA SA). In order to disinfect the skin before the incision, a povidone-iodine solution (Betadine, Mundipharma Medical Company) was used. Then a part of the scalp was removed using surgical scissors, the skull was exposed and the membrane of the periosteum was gently removed using a scalpel blade. The skull was then again disinfected, rinsed with Ringer solution and subsequently fully dried using cotton buds. Afterwards, a thin layer of cyanoacrylate glue was applied on the skull surface (Loctite 401, Henkel) and the metal head-post was placed on the right hemisphere. Finally, in order to strengthen the adhesion of the

post to the skull, as well as to create a chamber for later procedures, dental cement (Paladur, Kulzer) was added. Immediately after the implantation surgery, the center of the barrel field was determined using intrinsic optical signal (IOS) imaging, as previously described (Ferezou et al. 2007; Le Merre et al. 2018; Yamashita et al. 2018). At the end this procedure, the exposed skull was protected using a silicone elastomer (Kwik-Cast, WPI).

3.5.2 Single-cell Electroporation

After full recovery from the implantation, single-cell electroporation was performed under isoflurane anesthesia (4 % for induction, then 1%). The body temperature was controlled and maintained at 37°C. At least one hour before the surgery, the mice were injected with dexamethasone (5 mg/ml, 200 µl per mouse, intramuscular, Helvepharm, Zentiva) and just before the surgery with Carprofen (0.3 ml at 0.5 mg/ml, i.p., Rimadyl, Pfizer). The mice were head-fixed using the implanted metal head-post. The eyes were protected with a hydrating eye gel (VITA-POS, Pharma Medica AG). First, a circular craniotomy of around 3.5 mm was drilled around the center of the C2 barrel column using the blood vessel map. Depending on the mouse, a full durotomy was sometimes performed in order to facilitate access to the cortex. *In vivo* shadow single-cell electroporation was targeted to layer 2/3 neurons using a two-photon microscope (Judkewitz et al. 2009; Pala and Petersen 2015). Glass capillary pipettes with resistances of 10-17 MΩ were filled with intracellular solution containing (in mM): 135 potassium gluconate, 4 KCl, 10 HEPES, 10 sodium phosphocreatine, 4 MgATP, 0.3 Na₃GTP (adjusted to pH 7.3 with KOH) into which 100 µM Alexa 488 dye (ThermoFisher Scientific, A10436) and pCAG-EGFP (Addgene 11150) plasmids were added (final plasmid concentration at 200 ng/µl). During the electroporation, the pipette was inserted into the cortex while continuously reading the 3D position of the pipette tip using a micromanipulator (SM7-Luigs & Neumann). Layer 2/3 was identified by vertical subpial depth (at least 150 µm from pia surface) and by a sudden increase in cell density. After close contact to a randomly chosen layer 2/3 neuron (increase of the pipette resistance by 20%), 50 pulses of negative voltage steps (0.5 ms, -12 V) were delivered at 50 Hz using a pulse generator (Axoporation 800A, Molecular Devices). After the electroporation, the pipette was slowly retracted and the immediate visual appearance of the neuron was used to judge the success of the procedure (i.e. if the cell remained intact and filled with the intracellular dye). Typically, 2-3 cells were electroporated per animal. At the end of the procedure a triple glass window assembly, consisting of a 5 mm diameter and two 3 mm diameter coverslips of #1 thickness (CS-3R, Warner Instruments), was placed over the craniotomy and fixed on the skull using UV-curing adhesive (Thorlabs, NOA68). The mouse was then returned to its home-cage and was allowed to recover for at least 3 days. The expression of the GFP in the electroporated neurons was evaluated 3-5 days after the procedure, through the cranial window, using an epi-fluorescent microscope and/or the two-photon microscope. Only animals with a single expressing cell were selected for the following steps while animals with multiple cells were excluded. On average approximately one quarter of the electroporated mice contained a single brightly labelled neuron.

3.5.3 Sample Preparation and Two-photon Tomography

After single-cell expression of the fluorescent protein, the mice were transcardially perfused under deep anesthesia (pentobarbital 150 mg/kg, i.p.) using 4% paraformaldehyde (PFA) diluted in PBS (Electron Microscopy Science, USA), the brains were extracted and post-fixed in PFA overnight. After post-fixation the brain tissue underwent a passive clearing procedure using a modified-CUBIC (mCUBIC) solution (Susaki et al. 2015) consisting of 25% w/w N,N,N',N'-tetrakis(2-hydroxypropyl)ethylenediamine, 15% w/w of Triton-X and 60% w/w of dH₂O. Whole brains were firstly incubated in mCUBIC solution at 37°C in a shaker (at 90 RPM) for 4 days. At day 4, the solution was replaced with a fresh one and the incubation continued for another 4 days. After the clearing process, the tissue was washed 3 times for 1 hour using 50 mM phosphate-buffered (PB) solution. For 3 out of the 10 animals the cleared brain tissue was then incubated in 5% gelatin (Sigma G1890) for 2-4 hours at 37°C (for the rest of the brains this step was omitted as it did not seem to improve imaging quality). Finally, the brains were placed in 4% PFA for 24-36 hours at 4°C to cross-link and then washed with 50 mM PB. In order to increase the stability of the tissue during serial section two-photon tomography the tissue was embedded in 5% agarose (Type-I agarose, Merck KGaA, Germany, A6013).

Whole brain 3D imaging was performed using a custom-made two-photon serial sectioning microscope which was controlled by the MATLAB-based software ScanImage 2017b (Vidrio Technologies, USA, for the 2P imaging) and BakingTray (<https://github.com/SainsburyWellcomeCentre/BakingTray>) (for the serial sectioning). In summary, the imaging setup consists of a 2P microscope coupled with a vibratome head (VT1000S, Leica, Germany) and a X/Y/Z high precision stage (X/Y: V-580; Z: L-310, Physik Instrumente, Germany), similar to previously described (Han et al. 2018b). The vibratome was set to slice the brain at 50 µm physical slice thickness, and 10 optical sections per physical section were acquired using a high-precision piezo objective scanner (PIFOC pons-725, Physik Instrumente, Germany). A 16x water immersion objective was used with a resolution of 0.8 µm in X and Y and measured axial point spread function (PSF) at ~5 µm full width at half maximum. We collected fluorescence in the green channel (500 – 550 nm, ET525/50) and each section consisted of 1025 x 1025 µm tiles overlapping at 7%. The final voxel size was 0.8 x 0.8 x 5 µm (X, Y, Z).

After acquisition, the raw tiles were stitched using the MATLAB-based package StitchIt (<https://github.com/SainsburyWellcomeCentre/StitchIt>). This software applies illumination correction based on the average tile in each optical plane and stitches the tiles based on the actual position in 3D, as registered by the high precision motors.

3.5.4 Tracing of Axons and Dendrites

After stitching, the data were tera-converted using the Vaa3D-Terafly software suite and the whole brain was visualized in 3D at different scales (<http://home.penglab.com/proj/vaa3d/home/index.html>). Subsequently, we used the Vaa3D module for software-assisted neuron tracing in order to place nodes in 3D. The placement of the nodes was based on the fluorescent signal in the image. The final output of Vaa3D was a

.eswc file containing thousands of rows, each one consisting of nodeID, x,y,z coordinate, radius value, neurite type and parent node ID.

3.5.5 Extracting barrel column masks from the Digital Atlas

We used Ilastik v1.3.3 (Berg et al. 2019) to segment the barrel columns from the gray scale anatomical image of the Allen Common Coordinate Framework version 3 (CCF, Wang et al., 2020). In Ilastik, a human annotator labeled a few example pixels as the barrel column which was used to train a classifier to segment the entire image stack. Then the resultant mask image stack was used as a brain atlas parcellation file.

3.5.6 Registration to a Digital Atlas

The stitched brain slices and the annotated neurons were registered to the Allen CCF version 3 (Wang et al., 2020) using a Python custom-written script, inspired by the MATLAB-based ARA tools (https://github.com/SainsburyWellcomeCentre/ara_tools). At the first step, the data were down-sampled in X, Y, Z in order to match the 25 x 25 x 25 μm voxel size of the CCF. Next, the open source medical image registration suite Elastix (<https://github.com/SuperElastix/elastix>) was utilized in order to register the grayscale CCF anatomical image to the acquired brain slices in 3D, using rigid, affine and nonrigid transformations. Once this transformation was computed, it was also applied to the parcellation file of the CCF and thus every voxel of the imaged brain data was assigned with a brain area ID matching to a unique brain area. Finally, we apply the same transformation to the barrel column mask file for location of the neuron and visualizations.

3.5.7 Quantification of neurite length

For the quantification of the neurite length, the x,y,z node coordinates of the Vaa3D .eswc files were transformed to physical distances in μm using the imaging resolution values (0.8 μm in X and Y and 5 μm in Z). Afterwards the Vaa3D resampling plugin was used (https://github.com/Vaa3D/vaa3d_tools/tree/master/released_plugins/v3d_plugins/resample_swc) to resample the annotation points and space them equally every 1 μm . Finally, the number of points in every brain area was counted and transformed in neurite length in μm . If the annotation node of a neurite coincided with a given voxel, that node was assigned to the brain area corresponding to this voxel according to the CCF parcellation file.

3.5.8 Immunohistochemistry

In order to test for the presence of additional axonal arborizations that might not have been resolved in the two-photon tomography, we collected the 50 μm -thick slices immediately after two-photon tomographical imaging. We then amplified the GFP signal with immunostaining. During this process, the slices were firstly incubated in blocking buffer 0.3% Triton (Applichem, Germany) and 2% normal goat serum (NGS, Vector, S-1000-L020) in PBS (0.9% NaCl, 0.01 M phosphate buffer, pH 7.4) for an hour. Then, we incubated the sample for

48 h shaking at 4 °C in the primary anti-GFP antibody (rabbit polyclonal 1:5000, Abcam 290, UK) together with 0.3% Triton X-100 in PBS, followed by two washes with PBS for 10 min. Subsequently, the slices were placed in the secondary antibody (goat anti-rabbit conjugated to Alexa 488 1:200, Life Technologies A-11012) together with 0.3% Triton X-100 in PBS for 2-2.5 h at room temperature. At the final step, the slices were washed in PBS 3 times for 10 min and mounted on Superfrost slides using ,4-Diazabicyclo[2.2.2]octane (DABCO, Sigma-Aldrich D27802, USA) as mounting medium. Images of the stained sections were obtained using the two-photon tomography microscope at the same laser power levels as the original imaging, enabling direct comparison.

3.5.9 Data availability

The data and code will be made freely available in the Open Access CERN database Zenodo: <https://zenodo.org/communities/petersen-lab-data> with a doi hyperlink.

3.6 Additional information

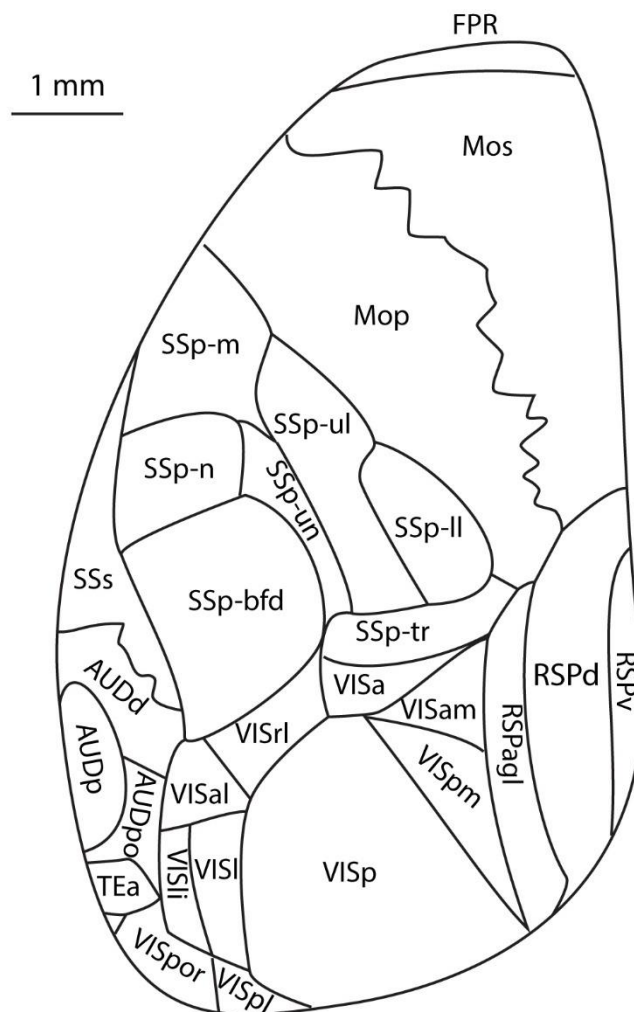


Figure 3-9 Supplementary Figure 1. Anatomical locations of different cortical areas in a horizontal view of the mouse dorsal cortex.

For definitions of area acronyms, please see Supplementary Table 1.

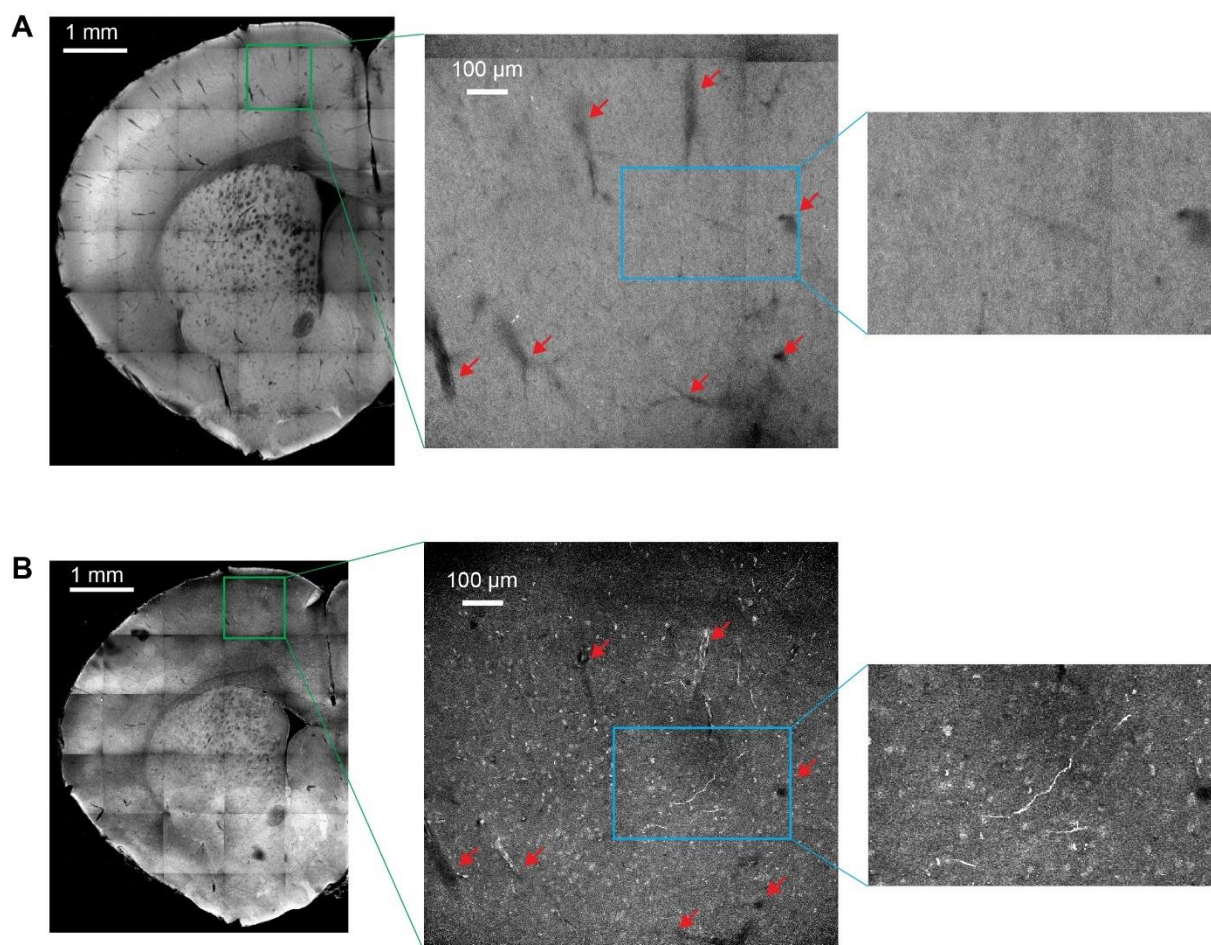


Figure 3-10 Supplementary Figure 2. Example section demonstrating that antibody staining reveals axonal structures not found in the two-photon tomography.

(A) Left, overview image acquired with two-photon tomography with a region of interest (ROI) indicated with a green frame. Middle, zoomed in view of the green ROI with arrows indicating blood vessel landmarks and a smaller ROI indicated with a blue frame. Right, zoomed in view of the blue ROI. (B) Left, overview of the same brain slice as (A) after signal amplification with anti-GFP antibody, mounted on a glass coverslip and imaged with the two-photon tomographic microscope. A region of interest (ROI) is indicated with a green frame. Middle, zoomed in view of the same green ROI as in (A), identified by blood vessel patterns (arrows). Both images are averaged images of 50 μm z-stacks. Note that the brain slice underwent shrinking and distortions during the immunohistochemical staining and mounting, thus landmarks do not match perfectly. A smaller ROI, similar to (A) is indicated with a blue frame. Right, zoomed in of the blue ROI. Note the presence of labelled axon segments in B that are not visible in A.

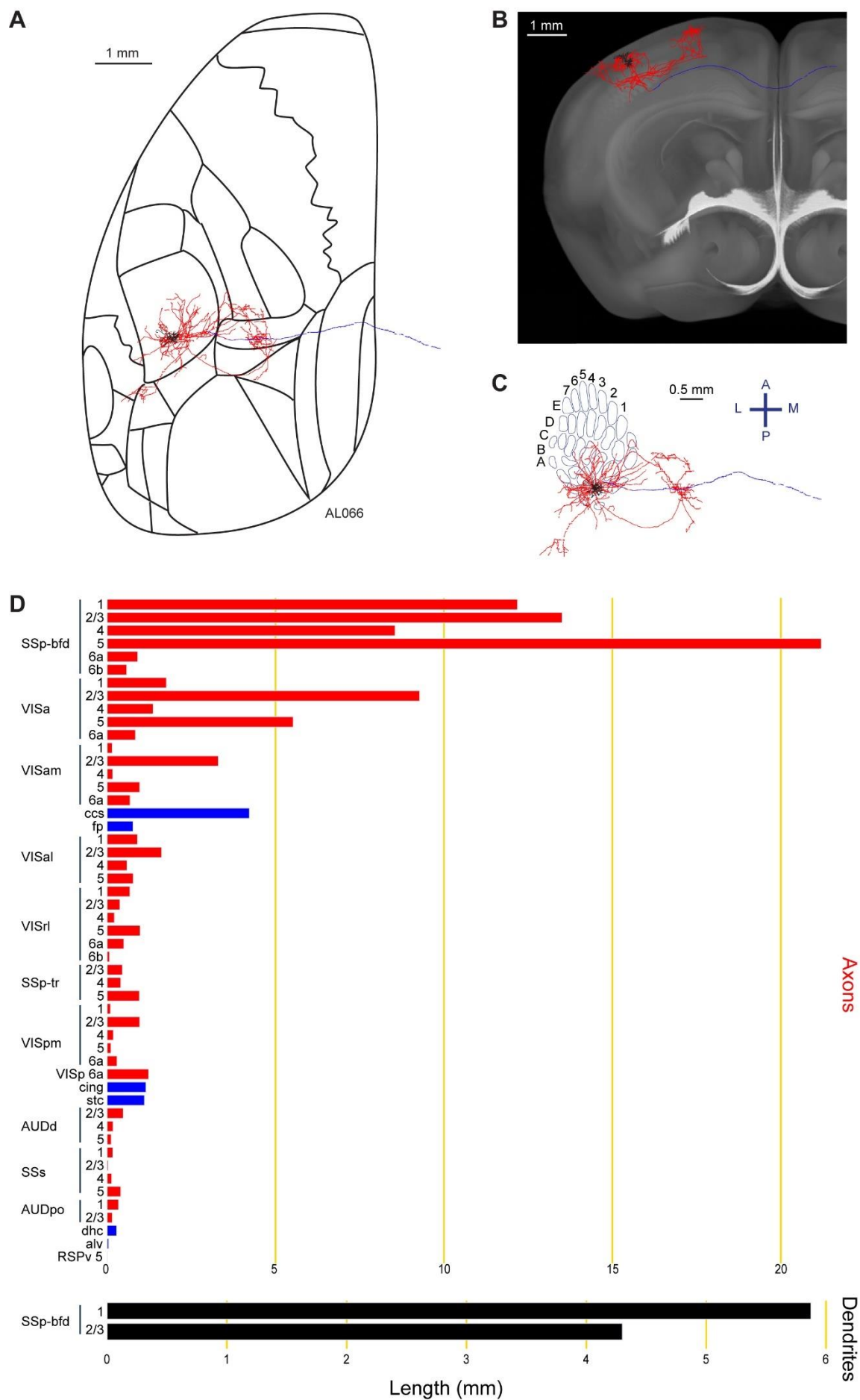


Figure 3-11 Supplementary Figure 3. Reconstruction and quantification of example neuron AL066 with projections to visual areas.

(A) Maximum projection of reconstructed axon and dendrites in horizontal view, aligned to the Allen Mouse CCFv3 to indicate boundaries between cortical regions. (B) Maximum projection of axon and dendrites in coronal view. (C) Maximum projection of axons and dendrites in tangential view (rotated 30 degrees) over the barrel field. The cell body was located in the B1 barrel column. (D) Quantification of axonal (top) and dendritic (bottom) length in respective brain regions identified by the Allen Mouse CCFv3. Dendrites are shown in black; axons in neocortical grey matter are shown in red; and axons in white matter are shown in blue.

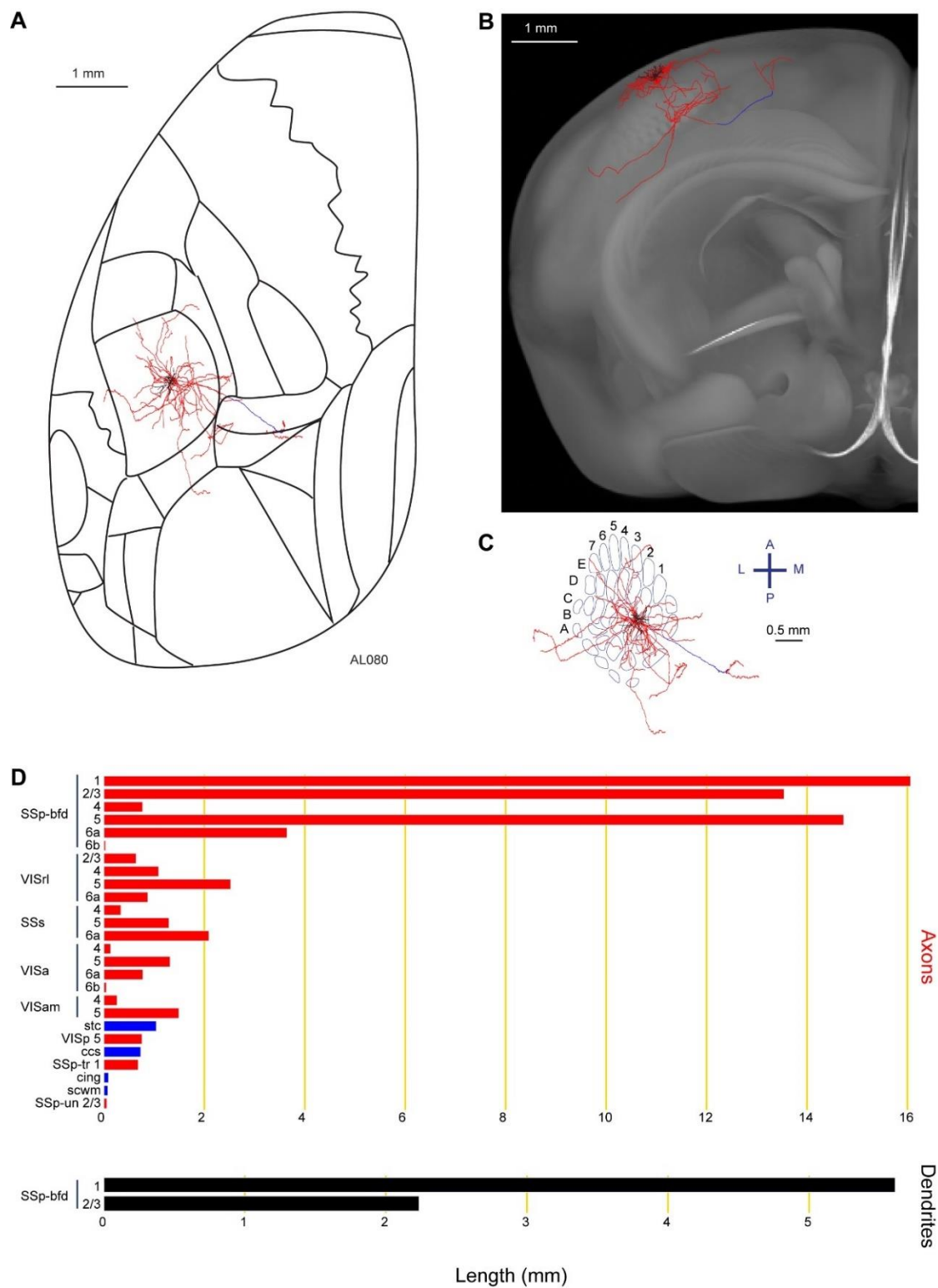


Figure 3-12 Supplementary Figure 4. Reconstruction and quantification of example neuron AL080 with projections to visual areas and the secondary somatosensory cortex.

(A) Maximum projection of axon and dendrites in horizontal view. (B) Maximum projection of axon and dendrites in coronal view. (C) Maximum projection of axon and dendrites in tangential view (rotated 30 degrees) over the barrel field. The soma of the neuron was located in the septa between the C2 and D2 barrel columns. (D) Quantification of axonal (top) and dendritic (bottom) length in respective brain regions identified by the Allen Mouse CCFv3. Dendrites are shown in black; axons in neocortical grey matter are shown in red; and axons in white matter are shown in blue.

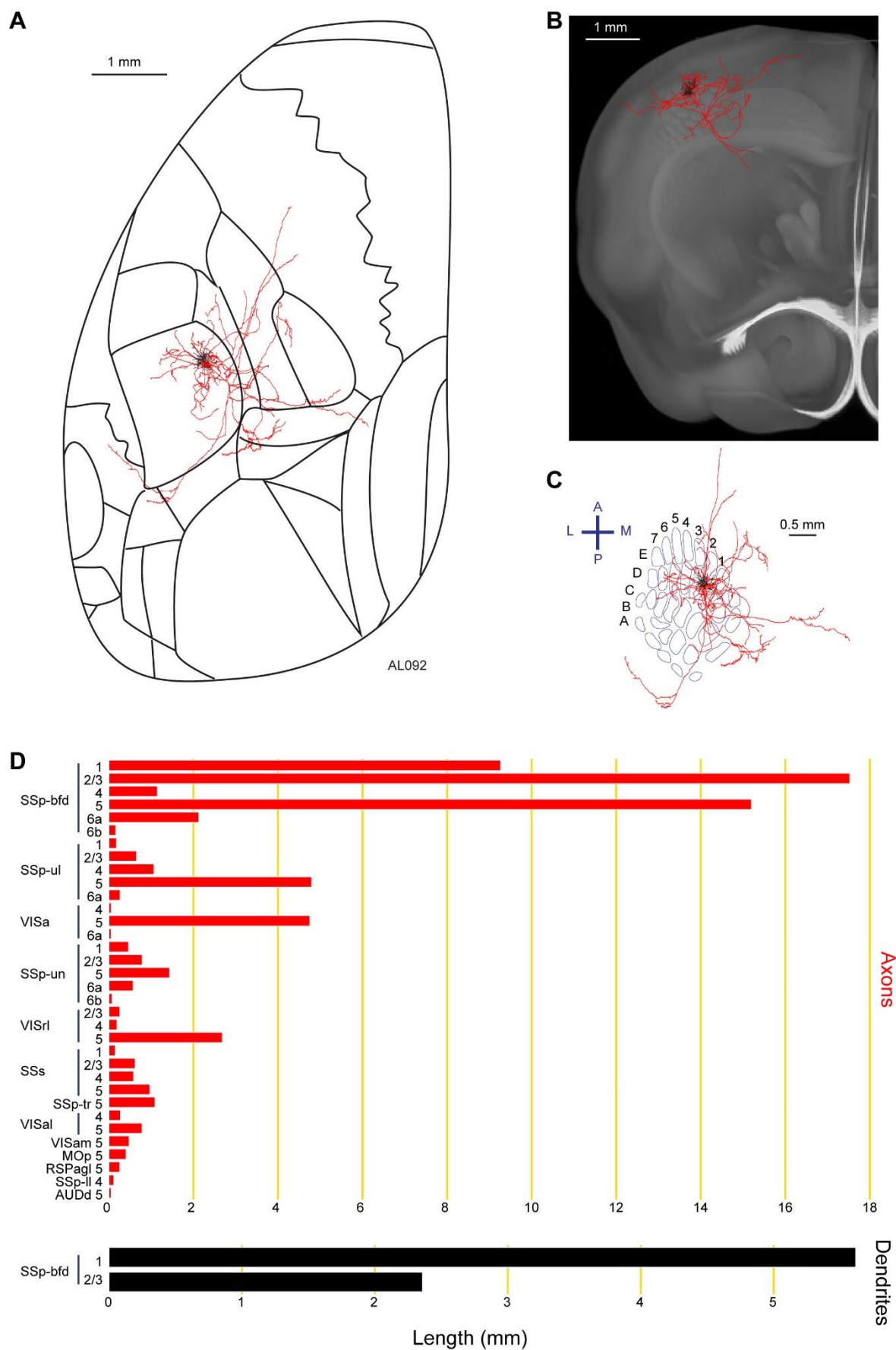


Figure 3-13 Supplementary Figure 5. Reconstruction and quantification of example neuron AL092 with projections to the primary somatosensory area upper limb area.

(A) Maximum projection of axon and dendrites in horizontal view. (B) Maximum projection of axon and dendrites in coronal view. (C) Maximum projection of axon and dendrites in tangential view (rotated 30 degrees) over the barrel field. The cell body was located in the D3 barrel column. (D) Quantification of axonal (top) and dendritic (bottom) length in respective brain regions identified by the Allen Mouse CCFv3. Dendrites are shown in black; and axon in neocortical grey matter is shown in red.

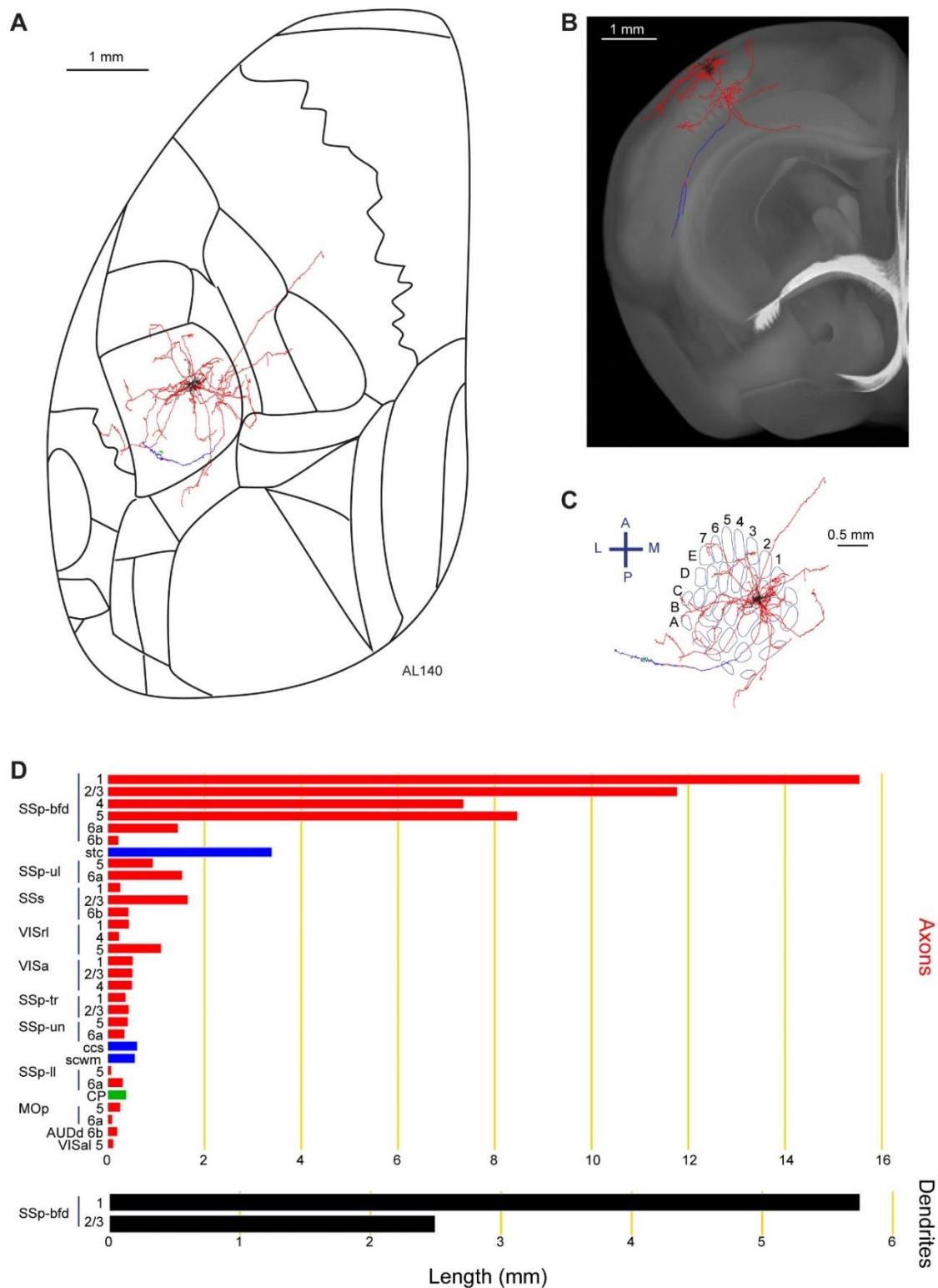


Figure 3-14 Supplementary Figure 6. Reconstruction and quantification of example neuron AL140 with projections to the primary somatosensory upper limb area, the secondary somatosensory area and visual areas.

(A) Maximum projection of axon and dendrites in horizontal view. (B) Maximum projection of axon and dendrites in coronal view. (C) Maximum projection of axon and dendrites in tangential view (rotated 30 degrees) over the barrel field. The cell body was in the D2 barrel column. (D) Quantification of axonal (top) and dendritic (bottom) length in respective brain regions identified by the Allen Mouse CCFv3. Dendrites are shown in black; axon in neocortical grey matter is shown in red; axon in striatum is shown in green; and axon in white matter is shown in blue.

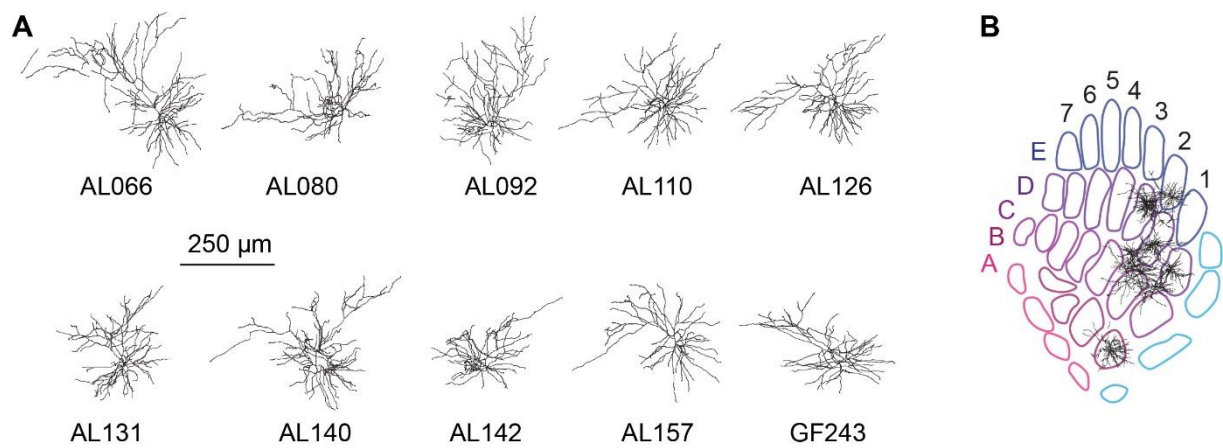


Figure 3-15 Supplementary Figure 7. Dendritic morphologies.

(A) Reconstruction of dendrites of all neurons in coronal representations ($n = 10$). (B) Location of dendrites superimposed on top of the mouse barrel field with arcs (1-7) and rows (A-E) labelled.

Chapter 4 Cell class dependent, layer specific projections from primary and secondary whisker-related somatosensory cortices.

Text and figures in this chapter are a part of a manuscript in preparation

Cell class dependent, layer specific projections from primary and secondary whisker-related somatosensory cortex.

Yanqi Liu, Lucas Délez, Sylvain Crochet, Carl C H Petersen

Being the first author, I am directly responsible for almost all procedures involved in sample preparation, image acquisition, data analysis and manuscript preparation. Training of the image segmentation network and part of the post-segmentation processing was done in collaboration with Lucas Délez, a Master's student under my supervision.

4.1 Introduction

Neurons are a basic functional unit of the nervous system that allow a wide range of functions related to the organisms' survival. In the neocortex, excitatory neurons receive information with their localized dendrites while sending information to other neurons in nearby and remote brain regions with their long axons. Axonal projection patterns are key anatomical features that contribute towards categorization of cell class. Various connectomes projects and single neuron reconstructions are underway to identify circuits in the mouse brain (Gong et al. 2013; Zingg et al. 2014; Oh et al. 2014; Han et al. 2018; Winnubst et al. 2019; Peng et al. 2021; Liu et al. 2022).

Parallel to the cerebral cortex, a generic six-layered cortical laminations can be observed based on the distribution of cell bodies and fibers. Such layering pattern differs greatly between patches on the cortex and allows identifications of cortical regions. In the mouse whisker-related primary somatosensory cortex (SSp-bfd), Layer 1 (L1) is composed of mostly interneurons and neural processes. Layer 2/3 (L2/3) contains pyramidal neurons that project both locally and over long-distances to other cortical and striatal regions. Specialized structures, 'barrels', can be found in layer 4 (L4) that are formed by organized innervations from the first order thalamic regions. The barrels are organized somatotopically such that each whisker has a corresponding barrel. Neurons in L4 are of pyramidal or stellate type that mostly send their axons locally to L2/3 and layer 5 (L5) as well as other layers but receive little intra-columnar excitation in return. L5 neurons are of pyramidal type and receive inputs from higher-order thalamic centers. A further division of L5 into upper L5 (L5a) and lower L5 (L5b) are based on the projection targets of its neurons. L5a neurons project both locally and remotely to other cortical and striatal regions. In comparison, L5b neurons project send dense

projections to subcortical and brain stem regions. Finally Layer 6 (L6) pyramidal neurons project mainly to thalamic regions but also show innervations in the cortex (Thomson 2010; Bosman et al. 2011; Feldmeyer 2012; K. D. Harris and Mrsic-Flogel 2013; Petersen 2019; Staiger and Petersen 2021).

Excitatory cells may be characterized also by their connectivity. Neurons that project to ipsilateral and contralateral telencephalon, are categorized as intra-telencephalic (IT). These neurons can be found in layers 2/3 and 5a but also in fewer amounts in L4 and L6. The pyramidal tract (PT) neurons send projections to ipsilateral cortex, striatum and thalamus as well as to the brainstem and spinal cord. These neurons are found primarily in L5b. In L6, cortical thalamic (CT) neurons are found and they extend their axons primarily to the ipsilateral thalamus (K. D. Harris and Mrsic-Flogel 2013; Gerfen, Paletzki, and Heintz 2013; K. D. Harris and Shepherd 2015; Petersen 2019).

Systemic screening of molecular markers now provides a repertoire of mouse lines for cell-type specific manipulation. Cortical expression patterns for certain genetic markers show region and layer specificities. Various groups generated transgenic mouse lines and carefully evaluated their expression pattern and projection type. In the cortex, the *Ntsr1* and *Ctgf* genes show specific expression in L6, *Sim1* and *Fzf2* is a strong indicator of PT type neurons in L5b, *Tlx3* and *Efr3a* is highly specific for L5 IT type neurons, and *Rbp4* is a mixture of both PT and IT type neurons in L5 (Gerfen, Paletzki, and Heintz 2013; E. J. Kim et al. 2015; J. A. Harris et al. 2014; Matho et al. 2021). In addition, *Scnn1a* and *Rorb* expression show layer specific specificity in L4. Genes such as *Rasgrf2*, *Cux1* and *Sepw1* are generally considered a marker for L2/3 (Madisen et al. 2010; J. A. Harris et al. 2014; Matho et al. 2021). These transgenic lines are excellent tools toward region-specific and cell-type specific circuit level characterizations.

Volumetric brain imaging is another critical step for the establishment of projection maps. Compared to the traditional slicing and mounting approach, whole-brain imaging offers advantages such as limited tissue distortion and automated alignment between tissue sections. Microscopy methods such as the serial two-photon tomography, the fluorescent micro-optical sectioning tomography and the light-sheet fluorescent microscopy are commonly used for this purpose (Ragan et al. 2012; Gong et al. 2013; Osten and Margrie 2013; Voigt et al. 2019). In combination with whole-brain imaging, the development of several whole-brain clearing procedures such as CUBIC, Clarity, and iDISCO further enhances image quality (Susaki et al. 2014; Tomer et al. 2014; Renier et al. 2014). Typically, the resulting image stacks are comprised of thousands of planes and the total volume can range from tens of gigabytes to terabytes depending on the resolution. Identifying structures of interest among these enormous volumes quickly evolves beyond manual capacities. However, automated procedures inspired from the field of computer vision are emerging to perform this otherwise impossible task (Quan et al. 2016; Falk et al. 2019; Friedmann et al. 2020; Tyson et al. 2021; Gongwer et al. 2022).

Mice rely heavily on their whiskers to sense their immediate environments. They have developed highly specialized system for whisker sensation such that somatotopy is maintained at multiple levels as information travels from the whisker follicle, trigeminal ganglion, trigeminal nucleus, thalamus and finally the SSp-bfd (Petersen 2007; Bosman et al. 2011;

Feldmeyer 2012; Staiger and Petersen 2021). Previous studies reported neurons in the SSp-bfd project to various cortical and subcortical regions such as the whisker related secondary somatosensory cortex (SSs), motor cortices, striatum, thalamus, and brainstem regions (Petreanu et al. 2007; Aronoff 2008; Yamashita et al. 2018; Mao et al. 2011; Oh et al. 2014; Zingg et al. 2014; C. Guo et al. 2017; Petersen 2019; Liu et al. 2022). Most of these studies involved bulk injections of tracers that are not cell-type specific or involved simple inspection to identify anatomical regions. The SSs also represents whisker information in a somatotopic manner and is activated nearly simultaneous with the SSp-bfd upon whisker stimulation (Aronoff et al., 2010; Esmaeili et al. 2021; Matteucci et al. 2022). However, there are much fewer studies that examines innervation patterns from this region. Studies focused on the SSs projections reported target regions in the SSp-bfd, frontal motor regions, and multisensory region caudal lateral to the SSs (Minamisawa et al. 2018; Santiago et al. 2019). The rodent whisker system is a great model to study sensory processing in the brain.

In this report, we aim to map out projection targets of the SSp-bfd and SSs regions in a cell-type specific and layer-specific manner. In combination of reporter virus injections, we take advantage of the *Rasgrf2-dCre*, *Scnn1a-Cre*, *Tlx3-Cre*, *Rbp4-Cre*, *Sim1-Cre* and the *Ntsr1-Cre* driver lines to achieve layer and cell-types specific labeling. We enhance signal intensity using immunolabeling-enabled three-dimensional imaging of solvent-cleared organs (iDISCO, Renier et al. 2014) in conjunction with mesoscale selective plane imaging microscopy (MesoSPIM, Voigt et al. 2019) to acquire volumetric brain images. Finally, axonal extensions were quantified using a three-dimensional (3D) convolutional network (TrailMap, Friedmann et al. 2020) and registered to the Allen Brain Institute Mouse common coordinate frame work (CCF, Wang et al. 2020).

4.2 Results

4.2.1 Sample preparation and analysis workflow

We developed frameworks for sample preparation, imaging and analysis methods to map cell-type specific axonal projections (Figure 4-1 to Figure 4-4) (N= 38 mice). To label specific populations of neurons, we used transgenic mouse lines *Rasgrf2-dCre*, *Scnn1a-Cre*, *Tlx3-Cre*, *Rbp4-Cre*, *Sim1-Cre* and *Ntsr1-Cre*. We then identified the SSp-bfd and SSs through intrinsic optical imaging (Ferezou et al. 2007) and injected Cre-dependent reporter viruses at depths corresponding to reported expression locations. After 4 weeks of expressions, brains were extracted and treated through iDISCO for signal amplification and clearing. Volumetric images were obtained using a MesoSPIM and registered to the Allen mouse brain CCF (Wang et al. 2020) with elastix (Klein et al. 2010; Shamonin 2013).

Injection sites were then segmented semi-automatically using Ilastik (Berg et al. 2019) (Figure 4-2A). Samples with at least 80% of injection site voxels located inside either SSp-bfd or SSs were included in the current data set (Figure 4-2A). We approximated the injection volume as a spherical shape to estimate the injection site radius. The injection radius and the

injection site voxel contribution for qualified samples are presented in Figure 4-2C and Figure 4-2E.

The injection center for SSp-bfd was 3.24 ± 0.07 mm, -1.58 ± 0.04 mm (mean \pm SEM) (Figure 4-2B). The injection site radius for SSp-bfd was 223.7 ± 9.6 μ m (Figure 4-2C). For SSp-bfd samples, percentage of voxels located in SSp-bfd are: Rasgrf2-dCre= 100%, 89.6%, 100%, Scnn1a-Cre = 100%, 100%, 100%, 100%, Tlx3-Cre= 100%, 100%, 100%, Rbp4-Cre= 100%, 100%, 100%, Sim1-Cre= 83.8%, 100%, 99.75%, and Ntsr1-Cre= 98.4%, 100%, 99.7% (Figure 4-2D).

The injection center for SSs was 4.0 ± 0.04 mm, -1.63 ± 0.04 mm (mean \pm SEM) (Figure 4-2B). The injection site radius for SSs was 197.5 ± 7.9 μ m (Figure 4-2E). For these samples, percentage of voxels located in SSs are: Rasgrf2-dCre= 94%, 99.8%, 98.9%, Scnn1a-Cre= 97.6%, 82.3%, 99.2%, Tlx3-Cre= 93.9%, 95.6%, 84.3%, Rbp4-Cre= 94%, 85.8%, 93.6%, Sim1-Cre= 86.2%, 92.8%, 100%, 100%, and Ntsr1-Cre= 100%, 98.1%, 81.3% (Figure 4-2F).

We observed that layer 1 (SSp-bfd1 or SSs1) contains injection site voxels for Rasgrf2-dCre (Figure 4-2D and Figure 4-2F), this is likely due to dense dendrites of layer 2/3 neurons. In combination with image down sample required for registration, nearby layer 1 voxels appear as bright clusters and could not be separated from the injection site in the below layer 2/3.

For each sample, pixels containing axons were segmented on the original image using TrailMap (Friedmann et al. 2020) (Figure 4-4A and B). We followed the author's guidelines for transfer learning (described on <https://github.com/albert597/TRAILMAP>) to familiarize the network with our own samples. In brief, we generated image sub-stacks and annotations (Figure 4-3 Image substack and labels for training Traillmap network and training curvesA) that captures a wide range of axon appearances to further train the network provided by the TrailMap authors. A total of 32 image sub-stacks from 8 samples and their annotations were included in the training, with 70% assigned as the training data set and 30% as the validation data set. The annotations consisted of hand labeled pixels containing axons and pixels containing artifacts as two separate categories. These image substacks were selected to encompass different morphologies of axons and artifacts. Training of the network was done in Python 3.9 with Tensorflow version 2.8.0 on a GPU (NVIDIA GeForce RTX 3090). Multiple models from many training sessions were examined visually to select the best one. The training session consisted of 100 epochs and the model that returned the lowest validation loss (using cross-entropy as the loss function) was selected, training and validation loss curves are shown in Figure 4-3 Image substack and labels for training Traillmap network and training curvesB. The resulting segmentation was skeletonized in to different bins based on the segmentation confidence and a weighted sum was performed to prevent disconnections arising from dimmer axons as described in Friedmann et al. 2020. Individual connected components of the skeleton with sizes of 10 000 pixels or above were kept and inspected visually to further remove artifacts (Figure 4-4C and D). Finally, axon skeletons were registered to the Allen brain CCF using parameters obtained when registering the image to the CCF atlas.

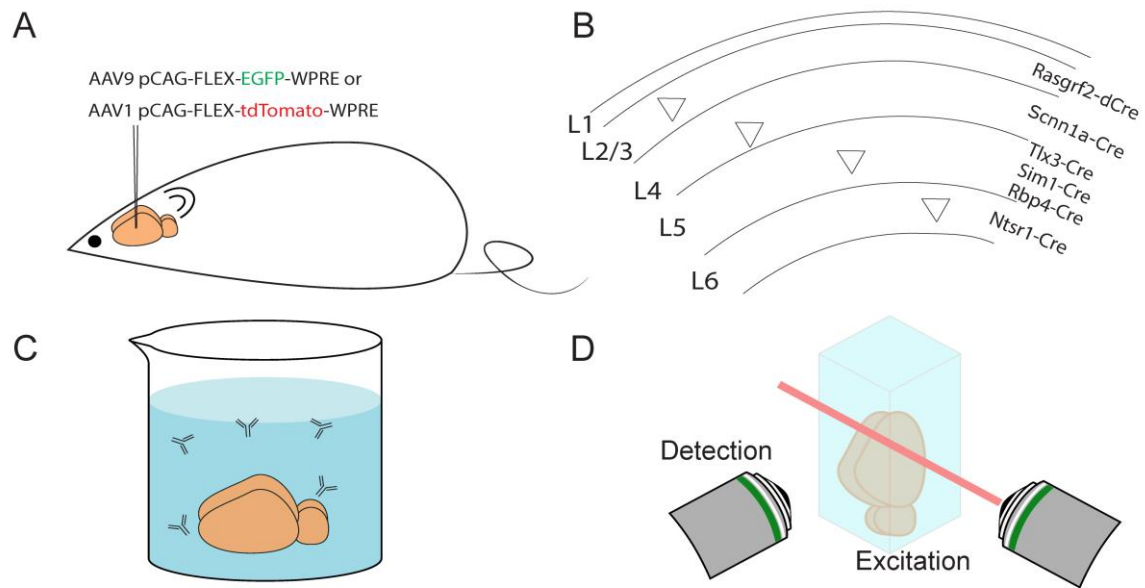


Figure 4-1. Sample preparation and injection site identification.

A) Injection of Cre-dependent reporter virus encoding for enhanced green fluorescent protein (EGFP) or tdTomato to the *SSp-bfd* or *SSs* in layer specific Cre-driver mice. B) Schematic of layer restricted expression patterns of the Cre-driver lines as reported by previous literature. *Rasgrf2* expression in layer 2/3 neurons, *Scnn1a* expression in layer 4 neurons, *Tlx3*, *Sim1*, and *Rbp4* represents different populations of layer 5 neurons, and *Ntsr1* expression for layer 6 neurons. C) iDISCO procedure for whole brain immunolabeling and clearing. This step enhances signal and renders the sample semi-clear for light sheet imaging. D) Volumetric imaging by MesoSPIM, a meso-scale light sheet microscope.

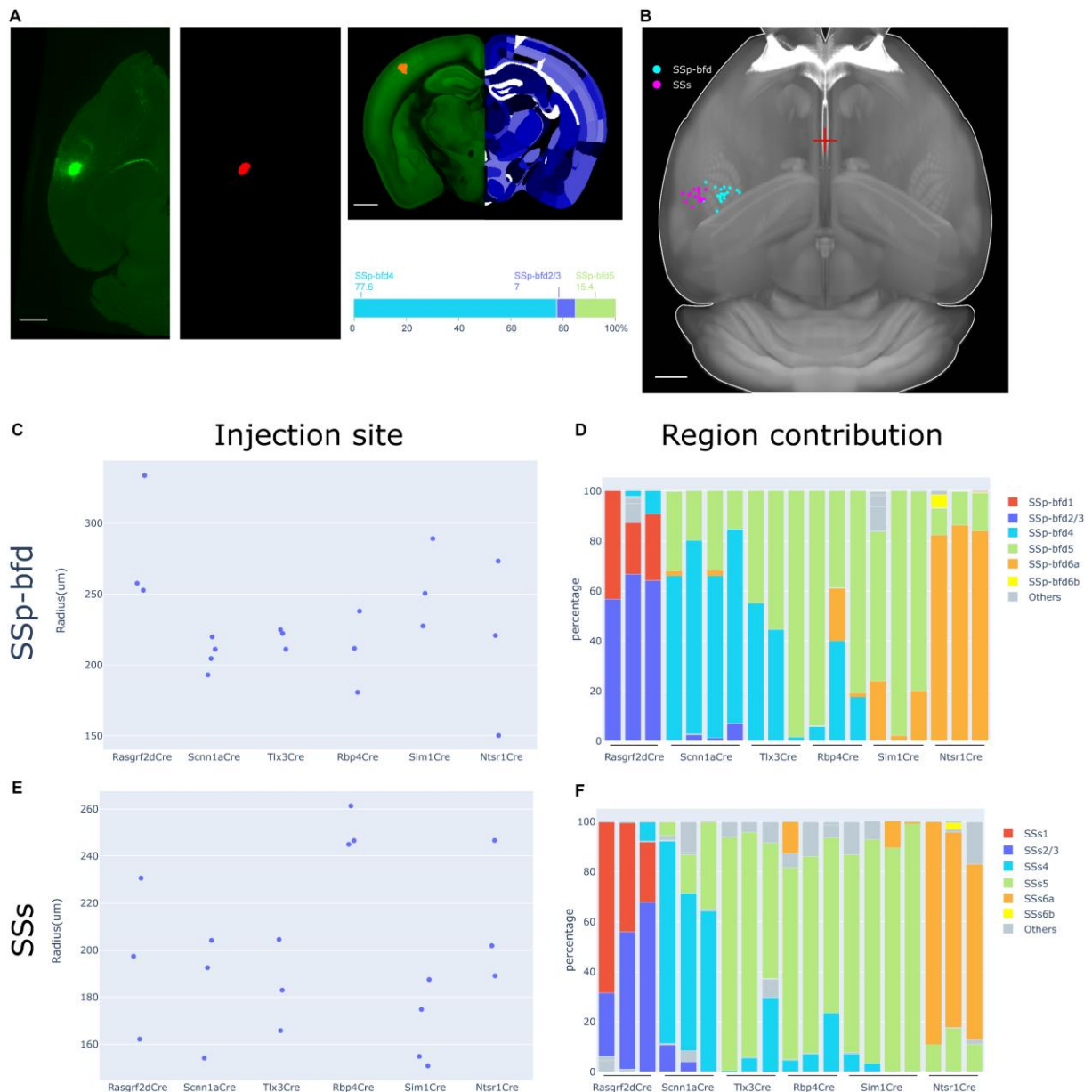


Figure 4-2 Identification of injection site size and location for SSp-bfd and SSs injections in the current study.

A) An example injection site segmentation and analysis for a Scnn1a-Cre sample. Left, Sample image in horizontal view after registration to Allen brain CCFv3. Middle, Semi-automatically segmented injection site. Right, top, Coronal section of the Allen brain atlas template (green) and atlas (blue) near center of injection (red). Right, bottom, Quantification of segmented voxels in % and their anatomical regions. Scale bars 1 mm.

B) Summary of injection sites for SSp-bfd (cyan) and SSs (magenta) in horizontal view. Red cross indicate location of bregma. Scale bar, 1 mm.

C) Injection site size for SSp-bfd samples calculated by approximating the injection volume as a spherical shape. Each dot represent data from an individual sample.

D) Contribution of brain regions towards injection site voxel for SSp-bfd injections. Voxels in places surrounding the region of interest are marked in grey as 'Others'.

E) Same as C but for SSs injections

F) Same as D but for SSs injections

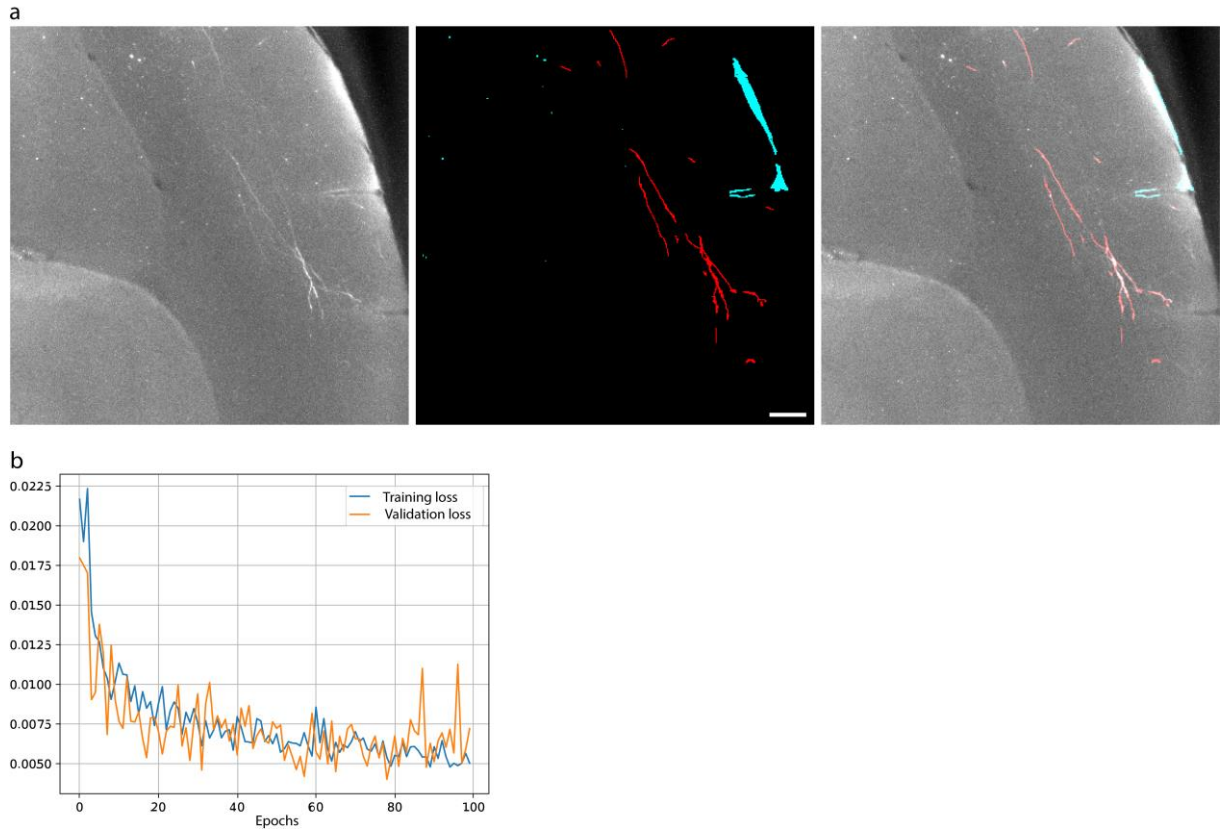


Figure 4-3 Image substack and labels for training Traillmap network and training curves

A) Left, an example image plane from an image substack used to further train the Traillmap network. This image contains axons with delineated morphologies and blood vessel artifact in the cortex. Middle, the corresponding label of the left image where red pixels indicates axons and cyan indicates artifacts. Right, overlay image of the raw image with the labels. Scale bar, 200 μm .

B) Training and validation loss values across training epochs for the final training session. The lowest validation loss occurs after the 78th training epoch and this model was used for all subsequent axon segmentation.

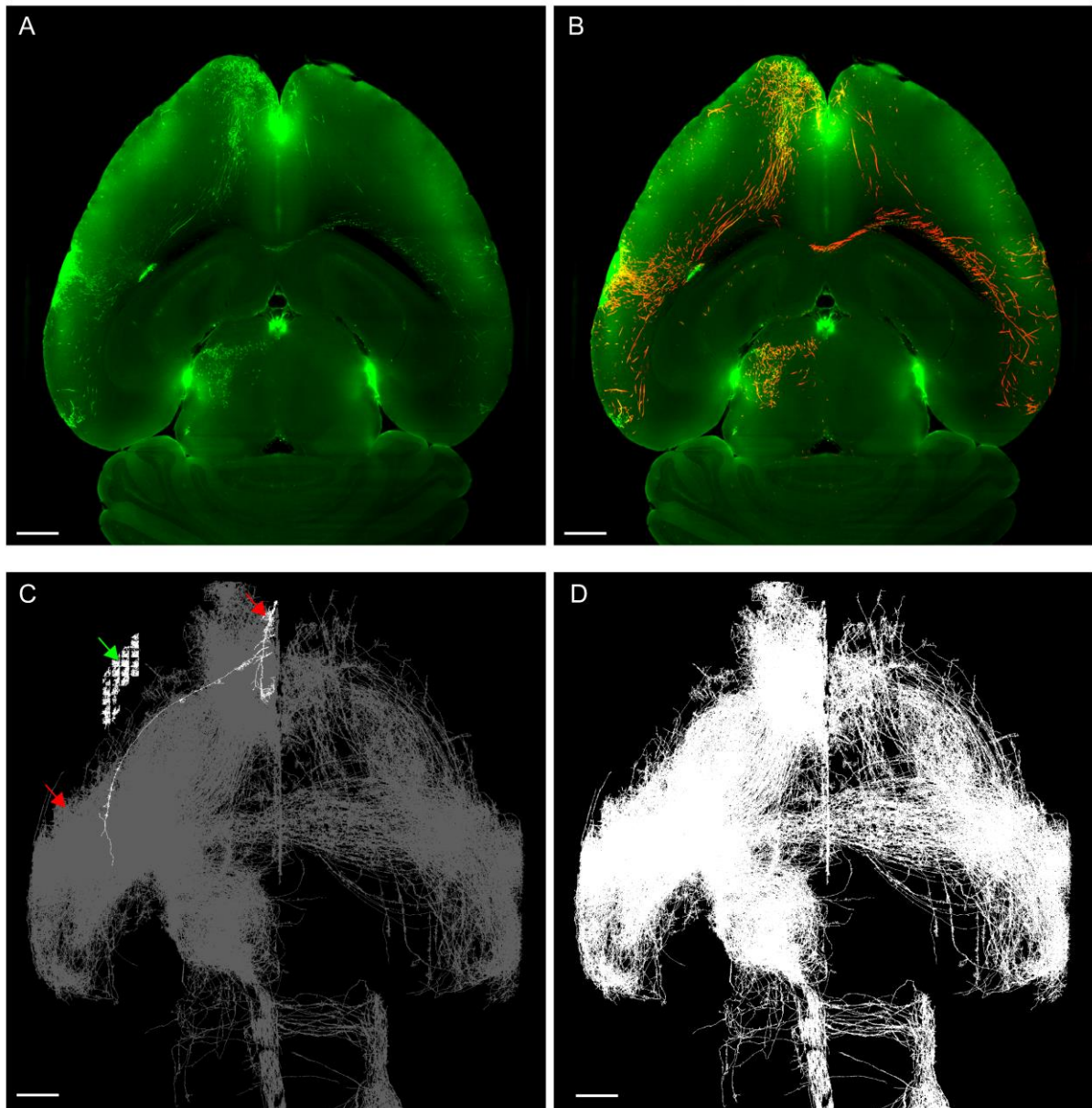


Figure 4-4 TrailMap segmentation and selections of connected components.

All images in this figure are taken from the same sample, this was a SSp-bfd injection in a Tlx3-Cre mice. A) An example raw image obtained from MesoSPIM. note the different morphologies of axons and corner artifacts. B) overlay of the left raw image (green) with output of TrailMap axon segmentation (red). C) max projected axon skeleton with 3 connected components above 10 000 voxels (two smaller component in white and a major component in grey). After careful visual inspection, the upper left component (green arrow) is identified as artifact and the other two components (red arrows) were combined as the final axon skeleton. D) Max projection of the final axon skeleton combining two red components in C.

We then tested the expressions of our reporter viruses in absence of Cre-recombinase. Samples were prepared with the same injection volume and viral vector concentrations, immunostained, cleared, imaged and analyzed in the same way but now in wild type mice. There were a handful of cell bodies being labeled but their processes were barely visible (Figure 4-5 A and C). Hence, we expect only noises would be segmented by TrailMap. This is indeed the case, connected components greater than 10 000 pixels were mainly artifacts near the midline (Figure 4-5 B and D). This would be eliminated by our final visual inspection step (Figure 4-4C). This control experiment shows that although there are Cre-independent reporter expressions, the strength of expression in axons are below detectable levels in our current paradigm.

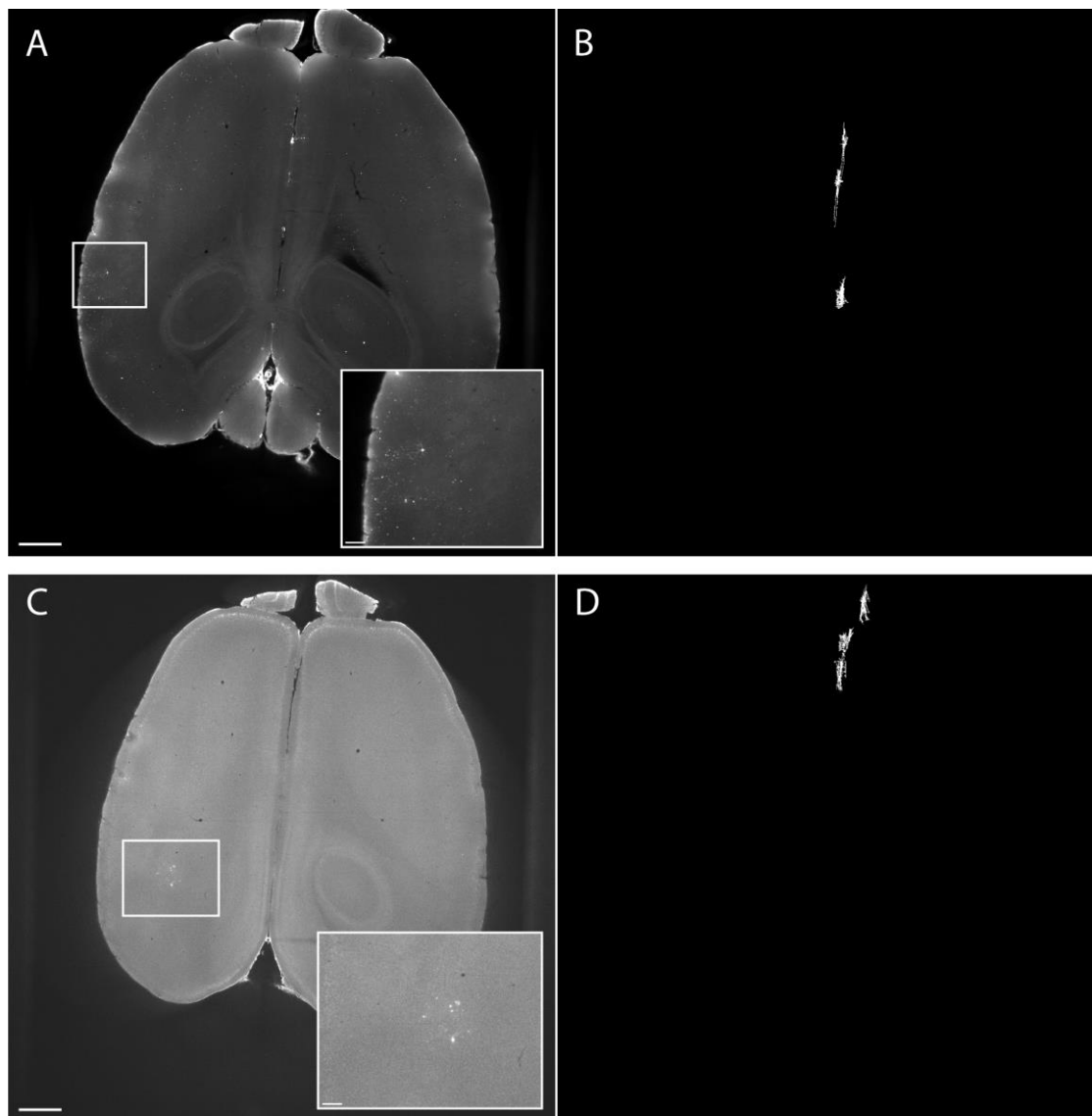


Figure 4-5 Cre-independent expression of reporter viruses and the subsequent TrailMap segmentations.

We repeated our sample preparation and analysis pipeline in wild type animals to test the cre-independent expressions of our reporter viruses. A) a raw image plane from sample injected with AAV9- FLEX-EGFP-WPRE in the SSp-bfd with region of interest indicating injection site (white box), scale bar 1 mm. Inlet, zoomed in image of the region of interest showing cell bodies with barely identifiable processes. Scale bar 200 μ m B) Max projection of connected components greater than 10 000 pixels, these are mainly composed of midline artifacts. C) Same as A but injected with AAV1-FLEX-tdTomato in the SSs.

4.2.2 Axonal projections from primary and secondary whisker related somatosensory cortex

We will describe axonal projections in brain regions in reference to the Allen Brain mouse CCF nomenclature. We begin by characterizing axons in broader brain regions such as the cerebrum, brainstem, and cerebellum and then in detail to subregions following the hierarchy shown in Figure 4-6.

In this study, results from 38 samples were included where there are 19 injections made in SSp-bfd and 19 in SSs. Samples involved for SSp-bfd and SSs were *Rasgrf2-2A-dCre* (SSp-bfd N= 3, SSs N= 3), *Scnn1a-Tg3-Cre* (SSp-bfd N= 4, SSs N= 3), *Tlx3-Cre* (SSp-bfd N= 3, SSs N= 3), *Sim1-Cre* (SSp-bfd N= 3, SSs N= 4), *Rbp4-Cre* (SSp-bfd N= 3, SSs N= 3), and *Ntsr1-Cre* (SSp-bfd N= 3, SSs N= 3), respectively. Each sample was normalized by the total amount of axons in this given sample and a group average was obtained by taking the average of all normalized samples of each group (ie. SSp-bfd injections in *Rasgrf2-dCre* mice). Average of the group averages for SSp-bfd or SSs give an overview of overall projection patterns across the six mouse lines (Figure 4-4-7). The first order impression is that projection patterns of SSp-bfd and SSs show resemblance qualitatively.

Each individual group average can be seen in Figure 4-7 with horizontal, coronal, and sagittal views. There are differential projection patterns across mouse lines for a given injection in terms of the amounts of axons in the cerebral cortex, deeper brain structures, brain stem, or regions in the contralateral hemispheres. On the other hand, differences are less obvious when comparing between the SSp-bfd and SSs injection sites in the same mouse line. Quantitative difference between SSp-bfd and SSs neurons or between transgenic lines with the same injection site will be discussed in more details in subsequent figures.

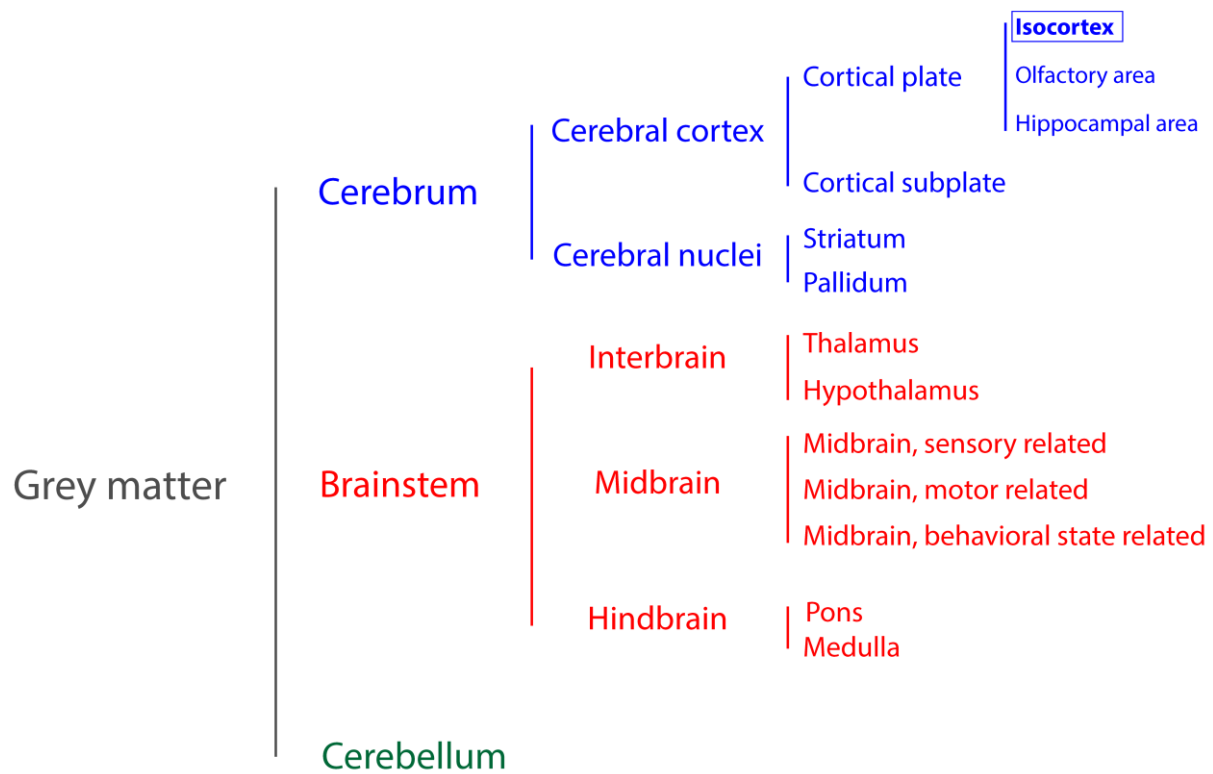


Figure 4-6 Hierarchy and Nomenclature of broad brain region categories based on the Allen brain institute mouse CCF.

Regions relevant to the current paper are expanded color coded. Detailed regarding the isocortex will be discussed in later part of the paper. Brain regions are organized as subregions to the parent region on its immediate left indicated by the vertical lines. For instance, thalamus and hypothalamus are subregions of the interbrain, which is then a part of the brain stem. In this report, we progress from left to right (broader regions to finer regions) and finally focus on regions within the isocortex.

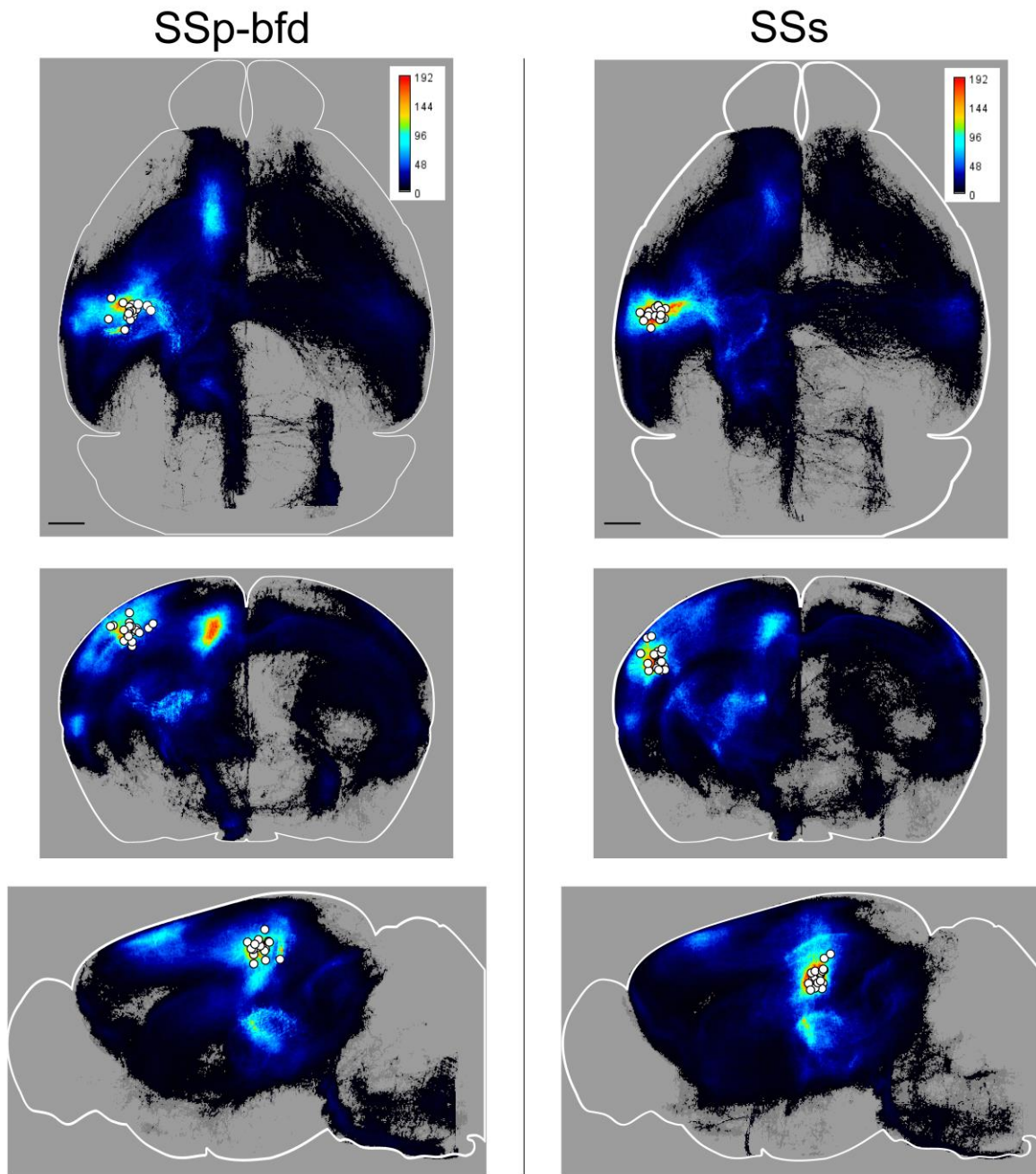


Figure 4-4-7 Overview of all SSp-bfd and SSs projections.

Averaged sum axonal projections combining all 6 mouse lines for SSp-bfd and SSs injections in horizontal, coronal and sagittal views. White dots represent the center of injection site for one injection ($N = 19$ for each site). Pixel intensity represents 10^{-6} fraction of total axons. Note that this color representation emphasizes on visualizing all axon values. Scale bars 1 mm.

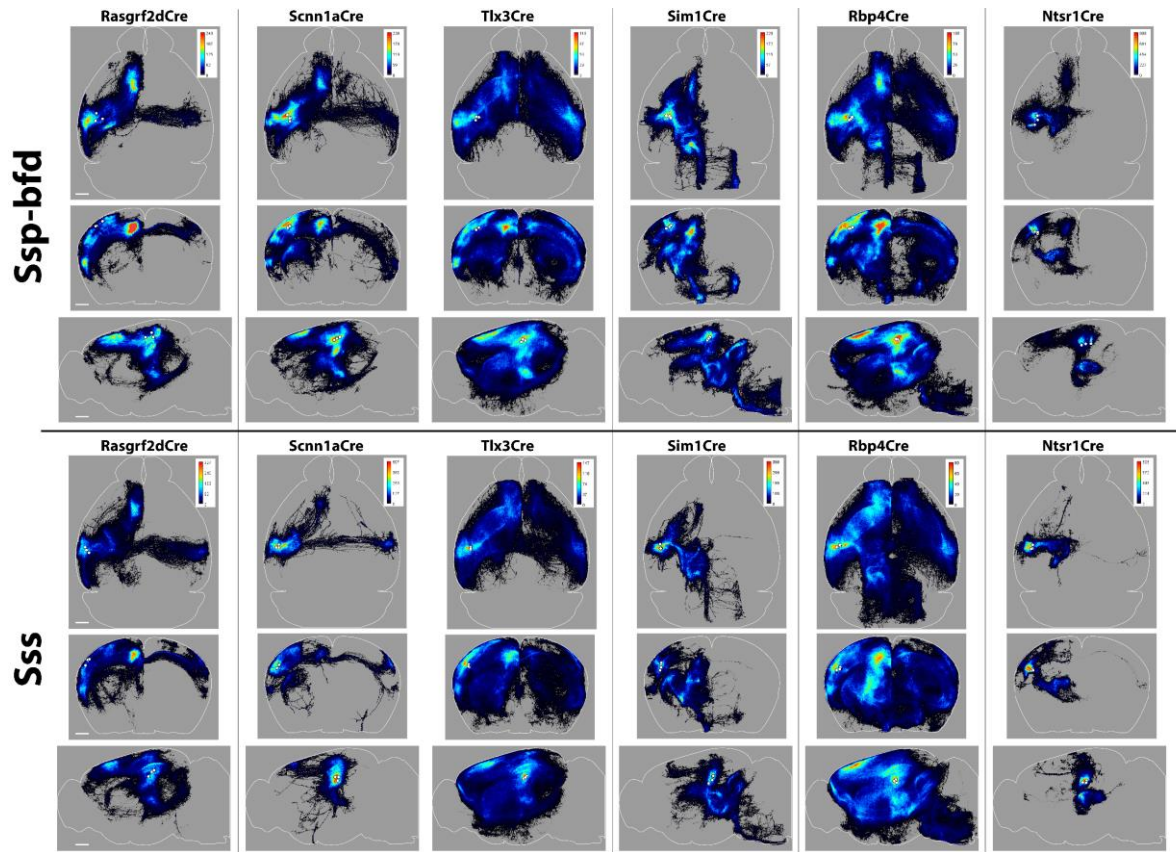


Figure 4-8 Averaged sum axonal projections for each of the six mouse lines for SSp-bfd and SSs injections.

Averaged sum axonal projections for each of the six mouse lines for SSp-bfd and SSs injections in horizontal, coronal and sagittal views. White dots represent the center of injection site for one injection. Pixel intensity represents 10^{-6} fraction of total axons. Note that this color representation emphasizes on visualizing all axon values. Scale bars 1mm.

SSp-bfd injections: Rasgrf2-dCre N=3, Scnn1a-Cre N=4, Tlx3-Cre N=3, Rbp4-Cre N=3, Sim1-Cre N=3 and Ntsr1-Cre N=3.

SSs injections: Rasgrf2-dCre N=3, Scnn1a-Cre N=3, Tlx3-Cre N=3, Rbp4-Cre N=3, Sim1-Cre N=4 and Ntsr1-Cre N=3.

Dissecting brain regions in to cerebrum, brainstem and the cerebellum allow a closer look in the axonal projection patterns (Figure 4-9). Ipsilateral to the injection sites, Rasgrf2-dCre, Scnn1a-Tg3-Cre and Tlx3-Cre samples show the majority of their axons within the cerebrum, consistent with of IT class projections. In SSp-bfd injections, the percentages of axons in the cerebrum are: $84.8\% \pm 2.9\%$ for Rasgrf2d-Cre, $84.3\% \pm 1.1\%$ for Scnn1a-Cre, $56.3\% \pm 2.3\%$ for Tlx3-Cre. In SSs injections, the percentages of axons in the ipsilateral cerebrum are: $77.7\% \pm 5.1\%$ ipsilateral for Rasgrf2d-Cre, $81.4\% \pm 11.6\%$ for Scnn1a-Cre, $70.4\% \pm 1.5\%$ for Tlx3-Cre. On the other hand, Rbp4-Cre, Sim1-Cre and Ntsr1-Cre samples axons are shared between cerebrum and brain stem. In SSp-bfd injections, the percentages of axons in the ipsilateral regions are: $55.6\% \pm 1.6\%$ in the cerebrum and $13.5\% \pm 2.8\%$ in brainstem for Rbp4-Cre, $44.5\% \pm 3.7\%$ in the cerebrum and $37.3\% \pm 2.8\%$ in brainstem for Sim1-Cre, $63.6\% \pm 14\%$ in the cerebrum and $29.7\% \pm 12.1\%$ in brainstem for Ntsr1-Cre. In SSs injections, the percentages of axons in the ipsilateral regions are: $51.3\% \pm 1.8\%$ in the cerebrum and $14.5\% \pm$

1.5% in brainstem for Rbp4-Cre, $44.6\% \pm 2.4\%$ in the cerebrum and $39.7\% \pm 2.6\%$ in brainstem for Sim1-Cre, $60.3\% \pm 5.7\%$ in the cerebrum and $31.5\% \pm 5.6\%$ in brainstem for Ntsr1-Cre.

Contralateral to the injection site, Rasgrf2-dCre, Scnn1a-Cre, Tlx3-Cre and Rbp4-Cre samples show axons in regions similar to the ipsilateral side but in lesser amounts. In SSp-bfd injections, the percentages of axons in the contralateral cerebrum are: $2.5\% \pm 1.1\%$ for Rasgrf2d-Cre, $6.9\% \pm 0.7\%$ for Scnn1a-Cre, and $33.4\% \pm 3.3\%$ for Tlx3-Cre. In SSs injections, the percentages of axons in the contralateral cerebrum are: $10.4\% \pm 3.1\%$ for Rasgrf2d-Cre, $9.4\% \pm 8.9\%$ for Scnn1a-Cre, $22.2\% \pm 1.3\%$ for Tlx3-Cre. For Rbp4-Cre samples in the contralateral side, $19.8\% \pm 3.5\%$ are in the cerebrum and $1.9\% \pm 0.2\%$ in the brainstem for SSp-bfd injections, $22.0\% \pm 2.5\%$ are in the cerebrum and $4.1\% \pm 0.4\%$ in the brainstem for SSs injections. In contrast, Sim1-Cre injections only had axons in the brain stem (SSp-bfd injections: $4.0\% \pm 0.7\%$, SSs injections: $1.6\% \pm 0.9\%$) while Ntsr1-Cre injections showed very little axons contralaterally. In general, SSp-bfd and SSs injections show similar patterns of axon distributions both contralaterally and ipsilaterally. There were no axons observed in the cerebellum this current study.

Evaluating subregions in the cerebrum and brain stem enable further comparisons of axonal projection patterns between different groups (Figure 4-10). Subregions belong to the cerebrum are: cortical plate (CTXpl), cortical subplate (CTXsp), striatum (STR), and pallidum (PAL). Those fall under brain stem regions are: thalamus, hypothalamus, sensory related midbrain (MBsen), motor related midbrain (MBmot), behavioral state related midbrain (MBsta), pons and medulla. In Rasgrf2-dCre samples, the majority of axons are present in the ipsilateral regions CTXpl ($82.7\% \pm 2.0\%$ in SSp-bfd, $75.3\% \pm 4.4\%$ in SSs) and STR ($18.4\% \pm 7.5\%$ in SSp-bfd, $19.6\% \pm 7.6\%$ in SSs) followed by the contralateral CTXpl for both SSp-bfd and SSs injections. There are more axons in the contralateral CTXpl for those injected in the SSs ($10.4\% \pm 3.1\%$) compared to SSp-bfd ($2.5\% \pm 1.2\%$). Axons are present primarily in the ipsilateral CTXpl ($72.3\% \pm 0.5\%$ in SSp-bfd, $72.8\% \pm 10.1\%$ in SSs), ipsilateral STR ($11.9\% \pm 0.6\%$ in SSp-bfd, $8.4\% \pm 1.9\%$ in SSs) and contralateral CTXpl ($6.0\% \pm 0.5\%$ in SSp-bfd, $8.9\% \pm 8.3\%$ in SSs) in Scnn1a-Cre samples for both injection sites. Tlx3-Cre samples follows a similar pattern as Scnn1a-Cre samples but with even more axons in the contralateral CTXpl ($26.3\% \pm 3.4\%$ in SSp-bfd, $19.1\% \pm 1.8\%$ in SSs) and contra lateral STR ($6.1\% \pm 0.9\%$ in SSp-bfd, $2.4\% \pm 1.0\%$ in SSs) for both SSp-bfd and SSs injections.

Brain stem subregions starts to get involved in the Rbp4-Cre, Sim1-Cre and Ntsr1-Cre mouse lines. Axons are observed in the ipsilateral thalamus ($3.4\% \pm 0.8\%$ SSp-bfd, $2.6\% \pm 0.5\%$ SSs), MBmot ($5.6\% \pm 1.2\%$ SSp-bfd, $5.2\% \pm 0.6\%$ SSs), pons ($1.3\% \pm 0.2\%$ SSp-bfd, $1.8\% \pm 0.4\%$ SSs) and bilateral medulla ($0.6\% \pm 0.07\%$ SSp-bfd and $1.3\% \pm 0.08\%$ SSs ipsilateral, $1.2\% \pm 0.1\%$ SSp-bfd and $1.7\% \pm 0.07\%$ SSs contralateral) in addition to axons in bilateral CTXpl ($47.8\% \pm 2.1\%$ SSp-bfd and $41.5\% \pm 3.1\%$ SSs ipsilateral, $14.9\% \pm 3.1\%$ SSp-bfd and $17.7\% \pm 2.6\%$ SSs contralateral) and STR ($7.6\% \pm 1.1\%$ SSp-bfd and $9.0\% \pm 1.3\%$ SSs ipsilateral, $4.2\% \pm 0.3\%$ SSp-bfd and $3.4\% \pm 0.3\%$ SSs contralateral) for Rbp4-Cre samples for both injection sites. In Sim1-Cre samples there are more axon contributions from the ipsilateral STR thalamus ($12.0\% \pm 0.7\%$ SSp-bfd, $14.9\% \pm 0.8\%$ SSs), thalamus ($9.8\% \pm 1.3\%$ SSp-bfd, $11.8\% \pm 1.1\%$ SSs) and MBmot ($15.0\% \pm 1.5\%$ SSp-bfd, $15.2\% \pm 1.3\%$ SSs) in addition to CTXpl ($32.5\% \pm 3.6\%$ SSp-bfd, 29.1%

$\pm 3.1\%$ SSs). There were also bilateral innervations from the Sim1-Cre neurons in pons ($3.7\% \pm 0.4\%$ SSp-bfd and $2.5\% \pm 0.8\%$ SSs ipsilateral, $1.0\% \pm 0.1\%$ SSp-bfd and $0.4\% \pm 0.2\%$ SSs contralateral) and medulla ($2.3\% \pm 0.2\%$ SSp-bfd and $0.6\% \pm 0.3\%$ SSs ipsilateral, $2.7\% \pm 0.8\%$ SSp-bfd and $0.8\% \pm 0.5\%$ SSs contralateral). Lastly, main projection targets for Ntsr1-Cre samples are ipsilateral CTXpl ($60.8\% \pm 13.6\%$ SSp-bfd, $54.8\% \pm 6.4\%$ SSs), thalamus ($28.9\% \pm 12.5\%$ SSp-bfd, $31\% \pm 5.5\%$ SSs), and STR ($2.6\% \pm 0.8\%$ SSp-bfd, $5.3\% \pm 0.8\%$ SSs) with almost no axons in the contralateral hemisphere. Still, there are not much obvious differences between SSp-bfd and SSs injections at this level of detail.

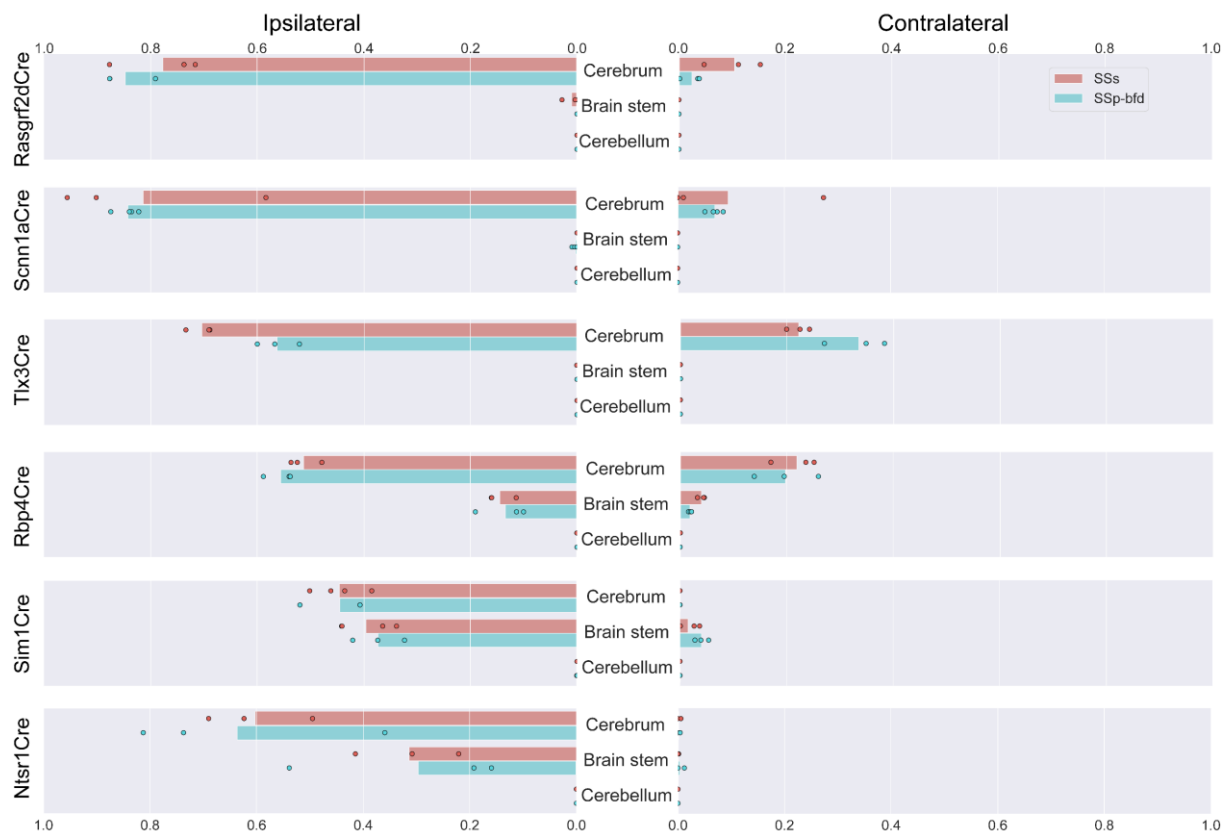


Figure 4-9 Quantification of axonal projections in cerebrum, brainstem and cerebellum.

Quantification of axonal projections in basic brain regions ipsilateral (left column) and contralateral (right column) to the injection site for SSp-bfd (blue) and SSs injections (red) for the six transgenic lines. Each dot represents data from one sample, bars represent average values, values represent the fraction of total axons.

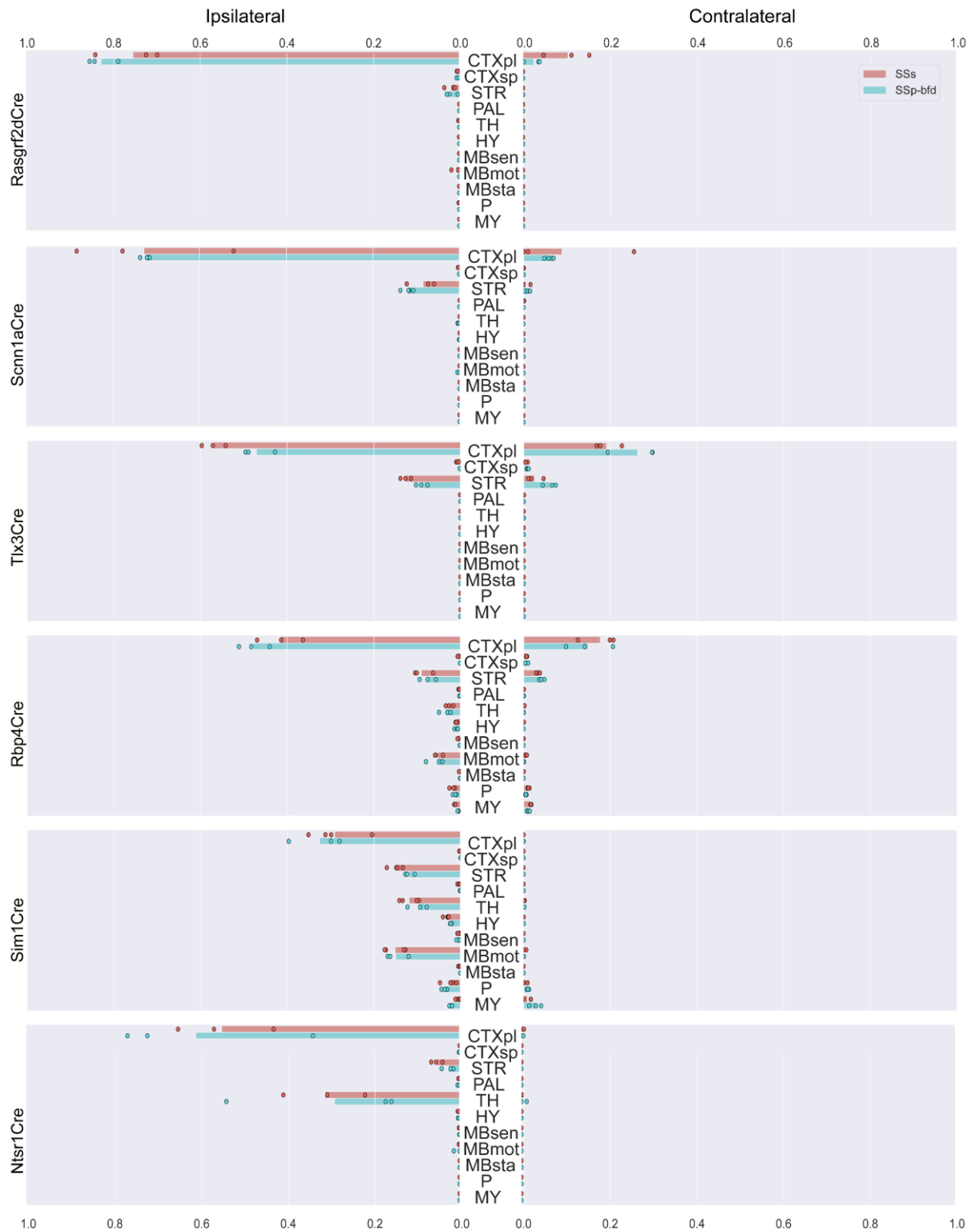


Figure 4-10 Quantification of axonal projections in brain subregions.

Quantification of axonal projections in brain subregions ipsilateral (left column) and contralateral (right column) to the injection site for SSs (red) and SSp-bfd (blue) injections for the six transgenic lines. Each dot represents data from one sample, bars represent average values, values represent the fraction of total axons. CTXpl, cortical plate, CTXsp, cortical subplate, STR, striatum, PAL, pallidum, TH, thalamus, HY, hypothalamus, MBsen, sensory related midbrain, MBmot, motor related midbrain, MBsta, behavioral state related midbrain, P, pons, and, MY, medulla.

Axons in more detailed subregions of the cerebrum and brain stem for all injections can be viewed in Figure 4-11 to Figure 4-14. Data representation in linear scale (Figure 4-11 and Figure 4-13) emphasizes strongest innervation targets while log scale representation (Figure 4-12 and Figure 4-14) redirects our attention to moderately innervated regions.

The most prominent targets for SSp-bfd injections (Figure 4-11) across all mouse lines are the secondary motor area (MOs), secondary somatosensory area (SSs) and caudoputamen (CP) ipsilaterally. Thalamic regions such as the ventral posterior complex of the thalamus (VP), the lateral group of the dorsal thalamus (LAT) and reticular nucleus of the thalamus (RT) are strong ipsilateral innervation targets for Sim1-Cre and Ntsr1-Cre expressing neurons. Brainstem regions such as the superior colliculus (SCiw, SCig), Zona incerta (ZI) and the midbrain reticular nucleus (MRN) are also strongly innervated by Rbp4-Cre and Sim1-Cre expressing neurons. On the contralateral side, there are overall less axons and in fewer brain regions. Strong contralateral target regions include the CP, MOs and SSp-bfd for Tlx3-Cre, and Rbp4-Cre injections.

Representing these data in log scale now redirects more attention to moderate-level innervation targets (Figure 4-12). The medium level ipsilateral targets for SSp-bfd injections are primary somatosensory area, lower limb, upper limb, trunk, and unspecified region (SSp-II, SSp-ul, SSp-tr, SSp-un) as well as primary motor area (MOp), and rostral visual area (VISrl) for all samples. Visceral area (VISC), dorsal auditory areas (AUDd), dorsal part of the anterior cingulate area (ACAd), posterior part of the agranular insula (Alp), temporal association area (TEa), perirhinal area (PERl), entorhinal areas (ECT), Lateral part of the entorhinal area (ENTl) and also higher order visual and auditory areas also receive part of axonal innervations from Rasgrf2-dCre, Scnn1a-Cre, Tlx3-Cre and Rbp4-Cre expressing neurons. Rbp4-Cre, Sim1-Cre, and Ntsr1-Cre also show innervations in the thalamic areas such as the Ventral group of the dorsal thalamus (VENT), Ventral posterior complex of the thalamus (VP), LAT and RT. Axons in more brainstem subregions is also revealed by the log scale representation, among which are the midbrain (MB), substantia nigra (SNr), anterior pretectal nucleus (APN), pons, pontine gray (PG), tegmental reticular nucleus (TRN) and medulla for Rbp4-Cre and Sim1-Cre injections. On the contralateral projections general follows a similar set of targets for Scnn1a, Tlx3-Cre, and Rbp4-Cre samples although in lesser amounts. For Rasgrf2-dCre samples, there are only axons observed in the contralateral somatosensory cortex (such as the SSp-bfd and the SSs) but not in the higher order cortices. In Sim1-Cre samples, axons are only present in the brainstem regions, notably the principal sensory nucleus of the trigeminal (PSV), inter polar part and oral part of the spinal nucleus of the trigeminal (SPVI and SPVO) and the medulla.

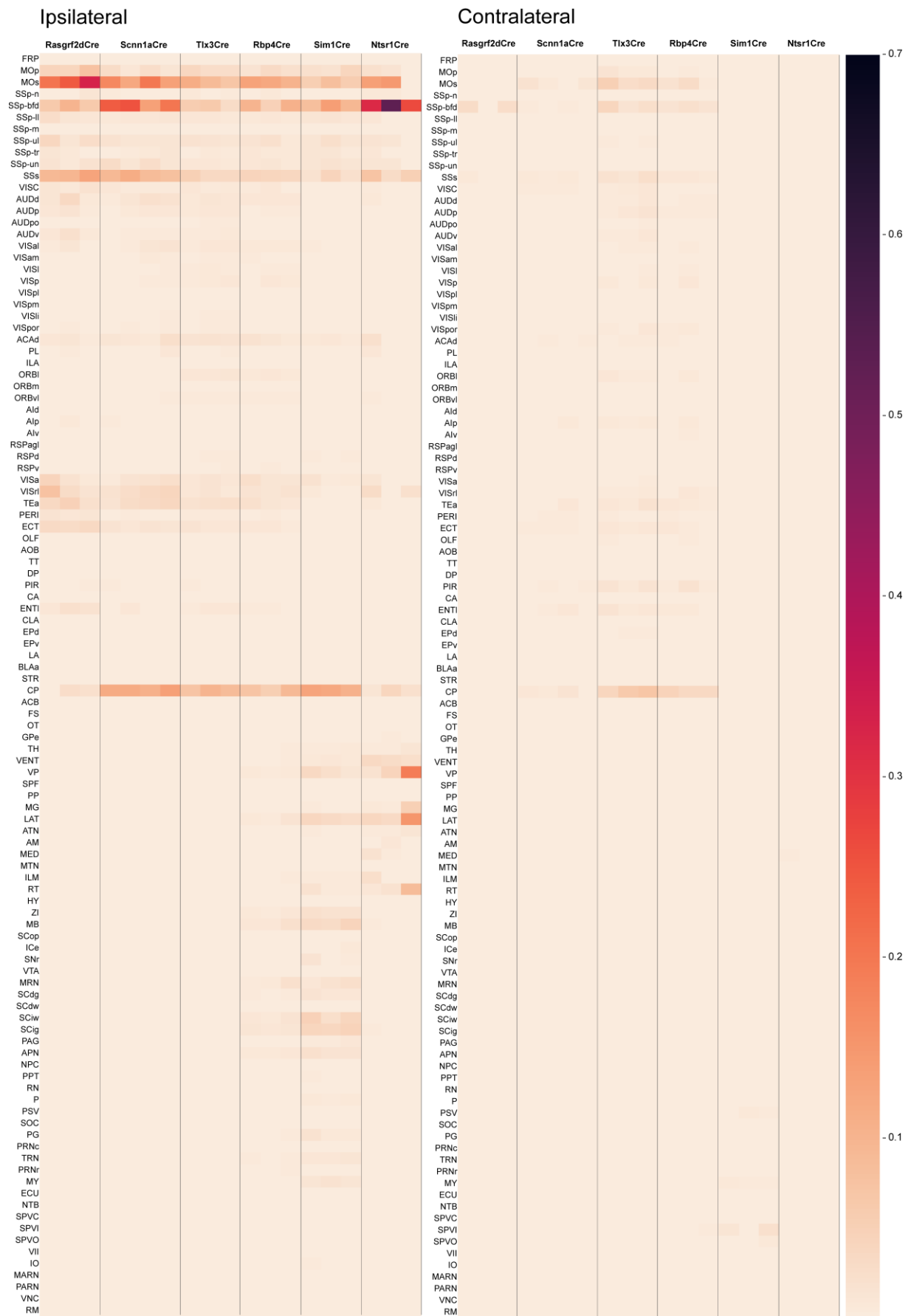


Figure 4-11 Axonal projections for samples with SSp-bfd injections in detailed subregions of cerebrum and brain stem, presented in linear color scale.

Left, ipsilateral to the injection site. Right, contralateral to the injection site. Each row represents an anatomical region and each column represents one brain. Values represent the fraction of total axons in the given sample. Subregions with greater than 0.001 fraction of axons in any sample across both hemispheres are included.

Rasgrf2-dCre N=3, Scnn1a-Cre N=4, Tlx3-Cre N=3, Rbp4-Cre N=3, Sim1-Cre N=3 and Ntsr1-Cre N=3.

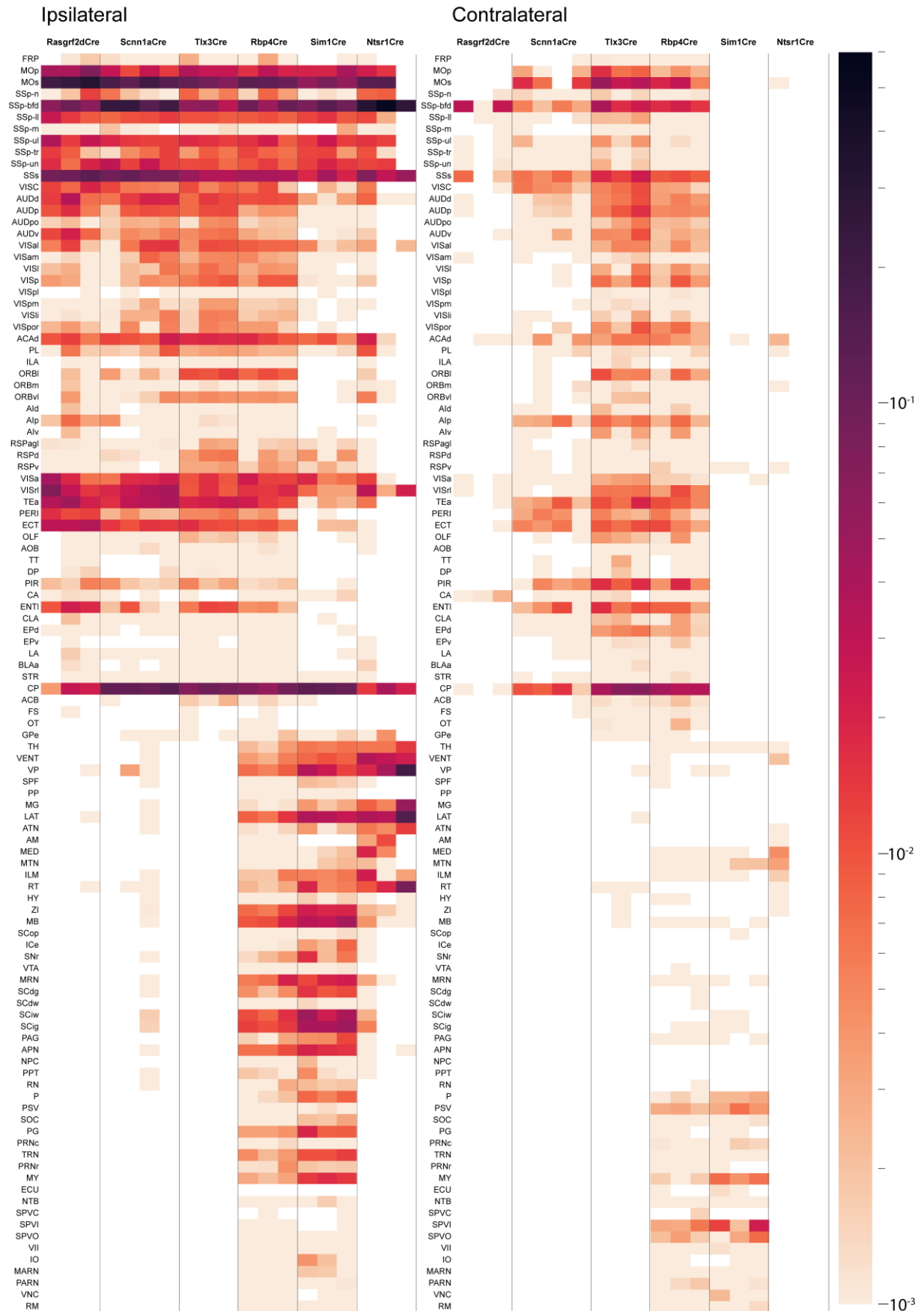


Figure 4-12 Axonal projections for samples with SSp-bfd injections in detailed subregions of cerebrum and brain stem, presented in logarithmic color scale.

Left, ipsilateral to the injection site. Right, contralateral to the injection site. Each row represents an anatomical region and each column represents one brain. Values represent the fraction of total axons in the given sample. Subregions with greater than 0.001 fraction of axons in any sample across both hemispheres are included.

Rasgrf2-dCre N=3, Scnn1a-Cre N=4, Tlx3-Cre N=3, Rbp4-Cre N=3, Sim1-Cre N=3 and Ntsr1-Cre N=3

Innervation targets of SSs neurons show mostly similarity in patterns to those of SSp-bfd neurons in the ipsilateral side (Figure 4-13 and Figure 4-14). Ipsilateral MOs, SSp, and CP are the most targeted region across all samples. Rasgrf2-dCre, Scnn1a-Cre, Tlx3-Cre and Rbp4-Cre expressing neurons show axonal projections in the ipsilateral somatosensory (SSp-II, SSp-ul, SSp-tr, SSp-un), motor (MOs and MOp), AUDd, Visrl, TEa, PERI, and ECT. Rbp4-Cre, Sim1-Cre and Ntsr1-Cre neurons innervate brainstem thalamic regions while other brainstem regions are innervated by the neurons expressing Rbp4-Cre and Sim1-Cre. Two exceptions are the Rasgrf2-dCre and Scnn1a-Cre samples. In contrast to SSp-bfd injections, Rasgrf2-dCre injections in the SSs now show similar contralateral innervation pattern to the ipsilateral side in addition to the contralateral SSp-bfd and SSs. Furthermore, SSs injections in the Scnn1a-Cre mouse show fewer innervation targets in the contralateral side compared to those observed in SSp-bfd injections. Axons are only the contralateral SSp-bfd, SSs, VISC, TEa, and CP with absence in regions such as the AUDd and Alp.

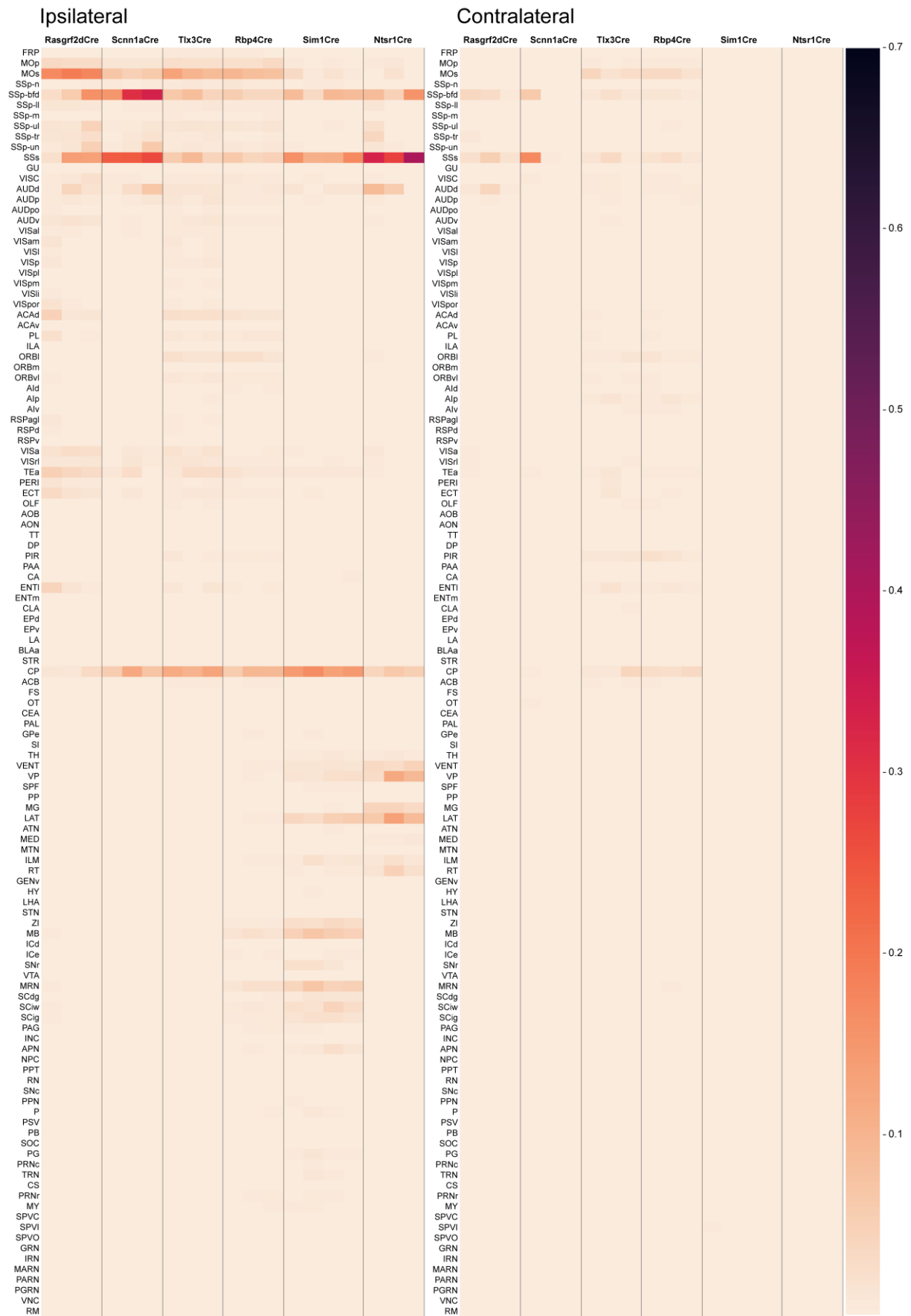


Figure 4-13 Axonal projections for samples with SSs injections in subregions of cerebrum and brain stem, presented in linear color scale.

Left, ipsilateral to the injection site. Right, contralateral to the injection site. Each row represents an anatomical region and each column represents one brain. Values represent the fraction of total axons in the given sample. Subregions with greater than 0.001 fraction of axons in any sample across both hemispheres are included.

Rasgrf2-dCre N=3, Scnn1a-Cre N=3, Tlx3-Cre N=3, Rbp4-Cre N=3, Sim1-Cre N=4 and Ntsr1-Cre N=3.

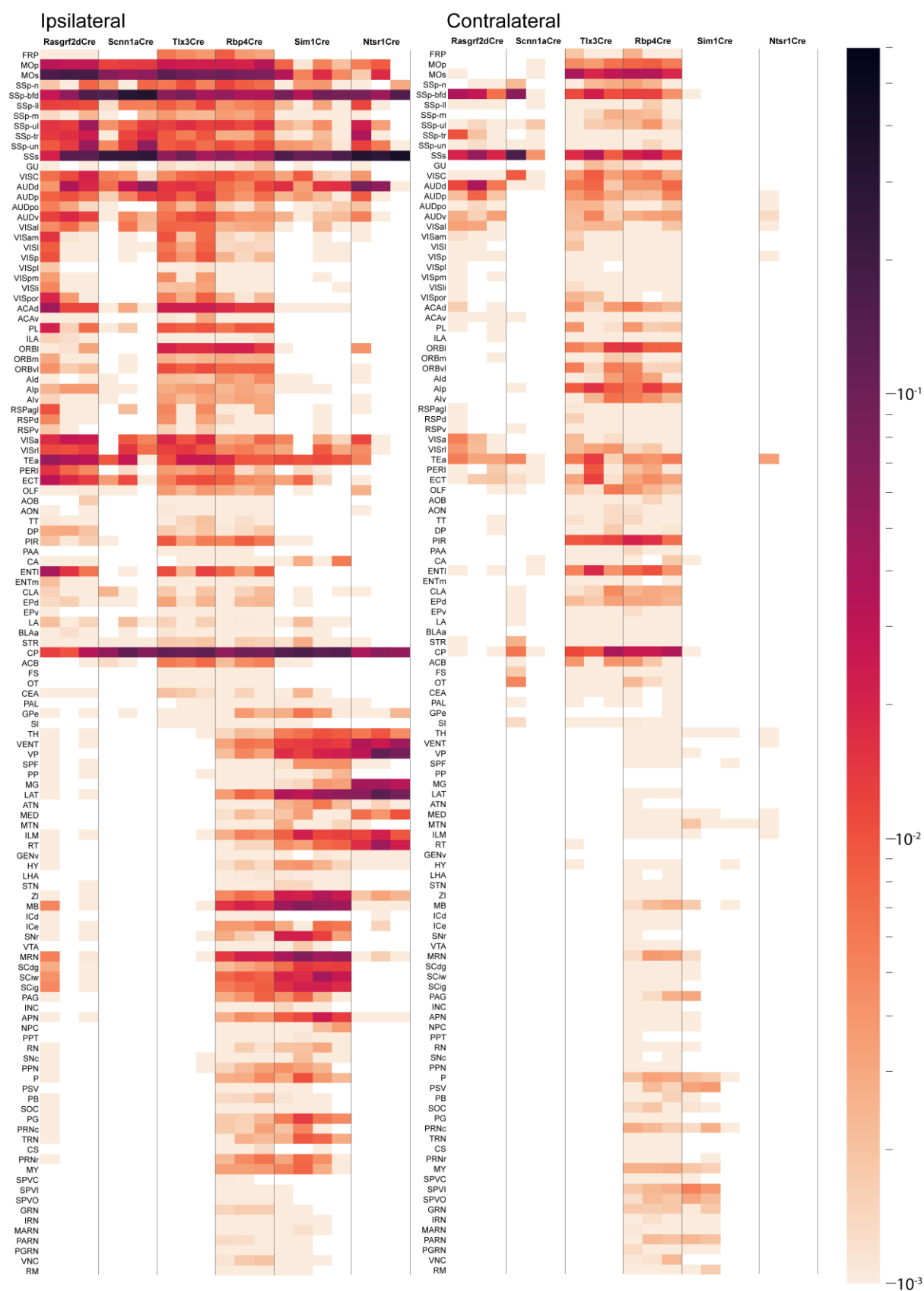


Figure 4-14 Axonal projections for samples with SSs injections in subregions of cerebrum and brain stem, presented in logarithmic color scale.

Left, ipsilateral to the injection site. Right, contralateral to the injection site. Each row represents an anatomical region and each column represents one brain. Values represent the fraction of total axons in the given sample. Subregions with greater than 0.001 fraction of axons in any sample across both hemispheres are included.

Rasgrf2-dCre N=3, Scnn1a-Cre N=3, Tlx3-Cre N=3, Rbp4-Cre N=3, Sim1-Cre N=4 and Ntsr1-Cre N=3.

Correlation plots were computed based on axons in all brain regions (including those presented above and various fiber tracts) with respect to the most detailed information possible (such as different layers of the cerebral cortex). Among SSp-bfd samples (Figure 4-15a), Rasgrf2-dCre, Sim1-Cre and Ntsr1-Cre injections show high correlation within themselves. In contrast Scnn1a-Cre, Tlx3-Cre, and Rbp4-Cre show strong correlation within groups but are also highly correlated with the others. For SSs injections (Figure 4-15b), Rasgrf2-dCre, Scnn1a-Cre and Ntsr1-Cre injections show correlation within groups. Tlx3-Cre and Rbp4-Cre samples are highly correlated with each other, while they also show high resemblance with Sim1-Cre samples.

Overall, projection patterns show great diversities across the six mouse lines under our investigation. This is consistent with previous literature describing projection neurons of inter-telencephalic, pyramidal tract and cortical thalamic types and their relative distributions across layers (Gerfen, Paletski, and Heintz 2013; K. D. Harris and Mrcic-Flogel 2013; K. D. Harris and Shepherd 2015). In general, there are less axons in the contralateral regions compared to the ipsilateral side. For both SSp-bfd and SSs injections, projection patterns of ipsilateral and contralateral regions show great degree of similarity for Tlx3-Cre and Rbp4-Cre. Between SSp-bfd and SSs, the general innervation patterns are also similar except for Rasgrf2-dCre and Scnn1a samples. More elaborate SSp-bfd vs. SSs comparisons for subregions in the isocortex will be discussed in the next section.

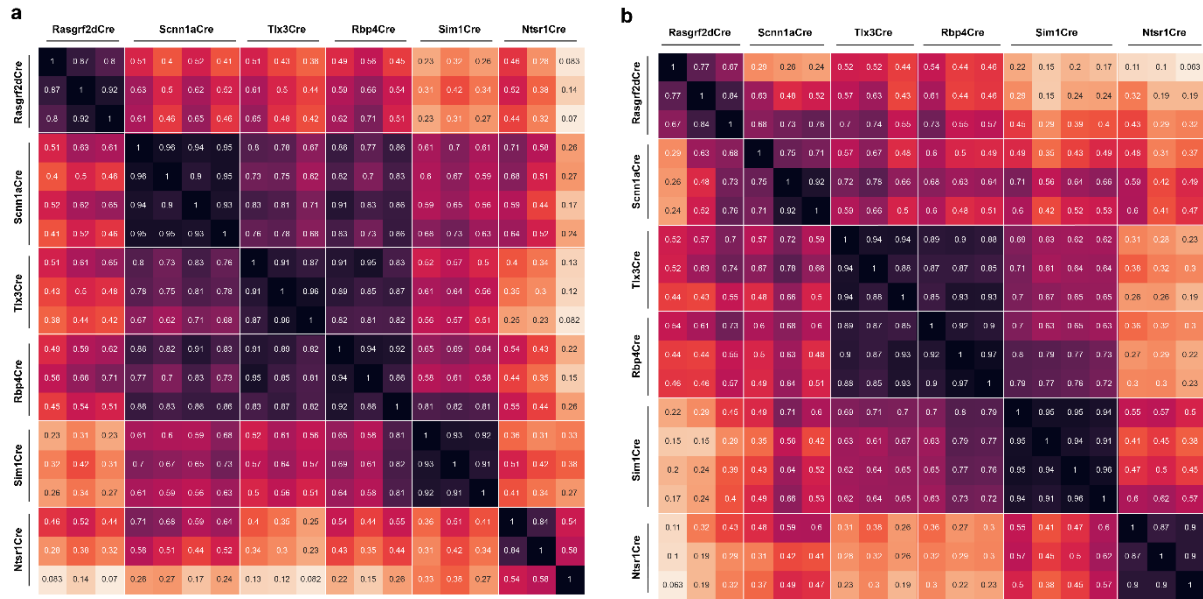


Figure 4-15 Correlation matrix comparing axonal projections in SSp-bfd and SSs samples.

Correlation matrix comparing axonal projections in SSp-bfd (a) and SSs (b) samples. Calculations based on all brain regions at the most detailed anatomical locations possible.

SSp-bfd injections: Rasgrf2-dCre N=3, Scnn1a-Cre N=4, Tlx3-Cre N=3, Rbp4-Cre N=3, Sim1-Cre N=3 and Ntsr1-Cre N=3.

SSs injections: Rasgrf2-dCre N=3, Scnn1a-Cre N=3, Tlx3-Cre N=3, Rbp4-Cre N=3, Sim1-Cre N=4 and Ntsr1-Cre N=3.

4.2.3 Projection targets within the isocortex

Next, we further elaborate our analysis on anatomical regions in the isocortex, a subregion of the CTXpl. Axons in the isocortex are projected in Figure 4-16 and Figure 4-17 in different ways of representation. Figure 4-16 enable visualizations of both stronger and weaker innervations and allow comparison of overall projection plans. In Rasgrf2-dCre samples, there are more contralateral regions innervated by neurons in the SSs compared to those in SSp-bfd. In contrast, the opposite is observed in Scnn1a-Cre samples where the SSp-bfd innervates more contralateral regions including both lateral and frontal regions. This observation is consistent with our findings from the previous section. In Rbp4-Cre samples, the isocortex of both hemispheres is almost completely covered with axons from SSs neurons. In the meantime, SSp-bfd projections spare regions anterior and lateral to the SSp-bfd bilaterally, corresponding to the agranular insula (AI), gustatory area (GU) and orbital areas (ORB). In addition, SSp-bfd neurons in Rbp4-Cre brains also project less to frontal regions of the contralateral hemisphere compared to SSs neurons.

On the other hand, Figure 4-17 emphasizes on the denser region and allow comparison of projection patterns in highly innervated regions between SSp-bfd and SSs injections. In Rasgrf2-dCre samples, SSp-bfd and SSs neurons show strong frontal projections with SSp-bfd

innervating more laterally. Axons from SSp-bfd injections innervate densely in a region posterior and medial to the SSp-bfd ipsilaterally, corresponding VISrl. In comparison, axons of SSs neurons project strongly to the contralateral somatosensory region. Similar pattern of innervation contralateral somatosensory region from SSs injections are also observed in Scnn1a-Cre samples. Projections of SSp-bfd and SSs neuron have less qualitative differences in Tlx3-Cre and Rbp4-Cre samples. In Sim1-Cre and Ntsr1-Cre samples, there are greater frontal innervation from SSp-bfd injections than those of SSs.

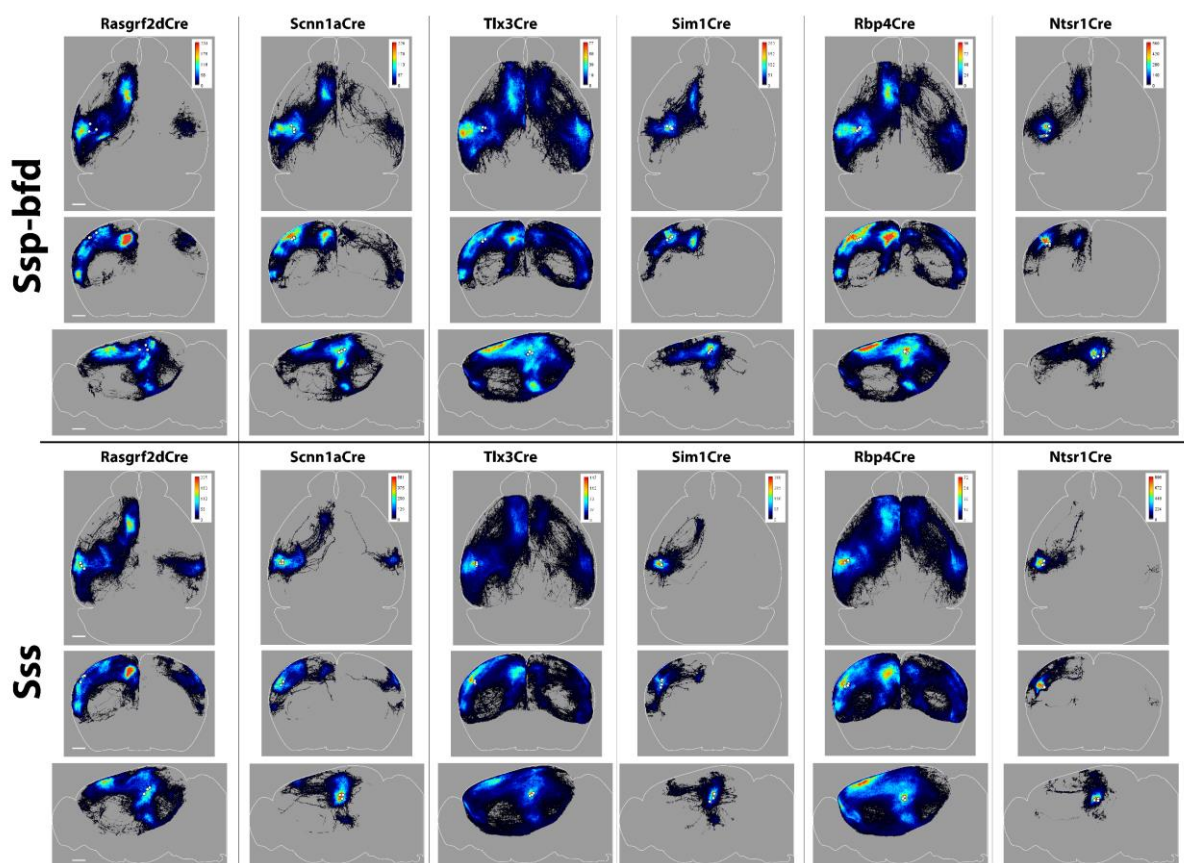


Figure 4-16 Averaged sum axonal projections in the isocortex for each mouse line for SSp-bfd and SSs injections.

Averaged sum axonal densities in the isocortex for each of the six mouse lines for SSp-bfd and SSs injections in horizontal, coronal and sagittal views. White dots represent the center of injection site for one injection. Pixel intensity represents 10^{-6} fraction of total axons. Note that this color scale reveal both stronger and weaker projection targets compared to Figure 4-17. Scale bars 1mm.

SSp-bfd injections: Rasgrf2-dCre N=3, Scnn1a-Cre N=4, Tlx3-Cre N=3, Rbp4-Cre N=3, Sim1-Cre N=3 and Ntsr1-Cre N=3.

SSs injections: Rasgrf2-dCre N=3, Scnn1a-Cre N=3, Tlx3-Cre N=3, Rbp4-Cre N=3, Sim1-Cre N=4 and Ntsr1-Cre N=3.

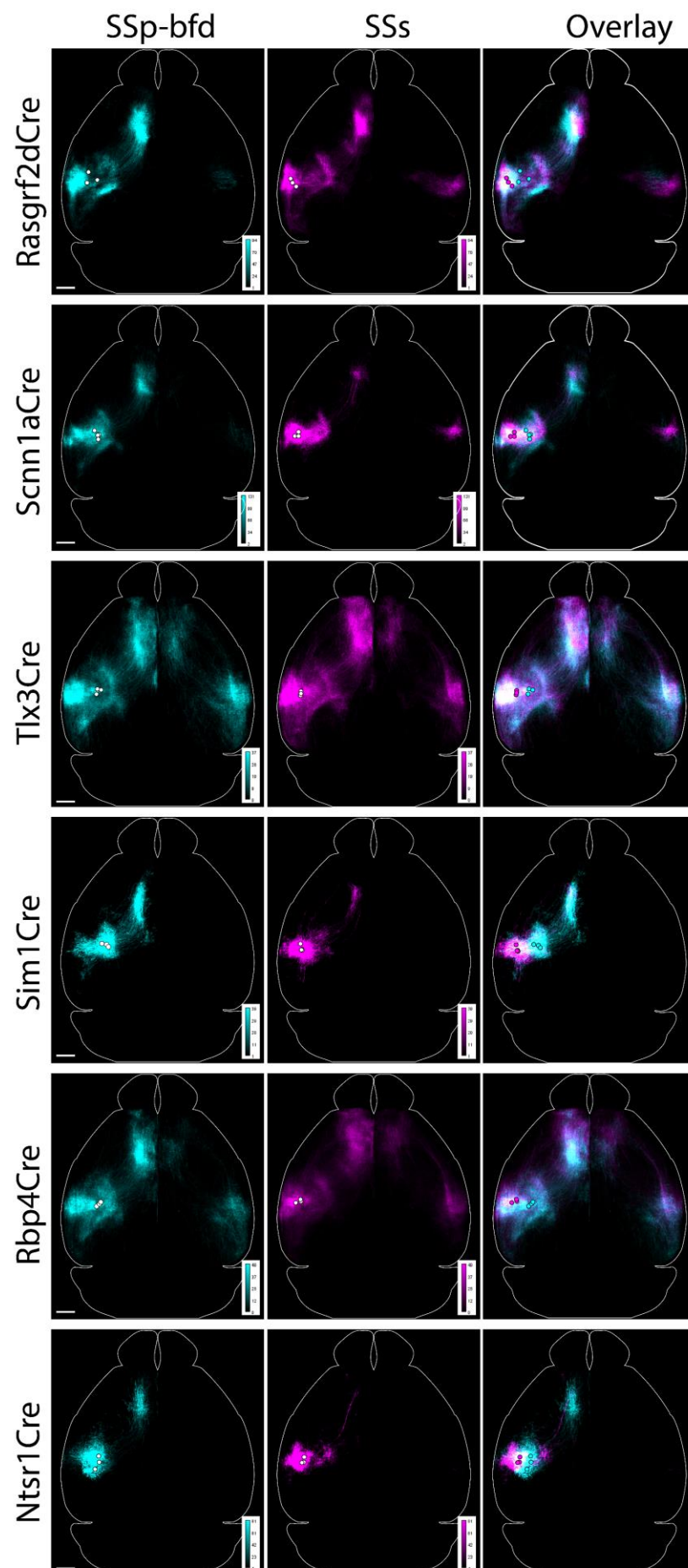


Figure 4-17 Averaged sum axonal projections in the isocortex for each mouse line for SSp-bfd and SSs injections in horizontal view.

White dots represent the center of injection site for one injection. Pixel intensity represents 10^{-6} fraction of total axons. Scale bars 1 mm. Note that this color scale emphasizes on the stronger projection targets compared to Figure 4-16.

SSp-bfd injections, cyan: Rasgrf2-dCre N=3, Scnn1a-Cre N=4, Tlx3-Cre N=3, Rbp4-Cre N=3, Sim1-Cre N=3 and Ntsr1-Cre N=3.

SSs injections, magenta: Rasgrf2-dCre N=3, Scnn1a-Cre N=3, Tlx3-Cre N=3, Rbp4-Cre N=3, Sim1-Cre N=4 and Ntsr1-Cre N=3.

To explore contributions from each cortical regions, we now normalize values to the total amount of axons inside the isocortex of both hemispheres. Axons in subregions of the isocortex from all injections can be viewed in Figures 4-15 to 4-18. Data representation in linear scale (Figure 4-18 and Figure 4-20) emphasizes strongest innervation targets while log scale representation (Figure 4-19 and Figure 4-21) redirect attention to regions with moderate levels of innervations.

In SSp-bfd injections, strongest targets among the isocortex are still the ipsilateral MOp, MOs, somatosensory regions (SS), SSs, and VISrl across all mouse lines (Figure 4-18 and Figure 4-19). Other ipsilateral regions worthy of mention are various somatosensory areas (SS), VISC, auditory areas (AUD), anterior cingulate area (ACA), prelimbic areas (PL), retrosplenial areas (RSP), anterior area (VISa), TEa, PERI, and ECT in almost all samples except for the Ntsr1-Cre brains. For Rasgrf2-dCre, Scnn1a-Cre, Tlx3-Cre and Rbp4-Cre brains, there are axons innervating the intralimbic areas (ILA) and the orbital areas (ORB. On the contralateral side, SSp-bfd and SSs are the main target regions for Rasgrf2-dCre, Scnn1a-Cre, Tlx3-Cre and Rbp4-Cre samples. Scnn1a-Cre, Tlx3-Cre and Rbp4-Cre samples show similar patterns in target regions including the SS, VISC, AUD, ACA, AI, TEa, PERI and ECT. Strong contralateral ORB innervations are only seen in Tlx3-Cre and Rbp4-Cre brains. In Sim1-Cre and Ntsr1-Cre brains, there are very few axons in the contralateral isocortex.

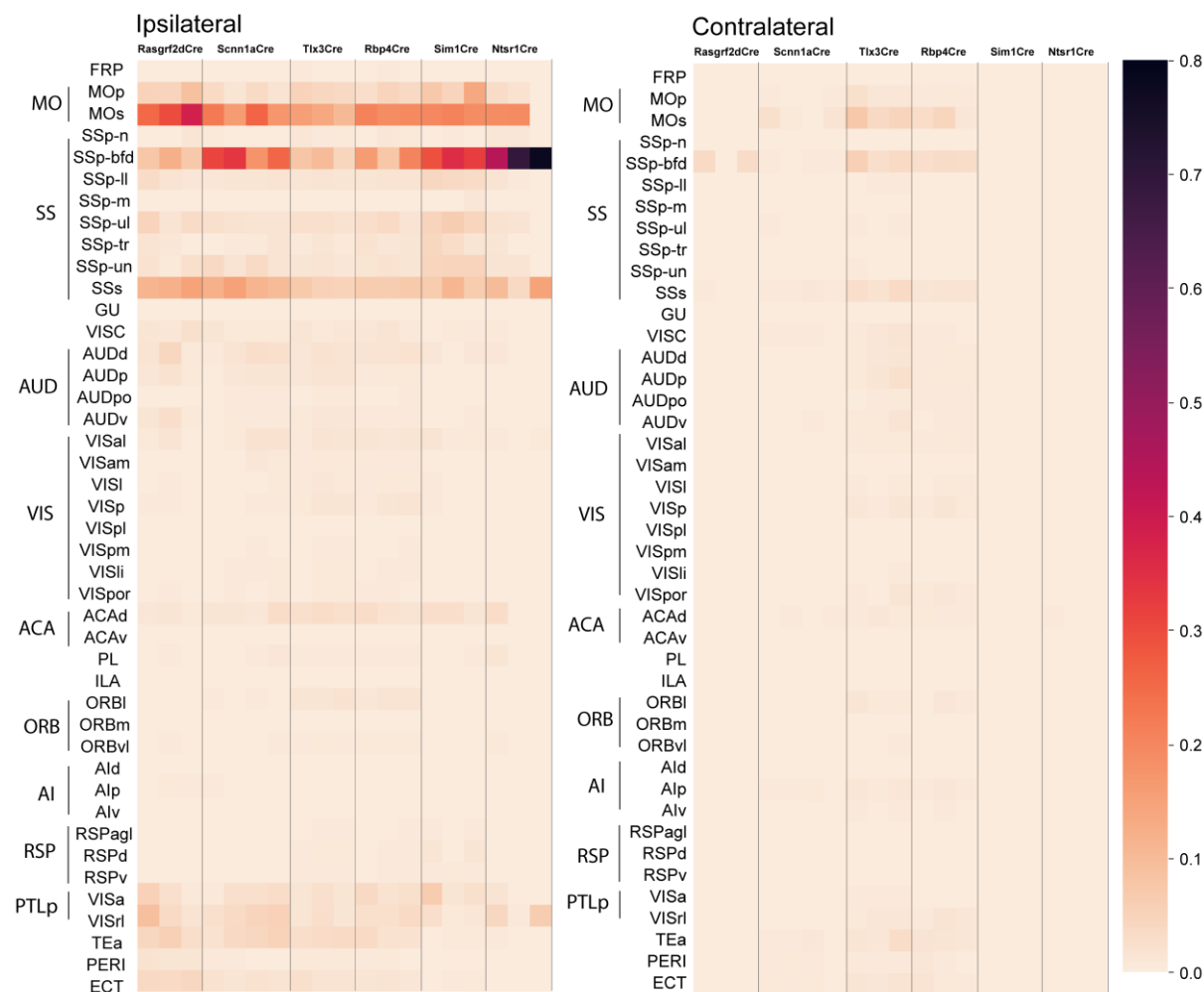


Figure 4-18 Axonal projections of samples with SSp-bfd injections in subregions of the isocortex, presented in linear color scale.

Left, ipsilateral to the injection site. Right, contralateral to the injection site. Each row represents an anatomical region and each column represents one sample. Values represent the fraction of total axons in the isocortex of the given sample.

Rasgrf2-dCre N=3, *Scnn1a-Cre* N=4, *Tlx3-Cre* N=3, *Rbp4-Cre* N=3, *Sim1-Cre* N=3 and *Ntsr1-Cre* N=3.

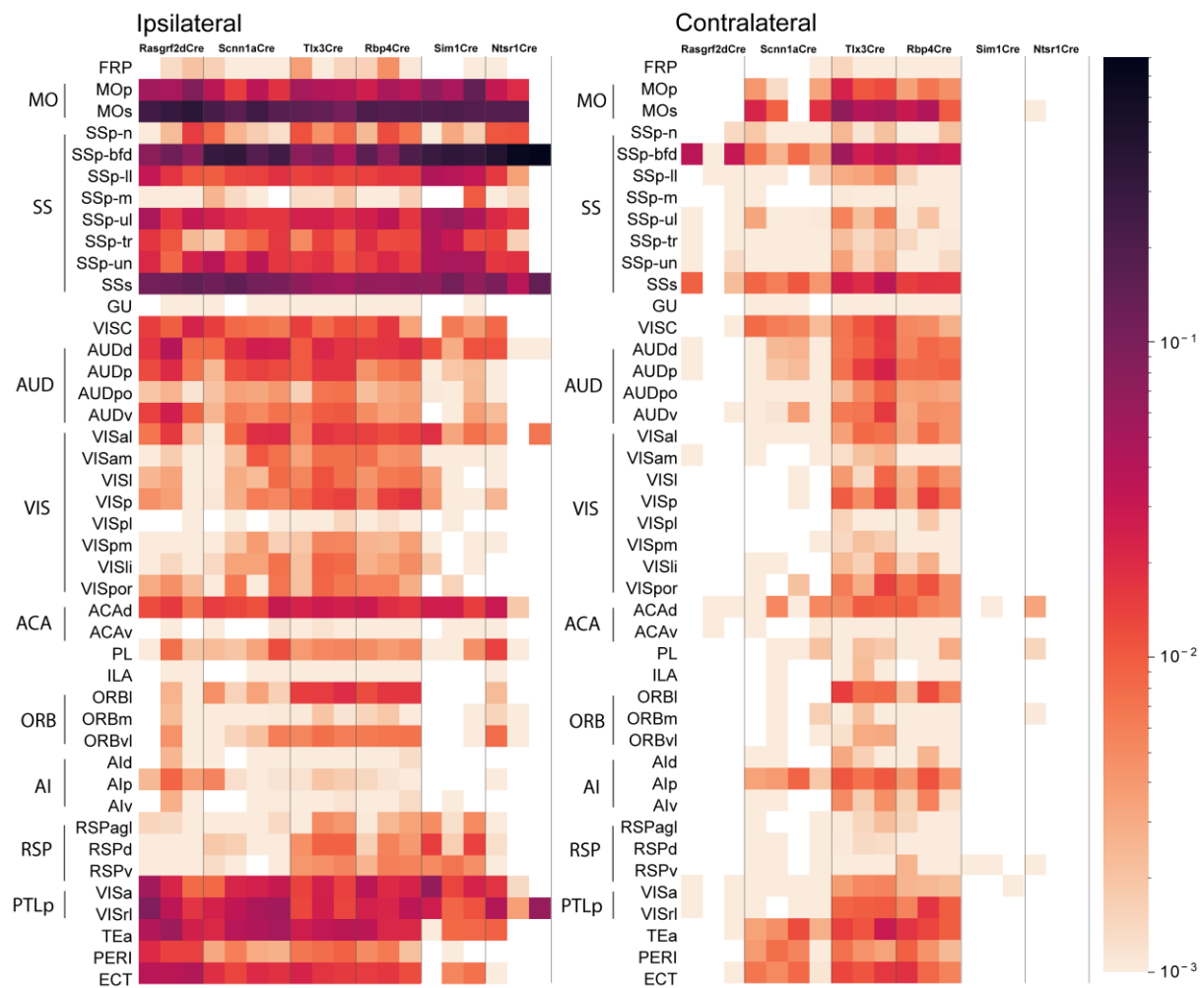


Figure 4-19 Axonal projections of samples with SSp-bfd injections in subregions of the isocortex, presented in logarithmic color scale.

Left, ipsilateral to the injection site. Right, contralateral to the injection site. Each row represents an anatomical region and each column represents one sample. Values represent the fraction of total axons in the isocortex of the given sample.

Rasgrf2-dCre N=3, Scnn1a-Cre N=4, Tlx3-Cre N=3, Rbp4-Cre N=3, Sim1-Cre N=3 and Ntsr1-Cre N=3.

Innervation targets of SSs neurons once again show similarity in patterns to those of SSp-bfd neurons on the ipsilateral side (Figure 4-20 and Figure 4-21). Ipsilateral MOp, MOs, and SSp-bfd are the most targeted region across all samples. Regions in the SS and AUD are also common targets. Similar to those of SSp-bfd neurons, the posterior parietal association areas (PTLp, includes VISa and VISrl), TEa, PERI, and ECT are shared targets for all mouse lines except for the Ntsr1-Cre. However, Rasgrf2-dCre, Tlx3-Cre and Rbp4-Cre expressing neurons also show axonal projections in VIS, ACA, ORB, AI and RSP. This was not the case in SSp-bfd injections where Scnn1a-Cre samples innervate most of these regions instead of Rasgrf2-dCre. In the hemisphere contralateral to the injection, projection plans for most of the cre lines remain similar to those of the SSp-bfd injections. Once again, the exception being Rasgrf2-dCre and Scnn1a-Cre appear to switch their range of target regions when comparing Figure 4-19 and Figure 4-21. In SSs injections, Rasgrf2-dCre brains now innervate more contralateral

regions such as the AUD, VIS, ACA, PTLp compared to Scnn1a-Cre samples. These differences could hint that these cell class assume slightly different roles in the cortical circuit hierarchy depending on their location.

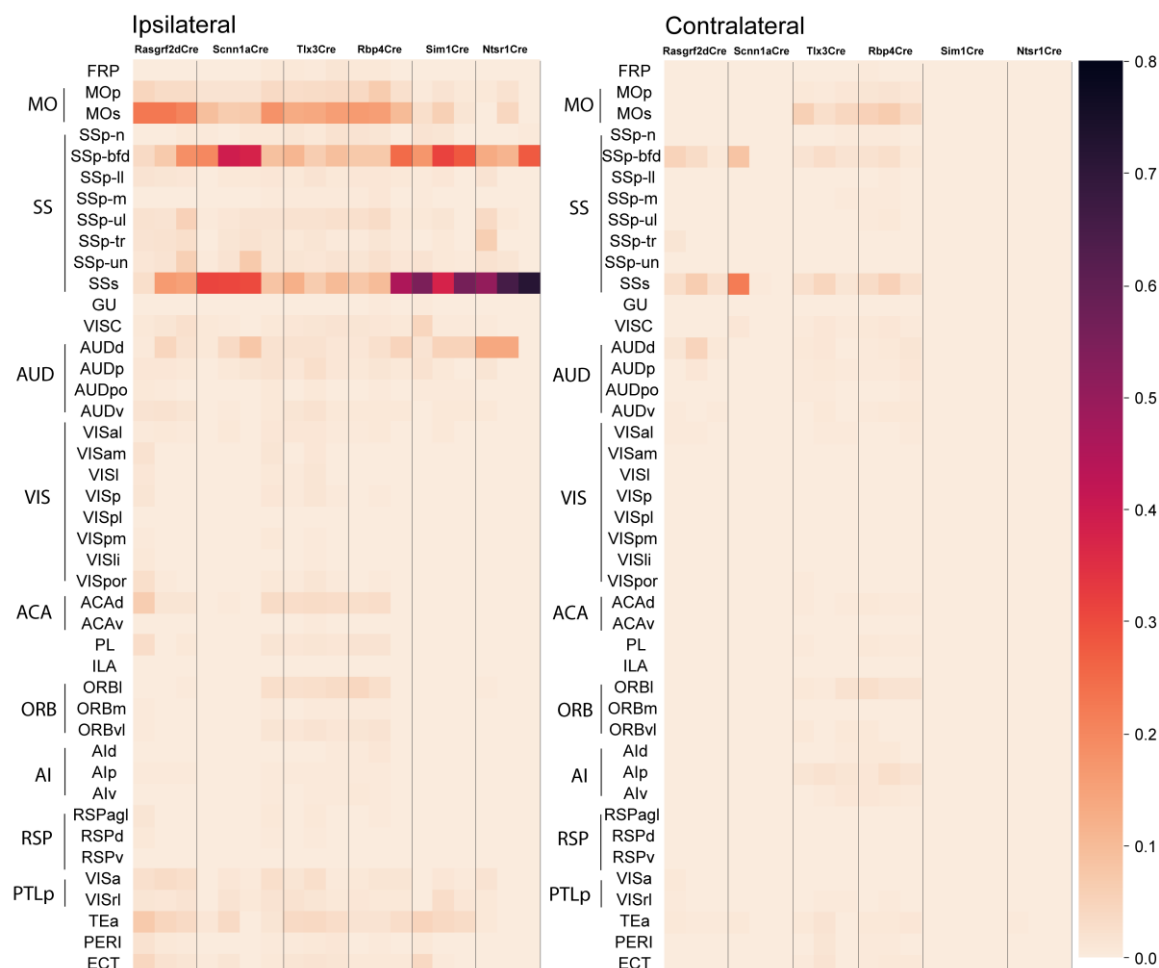


Figure 4-20 Axonal projections of samples with SSs injections in subregions of the isocortex, presented in linear color scale.

Left, ipsilateral to the injection site. Right, contralateral to the injection site. Each row represents an anatomical region and each column represents one sample. Values represent the fraction of total axons in the isocortex of the given sample.

Rasgrf2-dCre N=3, Scnn1a-Cre N=3, Tlx3-Cre N=3, Rbp4-Cre N=3, Sim1-Cre N=4 and Ntsr1-Cre N=3.

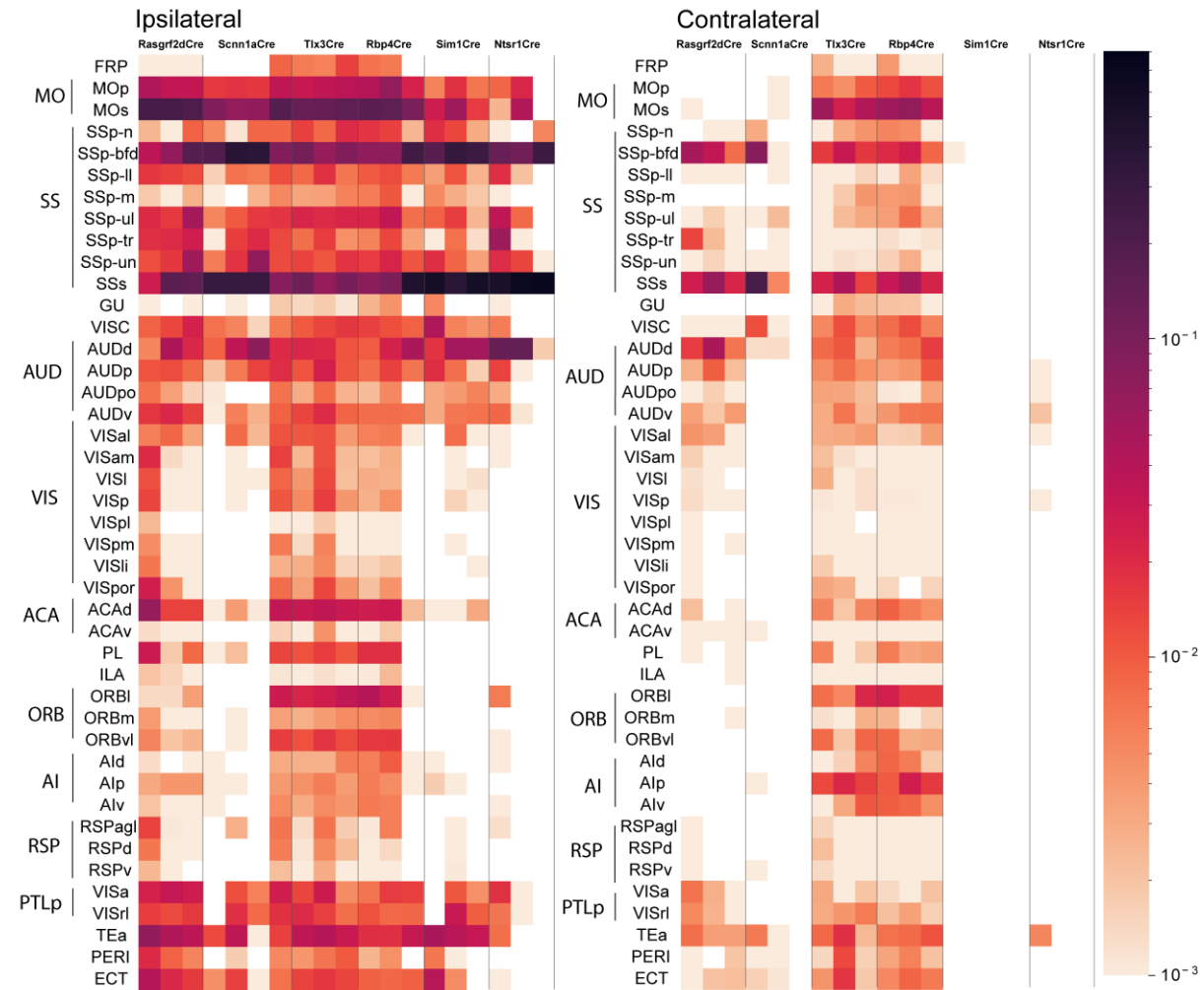


Figure 4-21 Axonal projections of samples with SSs injections in subregions of the isocortex, presented in logarithmic color scale.

Left, ipsilateral to the injection site. Right, contralateral to the injection site. Each row represents an anatomical region and each column represents one sample. Values represent the fraction of total axons in the isocortex of the given sample.

Rasgrf2-dCre N=3, *Scnn1a-Cre* N=3, *Tlx3-Cre* N=3, *Rbp4-Cre* N=3, *Sim1-Cre* N=4 and *Ntsr1-Cre* N=3.

Next, we focus on isocortex targets of SSp-bfd vs. SSs injections for each individual mouse line in more quantitative representations (Figures 4-19 to 4-24). In *Rasgrf2-dCre* samples (Figure 4-22), the overall patterns on the ipsilateral side are comparable between the two injection sites, perhaps with slightly more axons in the MOp and MOs regions from SSp-bfd neurons. However, there are innervations in the contralateral SSp-bfd, SSs, and AUDd from SSs injections while SSp-bfd neurons only show axons on the contralateral SSp-bfd.

In *Scnn1a-Cre* brains (Figure 4-23), axons from SSp-bfd neurons show greater innervations to the MOs, AUDp, anteromedial visual area (VISam), ACAd, VISa, VISrl, TEa and ECT in the ipsilateral isocortex. In the contralateral isocortex, SSp-bfd neurons have much sparser innervations that are spread out among several regions while SSs neurons project strongly only to the contralateral SSp-bfd and SSs.

In *Tlx3-Cre* samples (Figure 4-24), amounts of axons in target regions of SSp-bfd and SSs injections show mostly similarities. Minor differences could be observed in the ACAd, PL, ventral and lateral orbital areas (ORBI, ORBvl), dorsal and ventral agranular insular areas (Ald, Alv), and bilateral posterior agranular insular areas (Alp), where SSs neurons projections are slightly stronger. Likewise, *Rbp4-Cre* samples (Figure 4-25) also show mostly similarities between SSp-bfd and SSs injections with small differences. SSs neurons send slightly more axons to ipsilateral Ald, Alp, and AIV, contralateral MOs and SSs, as well as bilateral PL, ORBI, medial orbital area (ORBm), ORBvl compared to SSp-bfd neurons. In comparison, SSp-bfd neurons project stronger to ipsilateral MOs, Visal, VISam, VISa, VISrl and contralateral SSp-bfd.

SSp-bfd vs. SSs neuron projections differences are more obvious in the *Sim1-Cre* and *Ntsr1-Cre* samples. For *Sim1-Cre* samples (Figure 4-26), regions where SSp-bfd neurons have stronger projections include MOp, MOs, various SS regions such as SSp-II, SSp-ul, SSp-tr, SSp-un, ACAd, and RSP. In this mouse line, projections from the SSs neurons are stronger in the AUDd and TEa. Finally, in the *Ntsr1-Cre* group (Figure 4-27), SSp-bfd neurons have stronger projections in MOs and VISrl while SSs neurons show denser projections to the AUDd. As mentioned above, *Sim1-Cre* and *Ntsr1-Cre* samples had close to zero axons contralateral to the injection site.

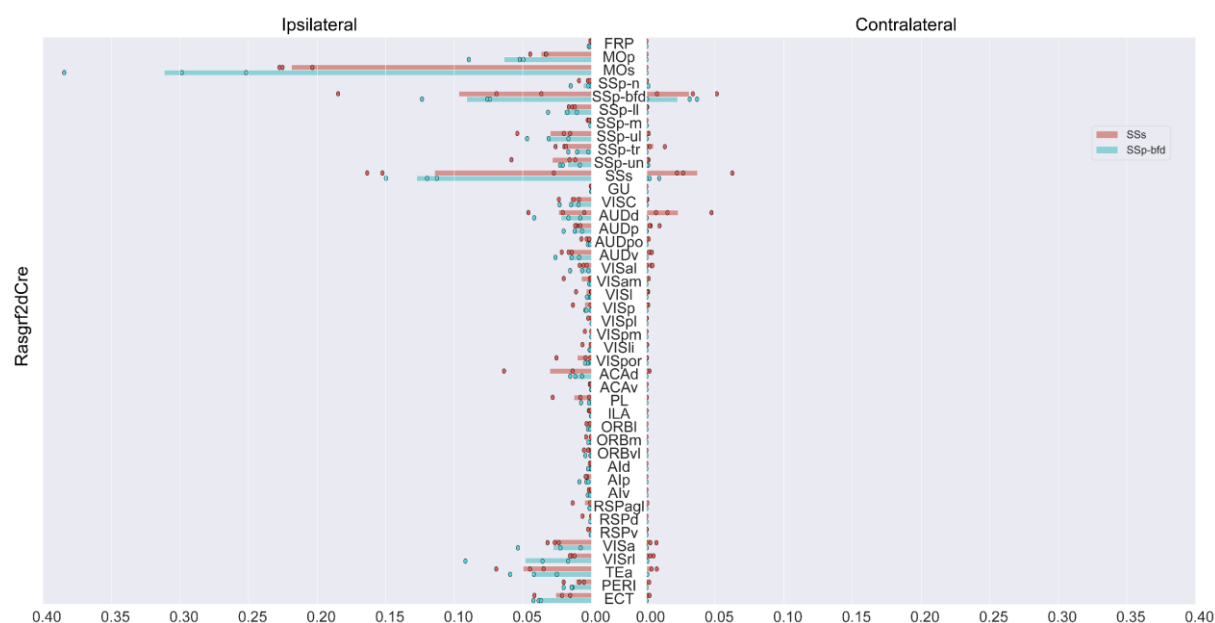


Figure 4-22 Amounts of axons in isocortex subregions for *Rasgrf2-dCre* brains injected in the SSp-bfd or SSs.

Values are fractions of total axons in the isocortex, normalized for each sample. Each dot represents data from one sample, and bars represent group average. Left, ipsilateral to the injection site. Right, contralateral to the injection site. SSp-bfd, red, $N=3$. SSs, blue, $N=3$.

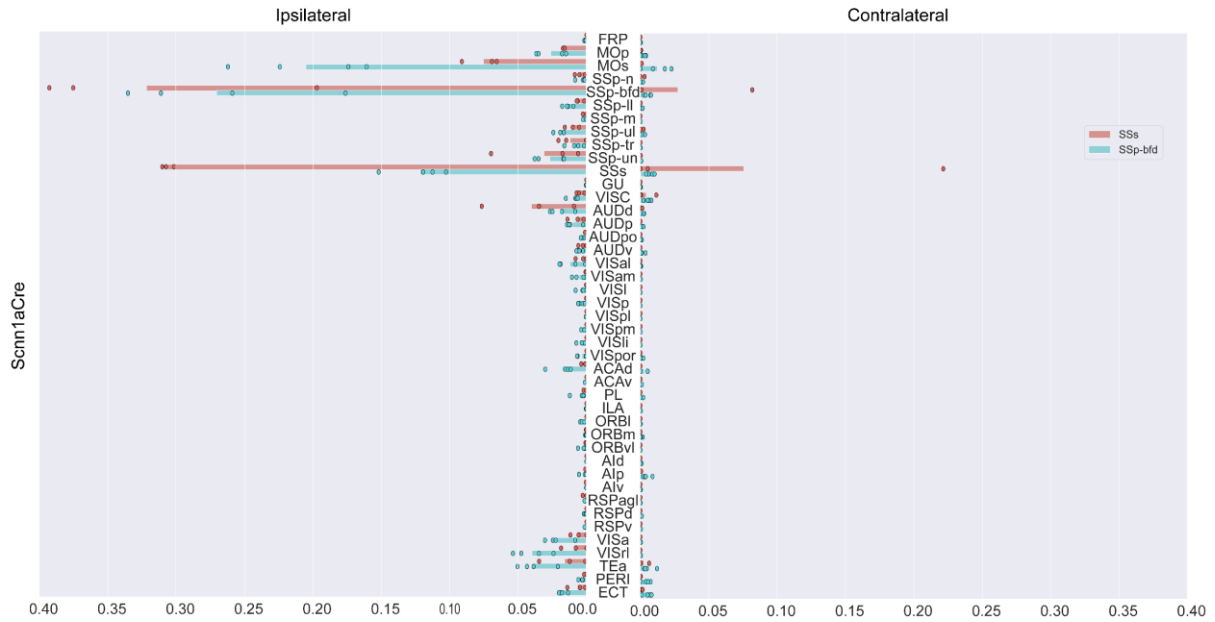


Figure 4-23 Amounts of axons in isocortex subregions for *Scnn1a-Cre* brains injected in the *SSp-bfd* or *SSs*.

Values are fractions of total axons in the isocortex, normalized for each sample. Each dot represents data from one sample, and bars represent group average. Left, ipsilateral to the injection site. Right, contralateral to the injection site. *SSp-bfd*, red, $N=4$. *SSs*, blue, $N=3$.

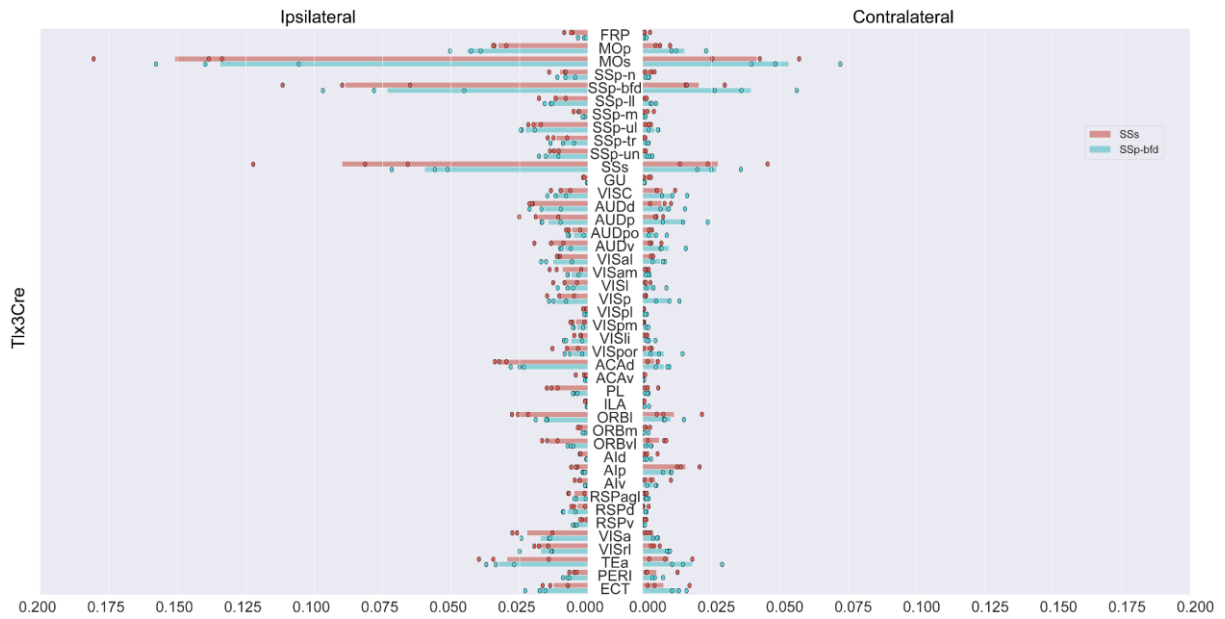


Figure 4-24 Amounts of axons in isocortex subregions for *Tlx3-Cre* brains injected in the *SSp-bfd* or *SSs*.

Values are fractions of total axons in the isocortex, normalized for each sample. Each dot represents data from one sample, and bars represent group average. Left, ipsilateral to the injection site. Right, contralateral to the injection site. *SSp-bfd*, red, $N=3$. *SSs*, blue, $N=3$.

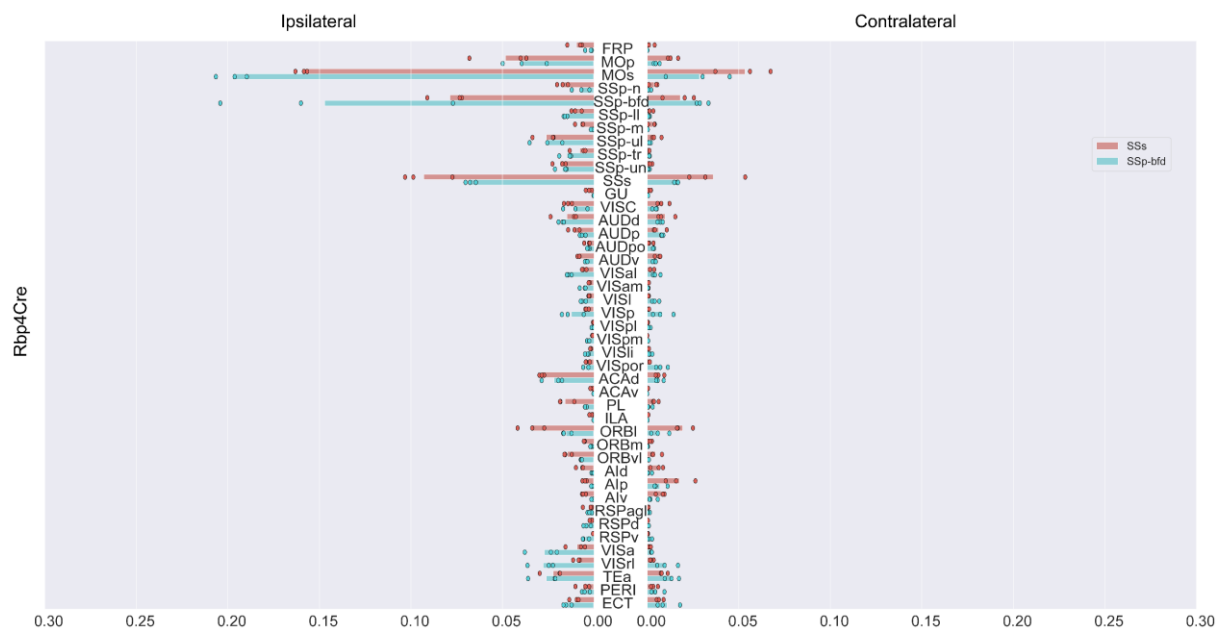


Figure 4-25 Amounts of axons in isocortex subregions for *Rbp4-Cre* brains injected in the *SSp-bfd* or *SSs*.

Values are fractions of total axons in the isocortex, normalized for each sample. Each dot represents data from one sample, and bars represent group average. Left, ipsilateral to the injection site. Right, contralateral to the injection site. *SSp-bfd*, red, $N=3$. *SSs*, blue, $N=3$.

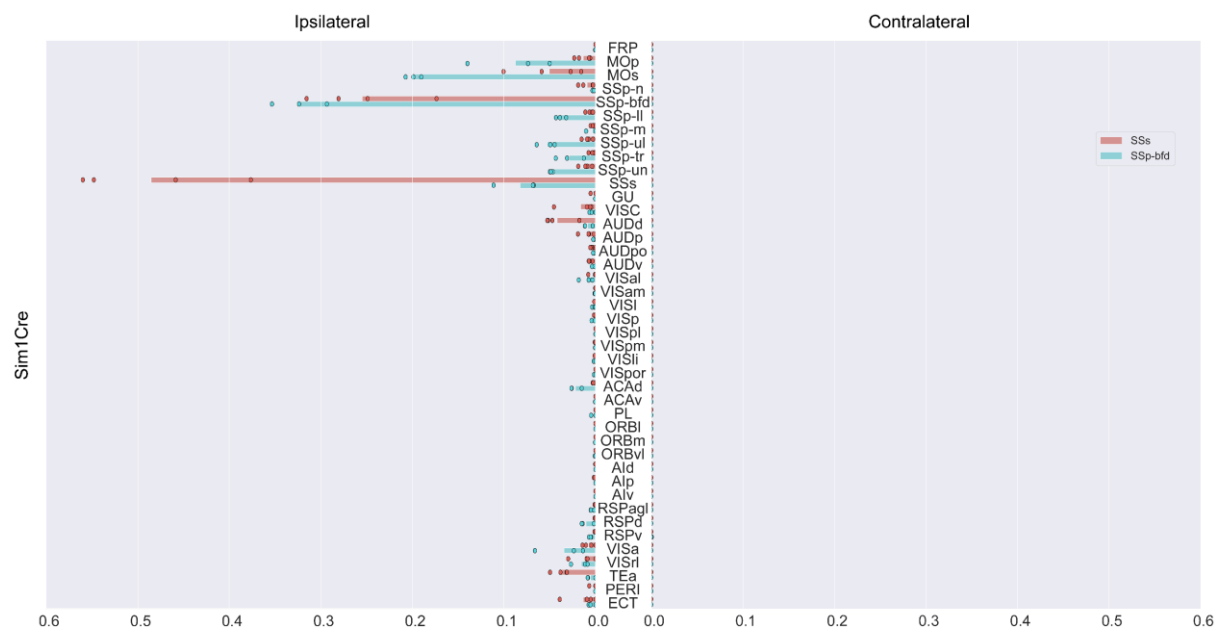


Figure 4-26. Amounts of axons in isocortex subregions for *Sim1-Cre* brains injected in the *SSp-bfd* or *SSs*.

Values are fractions of total axons in the isocortex, normalized for each sample. Each dot represents data from one sample, and bars represent group average. Left, ipsilateral to the injection site. Right, contralateral to the injection site. *SSp-bfd*, red, $N=3$. *SSs*, blue, $N=4$.

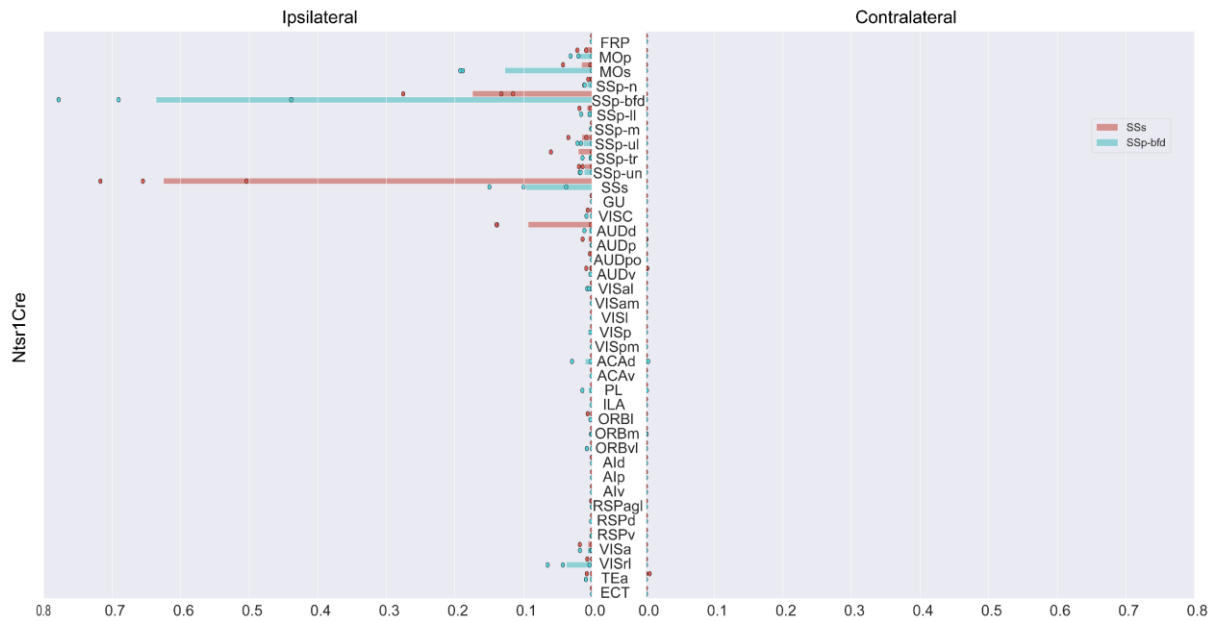


Figure 4-27 Amounts of axons in isocortex subregions for *Ntsr1-Cre* brains injected in the SSp-bfd or SSs.

Values are fractions of total axons in the isocortex, normalized for each sample. Each dot represents data from one sample, and bars represent group average. Left, ipsilateral to the injection site. Right, contralateral to the injection site. SSp-bfd, red, $N=3$. SSs, blue, $N=3$.

4.2.4 Projection patterns in the somatomotor regions

Finally, we focus our analysis on the somatomotor region (MO, including MOp and MOs) and axons distributions in different layers of this region. As one of the stronger target regions, axons in the MO are spotted across in all mouse lines. Horizontal sum projections of axons in layer 1, 2/3, 5, 6a and 6b of MO is presented in Figure 4-28 for SSp-bfd vs. SSs projection comparison. Once again, this representation reveals denser innervation patterns. In general, there is very little axon in layer 6b for all samples of all injection location. Axons in layer 6a of the MO seem to travel collectively in parallel. In comparison, axons in layer 5, 2/3 and 1 appear in either smaller patches or diffused pattern in different transgenic lines. In *Scnn1a-Cre*, *Sim1-Cre* and *Ntsr1-Cre*, there are more MO axons from SSp-bfd injections compared to SSs injections across all layers. This is consistent with our observations from Figure 4-23, Figure 4-26, and Figure 4-27. In *Rasgrf2-dCre* samples, SSp-bfd neurons seem to avoid layer 1. This observation agrees with previous finding reported in Aronoff et al, 2010.

In chapter 2 (Esmaeili et al. 2022), we reported that SSp-bfd and SSs display different innervation patterns in layer 2/3 of the frontal regions. Here, we approximate axon spread and ‘hot-spot’ location in MO layer 2/3 by indication of a contour that highlights brighter pixels calculated using the Otsu’s method (Figure 4-29). More diffused innervation type is observed in ipsilateral hemispheres of *Tlx3-Cre* and *Rbp4-Cre* samples while other cell class present a more focal pattern. Dense bilateral MO innervation is also highlighted in both SSp-bfd and SSs injections in *Tlx3-Cre* brains and SSs injections in the *Rbp4-Cre* samples. In *Rasgrf2-dCre* sample, center of axon innervations from SSp-bfd neurons (ML= 1.01 mm, AP= 1.45 mm) are slightly lateral to those of SSs (ML= 0.69 mm, AP= 1.38 mm). In other samples, centers of SSp-bfd innervations are slightly anterior to those of SSs. The centers of MO innervations are located ML= 0.81 mm, AP= 1.23 mm for SSp-bfd injections and ML= 0.81 mm, AP= 1.7 mm for

SSs injections in Scnn1a-Cre samples. For Tlx3-Cre samples: (ML= 0.91 mm, AP= 1.05 mm ipsilateral and ML= -0.84 mm, AP= 1.15 mm contralateral) for SSp-bfd injections and (ML= 0.86 mm, AP= 1.3 mm and ML= -0.74 mm, AP= 1.33 mm) for SSs injections. For Rbp4-Cre samples: (ML= 0.84 mm, AP= 1.15 mm for SSp-bfd injections and (ML= 0.94 mm, AP= 1.4 mm and ML= -0.86 mm, AP= 1.78 mm) for SSs injections. For Sim1-Cre samples: ML= 0.91 mm, AP= 1.03 mm for SSp-bfd injections and ML= 1.04 mm, AP= 1.58 mm for SSs injections. And finally, for Ntsr1-Cre samples: ML= 1.04 mm, AP= 1.45 mm for SSp-bfd injections and (ML= 0.91 mm, AP= 1.95 mm, ML= 0.99 mm, AP= 0.85 mm, and ML= 0.84 mm, AP= -0.45mm) for SSs injections.

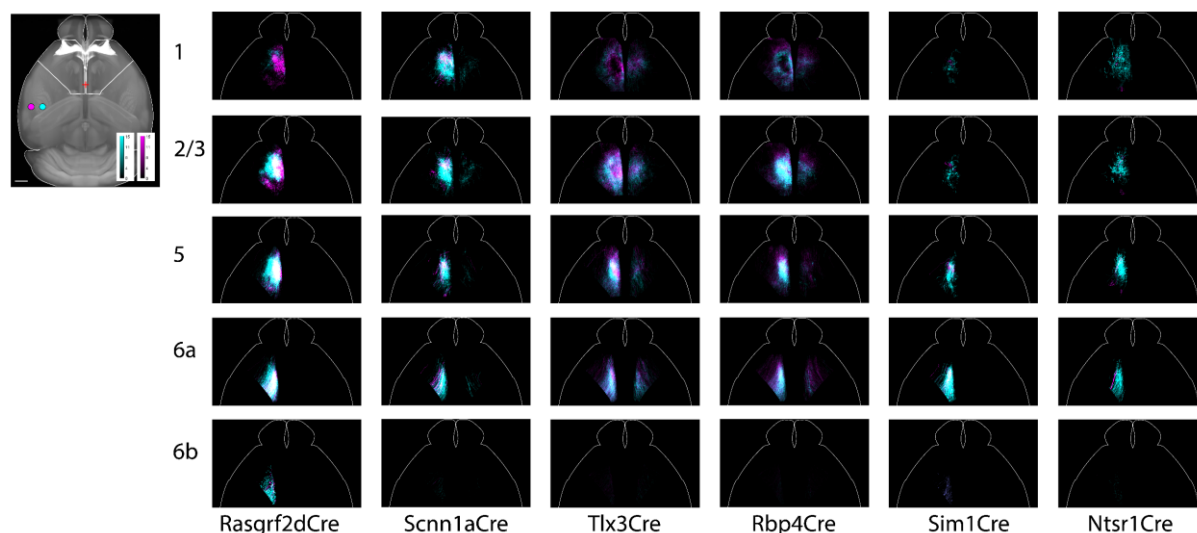


Figure 4-28 Averaged sum axonal projections in layers of the somatomotor regions in each mouse lines for SSp-bfd and SSs injections in horizontal views.

Each row represents sum projection of axons in a given layer and each column represents a transgenic line. Schematic on the top left outlines the location of the somatomotor regions, red cross indicates bregma. It also depicts color scales for pixel values and color code for SSp-bfd (cyan) and SSs (magenta) injection sites. Pixel intensity represents 10^{-6} fraction of total axons. Note that this color scale emphasizes on the pixels with higher intensities. Scale bar 1 mm.

SSp-bfd injections, cyan: Rasgrf2-dCre N=3, Scnn1a-Cre N=4, Tlx3-Cre N=3, Rbp4-Cre N=3, Sim1-Cre N=3 and Ntsr1-Cre N=3.

SSs injections, magenta: Rasgrf2-dCre N=3, Scnn1a-Cre N=3, Tlx3-Cre N=3, Rbp4-Cre N=3, Sim1-Cre N=4 and Ntsr1-Cre N=3.

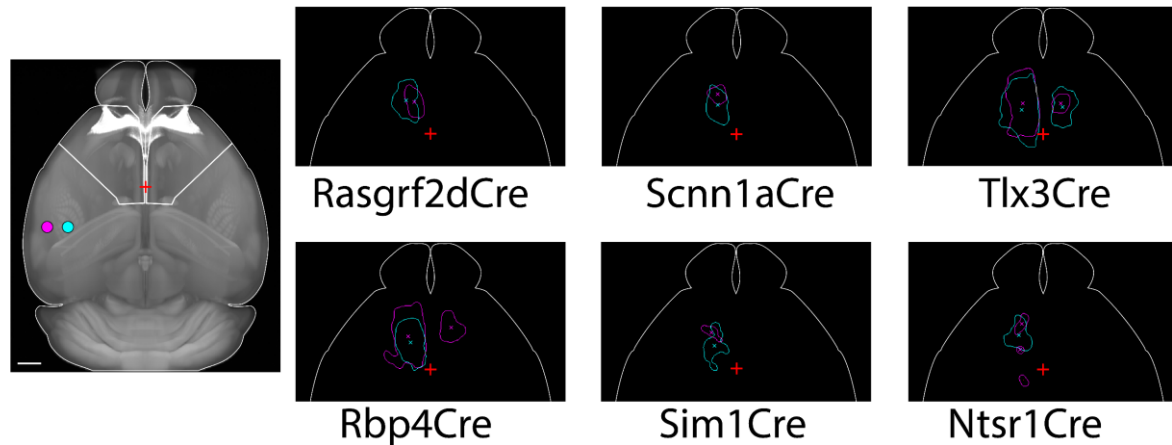


Figure 4-29 Contours and centers of axons hot spots in layer 2/3 of the MO region

The contours indicate higher pixel intensity values binarized with Otsu's method. Crosses indicates centers dense axon projections. Schematic on the top left outlines the location of the somatomotor regions and color code for SSp-bfd (cyan) and SSs (magenta) injection sites. Red crosses indicates position of bregma.

SSp-bfd injections, cyan: Rasgrf2-dCre N=3, Scnn1a-Cre N=4, Tlx3-Cre N=3, Rbp4-Cre N=3, Sim1-Cre N=3 and Ntsr1-Cre N=3.

SSs injections, magenta: Rasgrf2-dCre N=3, Scnn1a-Cre N=3, Tlx3-Cre N=3, Rbp4-Cre N=3, Sim1-Cre N=4 and Ntsr1-Cre N=3.

To identify relative layer contributions, axons within the same layer were summed together (ie. MOp 2/3 and MOs 2/3 are combined to form MO 2/3) and normalized by the total amount of axons in the MO region across all layers of both hemispheres (Figure 4-30). Axonal innervations in the MO layers are similar across SSp-bfd neurons and SSs neurons for Tlx3-Cre, Rbp4-Cre and Ntsr1-Cre where axons are distributed almost evenly across L2/3, L5, and L6a with less axons in L1. In comparison, axons are also distributed close to evenly for L2/3, L5, and L6a in Scnn1a-Cre but with more axons in L1. Rasgrf2-dCre projection mostly to L2/3 and L5 for both SSp-bfd and SSs injections. However, there are very few axons in L1 from SSp-bfd neurons in Rasgrf2-dCre compared to all other cre-lines and injections. While Rasgrf2-dCre, Scnn1a-Cre, Tlx3-Cre and Rbp4-Cre all project to contralateral cortical regions (Figure 4-16, Figure 4-18, Figure 4-25), only Tlx3-Cre and Rbp4-Cre neurons display contralateral MO innervation. In general, very few L6b axons are observed in all samples across both hemispheres.

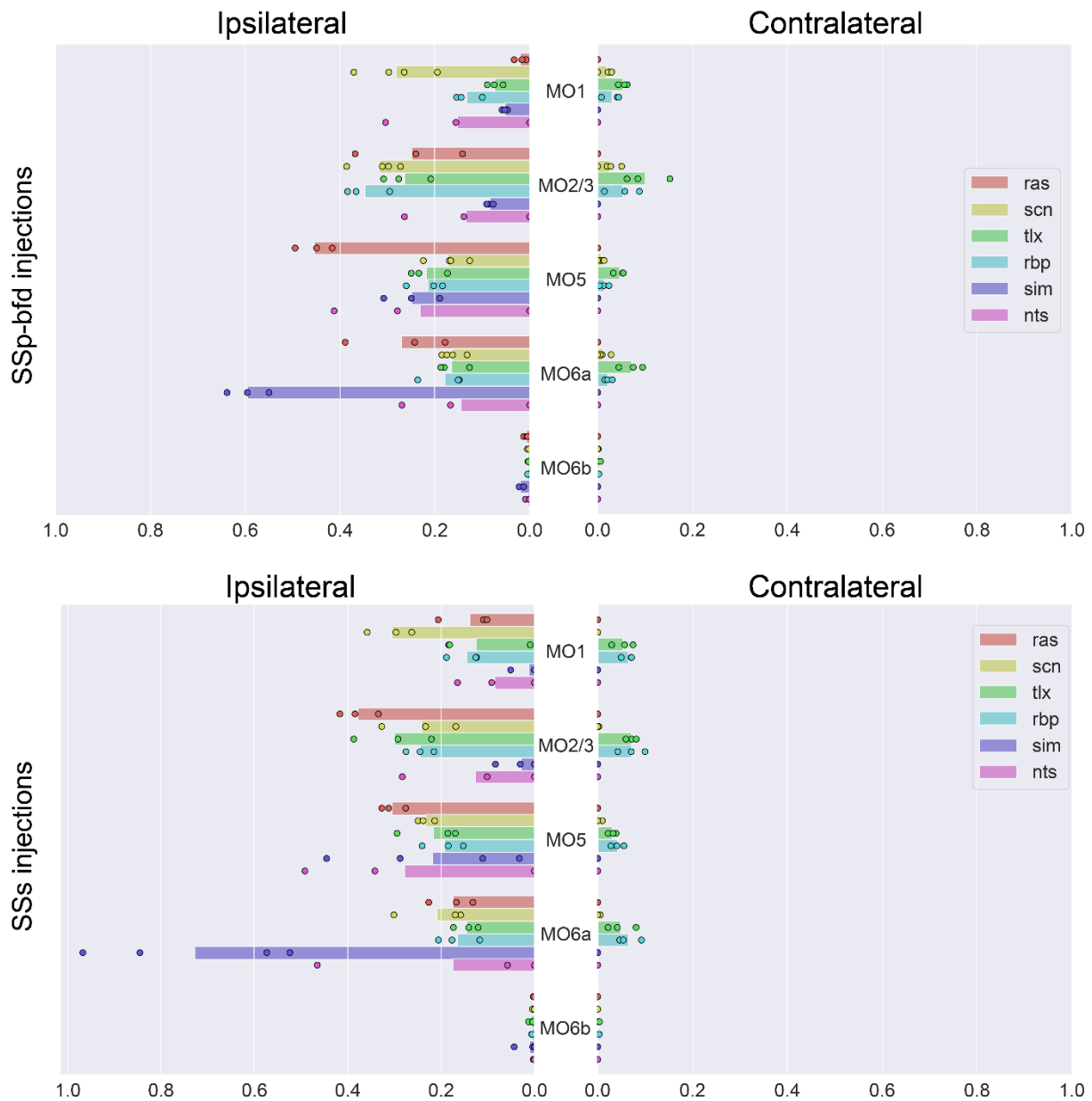


Figure 4-30 Amounts of axons in layers of the somatomotor regions for neurons of all six genotypes injected in the SSp-bfd or SSs.

Somatomotor regions, MO, includes MOs and MOp. Values for the same layer in MOs and MOp are summed together (ie. MO 2/3 is the sum of MOp 2/3 and MOs 2/3). Values are fractions of total axons in the MO, normalized to each sample. Each dot represents data from one sample, and bars represent group average. Left, ipsilateral to the injection site. Right, contralateral to the injection site.

SSp-bfd: *Rasgrf2-dCre* N=3, *Scnn1a-Cre* N=4, *Tlx3-Cre* N=3, *Rbp4-Cre* N=3, *Sim1-Cre* N=3 and *Ntsr1-Cre* N=3.

SSs: *Rasgrf2-dCre* N=3, *Scnn1a-Cre* N=3, *Tlx3-Cre* N=3, *Rbp4-Cre* N=3, *Sim1-Cre* N=4 and *Ntsr1-Cre* N=3.

4.3 Discussion

We mapped cell-type specific projection patterns from two whisker related somatosensory area. We took advantage of transgenic mouse lines *Rasgrf2-dCre*, *Scnn1a-Cre*, *Tlx3-Cre*, *Rbp4-Cre*, *Sim1-Cre* and *Ntsr1-Cre* and injected Cre-dependent viruses in to SSp-bfd or SSs. We established a work flow with virus injections, whole-brain immunostaining and clearing with iDISCO, imaging with Meso-scale selective plane imaging microscopy, pixel segmentation with 3D-convolutional network (TrailMap), registration to the Allen mouse brain common coordinate frame work, and custom data analysis scripts. Axons were visualized in the common coordinate frame work which allow quantifications and also comparisons across experiments.

We conclude 5 general observations from our analysis and discuss these findings further in the section below.

1) The projection patterns of the six transgenic lines involved largely agree with previous literature with respect to IT, PT, and CT excitatory subtypes. The distinct projection patterns across different transgenic lines can be already appreciated by simple inspections (Figure 4-7). In both injection sites, *Rasgrf2-dCre*, *Scnn1a-Cre*, *Tlx3-Cre* neurons confined their axons within the bilateral neocortex and the striatum. On the other hand, *Sim1-Cre* had fewer innervations to the ipsilateral isocortex but projected densely to the thalamus and brainstem. The *Ntsr1-Cre* also show very few cortical innervations but their axons are primarily observed in the thalamus. *Rbp4-Cre* samples showed projections to the cortex, striatum, thalamus, as well as the brainstem. These first order observations are consistent with previous literature where *Rasgrf2-dCre*, *Scnn1a-Cre*, *Tlx3-Cre* transgenic lines label IT type neurons, the *Sim1-Cre* being specific to PT type neurons, the *Ntsr1-Cre* mouse line labels CT type neurons and the *Rbp4-Cre* line labels both deep IT and PT types (Gerfen, Paletzki, and Heintz 2013; K. D. Harris and Mrsic-Flogel 2013b; J. A. Harris et al. 2014; K. D. Harris and Shepherd 2015a; E. J. Kim et al. 2015).

2) Consistent with previous literature, major target regions for SSp-bfd and SSs neurons are ipsilateral frontal regions, bilateral somatosensory regions and the bilateral striatum but a large repertoire of regions are also innervated, such high order sensory regions, orbital frontal regions and multimodal regions (Petreanu et al. 2007; Aronoff 2008; Yamashita et al. 2018b; Mao et al. 2011; Oh et al. 2014; Zingg et al. 2014; C. Guo et al. 2017a; Minamisawa et al. 2018; Petersen 2019; Santiago et al. 2019; Liu et al. 2022). Each transgenic line innervates a subset of the mentioned targets ranging from a few (ie. *Ntsr1* neurons) to many regions (ie. *Rbp4* neurons). Strongest projection targets of the SSp-bfd are the MO, SS, and CP for all samples. Other targets include, VISC, AUD, VIS, ACA, PL, RSP, PTLp, TEA, PERI, and ECT for *Rasgrf2-dCre*, *Scnn1a-Cre*, *Tlx3-Cre*, *Rbp4-Cre* and *Sim1-Cre* but not *Ntsr1-Cre*. In *Rbp4-Cre* and *Sim1-Cre*, denser brainstem innervation targets are SC, ZI, MRN, MB, SNr, APN, pons, PG, TRN, and medulla. Among the thalamic centers, the VP, LAT, and RT seemed to be the main targets for *Rbp4-Cre*, *Sim1-Cre*, and *Ntsr1-Cre*. Contralateral to the injection site, *Rasgrf2-dCre* samples only innervated somatosensory regions. *Scnn1a-Cre*, *Tlx3-Cre*, *Rbp4-Cre* innervated regions similar to those on the ipsilateral side. It is interesting to note that contralateral projections

for Sim1-Cre only occurs at the brain stem levels, with strong targets to PSV, SPV and medulla among others.

Projection patterns of the SSs show general resemblance to those of SSp-bfd qualitatively for most transgenic lines except for Rasgrf2-dCre and Scnn1a-Cre. Rasgrf2-dCre project to target regions in the contralateral side that are also present in the ipsilateral side. On the other hand, Scnn1a-Cre samples now innervate fewer contralateral sites, avoiding regions such as the AUD, ACA, AI, and RSP.

3) SSp-bfd and SSs neurons show similar projection patterns in the isocortex for Tlx3-Cre and Rbp4-Cre with quantitative differences but this is not the case in other transgenic lines. In Rasgrf2-dCre samples, more obvious difference occurs in the contralateral sites. SSp-bfd neurons only innervate the contralateral SSs while SSs neurons innervate the SSp-bfd, SSs, AUDd, PTLpp, and TEa. The observation is reversed in Scnn1a-Cre, where SSp-bfd neurons cover more regions than SSs neurons as mentioned above. Divergence of innervation pattern is even more prominent in the Sim1-Cre and Ntsr1-Cre samples. In Sim1-Cre samples, SSp-bfd neurons show stronger projections to the MO, SS, ACAd and RSP while SSs neurons project densely to the AUDd and TEa. SSp-bfd neurons in Ntsr1-Cre samples, have more axons in the MOs and VISrl while those of SSs project to AUDd instead.

4) Axons of SSp-bfd and SSs neurons are distributed evenly between L2/3 to L6a of MO with less in L1 and almost none in L6b in the ipsilateral somatomotor regions, with the exception of Rasgrf2-dCre and Scnn1a-Cre. In line with literature (Aronoff et al., 2010), there are almost no axons in L1 for SSp-bfd neurons in Rasgrf2-dCre brains. In contrast, there are slightly more axons in the L1 for Scnn1a-Cre samples.

5) While IT neurons are present in layers 2/3 to 5, only IT neurons in deeper layers project strongly to bilateral somatomotor regions.

Several pieces of observations points to the potential computational roles of each neuronal type in the microcircuit. L4 IT neurons receive strong innervation from first-order thalamic centers that carries simple but precise sensory information. These neurons typically innervate local cortical columns extensively to L2/3 but receive less in return. Hence, many suggest that the L4 IT are possibly the initial step in the local cortical circuits (Petersen 2019; Bosman et al. 2011; Feldmeyer 2012; K. D. Harris and Mrsic-Flogel 2013; K. D. Harris and Shepherd 2015; Staiger and Petersen 2021). However, we also observe extensive cortical-cortical axons in our Scnn1a-Cre samples with axons even to the contralateral SS. Cortical-cortical axons are also seen in three experiments that injects reporter virus to Scnn1a-Cre mice (experiments 183374804, 166459070, and 159888336) in the Allen Brain Institute connectome project (Oh et al. 2014). One factor that might give rise for these long-range axons could be that although Scnn1a-Cre injections mostly labeled neurons in L4, some neurons in the above L2/3 and the below L5 were also labeled (Figure 4-2). Projection pattern of Scnn1a-Cre samples show higher correlation to Tlx3-Cre neurons than Rasgrf2-dCre neurons, suggesting L5 neuron's contribution. This could be verified by injection of retrograde tracers in a remote region (ie. contralateral SS) and examine whether neurons in the ipsilateral

L4 are labeled. One experiment from the Mouse connectome project (Zingg et al. 2014) injected retrograde tracer fluorogold in to the SSp-bfd and observed cell bodies mostly in layer 2/3 of the contralateral ssp-bfd but also layer 4 and layer 5 (experiment SW120525-01A). Early in development, many L4 neurons possess transient contralaterally projecting axons but were later eliminated almost completely near P30 (De León Reyes et al. 2019b). L2/3 ITs are then considered as the second step where signal integration starts to occur, these neurons receive strong inputs from L4 and projects densely to local L5 and also over great distances to other cortical areas. In our data set, Rasgrf2-dCre neurons were located superficially in the L2/3 and Tlx3-Cre neurons were labeled in L5. These projection plans of these two sample groups also fall under the IT type since they only projected in the cerebrum. Projection targets are similar for these two groups on the ipsilateral side where they disseminate information all over the cortex for both SSp-bfd and SSs neurons. However, the numbers of contralateral target are greatly reduced in L2/3 ITs in SSp-bfd injections. It has also been shown that L2/3 stimulation modulates sensory evoked responses in L5 neurons (Quiquempoix et al. 2018). This might suggest that deeper IT neurons broadcast already integrated signal passed down from L2/3 to greater numbers of targets, especially to those in the contralateral regions.

In the later stage of the local circuit computation, PT type neurons located in L5b projects integrated information to subcortical and brainstem regions. L6 CT neurons projects to L5a and strongly to the thalamus. These CT neurons are often proposed a modulatory role throughout all stages in the local circuitry and are the least studied type. In our dataset, Sim1-Cre injections labeled neurons in L5 with axons primarily to the thalamus and brainstem regions, thus belonging to the PT group. Ntsr1-Cre injections labeled cell bodies in L6a with innervations primarily to the thalamus, thus fall under the CT group. These two groups had few isocortex innervation targets in general compared to the IT groups and especially absence in the prefrontal regions such as ILA and ORB. However, the Sim1-Cre samples show axons in bilateral brainstem regions such as the principal sensory nucleus of the trigeminal and spinal nucleus of the trigeminal. Neurons in these two brainstem regions are key relay stops in the lemniscal and paralemniscal pathways of ascending whisker sensation (Bosman et al. 2011; Feldmeyer 2012; Petersen 2019; Staiger and Petersen 2021). These observations suggest that the Sim1-Cre positive neurons may indeed be the final step of cortical computation, and is responsible for broadcasting top-down controls to subcortical regions. On the other hand, since L6 neurons Ntsr1-Cre neurons could sample integrated information from the outer layers with their upright pointing dendrites , they likely convey top-down information back to the thalamus (Thomson 2010).

The properties of deep layer IT and PT has been more extensively studied among other classes. The ITs in superficial L5 seems to be well located for signal integration since they could gain access to both simple sensory information from L4 directly or from L4 through L2/3 and abstract information from higher order thalamus that projects to L1 and L5a of the SSp-bfd (Baker et al. 2018; Petersen 2019; Feldmeyer 2012; Moberg and Takahashi 2022). The L5a IT neurons are regular spiking neurons that show AP frequency adaptation in response to depolarizing current pulses. On the other hand, the deeper L5b PT neurons are burst firing with little adaptations. These neurons have thick apical dendrites with extensive arborizations in L1 where many top-down projections from other cortical area arrives(Hattox and Nelson

2007; Moberg and Takahashi 2022). Based on these properties, several suggest that L5a IT neurons are the backbones for recurrent cortical network well suited for flexible cortical computation and L5b PT neurons outputs these computation to effectors in the subcortical regions (K. D. Harris and Mrsic-Flogel 2013b; K. D. Harris and Shepherd 2015a; Moberg and Takahashi 2022).

Classification of excitatory neurons into 3 classes based on their innervation patterns might be an over simplified concept. In our results, we observe discrepancy between the tentative IT type mousselines. *Rasgrf2*-Cre, *Scnn1a*-Cre, *Tlx3*-Cre all had different projection patterns despite all belong to the IT class. For instance, only *Tlx3*-Cre had strong projections to the contralateral somatomotor region. Furthermore, projection plans of neurons in *SSp-bfd* or *SSs* of the same transgenic line also shows major differences. These discrepancies could hint on the differential roles of neurons belonging to the same projection class in a region dependent manner. It is not completely surprising that neuronal morphology depends not only on expression of a certain marker but the location of cell body also matters. After examining thousands of individual neurons, Peng et al. 2021 concluded that similar molecular profiles of neurons do not guarantee the same morphology. These results further emphasize the importance of cell class classification at the finer scale.

In our data looking at axons in the isocortex, there are patches of dense axons near the *SSp-bfd* and the *SSs* for all IT class transgenic lines including *Rasgrf2-dCre*, *Scnn1a*-Cre, *Tlx3*-Cre, and *Rbp4*-Cre (*Figure 4-16* and *Figure 4-17*). In *SSp-bfd* injections, a thin strip of dense axon is located immediately posterior-medial to the *SSp-bfd*. This region is identified as the *VISrl* and might correspond to the innervation hot spots termed as 'PM' in Yamashita et al. 2018. In *SSs* injections, a strip of axon located immediately medial to the *SSp-bfd* appears and correspond to the *SSp-un* region. This region could be innervation hot spots termed as anteromedial dysgranula zone 'AM' and centromedial dysgranular zone 'CM' in Yamashita et al. 2018.

In Esmaeili et al. 2022 the authors labelled all layers of the *SSp-bfd* and *SSs* and observed two separate frontal innervation locations. The group found that *SSp-bfd* innervated densely 1.0 mm ML and 1.0 mm AP in a region identified as whisker-related primary motor region and the *SSs* innervated 1.0 mm ML and 1.7 mm AP in a location identified as the whisker-related secondary motor region. Differential location of of *SSp-bfd* and *SSs* innervation centers to frontal regions was also observed on the ipsilateral side in the current data sets. Centers of frontal innervation was in a medial-lateral arrangements particularly for *Rasgrf2-dCre* samples where *SSp-bfd* neurons innervated frontal region at 1.01 mm ML and 1.45 mm AP and *SSs* neurons innervated 0.69 mm ML and 1.38 mm AP. Centers of frontal innervations were also different in the anterior-posterior axis for other transgenic lines to various degree. In *Scnn1a*-Cre, *SSp-bfd* neuron projection centroids: ML= 0.81 mm, AP= 1.23 mm and *SSs* neuron projection centroids: ML= 0.81mm, AP= 1.7mm. In *Tlx3*-Cre, *SSp-bfd* neuron projection centroids: ML= 0.91 mm, AP= 1.05 mm and *SSs* neuron projection centroids: ML= 0.86 mm, AP= 1.3 mm. For *Rbp4*-Cre, *SSp-bfd* neuron projection centroids: ML= 0.84 mm, AP= 1.15 mm and *SSs* neuron projection centroids: ML= 0.94 mm, AP= 1.4 mm. *SSs* neurons in *Sim1*-Cre and *Ntsr1*-Cre had very little axons in the frontal regions and are unlikely

to contribute to this differential innervation spot. While we observe slightly separated frontal innervation centroids, the innervated areas were largely overlapping. Overall, the innervation centers of SSp-bfd vs. SSs were separated from each other in lesser extent compared to those observed in Esmaeili et al. 2022

The different observation might be attributed to the types of neurons labelled or the exact injection location of the SSp-bfd. Esmaeili et al. 2022 labelled all neurons across all layers with AAV mediated reporter proteins expression under the hSyn promoter. Meanwhile, specific neuronal types are infected with a genetic viral approach involving Cre-recombinase and Cre-dependent reporters in the current study. In future studies, other layer specific cre driver lines may be investigated to reproduce frontal projection patterns of SSp-bfd and SSs neurons to corroborate current findings. In the frontal regions projections from the SSp-bfd is also topographically arranged. Moving along the arcs in the same row from posterior to anterior correspond to shifts frontal innervation spot in the also in the posterior-anterior axis while a mirrored relationship was observed when moving across the rows from lateral to medial correspond to shifts in of frontal innervation spot in from medial to lateral (Ferezou et al. 2007; Mao et al. 2011). For instance, innervations from the C3 barrel would land in motor regions more anterior and lateral to those from the B1 barrel. In the current study, our injection sites were targeted the C2 representations which is relatively posterior-medial in the barrel field. Studies have also shown that somatotopic organisations in the SSs which mirrors those of SSp-bfd (Benison, Rector, and Barth 2007; Minamisawa et al. 2018). Barrel representation located more medially in the SSp-bfd correspond to regions more lateral in the SSs. Perhaps targeting barrels located more posterior-medial (for instance, the E1 barrel) would result in greater separations of the frontal innervation hot spots.

One limitation of the current study arises from the axon segmentation procedures using the 3D- convolutional network. The current network specializes in capturing sparse, dim and thin axons. In contrast, axons with denser morphologies are less recognized. These are often observed near the injection sites, in thick fiber bundles (such as the corpus callosum), and in heavily innervated thalamic centers. Hence, axons in samples with very strong thalamic innervations such as Ntsr1-Cre are underrepresented. To resolve this issue, future studies might utilize different models to capture different axon morphologies such as those in Gongwer et al. 2022. The authors trained separate models to account for regions with dense and fuzzy axons or bright and delineated axons, results of these models were applied to different regions and combined. An alternative approach would be preparing samples with fewer numbers of cells labeled, giving rise to less axons and thus avoiding dense morphologies. To limit the numbers of cells infected, one might consider sparse labeling strategy such as those used in Economo et al. 2016 involving limited Cre-recombinase availability, or those in Luo et al. 2016 for the use of a 'Supernova' construct. Future studies might also be interested in labeling axon terminals together with cytosolic markers to differentiate between passing axons and synaptic locations.

In the same sense, our current resolution is also not optimal to delineate densely packed axons. We opted to acquired image with the MesoSPIM at a 5.3 x 5.3 x 5 μm resolution for its fast imaging, big field of view and simplicity of data handling. However, when two or

more axonal branches travel very closely, they will appear as one in the image voxel. Overall, the amounts of axons are undercounted in our procedure. Acquire images at a higher resolution or the use of expansion microscopy could resolve this issue (Wassie, Zhao, and Boyden 2019).

Another caveat in axonal quantification is our method of normalization. The amounts of axons in a given region is represented as a fraction of total axons within a given sample. This was done to control for the size of injection site and balance samples with fewer or greater numbers of neurons labeled. While this might be reasonable for comparisons within a given transgenic line, this is less optimal to compare across lines. This strategy down plays then intrinsic projections characteristics of neurons where values for morphologies with longer axons, more target regions, and denser innervations are pushed down (such as the case seen in *Tlx3-Cre* and *Rbp4-Cre*). In contrast neurons with fewer axons covering less regions are leveled up (for instance, *Ntsr1-Cre*). Future studies should ideally normalize with the number of labeled neurons in each sample for more unbiased comparisons across cell-types. Unfortunately, the current imaging resolution and cell density did not allow clear differentiation of individual cell bodies.

Together with previous literature, the results of our current data provide anatomical basis for functional mappings in studies involving the mouse whisker system in a cell-type specific manner. Detailed examination of regions other than the isocortex is beyond the scope of this current report but will be discussed in the near future.

4.4 Methods

4.4.1 Animals

All experimental procedures were followed in compliance with protocol approved by the Swiss Federal Veterinary Office under license VD 1889.4.

Male and female mice of at least 6 weeks old of the following transgenic lines were involved: *Rasgrf2-2A-dCre* (IMSR_JAX:022864, Harris et al. 2014), *Scnn1a-Tg3-Cre* (IMSR_JAX:009613, Madisen et al. 2010), *Tlx3-Cre* (GENSAT, MMRRC_041158-UCD, Gerfen et al., 2013), *Sim1-Cre* (GENSAT, MMRRC 037650-UCD), *Rbp4-Cre* (GENSAT,MMRRC_037128-UCD), and *Ntsr1-Cre* (GENSAT, MMRRC SN 030648-UCD). In addition, 3 C57BL/6 mice was used as controls to test the Cre-independence of our reporter virus.

4.4.2 Headpost implantation and intrinsic optical imaging

Animals were weighed and anesthetized with isoflurane (3% with O₂ induction, then 1.5% maintenance). Body temperature was monitored and maintained at 37 °C through a heating pad and eye gel (VITA-POS, Pharma Medica AG) was applied to maintain eye moisture. Carprofen was injected subcutaneously (7.5 mg/kg at 1.5mg/mL) and lidocaine /bupivacaine mixture (20 µL; lidocaine 6 mg/kg bupivacaine 2.5 mg/kg.) was injected at the site of incision under the scalp. A piece of scalp was removed such that the skull underneath is revealed. The periosteum was carefully removed using a scalpel blade and the exposed surface was disinfected with a povidone-iodine solution (Betadine, Mundipharma Medical Company).

Then, a thin layer of super glue (Loctite 401, Henkel, Germany) was applied on the top of the skull and a custom-made metal head plate was positioned on top of the right hemisphere parallel to midline, with the animal's head tilted 30 degrees to the right on the anterior-posterior axis to position the left barrel cortex more horizontally. The head plate was further secured on the skull with dental acrylic (Paladur, Kulzer). All whiskers except for the C2 whisker on the right whisker pad were trimmed. After the procedure, the left barrel cortex and secondary somatosensory cortex were identified through intrinsic optical signal imaging as previously described (Ferezou et al. 2007)

4.4.3 Virus injection and perfusion

After at least 4 days of recovery, craniotomies were made to access the barrel cortex and secondary somatosensory cortex based on blood vessel patterns obtained from the intrinsic optical imaging. A total of 25 nL of AAV1-FLEX-tdTomato (Addgene # 28306, 1.2×10^{13} vg/mL) or AAV9- FLEX-EGFP-WPRE (Addgene # 51502, 1.9×10^{13} vg/mL) diluted 10 times with Ringers' solution were injected at a corresponding depth depending on the specific transgenic line. In some cases, we injected both sites each with a different virus in the same animal. The relevant injection depths were 200, 400, 500, 500, 700, and 850 μ m from the pia surface for Rasgrf2-2A-dCre, Scnn1a-Tg3-Cre, Tlx3-Cre, Sim1-Cre, Rbp4-Cre, and Ntsr1-Cre, respectively. Finally, craniotomies were sealed with UV-curing glue (NOA68, Thorlabs)

After 4 weeks of viral expression, animals were perfused with phosphate buffered saline (PBS, warmed up to 37 °C) with heparin solution (20 units / mL) followed by 4% paraformaldehyde (PFA, Electron Microscopy Science) in PBS. Brains were extracted, post fixed overnight in 4% PFA, rinsed and stored in PBS at 4 °C.

4.4.4 Whole brain immunostaining and clearing

We followed the procedure outlined on <https://idisco.info/idisco-protocol/> (Renier et al. 2014) for immunolabeling- enabled three-dimensional imaging of solvent-cleared organs (iDISCO). In brief, samples were dehydrated with methanol/dH₂O gradient, bleached, rehydrated, permeabilized and blocked before incubation with primary antibody for 7 days. Samples were washed for 2 days before incubation in secondary antibodies for another 7 days. After the incubation, samples were washed again for 2 days and dehydrated again in methanol/dH₂O gradient. Finally, the samples were immersed in ethyl cinnamate for refractive index matching and stored until light sheet imaging.

In our case, the immunostaining agents involved were: rabbit anti-GFP antibody (Ab290, Abcam, 1:1000 dilution), chicken anti-GFP antibody (GFP-1010, Aves Labs, 1:2000), and goat anti-tdTomato antibody (Ab8181, Sicgen, 1:600) as primary antibodies; alpaca anti-rabbit- Alexa 647 (SA5-10327, Invitrogen- Chronos, 1:800) , goat anti-chicken- Alexa 647(Ab150171, Abcam, 1:1000) , donkey anti-goat -Alexa 594 (A-11058, Invitrogen, 1:400), and Fab- donkey anti-goat-Alexa 594 (Fab 705-587-003, Jackson immunResearch, 1:600) as secondary antibodies.

4.4.5 Imaging

The cleared brains were imaged with a mesoscale selective brain image microscope (MesoSPIM, Voigt et al. 2019). The tissue was illuminated from the side of the injection site at 561 nm excitation with a LP561 filter and/or at 647 nm excitation with a LP663 filter. For most samples, an auto-fluorescent channel was also acquired at 488 nm illumination with a 530/43 filter. The final resolution of the image stack is $5.3 \times 5.3 \times 5 \mu\text{m}$ (x, y, z). Further technical details of the microscope can be found at <http://mesospim.org/> (Voigt et al. 2019).

4.4.6 Axon segmentations and post processing

Pixels containing axons were segmented from the images using TrailMap (Friedmann et al. 2020), a 3D convolutional network with U-net architecture specialized to identify elongated structures. We followed the author's guidelines for transfer learning (described on <https://github.com/albert597/TRAILMAP>) to familiarize the network with our own samples. Training of the network was done in Python 3.9 with Tensorflow version 2.8.0 on a GPU (NVIDIA GeForce RTX 3090). We labeled an additional 32 image sub-stacks from 8 samples to further train the model provided by the TrailMap authors to adapt to our own data. These image substacks were selected to encompass different morphologies of axons and artifacts, as well as different image appearances accounting for the two secondary antibodies (Alexa 591 or Alexa 647). Each substack consisted of 100 planes of original image cropped to a smaller dimension, the cropped sections were either 200×200 pixels or 400×400 pixels. We hand labeled pixels containing axons and pixels containing artifact as two separate categories. 70% of the new image sub-stacks as well as their annotations were assigned as the training data set and 30% were used as the validation data set. The training session consisted of 100 epochs and the model that returned the lowest validation loss using the cross-entropy loss function was selected. We obtained multiple models from many training sessions and evaluated the models based on visual examination of their segmentation result of three example full image stacks, each representing a potential challenge we encountered: a sample stack with higher levels of noise, a sample with lower axon intensity, and a sample with high level of bright artifacts at the edge and corners of the brain. The final model was selected such that it predicted well on all three types of image problems.

TrailMap's output, the probability for a given pixel to contain axon ranging from 0 to 1, was then used to compute a weighted axon skeleton as described in Friedmann et al. 2020. This step was done to prevent axonal disconnections caused by dim axons. In brief, the output image was binarized at 8 separate thresholds with 0.1 intervals from 0.2 to 0.9, this generates 8 binarized stacks. Skeletonization was done separately for each of the 8 stacks and the 8 skeletons were weighted by the initial threshold value and then summed up. We then compute all the connected components and excluded those with sizes less than 10 000 pixels to remove artifacts. The remaining connected components (typically ranged between 1 to 10) were carefully inspected to preserve bigger axon chunks that are disconnected and further eliminate artifacts.

The final axon skeletons were transformed into lists of x, y and z coordinate and down sampled to $25 \mu\text{m}^3$ voxel size for subsequent atlas registration.

4.4.7 Registration to Allen CCF v3 and injection site identification

The autofluorescence channel was down-sampled to 25 x25 x25 μm voxel size and align to the Allen CCF v3 (Q. Wang et al. 2020a) space using affined and bspline transformations via elastix (Klein et al. 2010; Shamonin 2013). The resultant transformation was then applied to the down-sampled signal channel and the list of axon coordinates. The transformed signal image stack was used to segment the site of injection semi-automatically through Ilastik (Berg et al. 2019). In Ilastik, a classifier is trained for each sample by sparsely annotating pixels in the background and pixels belong to the injection site. The classifier then segments out injection sites from the full stack. The size and the anatomical location of the injection site can be then identified since it has been already transformed to the CCF space. Samples that had at least 80% of its injection site voxels belonging to SSp-bfd or SSs were included in the subsequent analysis.

4.4.8 Analysis and visualizations

In order to characterize axon projections quantitatively, the numbers of axon voxels in the original resolution were summed according to its anatomical region after transformation. For each sample, the amounts of axons in each brain region are then divided by the total number of its axon containing pixels for normalization in order to compare between samples. Hence, values presented in quantitative graphs indicate fractions of total axons. Pearson's correlation was calculated among SSp-bfd and SSs samples on the normalized values on the most detailed levels of anatomical region. For this calculation, layers/ subregion information is retained as well as their left and right hemisphere location. In the later part of the paper, values are further normalized to its parent anatomical region (for instance, the isocortex, or the somatomotor regions).

To visualize axon patterns, the transformed list of down sampled axon coordinates is then replotted back as an image stack in the Allen atlas space. For each sample, every pixel represents a brain region with values as the amounts of axons in the original resolution. Then, each pixel value is normalized by the total numbers of axon for the given sample and hence represents a fraction of total axons. Summed projections are computed to view the image stack in horizontal, coronal and sagittal orientations.

In analysis with regards the somatomotor regions, axons within the same layer were masked, summed together (ie. MOp 2/3 and MOs 2/3 are combined to form MO 2/3) and normalized by the total amount of axons in the MO region across all layers of both hemispheres. In imageJ, axons in the MO 2/3 were sum projected horizontally, gaussian filtered with sigma= 4, and then binarized using with the Otsu's method. Outlines of each segmentation and their centroid locations are computed in custom python code.

Chapter 5 Conclusions and future directions

5.1 Conclusions

In the PhD thesis, I have highlighted the importance of neural projection maps in delineating neural mechanisms that underlies perception and behaviour. Chapter 2 (Esmaili et al. 2022) gives an example of sensory-motor task and describes changes in brain regions accompanying task learning. My contributions to Chapter 2 were to identify two pathways that convey whisker information to frontal motor regions. In Chapter 3 (Liu et al. 2022), I contribute towards neuronal type categorizations based on morphologies of single neurons. Finally, in Chapter 4, I move on to mapping neuronal connections in a populational level and in a cell-type specific manner.

5.1.1 Pathways involved in learning of whisker related sensorimotor task

In Chapter 2, we investigated datasets of silicon probe recordings obtained in a delayed sensory-motor task, where animals learn to associate whisker stimulation with a water reward (Esmaili et al. 2021; 2022). In this task, reward is only available when the animal licks 1 second after the whisker stimulation upon an auditory lick cue. This motor plans seemed to be maintained by sustained activity in secondary motor cortices during the delay period in expert animals. At the same time, there is an inhibition of activity during the delay time in the orofacial motor regions presumably to prevent time-out punishment due to early licking. Analysis on response latency times suggested that SSs might be a gateway to convey whisker information to frontal regions (Esmaili et al. 2021). In Chapter 2 (Esmaili et al. 2022), we visualize anatomical pathways of such connection using viral injections to label neurons in the SSp-bfd and SSs. We observed parallel pathways from SSp-bfd to the MOp and SSs to MOs, approximately 0.9 mm anterior to the SSp-bfd to MOp. The differential location of SSp-bfd and SSs innervation to frontal region is also observed in Chapter 4, mainly in Rasgrf2-dCre samples, although in medial-lateral arrangements and with less segregations. The different observation might be attributed to the types of neurons labelled. In Chapter 2, all neurons are labelled near the injection site with AAV mediated reporter proteins expression under the hSyn promoter. Meanwhile, specific neuronal types are infected with a genetic viral approach involving Cre-recombinase and Cre-dependent reporters in Chapter 4. In future studies, other layer specific cre driver lines may be investigated to reproduce frontal projection patterns of SSp-bfd and SSs neurons to corroborate findings in Chapter 2 or Chapter 4. For instance, the Sepw1 gene is also highly confined to L2/3 of the cerebral cortex, Rorb for L4, Efr3a for L5 and Ctgf for L6 neurons among many others (Madisen et al. 2010; Gerfen, Paletzki, and Heintz 2013; J. A. Harris et al. 2014).

5.1.2 Single neuron morphologies in layer 2/3 of the barrel cortex

In Chapter 3, we described projections of neurons in layer 2/3 of the SSp-bfd at finer scale for morphological categorizations of neurons. We labelled neurons randomly through two-photon guided *in vivo* electroporation which deliver plasmids encoding green fluorescent proteins. After a few days of expression, we extract the brain and treat it with modified CUBIC solution to improve signal to noise ratio. We then acquired whole-brain images with two-photon tomographic microscope and traced axons semi-automatically.

Finally, we register the brain images as well as the traces to the Allen mouse brain common coordinate frame work (CCF) to identify corresponding anatomical locations. We observed extremely diverse neuron morphologies in our 10 reconstructed neurons. Each neuron only projected to a subset of all target regions and there were no pairs of neurons with identical projections. We acknowledge that greater numbers of sample are required to appreciate the full repertoire of neuronal morphology. To ensure high throughput, strategies in all stages from sample preparation to image analysis must be carefully planned. Undoubtedly, projects of such scale are more realistic at a platform scale such as the MouseLight project at the Janelia research campus or the Big neuron project at the Allen Institute (Winnubst et al. 2019; Peng et al. 2021). In addition, we also appreciate that single neuron reconstruction is a strenuous yet delicate task. Axons are thin structures and difficult to visualize especially at distal regions, and our sample preparation procedure did not reveal axons to its entirety. Future experiments for neuronal reconstructions should consider sample preparation methods with signal amplification steps (Renier et al. 2014; Gong et al. 2013; C. Guo et al. 2017; Winnubst et al. 2019; Peng et al. 2021).

5.1.3 Cell-type specific projections of neurons in the whisker related primary and secondary somatosensory cortex

In Chapter 4, we examined population projections of neurons in the SSp-bfd or the SSs in a cell-type and layer specific manner. We took advantage of relatively layer constricted transgenic lines including Rasgrf2-dCre, Scnn1a-Cre, Tlx3-Cre, Rbp4-Cre, Sim1-Cre and Ntsr1-Cre in combination with injections of Cre-dependent reporter viruses. Lessons learned from Chapter 3, we adapted our procedures and treated samples through iDISCO, a whole-brain immunostaining and clearing protocol. We used Mesoscale selective plane imaging microscopy to obtain volumetric images of the cleared brains and segmented neuronal structures using a 3D convolutional network (TrailMap). Finally, brain images and segmentations were registered to the Allen CCF allowing quantifications of axons in anatomical regions and visualizations of projections in the same coordinate system. General projection patterns are consistent with previous literature describing the IT, PT, and CT projection classes and their inhabited layers (Gerfen, Paletzki, and Heintz 2013; K. D. Harris and Mrsic-Flogel 2013; J. A. Harris et al. 2014; K. D. Harris and Shepherd 2015; E. J. Kim et al. 2015). When the projections from all six transgenic lines are summed up, main target regions also correspond to previous findings on SSp-bfd neurons and SSs neurons (Petreanu et al. 2007; Aronoff 2008; Yamashita et al. 2018; Mao et al. 2011; Oh et al. 2014; Zingg et al. 2014; Guo et al. 2017; Minamisawa et al. 2018; Petersen 2019; Santiago et al. 2019; Liu et al. 2022). However, neurons of each transgenic line project to a few or many subsets of all regions, with Rbp4 expressing neurons showing the most comprehensive coverage.

Among the mouse line investigated, Sim1-Cre and Ntsr1-Cre neurons send the least numbers of areas coverage in the ipsilateral isocortex, and almost no axons in the contralateral cortex. Instead, they project strongly to the thalamus and brainstem regions. This could hint that they might be situated later in the cortical computation plan and receive already integrated information from other neurons as hypothesized by previous studies

(Petersen 2007; K. D. Harris and Mrsic-Flogel 2013; K. D. Harris and Shepherd 2015). Interestingly, although *Rasgrf2*-dCre, *Scnn1a*-Cre, *Tlx3*-Cre and *Rbp4*-Cre neurons all show projections to the contralateral cortex in various degree, the *Tlx3*-Cre and *Rbp4*-Cre neurons have far more contralateral projection targets (such as the somatomotor regions) compared to the other two. IT neurons situated in deeper layers might be critical for broadcasting whisker related information to the entire brain. This might suggest that they are situated in the early- mid stage in the cortical circuit for computation (K. D. Harris and Mrsic-Flogel 2013; K. D. Harris and Shepherd 2015; Moberg and Takahashi 2022).

We also present differences in projection patterns between neurons in the two injection sites but in the same mouse line, with the exception of *Tlx3*-Cre and *Rbp4*-Cre. This suggest that patterns of projections do not only depend on the expression of a single genetic marker but also rely on their location. This is not to our surprise because even neurons with similar molecular profiles show a large variety of morphology (Peng et al. 2021). Perhaps, these finding place more emphasize on the levels of brain region and their general location in the framework of information transmission and integration. On the other hand, morphologies of deep layer IT type neurons in *Tlx3*-Cre and *Rbp4*-Cre samples might be more preserved across regions.

5.2 Outlook

Establishing connectomes for more advance organisms provide valuable resource for functional studies that examines neural mechanisms of complex behaviours. High resolution imaging is absolutely need to capture small structures but larger volumes of tissue pose problems in both microscopy and data management. Problems associated with big data then press for more efficient data analytic algorithms. Some of these challenges are evident in this current report and we try to resolve these by mapping projections at a meso-scale level in the mouse brain. While some results from studies working with simpler organisms could be generalized to more complex species, many more abstract concepts could only be tested in higher organisms. To achieve similar goals in even more advance organisms such as primates or humans require major advancements in technology and extensive collaborations.

In order to disentangle the mysterious of the brain, we must gather as much information about the basic functional unit of the brain, neurons. Sparse labelling of cells allows single cell resolution, this could be using carefully designed virus constructs or single cell electroporation. In addition, various transgenic lines also provide access to particular cell groups. Visualization of synapses are also important to distinguish passing axons vs. true synaptic connections. The ultimate dream is to obtain a catalogue for each individual neuron in all aspects possible, including their molecular, morphological, electrophysiological and functional profiles.

Chapter 6 References

- Ahrens, Misha B, Michael B Orger, Drew N Robson, Jennifer M Li, and Philipp J Keller. 2013. "Whole-Brain Functional Imaging at Cellular Resolution Using Light-Sheet Microscopy." *Nature Methods* 10 (5): 413–20. <https://doi.org/10.1038/nmeth.2434>.
- Allen, William E., Isaac V. Kauvar, Michael Z. Chen, Ethan B. Richman, Samuel J. Yang, Ken Chan, Viviana Gradinaru, Benjamin E. Deverman, Liqun Luo, and Karl Deisseroth. 2017. "Global Representations of Goal-Directed Behavior in Distinct Cell Types of Mouse Neocortex." *Neuron* 94 (4): 891–907.e6. <https://doi.org/10.1016/j.neuron.2017.04.017>.
- Anastasiades, Paul G., David P. Collins, and Adam G. Carter. 2021. "Mediodorsal and Ventromedial Thalamus Engage Distinct L1 Circuits in the Prefrontal Cortex." *Neuron* 109 (2): 314–330.e4. <https://doi.org/10.1016/j.neuron.2020.10.031>.
- Antoine, Michelle W., Tomer Langberg, Philipp Schnepel, and Daniel E. Feldman. 2019. "Increased Excitation-Inhibition Ratio Stabilizes Synapse and Circuit Excitability in Four Autism Mouse Models." *Neuron* 101 (4): 648–661.e4. <https://doi.org/10.1016/j.neuron.2018.12.026>.
- Aronoff, Rachel. 2008. "Layer, Column and Cell-Type Specific Genetic Manipulation in Mouse Barrel Cortex." *Frontiers in Neuroscience* 2 (1): 64–71. <https://doi.org/10.3389/neuro.01.001.2008>.
- Aronoff, Rachel, Ferenc Matyas, Celine Mateo, Carine Ciron, Bernard Schneider, and Carl C. H. Petersen. 2010. "Long-Range Connectivity of Mouse Primary Somatosensory Barrel Cortex." *The European Journal of Neuroscience* 31 (12): 2221–33. <https://doi.org/10.1111/j.1460-9568.2010.07264.x>.
- Avermann, Michael, Christian Tamm, Celine Mateo, Wulfram Gerstner, and Carl C. H. Petersen. 2012. "Microcircuits of Excitatory and Inhibitory Neurons in Layer 2/3 of Mouse Barrel Cortex." *Journal of Neurophysiology* 107 (11): 3116–34. <https://doi.org/10.1152/jn.00917.2011>.
- Bagnall, Martha W., Court Hull, Eric A. Bushong, Mark H. Ellisman, and Massimo Scanziani. 2011. "Multiple Clusters of Release Sites Formed by Individual Thalamic Afferents onto Cortical Interneurons Ensure Reliable Transmission." *Neuron* 71 (1): 180–94. <https://doi.org/10.1016/j.neuron.2011.05.032>.
- Baker, Arielle, Brian Kalmbach, Mieko Morishima, Juhyun Kim, Ashley Juavinett, Nuo Li, and Nikolai Dembrow. 2018. "Specialized Subpopulations of Deep-Layer Pyramidal Neurons in the Neocortex: Bridging Cellular Properties to Functional Consequences." *The Journal of Neuroscience* 38 (24): 5441–55. <https://doi.org/10.1523/JNEUROSCI.0150-18.2018>.
- Bakker, Rembrandt, Thomas Wachtler, and Markus Diesmann. 2012. "CoCoMac 2.0 and the Future of Tract-Tracing Databases." *Frontiers in Neuroinformatics* 6. <https://doi.org/10.3389/fninf.2012.00030>.
- Batista Napotnik, Tina, Tamara Polajžer, and Damijan Miklavčič. 2021. "Cell Death Due to Electroporation – A Review." *Bioelectrochemistry* 141 (October): 107871. <https://doi.org/10.1016/j.bioelechem.2021.107871>.
- Becker, Klaus, Nina Jährling, Saiedeh Saghaei, Reto Weiler, and Hans-Ulrich Dodt. 2012. "Chemical Clearing and Dehydration of GFP Expressing Mouse Brains." Edited by Malú G. Tansey. *PLoS ONE* 7 (3): e33916. <https://doi.org/10.1371/journal.pone.0033916>.
- Benison, Alexander M., David M. Rector, and Daniel S. Barth. 2007. "Hemispheric Mapping of Secondary Somatosensory Cortex in the Rat." *Journal of Neurophysiology* 97 (1): 200–207. <https://doi.org/10.1152/jn.00673.2006>.
- Berg, Stuart, Dominik Kutra, Thorben Kroeger, Christoph N. Straehle, Bernhard X. Kausler, Carsten Haubold, Martin Schiegg, et al. 2019. "Ilastik: Interactive Machine Learning for (Bio)Image Analysis." *Nature Methods* 16 (12): 1226–32. <https://doi.org/10.1038/s41592-019-0582-9>.
- Bokinić, Phillip, Clarissa J Whitmire, Tobias M Leva, and James F A Poulet. 2022. "Brain-Wide Connectivity Map of Mouse Somatosensory Cortices." *Cerebral Cortex*, October, bhac386. <https://doi.org/10.1093/cercor/bhac386>.

- Bosman, Laurens W. J., Arthur R. Houweling, Cullen B. Owens, Nouk Tanke, Olesya T. Shevchouk, Negah Rahmati, Wouter H. T. Teunissen, et al. 2011. "Anatomical Pathways Involved in Generating and Sensing Rhythmic Whisker Movements." *Frontiers in Integrative Neuroscience* 5. <https://doi.org/10.3389/fnint.2011.00053>.
- Brecht, Michael. 2007. "Barrel Cortex and Whisker-Mediated Behaviors." *Current Opinion in Neurobiology* 17 (4): 408–16. <https://doi.org/10.1016/j.conb.2007.07.008>.
- Brodmann, Korbinian, and Laurence J. Gary. 2006. *Brodmann's Localisation in the Cerebral Cortex: The Principles of Comparative Localisation in the Cerebral Cortex Based on Cytoarchitectonics*. New York, NY: Springer.
- Brown, Jennifer, Ian Antón Oldenburg, Gregory I. Telian, Sandon Griffin, Mieke Voges, Vedant Jain, and Hillel Adesnik. 2021. "Spatial Integration during Active Tactile Sensation Drives Orientation Perception." *Neuron* 109 (10): 1707–1720.e7. <https://doi.org/10.1016/j.neuron.2021.03.020>.
- Cajal, Santiago Ramón y. 1995. *Histology of the Nervous System of Man and Vertebrates*.
- Cardin, Jessica A. 2018. "Inhibitory Interneurons Regulate Temporal Precision and Correlations in Cortical Circuits." *Trends in Neurosciences* 41 (10): 689–700. <https://doi.org/10.1016/j.tins.2018.07.015>.
- Chabrol, Francois P., Antonin Blot, and Thomas D. Mrsic-Flogel. 2019. "Cerebellar Contribution to Preparatory Activity in Motor Neocortex." *Neuron* 103 (3): 506–519.e4. <https://doi.org/10.1016/j.neuron.2019.05.022>.
- Chen, Jerry L., Stefano Carta, Joana Soldado-Magraner, Bernard L. Schneider, and Fritjof Helmchen. 2013. "Behaviour-Dependent Recruitment of Long-Range Projection Neurons in Somatosensory Cortex." *Nature* 499 (7458): 336–40. <https://doi.org/10.1038/nature12236>.
- Chen, Jerry L., David J. Margolis, Atanas Stankov, Lazar T. Sumanovski, Bernard L. Schneider, and Fritjof Helmchen. 2015. "Pathway-Specific Reorganization of Projection Neurons in Somatosensory Cortex during Learning." *Nature Neuroscience* 18 (8): 1101–8. <https://doi.org/10.1038/nn.4046>.
- Chen, Simon X., An Na Kim, Andrew J. Peters, and Takaki Komiyama. 2015. "Subtype-Specific Plasticity of Inhibitory Circuits in Motor Cortex during Motor Learning." *Nature Neuroscience* 18 (8): 1109–15. <https://doi.org/10.1038/nn.4049>.
- Chiang, Ann-Shyn, Chih-Yung Lin, Chao-Chun Chuang, Hsiu-Ming Chang, Chang-Huain Hsieh, Chang-Wei Yeh, Chi-Tin Shih, et al. 2011. "Three-Dimensional Reconstruction of Brain-Wide Wiring Networks in Drosophila at Single-Cell Resolution." *Current Biology* 21 (1): 1–11. <https://doi.org/10.1016/j.cub.2010.11.056>.
- Chittajallu, Ramesh, and John T. R. Isaac. 2010. "Emergence of Cortical Inhibition by Coordinated Sensory-Driven Plasticity at Distinct Synaptic Loci." *Nature Neuroscience* 13 (10): 1240–48. <https://doi.org/10.1038/nn.2639>.
- Chon, Uree, Daniel J. Vanselow, Keith C. Cheng, and Yongsoo Kim. 2019. "Enhanced and Unified Anatomical Labeling for a Common Mouse Brain Atlas." *Nature Communications* 10 (1): 5067. <https://doi.org/10.1038/s41467-019-13057-w>.
- Chung, Kwanghun, Jenelle Wallace, Sung-Yon Kim, Sandhiya Kalyanasundaram, Aaron S. Andalman, Thomas J. Davidson, Julie J. Mirzabekov, et al. 2013. "Structural and Molecular Interrogation of Intact Biological Systems." *Nature* 497 (7449): 332–37. <https://doi.org/10.1038/nature12107>.
- Cook, Steven J., Travis A. Jarrell, Christopher A. Brittin, Yi Wang, Adam E. Bloniarz, Maksim A. Yakovlev, Ken C. Q. Nguyen, et al. 2019. "Whole-Animal Connectomes of Both Caenorhabditis Elegans Sexes." *Nature* 571 (7763): 63–71. <https://doi.org/10.1038/s41586-019-1352-7>.
- Cruikshank, Scott J., Timothy J. Lewis, and Barry W. Connors. 2007. "Synaptic Basis for Intense Thalamocortical Activation of Feedforward Inhibitory Cells in Neocortex." *Nature Neuroscience* 10 (4): 462–68. <https://doi.org/10.1038/nn1861>.

- Cutts, Catherine S., and Stephen J. Eglen. 2014. "Detecting Pairwise Correlations in Spike Trains: An Objective Comparison of Methods and Application to the Study of Retinal Waves." *The Journal of Neuroscience: The Official Journal of the Society for Neuroscience* 34 (43): 14288–303. <https://doi.org/10.1523/JNEUROSCI.2767-14.2014>.
- De León Reyes, N. S., S. Mederos, I. Varela, L. A. Weiss, G. Perea, M. J. Galazo, and M. Nieto. 2019. "Transient Callosal Projections of L4 Neurons Are Eliminated for the Acquisition of Local Connectivity." *Nature Communications* 10 (1): 4549. <https://doi.org/10.1038/s41467-019-12495-w>.
- Delevich, Kristen, Jason Tucciarone, Z. Josh Huang, and Bo Li. 2015. "The Mediodorsal Thalamus Drives Feedforward Inhibition in the Anterior Cingulate Cortex via Parvalbumin Interneurons." *The Journal of Neuroscience: The Official Journal of the Society for Neuroscience* 35 (14): 5743–53. <https://doi.org/10.1523/JNEUROSCI.4565-14.2015>.
- Dent, Joseph A., Andrew G. Polson, and Michael W. Klymkowsky. 1989. "A Whole-Mount Immunocytochemical Analysis of the Expression of the Intermediate Filament Protein Vimentin in *Xenopus*." *Development* 105 (1): 61–74. <https://doi.org/10.1242/dev.105.1.61>.
- Diamond, Mathew E., Moritz von Heimendahl, Per Magne Knutsen, David Kleinfeld, and Ehud Ahissar. 2008. "'Where' and 'What' in the Whisker Sensorimotor System." *Nature Reviews. Neuroscience* 9 (8): 601–12. <https://doi.org/10.1038/nrn2411>.
- Economo, Michael N, Nathan G Clack, Luke D Lavis, Charles R Gerfen, Karel Svoboda, Eugene W Myers, and Jayaram Chandrashekar. 2016a. "A Platform for Brain-Wide Imaging and Reconstruction of Individual Neurons." *ELife* 5 (January): e10566. <https://doi.org/10.7554/eLife.10566>.
- Economo, Michael N., Nathan G. Clack, Luke D. Lavis, Charles R. Gerfen, Karel Svoboda, Eugene W. Myers, and Jayaram Chandrashekar. 2016b. "A Platform for Brain-Wide Imaging and Reconstruction of Individual Neurons." *ELife* 5 (January): e10566. <https://doi.org/10.7554/eLife.10566>.
- Economo, Michael N., Sarada Viswanathan, Bosiljka Tasic, Erhan Bas, Johan Winnubst, Vilas Menon, Lucas T. Graybuck, et al. 2018. "Distinct Descending Motor Cortex Pathways and Their Roles in Movement." *Nature* 563 (7729): 79–84. <https://doi.org/10.1038/s41586-018-0642-9>.
- Egger, Robert, Rajeevan T. Narayanan, Jason M. Guest, Arco Bast, Daniel Udvary, Luis F. Messori, Suman Das, Christiaan P. J. de Kock, and Marcel Oberlaender. 2020. "Cortical Output Is Gated by Horizontally Projecting Neurons in the Deep Layers." *Neuron* 105 (1): 122–137.e8. <https://doi.org/10.1016/j.neuron.2019.10.011>.
- El-Boustani, Sami, B. Semihcan Sermet, Georgios Foustoukos, Tess B. Oram, Ofer Yizhar, and Carl C. H. Petersen. 2020. "Anatomically and Functionally Distinct Thalamocortical Inputs to Primary and Secondary Mouse Whisker Somatosensory Cortices." *Nature Communications* 11 (1): 3342. <https://doi.org/10.1038/s41467-020-17087-7>.
- Erickson, Bradley J., Panagiotis Korfiatis, Zeynettin Akkus, and Timothy L. Kline. 2017. "Machine Learning for Medical Imaging." *RadioGraphics* 37 (2): 505–15. <https://doi.org/10.1148/rg.2017160130>.
- Ertürk, Ali, Klaus Becker, Nina Jährling, Christoph P Mauch, Caroline D Hojer, Jackson G Egen, Farida Hellal, Frank Bradke, Morgan Sheng, and Hans-Ulrich Dodt. 2012. "Three-Dimensional Imaging of Solvent-Cleared Organs Using 3DISCO." *Nature Protocols* 7 (11): 1983–95. <https://doi.org/10.1038/nprot.2012.119>.
- Esmaili, Vahid, and Mathew E. Diamond. 2019. "Neuronal Correlates of Tactile Working Memory in Prefrontal and Vibrissal Somatosensory Cortex." *Cell Reports* 27 (11): 3167–3181.e5. <https://doi.org/10.1016/j.celrep.2019.05.034>.
- Esmaili, Vahid, Anastasiia Oryshchuk, Reza Asri, Keita Tamura, Georgios Foustoukos, Yanqi Liu, Romain Guet, Sylvain Crochet, and Carl C. H. Petersen. 2022. "Learning-Related Congruent and Incongruent Changes of Excitation and Inhibition in Distinct Cortical Areas." Edited by Alberto Bacci. *PLOS Biology* 20 (5): e3001667. <https://doi.org/10.1371/journal.pbio.3001667>.

- Esmaeili, Vahid, Keita Tamura, Georgios Foustoukos, Anastasiia Oryshchuk, Sylvain Crochet, and Carl Ch Petersen. 2020. "Cortical Circuits for Transforming Whisker Sensation into Goal-Directed Licking." *Current Opinion in Neurobiology* 65 (December): 38–48. <https://doi.org/10.1016/j.conb.2020.08.003>.
- Esmaeili, Vahid, Keita Tamura, Samuel P. Muscinelli, Alireza Modirshanechi, Marta Boscaglia, Ashley B. Lee, Anastasiia Oryshchuk, et al. 2021. "Rapid Suppression and Sustained Activation of Distinct Cortical Regions for a Delayed Sensory-Triggered Motor Response." *Neuron* 109 (13): 2183–2201.e9. <https://doi.org/10.1016/j.neuron.2021.05.005>.
- Falk, Thorsten, Dominic Mai, Robert Bensch, Özgün Çiçek, Ahmed Abdulkadir, Yassine Marrakchi, Anton Böhm, et al. 2019. "U-Net: Deep Learning for Cell Counting, Detection, and Morphometry." *Nature Methods* 16 (1): 67–70. <https://doi.org/10.1038/s41592-018-0261-2>.
- Fan, Xue, and Henry Markram. 2019. "A Brief History of Simulation Neuroscience." *Frontiers in Neuroinformatics* 13 (May): 32. <https://doi.org/10.3389/fninf.2019.00032>.
- Feldmeyer, Dirk. 2012. "Excitatory Neuronal Connectivity in the Barrel Cortex." *Frontiers in Neuroanatomy* 6. <https://doi.org/10.3389/fnana.2012.00024>.
- Feldmeyer, Dirk, Michael Brecht, Fritjof Helmchen, Carl C. H. Petersen, James F. A. Poulet, Jochen F. Staiger, Heiko J. Luhmann, and Cornelius Schwarz. 2013. "Barrel Cortex Function." *Progress in Neurobiology* 103 (April): 3–27. <https://doi.org/10.1016/j.pneurobio.2012.11.002>.
- Feldmeyer, Dirk, Joachim Lübke, and Bert Sakmann. 2006. "Efficacy and Connectivity of Intracolumnar Pairs of Layer 2/3 Pyramidal Cells in the Barrel Cortex of Juvenile Rats." *The Journal of Physiology* 575 (Pt 2): 583–602. <https://doi.org/10.1113/jphysiol.2006.105106>.
- Feng, Qiru, Sile An, Ruiyu Wang, Rui Lin, Anan Li, Hui Gong, and Minmin Luo. 2021. "Whole-Brain Reconstruction of Neurons in the Ventral Pallidum Reveals Diverse Projection Patterns." *Frontiers in Neuroanatomy* 15 (December): 801354. <https://doi.org/10.3389/fnana.2021.801354>.
- Ferezou, Isabelle, Florent Haiss, Luc J. Gentet, Rachel Aronoff, Bruno Weber, and Carl C. H. Petersen. 2007. "Spatiotemporal Dynamics of Cortical Sensorimotor Integration in Behaving Mice." *Neuron* 56 (5): 907–23. <https://doi.org/10.1016/j.neuron.2007.10.007>.
- Freund, Tamás F., and Miklós Antal. 1988. "GABA-Containing Neurons in the Septum Control Inhibitory Interneurons in the Hippocampus." *Nature* 336 (6195): 170–73. <https://doi.org/10.1038/336170a0>.
- Freund, Tamás F., and István Katona. 2007. "Perisomatic Inhibition." *Neuron* 56 (1): 33–42. <https://doi.org/10.1016/j.neuron.2007.09.012>.
- Frick, Andreas, Dirk Feldmeyer, Moritz Helmstaedter, and Bert Sakmann. 2008. "Monosynaptic Connections between Pairs of L5A Pyramidal Neurons in Columns of Juvenile Rat Somatosensory Cortex." *Cerebral Cortex (New York, N.Y.: 1991)* 18 (2): 397–406. <https://doi.org/10.1093/cercor/bhm074>.
- Friedmann, Drew, Albert Pun, Eliza L. Adams, Jan H. Lui, Justus M. Kebschull, Sophie M. Grutzner, Caitlin Castagnola, Marc Tessier-Lavigne, and Liqun Luo. 2020. "Mapping Mesoscale Axonal Projections in the Mouse Brain Using a 3D Convolutional Network." *Proceedings of the National Academy of Sciences* 117 (20): 11068–75. <https://doi.org/10.1073/pnas.1918465117>.
- Froemke, Robert C. 2015. "Plasticity of Cortical Excitatory-Inhibitory Balance." *Annual Review of Neuroscience* 38 (July): 195–219. <https://doi.org/10.1146/annurev-neuro-071714-034002>.
- Frostig, Ron D., Ying Xiong, Cynthia H. Chen-Bee, Eugen Kvasnák, and Jimmy Stehberg. 2008. "Large-Scale Organization of Rat Sensorimotor Cortex Based on a Motif of Large Activation Spreads." *The Journal of Neuroscience: The Official Journal of the Society for Neuroscience* 28 (49): 13274–84. <https://doi.org/10.1523/JNEUROSCI.4074-08.2008>.
- Fu, Yu, Jason M. Tucciarone, J. Sebastian Espinosa, Nengyin Sheng, Daniel P. Darcy, Roger A. Nicoll, Z. Josh Huang, and Michael P. Stryker. 2014. "A Cortical Circuit for Gain Control by Behavioral State." *Cell* 156 (6): 1139–52. <https://doi.org/10.1016/j.cell.2014.01.050>.

- Gabernet, Laetitia, Shantanu P. Jadhav, Daniel E. Feldman, Matteo Carandini, and Massimo Scanziani. 2005. "Somatosensory Integration Controlled by Dynamic Thalamocortical Feed-Forward Inhibition." *Neuron* 48 (2): 315–27. <https://doi.org/10.1016/j.neuron.2005.09.022>.
- Gainey, Melanie A., Joseph W. Aman, and Daniel E. Feldman. 2018. "Rapid Disinhibition by Adjustment of PV Intrinsic Excitability during Whisker Map Plasticity in Mouse S1." *The Journal of Neuroscience: The Official Journal of the Society for Neuroscience* 38 (20): 4749–61. <https://doi.org/10.1523/JNEUROSCI.3628-17.2018>.
- Gao, Le, Sang Liu, Lingfeng Gou, Yachuang Hu, Yanhe Liu, Li Deng, Danyi Ma, et al. 2022. "Single-Neuron Projectome of Mouse Prefrontal Cortex." *Nature Neuroscience* 25 (4): 515–29. <https://doi.org/10.1038/s41593-022-01041-5>.
- Gao, Zhenyu, Courtney Davis, Alyse M. Thomas, Michael N. Economo, Amada M. Abrego, Karel Svoboda, Chris I. De Zeeuw, and Nuo Li. 2018. "A Cortico-Cerebellar Loop for Motor Planning." *Nature* 563 (7729): 113–16. <https://doi.org/10.1038/s41586-018-0633-x>.
- Gasselín, Célia, Benoît Hohl, Arthur Vernet, Sylvain Crochet, and Carl C. H. Petersen. 2021. "Cell-Type-Specific Nicotinic Input Disinhibits Mouse Barrel Cortex during Active Sensing." *Neuron* 109 (5): 778–787.e3. <https://doi.org/10.1016/j.neuron.2020.12.018>.
- Gehrlach, Daniel A, Caroline Weiand, Thomas N Gaitanos, Eunjae Cho, Alexandra S Klein, Alexandru A Hennrich, Karl-Klaus Conzelmann, and Nadine Gogolla. 2020. "A Whole-Brain Connectivity Map of Mouse Insular Cortex." *eLife* 9 (September): e55585. <https://doi.org/10.7554/eLife.55585>.
- Gerfen, Charles R., Ronald Paletzki, and Nathaniel Heintz. 2013. "GENSAT BAC Cre-Recombinase Driver Lines to Study the Functional Organization of Cerebral Cortical and Basal Ganglia Circuits." *Neuron* 80 (6): 1368–83. <https://doi.org/10.1016/j.neuron.2013.10.016>.
- Gilad, Ariel, Yasir Gallero-Salas, Dominik Groos, and Fritjof Helmchen. 2018. "Behavioral Strategy Determines Frontal or Posterior Location of Short-Term Memory in Neocortex." *Neuron* 99 (4): 814–828.e7. <https://doi.org/10.1016/j.neuron.2018.07.029>.
- Gong, Hui, Dongli Xu, Jing Yuan, Xiangning Li, Congdi Guo, Jie Peng, Yuxin Li, et al. 2016. "High-Throughput Dual-Colour Precision Imaging for Brain-Wide Connectome with Cytoarchitectonic Landmarks at the Cellular Level." *Nature Communications* 7 (1): 12142. <https://doi.org/10.1038/ncomms12142>.
- Gong, Hui, Shaoqun Zeng, Cheng Yan, Xiaohua Lv, Zhongqin Yang, Tonghui Xu, Zhao Feng, et al. 2013. "Continuously Tracing Brain-Wide Long-Distance Axonal Projections in Mice at a One-Micron Voxel Resolution." *NeuroImage* 74 (July): 87–98. <https://doi.org/10.1016/j.neuroimage.2013.02.005>.
- Gongwer, Michael W., Cassandra B. Klune, João Couto, Benita Jin, Alexander S. Enos, Rita Chen, Drew Friedmann, and Laura A. DeNardo. 2022. "Brain-Wide Projections and Differential Encoding of Prefrontal Neuronal Classes Underlying Learned and Innate Threat Avoidance." Preprint. Neuroscience. <https://doi.org/10.1101/2022.03.31.486619>.
- Grant, Robyn A., Vicki Breakell, and Tony J. Prescott. 2018. "Whisker Touch Sensing Guides Locomotion in Small, Quadrupedal Mammals." *Proceedings. Biological Sciences* 285 (1880). <https://doi.org/10.1098/rspb.2018.0592>.
- Guo, Congdi, Jie Peng, Yalun Zhang, Anan Li, Yuxin Li, Jing Yuan, Xiaofeng Xu, Miao Ren, Hui Gong, and Shangbin Chen. 2017. "Single-Axon Level Morphological Analysis of Corticofugal Projection Neurons in Mouse Barrel Field." *Scientific Reports* 7 (1): 2846. <https://doi.org/10.1038/s41598-017-03000-8>.
- Guo, Zengcai V., Hidehiko K. Inagaki, Kayvon Daie, Shaul Druckmann, Charles R. Gerfen, and Karel Svoboda. 2017. "Maintenance of Persistent Activity in a Frontal Thalamocortical Loop." *Nature* 545 (7653): 181–86. <https://doi.org/10.1038/nature22324>.
- Guo, Zengcai V., Nuo Li, Daniel Huber, Eran Ophir, Diego Gutnisky, Jonathan T. Ting, Guoping Feng, and Karel Svoboda. 2014. "Flow of Cortical Activity Underlying a Tactile Decision in Mice." *Neuron* 81 (1): 179–94. <https://doi.org/10.1016/j.neuron.2013.10.020>.

- Haider, Bilal, Michael Häusser, and Matteo Carandini. 2013. "Inhibition Dominates Sensory Responses in the Awake Cortex." *Nature* 493 (7430): 97–100. <https://doi.org/10.1038/nature11665>.
- Hama, Hiroshi, Hiroshi Kurokawa, Hiroyuki Kawano, Ryoko Ando, Tomomi Shimogori, Hisayori Noda, Kiyoko Fukami, Asako Sakaue-Sawano, and Atsushi Miyawaki. 2011. "Scale: A Chemical Approach for Fluorescence Imaging and Reconstruction of Transparent Mouse Brain." *Nature Neuroscience* 14 (11): 1481–88. <https://doi.org/10.1038/nn.2928>.
- Han, Yunyun, Justus M. Kebschull, Robert A. A. Campbell, Devon Cowan, Fabia Imhof, Anthony M. Zador, and Thomas D. Mrsic-Flogel. 2018. "The Logic of Single-Cell Projections from Visual Cortex." *Nature* 556 (7699): 51–56. <https://doi.org/10.1038/nature26159>.
- Hangya, Balázs, Sachin P. Ranade, Maja Lorenc, and Adam Kepecs. 2015. "Central Cholinergic Neurons Are Rapidly Recruited by Reinforcement Feedback." *Cell* 162 (5): 1155–68. <https://doi.org/10.1016/j.cell.2015.07.057>.
- Harris, Julie A., Karla E. Hirokawa, Staci A. Sorensen, Hong Gu, Maya Mills, Lydia L. Ng, Phillip Bohn, et al. 2014. "Anatomical Characterization of Cre Driver Mice for Neural Circuit Mapping and Manipulation." *Frontiers in Neural Circuits* 8 (July). <https://doi.org/10.3389/fncir.2014.00076>.
- Harris, Kenneth D., and Thomas D. Mrsic-Flogel. 2013. "Cortical Connectivity and Sensory Coding." *Nature* 503 (7474): 51–58. <https://doi.org/10.1038/nature12654>.
- Harris, Kenneth D., and Gordon M G Shepherd. 2015. "The Neocortical Circuit: Themes and Variations." *Nature Neuroscience* 18 (2): 170–81. <https://doi.org/10.1038/nn.3917>.
- Hattox, Alexis M., and Sacha B. Nelson. 2007. "Layer V Neurons in Mouse Cortex Projecting to Different Targets Have Distinct Physiological Properties." *Journal of Neurophysiology* 98 (6): 3330–40. <https://doi.org/10.1152/jn.00397.2007>.
- He, Miao, Jason Tucciarone, SooHyun Lee, Maximiliano José Nigro, Yongsoo Kim, Jesse Maurica Levine, Sean Michael Kelly, et al. 2016. "Strategies and Tools for Combinatorial Targeting of GABAergic Neurons in Mouse Cerebral Cortex." *Neuron* 91 (6): 1228–43. <https://doi.org/10.1016/j.neuron.2016.08.021>.
- Hillman, Elizabeth M.C., Venkatakaushik Voleti, Wenzhe Li, and Hang Yu. 2019. "Light-Sheet Microscopy in Neuroscience." *Annual Review of Neuroscience* 42 (1): 295–313. <https://doi.org/10.1146/annurev-neuro-070918-050357>.
- Hofer, Sonja B., Ho Ko, Bruno Pichler, Joshua Vogelstein, Hana Ros, Hongkui Zeng, Ed Lein, Nicholas A. Lesica, and Thomas D. Mrsic-Flogel. 2011. "Differential Connectivity and Response Dynamics of Excitatory and Inhibitory Neurons in Visual Cortex." *Nature Neuroscience* 14 (8): 1045–52. <https://doi.org/10.1038/nn.2876>.
- Hong, Y. Kate, Clay O. Lacefield, Chris C. Rodgers, and Randy M. Bruno. 2018. "Sensation, Movement and Learning in the Absence of Barrel Cortex." *Nature* 561 (7724): 542–46. <https://doi.org/10.1038/s41586-018-0527-y>.
- Hu, Hua, Jian Gan, and Peter Jonas. 2014. "Interneurons. Fast-Spiking, Parvalbumin⁺ GABAergic Interneurons: From Cellular Design to Microcircuit Function." *Science (New York, N.Y.)* 345 (6196): 1255–63. <https://doi.org/10.1126/science.1255263>.
- Huang, Qing, Yijun Chen, Shijie Liu, Cheng Xu, Tingting Cao, Yongchao Xu, Xiaojun Wang, et al. 2020. "Weakly Supervised Learning of 3D Deep Network for Neuron Reconstruction." *Frontiers in Neuroanatomy* 14: 38. <https://doi.org/10.3389/fnana.2020.00038>.
- Huang, Z. Josh. 2014. "Toward a Genetic Dissection of Cortical Circuits in the Mouse." *Neuron* 83 (6): 1284–1302. <https://doi.org/10.1016/j.neuron.2014.08.041>.
- Isaacson, Jeffry S., and Massimo Scanziani. 2011. "How Inhibition Shapes Cortical Activity." *Neuron* 72 (2): 231–43. <https://doi.org/10.1016/j.neuron.2011.09.027>.
- Isett, Brian R., Sierra H. Feasel, Monet A. Lane, and Daniel E. Feldman. 2018. "Slip-Based Coding of Local Shape and Texture in Mouse S1." *Neuron* 97 (2): 418–433.e5. <https://doi.org/10.1016/j.neuron.2017.12.021>.
- Johnson, B. A., and R. D. Frostig. 2016. "Long, Intrinsic Horizontal Axons Radiating through and beyond Rat Barrel Cortex Have Spatial Distributions Similar to Horizontal Spreads of Activity

- Evoked by Whisker Stimulation." *Brain Structure & Function* 221 (7): 3617–39.
<https://doi.org/10.1007/s00429-015-1123-7>.
- Johnson, Brett A., and Ron D. Frostig. 2018. "Long-Range, Border-Crossing, Horizontal Axon Radiations Are a Common Feature of Rat Neocortical Regions That Differ in Cytoarchitecture." *Frontiers in Neuroanatomy* 12: 50.
<https://doi.org/10.3389/fnana.2018.00050>.
- Jones, Edward G. 1994. "Santiago Ram6ny CajalandtheCroonianLecture,March]094" 17 (5).
- Judkewitz, Benjamin, Matteo Rizzi, Kazuo Kitamura, and Michael Häusser. 2009. "Targeted Singlecell Electroporation of Mammalian Neurons in Vivo." In *Nature Protocols*.
- Keller, Philipp J., and Misha B. Ahrens. 2015. "Visualizing Whole-Brain Activity and Development at the Single-Cell Level Using Light-Sheet Microscopy." *Neuron* 85 (3): 462–83.
<https://doi.org/10.1016/j.neuron.2014.12.039>.
- Kim, Euseok J., Ashley L. Juavinett, Espoir M. Kyubwa, Matthew W. Jacobs, and Edward M. Callaway. 2015. "Three Types of Cortical Layer 5 Neurons That Differ in Brain-Wide Connectivity and Function." *Neuron* 88 (6): 1253–67. <https://doi.org/10.1016/j.neuron.2015.11.002>.
- Kim, Yongsoo, Guangyu Robert Yang, Kith Pradhan, Kannan Umadevi Venkataraju, Mihail Bota, Luis Carlos García Del Molino, Greg Fitzgerald, et al. 2017. "Brain-Wide Maps Reveal Stereotyped Cell-Type-Based Cortical Architecture and Subcortical Sexual Dimorphism." *Cell* 171 (2): 456–469.e22. <https://doi.org/10.1016/j.cell.2017.09.020>.
- Klein, S., M. Staring, K. Murphy, M.A. Viergever, and J. Pluim. 2010. "Elastix: A Toolbox for Intensity-Based Medical Image Registration." *IEEE Transactions on Medical Imaging* 29 (1): 196–205.
<https://doi.org/10.1109/TMI.2009.2035616>.
- Knutsen, Per Magne, Maciej Pietr, and Ehud Ahissar. 2006. "Haptic Object Localization in the Vibrissal System: Behavior and Performance." *The Journal of Neuroscience: The Official Journal of the Society for Neuroscience* 26 (33): 8451–64. <https://doi.org/10.1523/JNEUROSCI.1516-06.2006>.
- Koralek, K. A., J. Olavarria, and H. P. Killackey. 1990. "Areal and Laminar Organization of Corticocortical Projections in the Rat Somatosensory Cortex." *The Journal of Comparative Neurology* 299 (2): 133–50. <https://doi.org/10.1002/cne.902990202>.
- Kötter, Rolf. 2004. "Online Retrieval, Processing, and Visualization of Primate Connectivity Data From the CoCoMac Database." *Neuroinformatics* 2 (2): 127–44.
<https://doi.org/10.1385/NI:2:2:127>.
- Kvitsiani, D., S. Ranade, B. Hangya, H. Taniguchi, J. Z. Huang, and A. Kepecs. 2013. "Distinct Behavioural and Network Correlates of Two Interneuron Types in Prefrontal Cortex." *Nature* 498 (7454): 363–66. <https://doi.org/10.1038/nature12176>.
- Kwon, Sung Eun, Hongdian Yang, Genki Minamisawa, and Daniel H. O'Connor. 2016. "Sensory and Decision-Related Activity Propagate in a Cortical Feedback Loop during Touch Perception." *Nature Neuroscience* 19 (9): 1243–49. <https://doi.org/10.1038/nn.4356>.
- Le Merre, Pierre, Vahid Esmaeili, Eloïse Charrière, Katia Galan, Paul-A. Salin, Carl C. H. Petersen, and Sylvain Crochet. 2018. "Reward-Based Learning Drives Rapid Sensory Signals in Medial Prefrontal Cortex and Dorsal Hippocampus Necessary for Goal-Directed Behavior." *Neuron* 97 (1): 83–91.e5. <https://doi.org/10.1016/j.neuron.2017.11.031>.
- Lee, Soohyun, Illya Kruglikov, Z. Josh Huang, Gord Fishell, and Bernardo Rudy. 2013. "A Disinhibitory Circuit Mediates Motor Integration in the Somatosensory Cortex." *Nature Neuroscience* 16 (11): 1662–70. <https://doi.org/10.1038/nn.3544>.
- Lee, Taehee, and Uhnoh Kim. 2012. "Descending Projections from the Dysgranular Zone of Rat Primary Somatosensory Cortex Processing Deep Somatic Input." *Journal of Comparative Neurology* 520 (5): 1021–46. <https://doi.org/10.1002/cne.22767>.
- Lefort, Sandrine, Christian Tómm, J.-C. Floyd Sarria, and Carl C.H. Petersen. 2009. "The Excitatory Neuronal Network of the C2 Barrel Column in Mouse Primary Somatosensory Cortex." *Neuron* 61 (2): 301–16. <https://doi.org/10.1016/j.neuron.2008.12.020>.

- Letzkus, Johannes J., Steffen B. E. Wolff, Elisabeth M. M. Meyer, Philip Tovote, Julien Courtin, Cyril Herry, and Andreas Lüthi. 2011. "A Disinhibitory Microcircuit for Associative Fear Learning in the Auditory Cortex." *Nature* 480 (7377): 331–35. <https://doi.org/10.1038/nature10674>.
- Li, Anan, Hui Gong, Bin Zhang, Qingdi Wang, Cheng Yan, Jingpeng Wu, Qian Liu, Shaoqun Zeng, and Qingming Luo. 2010. "Micro-Optical Sectioning Tomography to Obtain a High-Resolution Atlas of the Mouse Brain." *Science* 330 (6009): 1404–8. <https://doi.org/10.1126/science.1191776>.
- Li, Qiufu, and Linlin Shen. 2020. "3D Neuron Reconstruction in Tangled Neuronal Image With Deep Networks." *IEEE Transactions on Medical Imaging* 39 (2): 425–35. <https://doi.org/10.1109/TMI.2019.2926568>.
- Liu, Yanqi, Georgios Foustoukos, Sylvain Crochet, and Carl C.H. Petersen. 2022. "Axonal and Dendritic Morphology of Excitatory Neurons in Layer 2/3 Mouse Barrel Cortex Imaged Through Whole-Brain Two-Photon Tomography and Registered to a Digital Brain Atlas." *Frontiers in Neuroanatomy* 15 (January): 791015. <https://doi.org/10.3389/fnana.2021.791015>.
- Lübke, Joachim, and Dirk Feldmeyer. 2007. "Excitatory Signal Flow and Connectivity in a Cortical Column: Focus on Barrel Cortex." *Brain Structure and Function* 212 (1): 3–17. <https://doi.org/10.1007/s00429-007-0144-2>.
- Luo, Liquan, Edward M. Callaway, and Karel Svoboda. 2018. "Genetic Dissection of Neural Circuits: A Decade of Progress." *Neuron* 98 (2): 256–81. <https://doi.org/10.1016/j.neuron.2018.03.040>.
- Luo, Wenshu, Hidenobu Mizuno, Ryohei Iwata, Shingo Nakazawa, Kosuke Yasuda, Shigeyoshi Itohara, and Takuji Iwasato. 2016. "Supernova: A Versatile Vector System for Single-Cell Labeling and Gene Function Studies in Vivo." *Scientific Reports* 6 (1): 35747. <https://doi.org/10.1038/srep35747>.
- Madisen, Linda, Theresa A Zwingman, Susan M Sunkin, Seung Wook Oh, Hatim A Zariwala, Hong Gu, Lydia L Ng, et al. 2010. "A Robust and High-Throughput Cre Reporting and Characterization System for the Whole Mouse Brain." *Nature Neuroscience* 13 (1): 133–40. <https://doi.org/10.1038/nn.2467>.
- Magliaro, Chiara, Alejandro L. Callara, Nicola Vanello, and Arti Ahluwalia. 2019. "Gotta Trace 'em All: A Mini-Review on Tools and Procedures for Segmenting Single Neurons Toward Deciphering the Structural Connectome." *Frontiers in Bioengineering and Biotechnology* 7: 202. <https://doi.org/10.3389/fbioe.2019.00202>.
- Mao, Tianyi, Deniz Kusefoglul, Bryan M. Hooks, Daniel Huber, Leopoldo Petreanu, and Karel Svoboda. 2011a. "Long-Range Neuronal Circuits Underlying the Interaction between Sensory and Motor Cortex." *Neuron* 72 (1): 111–23. <https://doi.org/10.1016/j.neuron.2011.07.029>.
- Mao, Tianyi, Deniz Kusefoglul, Bryan M. Hooks, Daniel Huber, Leopoldo Petreanu, and Karel Svoboda. 2011b. "Long-Range Neuronal Circuits Underlying the Interaction between Sensory and Motor Cortex." *Neuron* 72 (1): 111–23. <https://doi.org/10.1016/j.neuron.2011.07.029>.
- Mateo, Celine, Michael Avermann, Luc J. Gentet, Feng Zhang, Karl Deisseroth, and Carl C. H. Petersen. 2011. "In Vivo Optogenetic Stimulation of Neocortical Excitatory Neurons Drives Brain-State-Dependent Inhibition." *Current Biology: CB* 21 (19): 1593–1602. <https://doi.org/10.1016/j.cub.2011.08.028>.
- Matho, Katherine S., Dhananjay Huilgol, William Galbavy, Miao He, Gukhan Kim, Xu An, Jiangteng Lu, et al. 2021. "Genetic Dissection of the Glutamatergic Neuron System in Cerebral Cortex." *Nature* 598 (7879): 182–87. <https://doi.org/10.1038/s41586-021-03955-9>.
- Matteucci, Giulio, Maëlle Guyoton, Johannes M. Mayrhofer, Matthieu Auffret, Georgios Foustoukos, Carl C.H. Petersen, and Sami El-Boustani. 2022. "Cortical Sensory Processing across Motivational States during Goal-Directed Behavior." *Neuron* 110 (24): 4176–4193.e10. <https://doi.org/10.1016/j.neuron.2022.09.032>.
- Matyas, Ferenc, Varun Sreenivasan, Fred Marbach, Catherine Wacongne, Boglarka Barsy, Celine Mateo, Rachel Aronoff, and Carl C. H. Petersen. 2010. "Motor Control by Sensory Cortex." *Science (New York, N.Y.)* 330 (6008): 1240–43. <https://doi.org/10.1126/science.1195797>.

- Mayrhofer, Johannes M., Sami El-Boustani, Georgios Foustoukos, Matthieu Auffret, Keita Tamura, and Carl C. H. Petersen. 2019. "Distinct Contributions of Whisker Sensory Cortex and Tongue-Jaw Motor Cortex in a Goal-Directed Sensorimotor Transformation." *Neuron* 103 (6): 1034–1043.e5. <https://doi.org/10.1016/j.neuron.2019.07.008>.
- McCormick, D. A., B. W. Connors, J. W. Lighthall, and D. A. Prince. 1985. "Comparative Electrophysiology of Pyramidal and Sparsely Spiny Stellate Neurons of the Neocortex." *Journal of Neurophysiology* 54 (4): 782–806. <https://doi.org/10.1152/jn.1985.54.4.782>.
- Mehta, Samar B., Diane Whitmer, Rodolfo Figueroa, Ben A. Williams, and David Kleinfeld. 2007. "Active Spatial Perception in the Vibrissa Scanning Sensorimotor System." *PLoS Biology* 5 (2): e15. <https://doi.org/10.1371/journal.pbio.0050015>.
- Minamisawa, Genki, Sung Eun Kwon, Maxime Chevé, Solange P. Brown, and Daniel H. O'Connor. 2018. "A Non-Canonical Feedback Circuit for Rapid Interactions between Somatosensory Cortices." *Cell Reports* 23 (9): 2718–2731.e6. <https://doi.org/10.1016/j.celrep.2018.04.115>.
- Miyashita, Toshio, and Daniel E. Feldman. 2013. "Behavioral Detection of Passive Whisker Stimuli Requires Somatosensory Cortex." *Cerebral Cortex (New York, N.Y.: 1991)* 23 (7): 1655–62. <https://doi.org/10.1093/cercor/bhs155>.
- Moberg, Sara, and Naoya Takahashi. 2022. "Neocortical Layer 5 Subclasses: From Cellular Properties to Roles in Behavior." *Frontiers in Synaptic Neuroscience* 14 (October): 1006773. <https://doi.org/10.3389/fnsyn.2022.1006773>.
- Narayanan, Rajeevan T., Robert Egger, Andrew S. Johnson, Huibert D. Mansvelder, Bert Sakmann, Christiaan P. J. de Kock, and Marcel Oberlaender. 2015. "Beyond Columnar Organization: Cell Type- and Target Layer-Specific Principles of Horizontal Axon Projection Patterns in Rat Vibrissa Cortex." *Cerebral Cortex (New York, N.Y.: 1991)* 25 (11): 4450–68. <https://doi.org/10.1093/cercor/bhv053>.
- Oberlaender, Marcel, Zimbo S. R. M. Boudewijns, Tatjana Kleele, Huibert D. Mansvelder, Bert Sakmann, and Christiaan P. J. de Kock. 2011. "Three-Dimensional Axon Morphologies of Individual Layer 5 Neurons Indicate Cell Type-Specific Intracortical Pathways for Whisker Motion and Touch." *Proceedings of the National Academy of Sciences of the United States of America* 108 (10): 4188–93. <https://doi.org/10.1073/pnas.1100647108>.
- O'Connor, Daniel H., Simon P. Peron, Daniel Huber, and Karel Svoboda. 2010. "Neural Activity in Barrel Cortex Underlying Vibrissa-Based Object Localization in Mice." *Neuron* 67 (6): 1048–61. <https://doi.org/10.1016/j.neuron.2010.08.026>.
- Oh, Seung Wook, Julie A. Harris, Lydia Ng, Brent Winslow, Nicholas Cain, Stefan Mihalas, Quanxin Wang, et al. 2014. "A Mesoscale Connectome of the Mouse Brain." *Nature* 508 (7495): 207–14. <https://doi.org/10.1038/nature13186>.
- Osten, Pavel, and Troy W Margrie. 2013. "Mapping Brain Circuitry with a Light Microscope." *Nature Methods* 10 (6): 515–23. <https://doi.org/10.1038/nmeth.2477>.
- Pala, Aurélie, and Carl C. H. Petersen. 2015. "In Vivo Measurement of Cell-Type-Specific Synaptic Connectivity and Synaptic Transmission in Layer 2/3 Mouse Barrel Cortex." *Neuron* 85 (1): 68–75. <https://doi.org/10.1016/j.neuron.2014.11.025>.
- Peng, Hanchuan, Peng Xie, Lijuan Liu, Xiuli Kuang, Yimin Wang, Lei Qu, Hui Gong, et al. 2021. "Morphological Diversity of Single Neurons in Molecularly Defined Cell Types." *Nature* 598 (7879): 174–81. <https://doi.org/10.1038/s41586-021-03941-1>.
- Perkel, D. H., G. L. Gerstein, and G. P. Moore. 1967. "Neuronal Spike Trains and Stochastic Point Processes. II. Simultaneous Spike Trains." *Biophysical Journal* 7 (4): 419–40. [https://doi.org/10.1016/S0006-3495\(67\)86597-4](https://doi.org/10.1016/S0006-3495(67)86597-4).
- Petersen, Carl C. H. 2019. "Sensorimotor Processing in the Rodent Barrel Cortex." *Nature Reviews Neuroscience* 20 (9): 533–46. <https://doi.org/10.1038/s41583-019-0200-y>.
- Petersen, Carl C.H. 2007. "The Functional Organization of the Barrel Cortex." *Neuron* 56 (2): 339–55. <https://doi.org/10.1016/j.neuron.2007.09.017>.

- Petreaanu, Leopoldo, Daniel Huber, Aleksander Sobczyk, and Karel Svoboda. 2007. "Channelrhodopsin-2-Assisted Circuit Mapping of Long-Range Callosal Projections." *Nature Neuroscience* 10 (5): 663–68. <https://doi.org/10.1038/nn1891>.
- Pfeffer, Carsten K., Mingshan Xue, Miao He, Z. Josh Huang, and Massimo Scanziani. 2013. "Inhibition of Inhibition in Visual Cortex: The Logic of Connections between Molecularly Distinct Interneurons." *Nature Neuroscience* 16 (8): 1068–76. <https://doi.org/10.1038/nn.3446>.
- Pi, Hyun-Jae, Balázs Hangya, Duda Kvitsiani, Joshua I. Sanders, Z. Josh Huang, and Adam Kepecs. 2013. "Cortical Interneurons That Specialize in Disinhibitory Control." *Nature* 503 (7477): 521–24. <https://doi.org/10.1038/nature12676>.
- Pinto, Lucas, and Yang Dan. 2015. "Cell-Type-Specific Activity in Prefrontal Cortex during Goal-Directed Behavior." *Neuron* 87 (2): 437–50. <https://doi.org/10.1016/j.neuron.2015.06.021>.
- Poort, Jasper, Katharina A. Wilmes, Antonin Blot, Angus Chadwick, Maneesh Sahani, Claudia Clopath, Thomas D. Mrsic-Flogel, Sonja B. Hofer, and Adil G. Khan. 2022. "Learning and Attention Increase Visual Response Selectivity through Distinct Mechanisms." *Neuron* 110 (4): 686–697.e6. <https://doi.org/10.1016/j.neuron.2021.11.016>.
- Quan, Tingwei, Hang Zhou, Jing Li, Shiwei Li, Anan Li, Yuxin Li, Xiaohua Lv, Qingming Luo, Hui Gong, and Shaoqun Zeng. 2016. "NeuroGPS-Tree: Automatic Reconstruction of Large-Scale Neuronal Populations with Dense Neurites." *Nature Methods* 13 (1): 51–54. <https://doi.org/10.1038/nmeth.3662>.
- Quiquempoix, Michael, Sophie L. Fayad, Katia Boutourlinsky, Nathalie Leresche, Régis C. Lambert, and Thomas Bessaih. 2018. "Layer 2/3 Pyramidal Neurons Control the Gain of Cortical Output." *Cell Reports* 24 (11): 2799–2807.e4. <https://doi.org/10.1016/j.celrep.2018.08.038>.
- Ragan, Timothy, Lolahon R Kadiri, Kannan Umadevi Venkataraju, Karsten Bahlmann, Jason Sutin, Julian Taranda, Ignacio Arganda-Carreras, Yongsoo Kim, H Sebastian Seung, and Pavel Osten. 2012. "Serial Two-Photon Tomography for Automated Ex Vivo Mouse Brain Imaging." *Nature Methods* 9 (3): 255–58. <https://doi.org/10.1038/nmeth.1854>.
- Renier, Nicolas, Zhuohao Wu, David J. Simon, Jing Yang, Pablo Ariel, and Marc Tessier-Lavigne. 2014a. "IDISCO: A Simple, Rapid Method to Immunolabel Large Tissue Samples for Volume Imaging." *Cell* 159 (4): 896–910. <https://doi.org/10.1016/j.cell.2014.10.010>.
- Renier, Nicolas, Zhuohao Wu, David J. Simon, Jing Yang, Pablo Ariel, and Marc Tessier-Lavigne. 2014b. "IDISCO: A Simple, Rapid Method to Immunolabel Large Tissue Samples for Volume Imaging." *Cell* 159 (4): 896–910. <https://doi.org/10.1016/j.cell.2014.10.010>.
- Richardson, Douglas S., and Jeff W. Lichtman. 2015. "Clarifying Tissue Clearing." *Cell* 162 (2): 246–57. <https://doi.org/10.1016/j.cell.2015.06.067>.
- Rodgers, Chris C., Ramon Nogueira, B. Christina Pil, Esther A. Greeman, Jung M. Park, Y. Kate Hong, Stefano Fusi, and Randy M. Bruno. 2021. "Sensorimotor Strategies and Neuronal Representations for Shape Discrimination." *Neuron* 109 (14): 2308–2325.e10. <https://doi.org/10.1016/j.neuron.2021.05.019>.
- Rodriguez-Moreno, Javier, Cesar Porrero, Astrid Rollenhagen, Mario Rubio-Teves, Diana Casas-Torremocha, Lidia Alonso-Nanclares, Rachida Yakoubi, et al. 2020. "Area-Specific Synapse Structure in Branched Posterior Nucleus Axons Reveals a New Level of Complexity in Thalamocortical Networks." *The Journal of Neuroscience: The Official Journal of the Society for Neuroscience* 40 (13): 2663–79. <https://doi.org/10.1523/JNEUROSCI.2886-19.2020>.
- Rojas-Piloni, Gerardo, Jason M. Guest, Robert Egger, Andrew S. Johnson, Bert Sakmann, and Marcel Oberlaender. 2017. "Relationships between Structure, in Vivo Function and Long-Range Axonal Target of Cortical Pyramidal Tract Neurons." *Nature Communications* 8 (1): 870. <https://doi.org/10.1038/s41467-017-00971-0>.
- Sachidhanandam, Shankar, B. Semihcan Sermet, and Carl C. H. Petersen. 2016. "Parvalbumin-Expressing GABAergic Neurons in Mouse Barrel Cortex Contribute to Gating a Goal-Directed Sensorimotor Transformation." *Cell Reports* 15 (4): 700–706. <https://doi.org/10.1016/j.celrep.2016.03.063>.

- Sachidhanandam, Shankar, Varun Sreenivasan, Alexandros Kyriakatos, Yves Kremer, and Carl C. H. Petersen. 2013. "Membrane Potential Correlates of Sensory Perception in Mouse Barrel Cortex." *Nature Neuroscience* 16 (11): 1671–77. <https://doi.org/10.1038/nn.3532>.
- Santiago, Lucidia F., Marco Aurelio M. Freire, Cristovam W. Picanço-Diniz, João G. Franca, and Antonio Pereira. 2019. "The Organization and Connections of Second Somatosensory Cortex in the Agouti." *Frontiers in Neuroanatomy* 12 (January): 118. <https://doi.org/10.3389/fnana.2018.00118>.
- Sanzeni, Alessandro, Bradley Akitake, Hannah C. Goldbach, Caitlin E. Leedy, Nicolas Brunel, and Mark H. Histed. 2020. "Inhibition Stabilization Is a Widespread Property of Cortical Networks." *ELife* 9 (June): e54875. <https://doi.org/10.7554/eLife.54875>.
- Scheffer, Louis K, C Shan Xu, Michal Januszewski, Zhiyuan Lu, Shin-ya Takemura, Kenneth J Hayworth, Gary B Huang, et al. 2020. "A Connectome and Analysis of the Adult Drosophila Central Brain." *ELife* 9 (September): e57443. <https://doi.org/10.7554/eLife.57443>.
- Schubert, D., R. Kötter, H. J. Luhmann, and J. F. Staiger. 2006. "Morphology, Electrophysiology and Functional Input Connectivity of Pyramidal Neurons Characterizes a Genuine Layer va in the Primary Somatosensory Cortex." *Cerebral Cortex (New York, N.Y.: 1991)* 16 (2): 223–36. <https://doi.org/10.1093/cercor/bhi100>.
- Schubert, D., J. F. Staiger, N. Cho, R. Kötter, K. Zilles, and H. J. Luhmann. 2001. "Layer-Specific Intracolumnar and Transcolumnar Functional Connectivity of Layer V Pyramidal Cells in Rat Barrel Cortex." *The Journal of Neuroscience: The Official Journal of the Society for Neuroscience* 21 (10): 3580–92.
- Sermet, B. Semihcan, Pavel Truschow, Michael Feyerabend, Johannes M. Mayrhofer, Tess B. Oram, Ofer Yizhar, Jochen F. Staiger, and Carl Ch Petersen. 2019. "Pathway-, Layer- and Cell-Type-Specific Thalamic Input to Mouse Barrel Cortex." *ELife* 8 (December). <https://doi.org/10.7554/eLife.52665>.
- Shamonin, Denis. 2013. "Fast Parallel Image Registration on CPU and GPU for Diagnostic Classification of Alzheimer's Disease." *Frontiers in Neuroinformatics* 7. <https://doi.org/10.3389/fninf.2013.00050>.
- Shepherd, Gordon M. G., and Naoki Yamawaki. 2021. "Untangling the Cortico-Thalamo-Cortical Loop: Cellular Pieces of a Knotty Circuit Puzzle." *Nature Reviews. Neuroscience* 22 (7): 389–406. <https://doi.org/10.1038/s41583-021-00459-3>.
- Simons, D. J. 1978. "Response Properties of Vibrissa Units in Rat SI Somatosensory Neocortex." *Journal of Neurophysiology* 41 (3): 798–820. <https://doi.org/10.1152/jn.1978.41.3.798>.
- Sippy, Tanya, Damien Lapray, Sylvain Crochet, and Carl C. H. Petersen. 2015. "Cell-Type-Specific Sensorimotor Processing in Striatal Projection Neurons during Goal-Directed Behavior." *Neuron* 88 (2): 298–305. <https://doi.org/10.1016/j.neuron.2015.08.039>.
- Sohal, Vikaas S., and John L. R. Rubenstein. 2019. "Excitation-Inhibition Balance as a Framework for Investigating Mechanisms in Neuropsychiatric Disorders." *Molecular Psychiatry* 24 (9): 1248–57. <https://doi.org/10.1038/s41380-019-0426-0>.
- Sorensen, Staci A., Amy Bernard, Vilas Menon, Joshua J. Royall, Katie J. Glattfelder, Tsega Desta, Karla Hirokawa, et al. 2015. "Correlated Gene Expression and Target Specificity Demonstrate Excitatory Projection Neuron Diversity." *Cerebral Cortex (New York, N.Y.: 1991)* 25 (2): 433–49. <https://doi.org/10.1093/cercor/bht243>.
- Sreenivasan, Varun, Vahid Esmaeili, Taro Kiritani, Katia Galan, Sylvain Crochet, and Carl C. H. Petersen. 2016. "Movement Initiation Signals in Mouse Whisker Motor Cortex." *Neuron* 92 (6): 1368–82. <https://doi.org/10.1016/j.neuron.2016.12.001>.
- Sreenivasan, Varun, Kajari Karmakar, Filippo M. Rijli, and Carl C. H. Petersen. 2015. "Parallel Pathways from Motor and Somatosensory Cortex for Controlling Whisker Movements in Mice." *The European Journal of Neuroscience* 41 (3): 354–67. <https://doi.org/10.1111/ejn.12800>.
- Sreenivasan, Varun, Alexandros Kyriakatos, Celine Mateo, Dieter Jaeger, and Carl C. H. Petersen. 2017. "Parallel Pathways from Whisker and Visual Sensory Cortices to Distinct Frontal

- Regions of Mouse Neocortex." *Neurophotonics* 4 (3): 031203.
<https://doi.org/10.1117/1.NPh.4.3.031203>.
- Staiger, Jochen F., Ingo Bojak, Stéphanie Miceli, and Dirk Schubert. 2015. "A Gradual Depth-Dependent Change in Connectivity Features of Supragranular Pyramidal Cells in Rat Barrel Cortex." *Brain Structure & Function* 220 (3): 1317–37. <https://doi.org/10.1007/s00429-014-0726-8>.
- Staiger, Jochen F., and Carl C. H. Petersen. 2021. "Neuronal Circuits in Barrel Cortex for Whisker Sensory Perception." *Physiological Reviews* 101 (1): 353–415.
<https://doi.org/10.1152/physrev.00019.2019>.
- Stehberg, Jimmy, Phat T. Dang, and Ron D. Frostig. 2014. "Unimodal Primary Sensory Cortices Are Directly Connected by Long-Range Horizontal Projections in the Rat Sensory Cortex." *Frontiers in Neuroanatomy* 8: 93. <https://doi.org/10.3389/fnana.2014.00093>.
- Stephan, Klass E., Lars Kamper, Ahmet Bozkurt, Gully A. P. C. Burns, Malcolm P. Young, and Rolf Kötter. 2001. "Advanced Database Methodology for the Collation of Connectivity Data on the Macaque Brain (CoCoMac)." Edited by R. Kötter. *Philosophical Transactions of the Royal Society of London. Series B: Biological Sciences* 356 (1412): 1159–86.
<https://doi.org/10.1098/rstb.2001.0908>.
- Sumser, Anton, Rebecca A. Mease, Bert Sakmann, and Alexander Groh. 2017. "Organization and Somatotopy of Corticothalamic Projections from L5B in Mouse Barrel Cortex." *Proceedings of the National Academy of Sciences of the United States of America* 114 (33): 8853–58.
<https://doi.org/10.1073/pnas.1704302114>.
- Sun, Yujiao J., Guangying K. Wu, Bao-Hua Liu, Pingyang Li, Mu Zhou, Zhongju Xiao, Huizhong W. Tao, and Li I. Zhang. 2010. "Fine-Tuning of Pre-Balanced Excitation and Inhibition during Auditory Cortical Development." *Nature* 465 (7300): 927–31. <https://doi.org/10.1038/nature09079>.
- Susaki, Etsuo A., Kazuki Tainaka, Dimitri Perrin, Hiroko Yukinaga, Akihiro Kuno, and Hiroki R. Ueda. 2015. "Advanced CUBIC Protocols for Whole-Brain and Whole-Body Clearing and Imaging." *Nature Protocols* 10 (11): 1709–27. <https://doi.org/10.1038/nprot.2015.085>.
- Susaki, Etsuo A., Kazuki Tainaka, Dimitri Perrin, Fumiaki Kishino, Takehiro Tawara, Tomonobu M. Watanabe, Chihiro Yokoyama, et al. 2014. "Whole-Brain Imaging with Single-Cell Resolution Using Chemical Cocktails and Computational Analysis." *Cell* 157 (3): 726–39.
<https://doi.org/10.1016/j.cell.2014.03.042>.
- Svoboda, Karel, and Nuo Li. 2018. "Neural Mechanisms of Movement Planning: Motor Cortex and Beyond." *Current Opinion in Neurobiology* 49: 33–41.
<https://doi.org/10.1016/j.conb.2017.10.023>.
- Takahashi, Naoya, Christian Ebner, Johanna Sigl-Glöckner, Sara Moberg, Svenja Nierwetberg, and Matthew E. Larkum. 2020. "Active Dendritic Currents Gate Descending Cortical Outputs in Perception." *Nature Neuroscience* 23 (10): 1277–85. <https://doi.org/10.1038/s41593-020-0677-8>.
- Takahashi, Naoya, Thomas G. Oertner, Peter Hegemann, and Matthew E. Larkum. 2016. "Active Cortical Dendrites Modulate Perception." *Science (New York, N.Y.)* 354 (6319): 1587–90.
<https://doi.org/10.1126/science.aah6066>.
- Tamamaki, Nobuaki, and Ryohei Tomioka. 2010. "Long-Range GABAergic Connections Distributed throughout the Neocortex and Their Possible Function." *Frontiers in Neuroscience* 4.
<https://doi.org/10.3389/fnins.2010.00202>.
- Taniguchi, Hiroki, Miao He, Priscilla Wu, Sangyong Kim, Raehum Paik, Ken Sugino, Duda Kvitsiani, et al. 2011. "A Resource of Cre Driver Lines for Genetic Targeting of GABAergic Neurons in Cerebral Cortex." *Neuron* 71 (6): 995–1013. <https://doi.org/10.1016/j.neuron.2011.07.026>.
- Tasic, Bosiljka, Zizhen Yao, Lucas T. Graybiel, Kimberly A. Smith, Thuc Nghi Nguyen, Darren Bertagnoli, Jeff Goldy, et al. 2018. "Shared and Distinct Transcriptomic Cell Types across Neocortical Areas." *Nature* 563 (7729): 72–78. <https://doi.org/10.1038/s41586-018-0654-5>.
- Thomson. 2010. "Neocortical Layer 6, a Review." *Frontiers in Neuroanatomy*.
<https://doi.org/10.3389/fnana.2010.00013>.

- Tomer, Raju, Li Ye, Brian Hsueh, and Karl Deisseroth. 2014. "Advanced CLARITY for Rapid and High-Resolution Imaging of Intact Tissues." *Nature Protocols* 9 (7): 1682–97. <https://doi.org/10.1038/nprot.2014.123>.
- Towilson, Emma K., Petra E. Vértés, Sebastian E. Ahnert, William R. Schafer, and Edward T. Bullmore. 2013. "The Rich Club of the *C. Elegans* Neuronal Connectome." *The Journal of Neuroscience* 33 (15): 6380–87. <https://doi.org/10.1523/JNEUROSCI.3784-12.2013>.
- Tremblay, Robin, Soohyun Lee, and Bernardo Rudy. 2016. "GABAergic Interneurons in the Neocortex: From Cellular Properties to Circuits." *Neuron* 91 (2): 260–92. <https://doi.org/10.1016/j.neuron.2016.06.033>.
- Tyson, Adam L., Charly V. Rousseau, Christian J. Niedworok, Sepiedeh Keshavarzi, Chryssanthi Tsitoura, Lee Cossell, Molly Strom, and Troy W. Margrie. 2021. "A Deep Learning Algorithm for 3D Cell Detection in Whole Mouse Brain Image Datasets." Edited by Hugues Berry. *PLOS Computational Biology* 17 (5): e1009074. <https://doi.org/10.1371/journal.pcbi.1009074>.
- Tyson, Adam L., Mateo Vélez-Fort, Charly V. Rousseau, Lee Cossell, Chryssanthi Tsitoura, Stephen C. Lenzi, Horst A. Obenaus, Federico Claudi, Tiago Branco, and Troy W. Margrie. 2022. "Accurate Determination of Marker Location within Whole-Brain Microscopy Images." *Scientific Reports* 12 (1): 867. <https://doi.org/10.1038/s41598-021-04676-9>.
- Ueda, Hiroki R., Hans-Ulrich Dodt, Pavel Osten, Michael N. Economo, Jayaram Chandrashekar, and Philipp J. Keller. 2020. "Whole-Brain Profiling of Cells and Circuits in Mammals by Tissue Clearing and Light-Sheet Microscopy." *Neuron* 106 (3): 369–87. <https://doi.org/10.1016/j.neuron.2020.03.004>.
- Urrutia-Piñones, Jocelyn, Camila Morales-Moraga, Nicole Sanguinetti-González, Angelica P. Escobar, and Chiayu Q. Chiu. 2022. "Long-Range GABAergic Projections of Cortical Origin in Brain Function." *Frontiers in Systems Neuroscience* 16 (March): 841869. <https://doi.org/10.3389/fnsys.2022.841869>.
- Van Den Heuvel, Martijn P., Edward T. Bullmore, and Olaf Sporns. 2016. "Comparative Connectomics." *Trends in Cognitive Sciences* 20 (5): 345–61. <https://doi.org/10.1016/j.tics.2016.03.001>.
- Varshney, Lav R., Beth L. Chen, Eric Paniagua, David H. Hall, and Dmitri B. Chklovskii. 2011. "Structural Properties of the Caenorhabditis Elegans Neuronal Network." Edited by Olaf Sporns. *PLoS Computational Biology* 7 (2): e1001066. <https://doi.org/10.1371/journal.pcbi.1001066>.
- Vavladeli, Angeliki, Tanya Daigle, Hongkui Zeng, Sylvain Crochet, and Carl C H Petersen. 2020. "Projection-Specific Activity of Layer 2/3 Neurons Imaged in Mouse Primary Somatosensory Barrel Cortex During a Whisker Detection Task." *Function* 1 (1). <https://doi.org/10.1093/function/zqaa008>.
- Voigt, Fabian F., Daniel Kirschenbaum, Evgenia Platonova, Stéphane Pagès, Robert A. A. Campbell, Rahel Kastli, Martina Schaettin, et al. 2019. "The MesoSPIM Initiative: Open-Source Light-Sheet Microscopes for Imaging Cleared Tissue." *Nature Methods* 16 (11): 1105–8. <https://doi.org/10.1038/s41592-019-0554-0>.
- Wang, Meng, Ke Liu, Junxia Pan, Jialin Li, Pei Sun, Yongsheng Zhang, Longhui Li, et al. 2022. "Brain-Wide Projection Reconstruction of Single Functionally Defined Neurons." *Nature Communications* 13 (1): 1531. <https://doi.org/10.1038/s41467-022-29229-0>.
- Wang, Quanxin, Song-Lin Ding, Yang Li, Josh Royall, David Feng, Phil Lesnar, Nile Graddis, et al. 2020. "The Allen Mouse Brain Common Coordinate Framework: A 3D Reference Atlas." *Cell* 181 (4): 936–953.e20. <https://doi.org/10.1016/j.cell.2020.04.007>.
- Wang, Xiaojun, Jason Tucciarone, Siqi Jiang, Fangfang Yin, Bor-Shuen Wang, Dingkan Wang, Yao Jia, et al. 2019. "Genetic Single Neuron Anatomy Reveals Fine Granularity of Cortical Axo-Axonic Cells." *Cell Reports* 26 (11): 3145–3159.e5. <https://doi.org/10.1016/j.celrep.2019.02.040>.
- Wassie, Asmamaw T., Yongxin Zhao, and Edward S. Boyden. 2019. "Expansion Microscopy: Principles and Uses in Biological Research." *Nature Methods* 16 (1): 33–41. <https://doi.org/10.1038/s41592-018-0219-4>.

- Welker, E., P. V. Hoogland, and H. Van der Loos. 1988. "Organization of Feedback and Feedforward Projections of the Barrel Cortex: A PHA-L Study in the Mouse." *Experimental Brain Research* 73 (2): 411–35.
- White, E. L., and R. A. DeAmicis. 1977. "Afferent and Efferent Projections of the Region in Mouse SmL Cortex Which Contains the Posteromedial Barrel Subfield." *The Journal of Comparative Neurology* 175 (4): 455–82. <https://doi.org/10.1002/cne.901750405>.
- Winnubst, Johan, Erhan Bas, Tiago A. Ferreira, Zhuohao Wu, Michael N. Economo, Patrick Edson, Ben J. Arthur, et al. 2019. "Reconstruction of 1,000 Projection Neurons Reveals New Cell Types and Organization of Long-Range Connectivity in the Mouse Brain." *Cell* 179 (1): 268–281.e13. <https://doi.org/10.1016/j.cell.2019.07.042>.
- Woloszyn, Luke, and David L. Sheinberg. 2012. "Effects of Long-Term Visual Experience on Responses of Distinct Classes of Single Units in Inferior Temporal Cortex." *Neuron* 74 (1): 193–205. <https://doi.org/10.1016/j.neuron.2012.01.032>.
- Woolsey, T. A., and H. Van der Loos. 1970. "The Structural Organization of Layer IV in the Somatosensory Region (SI) of Mouse Cerebral Cortex. The Description of a Cortical Field Composed of Discrete Cytoarchitectonic Units." *Brain Research* 17 (2): 205–42.
- Yamashita, Takayuki, Aurélie Pala, Leticia Pedrido, Yves Kremer, Egbert Welker, and Carl C. H. Petersen. 2013. "Membrane Potential Dynamics of Neocortical Projection Neurons Driving Target-Specific Signals." *Neuron* 80 (6): 1477–90. <https://doi.org/10.1016/j.neuron.2013.10.059>.
- Yamashita, Takayuki, and Carl Ch Petersen. 2016. "Target-Specific Membrane Potential Dynamics of Neocortical Projection Neurons during Goal-Directed Behavior." *ELife* 5. <https://doi.org/10.7554/eLife.15798>.
- Yamashita, Takayuki, Angeliki Vavladeli, Aurélie Pala, Katia Galan, Sylvain Crochet, Sara S. A. Petersen, and Carl C. H. Petersen. 2018. "Diverse Long-Range Axonal Projections of Excitatory Layer 2/3 Neurons in Mouse Barrel Cortex." *Frontiers in Neuroanatomy* 12: 33. <https://doi.org/10.3389/fnana.2018.00033>.
- Yang, Hongdian, Sung E. Kwon, Kyle S. Severson, and Daniel H. O'Connor. 2016. "Origins of Choice-Related Activity in Mouse Somatosensory Cortex." *Nature Neuroscience* 19 (1): 127–34. <https://doi.org/10.1038/nn.4183>.
- Yizhar, Ofer, Lief E. Fenno, Matthias Prigge, Franziska Schneider, Thomas J. Davidson, Daniel J. O'Shea, Vikaas S. Sohal, et al. 2011. "Neocortical Excitation/Inhibition Balance in Information Processing and Social Dysfunction." *Nature* 477 (7363): 171–78. <https://doi.org/10.1038/nature10360>.
- Zakiewicz, Izabela, Jan Bjaalie, and Trygve Leergaard. 2014. "Brain-Wide Map of Efferent Projections from Rat Barrel Cortex." *Frontiers in Neuroinformatics* 8: 5. <https://doi.org/10.3389/fninf.2014.00005>.
- Zhao, Shengli, Jonathan T. Ting, Hisham E. Atallah, Li Qiu, Jie Tan, Bernd Gloss, George J. Augustine, et al. 2011. "Cell Type-Specific Channelrhodopsin-2 Transgenic Mice for Optogenetic Dissection of Neural Circuitry Function." *Nature Methods* 8 (9): 745–52. <https://doi.org/10.1038/nmeth.1668>.
- Zheng, Zhihao, J. Scott Lauritzen, Eric Perlman, Camenzind G. Robinson, Matthew Nichols, Daniel Milkie, Omar Torrens, et al. 2018. "A Complete Electron Microscopy Volume of the Brain of Adult Drosophila Melanogaster." *Cell* 174 (3): 730–743.e22. <https://doi.org/10.1016/j.cell.2018.06.019>.
- Zhou, Zhi, Hsien-Chi Kuo, Hanchuan Peng, and Fuhui Long. 2018. "DeepNeuron: An Open Deep Learning Toolbox for Neuron Tracing." *Brain Informatics* 5 (2): 3. <https://doi.org/10.1186/s40708-018-0081-2>.
- Zingg, Brian, Houri Hintiryan, Lin Gou, Monica Y. Song, Maxwell Bay, Michael S. Bienkowski, Nicholas N. Foster, et al. 2014a. "Neural Networks of the Mouse Neocortex." *Cell* 156 (5): 1096–1111. <https://doi.org/10.1016/j.cell.2014.02.023>.

Chapter 7 List of anatomical regions

AAA - NI		NLL - ZI	
AAA	Anterior amygdalar area	NLL	Nucleus of the lateral lemniscus
ACAAd	Anterior cingulate area, dorsal part	NLOT	Nucleus of the lateral olfactory tract
ACAv	Anterior cingulate area, ventral part	NOT	Nucleus of the optic tract
ACB	Nucleus accumbens	NPC	Nucleus of the posterior commissure
Acs5	Accessory trigeminal nucleus	NTB	Nucleus of the trapezoid body
AHN	Anterior hypothalamic nucleus	NTS	Nucleus of the solitary tract
AId	Agranular insular area, dorsal part	OLF	Olfactory areas
Alp	Agranular insular area, posterior part	OP	Olivary pretectal nucleus
Alv	Agranular insular area, ventral part	ORBI	Orbital area, lateral part
alv	alveus	ORBm	Orbital area, medial part
AM	Anteromedial nucleus	ORBvl	Orbital area, ventrolateral part
AMB	Nucleus ambiguus	OT	Olfactory tubercle
AOB	Accessory olfactory bulb	P5	Peritrigeminal zone
AON	Anterior olfactory nucleus	Pa4	Paratrochlear nucleus
APN	Anterior pretectal nucleus	Pa5	Paratrigeminal nucleus
AT	Anterior tegmental nucleus	PAA	Piriform-amygdalar area
ATN	Anterior group of the dorsal thalamus	PAG	Periaqueductal gray
AUDd	Dorsal auditory area	PAL	Pallidum
AUDp	Primary auditory area	PARN	Parvicellular reticular nucleus
AUDpo	Posterior auditory area	PAS	Parasolitary nucleus
AUDv	Ventral auditory area	PB	Parabrachial nucleus
B	Barrington's nucleus	PBG	Parabigeminal nucleus
BAC	Bed nucleus of the anterior commissure	PC5	Parvicellular motor 5 nucleus
BLAa	Basolateral amygdalar nucleus, anterior part	PCG	Pontine central gray
BLAp	Basolateral amygdalar nucleus, posterior part	PDTg	Posterodorsal tegmental nucleus
BLAv	Basolateral amygdalar nucleus, ventral part	PeF	Perifornical nucleus
BMAa	Basomedial amygdalar nucleus, anterior part	PERI	Perirhinal area
BMAp	Basomedial amygdalar nucleus, posterior part	PG	Pontine gray
BST	Bed nuclei of the stria terminalis	PGRN	Paragigantocellular reticular nucleus
CA	Ammon's horn	PH	Posterior hypothalamic nucleus
cc	corpus callosum	PHY	Perihypoglossal nuclei
ccb	corpus callosum, body	PIR	Piriform area
ccs	corpus callosum, splenium	PL	Prelimbic area
CEA	Central amygdalar nucleus	PMd	Dorsal premammillary nucleus
CENT3	Lobule III	PP	Peripeduncular nucleus
cerebrum	Cerebrum	PPN	Pedunculo pontine nucleus
cing	cingulum bundle	PPT	Posterior pretectal nucleus
CLA	Clastrum	PPY	Parapyramidal nucleus
CLI	Central linear nucleus raphe	PRC	Precommissural nucleus
CN	Cochlear nuclei	PRNc	Pontine reticular nucleus, caudal part
COA	Cortical amygdalar area	PRNr	Pontine reticular nucleus
COAp	Cortical amygdalar area, posterior part	PST	Preparasubthalamic nucleus
CP	Caudoputamen	PSTN	Parasubthalamic nucleus
CS	Superior central nucleus raphe	PSV	Principal sensory nucleus of the trigeminal

CTXpl	Cortical plate	PVH	Paraventricular hypothalamic nucleus
CTXsp	Cortical subplate	PVHd	Paraventricular hypothalamic nucleus, descending division
CUL4, 5	Lobules IV-V	PYR	Pyramus (VIII)
CUN	Cuneiform nucleus	RHP	Retrohippocampal region
DCN	Dorsal column nuclei	RL	Rostral linear nucleus raphe
DG	Dentate gyrus	RM	Nucleus raphe magnus
dhc	dorsal hippocampal commissure	RN	Red nucleus
DMH	Dorsomedial nucleus of the hypothalamus	RO	Nucleus raphe obscurus
DMX	Dorsal motor nucleus of the vagus nerve	RPA	Nucleus raphe pallidus
DN	Dentate nucleus	RPF	Retroparafascicular nucleus
DP	Dorsal peduncular area	RPO	Nucleus raphe pontis
DR	Dorsal nucleus raphe	RR	Midbrain reticular nucleus, retrorubral area
DT	Dorsal terminal nucleus of the accessory optic tract	RSPagl	Retrosplenial area, lateral agranular part
ec	external capsule	RSPagl5	Retrosplenial area, lateral agranular part, layer 5
ECT	Ectorhinal area	RSPd	Retrosplenial area, dorsal part
ENTl	Entorhinal area, lateral part	RSPv	Retrosplenial area, ventral part
ENTm	Entorhinal area, medial part, dorsal zone	RSPv	Retrosplenial area, ventral part
EPd	Endopiriform nucleus, dorsal part	RSPv5	Retrosplenial area, ventral part, layer 5
EPv	Endopiriform nucleus, ventral part	RT	Reticular nucleus of the thalamus
EW	Edinger-Westphal nucleus	SAG	Nucleus sagulum
fa	corpus callosum, anterior forceps	SCdg	Superior colliculus, motor related, deep gray layer
FL	Flocculus	SCdw	Superior colliculus, motor related, deep white layer
FN	Fastigial nucleus	SCig	Superior colliculus, motor related, intermediate gray layer
fp	corpus callosum, posterior forceps	SCiw	Superior colliculus, motor related, intermediate white layer
FRP	Frontal pole, cerebral cortex	SCop	Superior colliculus, optic layer
FS	Fundus of striatum	SCsg	Superior colliculus, superficial gray layer
fxs	fornix system	scwm	supra-callosal cerebral white matter
GENv	Geniculate group, ventral thalamus	SCzo	Superior colliculus, zonal layer
GPe	Globus pallidus, external segment	SF	Septofimbrial nucleus
GPi	Globus pallidus, internal segment	SG	Supragenual nucleus
GRN	Gigantocellular reticular nucleus	SH	Septohippocampal nucleus
GU	Gustatory areas	SI	Substantia innominata
hc	hippocampal commissures	SIM	Simple lobule
HIP	Hippocampal region	SLC	Subceruleus nucleus
HPF	Hippocampal formation	SLD	Sublaterodorsal nucleus
HY	Hypothalamus	SNc	Substantia nigra, compact part
HY	Hypothalamus	SNr	Substantia nigra, reticular part
I5	Intertrigeminal nucleus	SOC	Superior olivary complex
IA	Intercalated amygdalar nucleus	SPA	Subparafascicular area
ICB	Infracerebellar nucleus	SPF	Subparafascicular nucleus
ICc	Inferior colliculus, central nucleus	SPVC	Spinal nucleus of the trigeminal, caudal part
ICd	Inferior colliculus, dorsal nucleus	SPVI	Spinal nucleus of the trigeminal, interpolar part
ICe	Inferior colliculus, external nucleus	SPVO	Spinal nucleus of the trigeminal, oral part
IF	Interfascicular nucleus raphe	SS	Somatosensory areas
III	Oculomotor nucleus	SSp-bfd	Primary somatosensory area, barrel field
ILA	Infralimbic area	SSp-II	Primary somatosensory area, lower limb

ILM	Intralaminar nuclei of the dorsal thalamus	SSp-m	Primary somatosensory area, mouth
INC	Interstitial nucleus of Cajal	SSp-n	Primary somatosensory area, nose
IO	Inferior olivary complex	SSp-tr	Primary somatosensory area, trunk
IP	Interposed nucleus	SSp-ul	Primary somatosensory area, upper limb
IPN	Interpeduncular nucleus	SSp-un	Primary somatosensory area, unassigned
IRN	Intermediate reticular nucleus	SSs	Supplemental somatosensory area
IV	Trochlear nucleus	St	stria terminalis
LA	Lateral amygdalar nucleus	stc	commissural branch of stria terminalis
LAT	Lateral group of the dorsal thalamus	STN	Subthalamic nucleus
LC	Locus ceruleus	STR	Striatum
LDT	Laterodorsal tegmental nucleus	STRd	Striatum dorsal region
LGd	Dorsal part of the lateral geniculate complex	Su3	Supraoculomotor periaqueductal gray
LHA	Lateral hypothalamic area	SUT	Supratrigeminal nucleus
LIN	Linear nucleus of the medulla	TEa	Temporal association areas
LPO	Lateral preoptic area	TR	Postpiriform transition area
LRN	Lateral reticular nucleus	TRN	Tegmental reticular nucleus
LS	Lateral septal nucleus	TRS	Triangular nucleus of septum
LT	Lateral terminal nucleus of the accessory optic tract	TT	Taenia tecta
MA	Magnocellular nucleus	UVU	Uvula (IX)
MA3	Medial accessory oculomotor nucleus	V	Motor nucleus of trigeminal
MARN	Magnocellular reticular nucleus	VeCB	Vestibulocerebellar nucleus
MB	Midbrain	VENT	Ventral group of the dorsal thalamus
Mbmot	Midbrain, motor related	VI	Abducens nucleus
MBsen	Midbrain, sensory related	VII	Facial motor nucleus
Mbsta	Midbrain, behavioral state related	VISa	Anterior area
MDRN	Medullary reticular nucleus	VISal	Anterolateral visual area
MEA	Medial amygdalar nucleus	VISam	Anteromedial visual area
MED	Medial group of the dorsal thalamus	VISC	Visceral area
MEV	Midbrain trigeminal nucleus	VISI	Lateral visual area
mfbc	cerebrum related	VISli	Laterointermediate area
MG	Medial geniculate complex	VISp	Primary visual area
MO	Somatomotor areas	VISpl	Posterolateral visual area
MOB	Main olfactory bulb	VISpm	posteromedial visual area
MOp	Primary motor area	VISpor	Postrhinal area
MOs	Secondary motor area	VISrl	Rostrolateral visual area
MPT	Medial pretectal area	VNC	Vestibular nuclei
MRN	Midbrain reticular nucleus	VP	Ventral posterior complex of the thalamus
MT	Medial terminal nucleus of the accessory optic tract	VTA	Ventral tegmental area
MTN	Midline group of the dorsal thalamus	VTN	Ventral tegmental nucleus
NB	Nucleus of the brachium of the inferior colliculus	x	Nucleus x
ND	Nucleus of Darkschewitsch	XII	Hypoglossal nucleus
NI	Nucleus incertus	ZI	Zona incerta

Table 1 List of anatomical regions and their acronyms.

YANQI LIU

PERSONAL INFORMATION

DATE OF BIRTH:	07 October 1993
ADDRESS:	AI 3102 (Bâtiment AI) Station 19, 1015 Lausanne
PHONE:	+410789807077
EMAIL:	yanqi.liu@epfl.ch
NATIONALITY:	Canadian
LANGUAGES	Mandarin (native) English (bilingual) French (elementary)

EDUCATION

09.2018- PRESENT	PhD in Neuroscience , Ecole polytechnique fédérale de Lausanne, Switzerland The laboratory of sensory processing, lead by Prof. Carl Petersen PhD project "Layer specific, cell type specific projections from the barrel cortex"
09.2015- 02.2018	Master of Science , The University of British Columbia Vancouver, Canada Specialization in Neuroscience Grade point average: 87.7% Master's thesis "The role of SLC26A11 chloride channel in neuronal swelling associated with spreading depolarization" with Dr. Brian MacVicar
09.2011- 05.2015	B.Sc (Hon.) Life Science , Queen's University, Kingston, Canada Specialization in Neuroscience Grade point average: 3.81/4.3 Honour's thesis: "Inducing LTP in ALDH2 ^{-/-} mice: an oxidative stress model of Alzheimer's disease" with Dr. David Andrew

LABORATORY EXPERIENCE

MICROSCOPY	Two-photon Microscopy and Two-photon Tomography Mesoscale Selective Plane Illumination Microscopy Zeiss Lightsheet 7
ELECTROPHYSIOLOGY	Extracellular stimulation and recordings <i>in vitro</i> Two-photon guided <i>in vivo</i> single cell electroporation
RODENT SURGERIES	Stereotaxic injections Neonatal intraventricular injections Craniectomy and chronic cranial windows Transcardial perfusion and brain extraction
BIOCHEMISTRY	Immunolabeling-enabled 3-D Imaging of Solvent-Cleared Organs (iDISCO) Plasmid amplification and purification Quantitative real-time PCR Western blots
LANGUAGES AND TOOLS	Python Matlab ImageJ Ilastik Vaa3d GraphPad Prism Adobe Illustrator Adobe InDesign
MACHINE LEARNING	Convolutional neural network, clustering

PUBLICATIONS

- 2022 | **Learning-related congruent and incongruent changes of excitation and inhibition in distinct cortical areas.**
PLOS Biology. doi: 10.1371/journal.pbio.3001667
Vahid Esmaeili, Anastasiia Oryshchuk, Reza Asri, Keita Tamura, Georgios Foustoukos, Yanqi Liu, Romain Guet, Sylvain Crochet, Carl C. H. Petersen
- 2022 | **Axonal and dendritic morphology of excitatory neurons in layer 2/3 mouse barrel cortex imaged through whole-brain two-photon tomography and registered to a digital brain atlas.**
Frontiers in Neuroanatomy. doi: 10.3389/fnana.2021.791015.
Yanqi Liu*, Georgios Foustoukos*, Sylvain Crochet, Carl Petersen
- 2021 | **Rapid suppression and sustained activation of distinct cortical regions for a delayed sensory-triggered motor response.**
Neuron doi: 10.1016/j.neuron.2021.05.005.
Vahid Esmaeili, Keita Tamura, Samuel P. Muscinelli, Alireza Modirshanechi, Marta Boscaglia, Ashley B. Lee, Anastasiia Oryshchuk, Georgios Foustoukos, Yanqi Liu, Sylvain Crochet, Wulfram Gerstner, Carl C. H. Petersen

ACADEMIC CONFERENCES

- 11.2022 | **Poster presentation**, Society for Neuroscience meeting 2022
San Diego, United States
"Quantification of axonal projections from neurons located in layers 2/3, 4, 5 and 6 of mouse barrel cortex"
- 11.2021 | **Virtual Poster presentation**, Society for Neuroscience meeting 2021
"Long-range axonal projections of individual neurons in mouse layer 2/3 barrel cortex "
- 05.2018 | **Poster presentation**, Canadian neuroscience meeting 2018
Vancouver, Canada
"The effect of mild Na⁺/K⁺ ATPase inhibition by ouabain during spreading depolarization"

TEACHING

- 02 - 07.2022 | **Master project supervision**
Ecole polytechnique fédérale de Lausanne, Switzerland
L. Délez, "Comparison of projection patterns of neurons in cortical layers 2/3 and layer 5 of the mouse barrel cortex"
- 2019-2021 | **Teaching assistant**, Neuroscience: Cellular and circuit mechanisms
Ecole polytechnique fédérale de Lausanne, Switzerland
Supervise student exercise sessions and assist students project with analyzing electrophysiology data using MATLAB or Python.
- 2020-2021 | **Teaching assistant**, Cellular Mechanisms of Brain Function
Self-paced online Edx course
Update course content and address questions in the discussion forum.

HOBBIES

Hiking, Alpine Skiing, Reading, Traveling, Running, Video gaming, Baking